RESPONSE OF THIN-WALLED CYLINDERS TO AERODYNAMIC EXCITATION

by

RAJASEKHARIAH NATARAJA

B.E., M.E.

A Doctoral Thesis

Submitted in partial fulfilment of the requirements

for the award of

Doctor of Philosophy of the

Loughborough University of Technology

November 1974

Supervisor: Prof. D. J. Johns,

Ph.D., C.Eng., F.R.Ae.S., A.F.A.I.A.A.

Department of Transport Technology

RESPONSE OF THIN-WALLED CYLINDERS TO

AERODYNAMIC EXCITATION

SUMMARY

Non-linear vibrations of thin-walled shells under aerodynamic excitation are investigated using Flugge's thin shell theory, modified to include the effects of large deformations. The theory is applicable to any type of boundary conditions and various types of normal loading. The formulation includes mean or initial deformations of the median surface. A probabilistic-deterministic analysis of fatigue, representative of wind effects on earth-borne structures, is proposed based on the derived stresses and the Palmgren-Miner rule. Extentions of the non-linear theory to include structural damping and to analyse single mode static collapse of thin shells are also outlined.

In the random vibration analysis, based on energy methods, the multi-mode random response of thin shells under wind loading are studied. A fixed-free shell configuration is investigated in detail, though the formulation is applicable to any type of boundary conditions.

Oscillatory pressures round rigid cylinders and flexible shells are measured in the tests conducted in the 43" x 30" low speed wind tunnel. Three low pressure transducers-DISA type 51F32-are employed for the purpose. The tests cover the range of Reynolds numbers of 0.4×10^5 to 2.85×10^5.

The effect of shell flexibility on the shedding of vortices is studied by comparison with the results of the rigid cylinder pressure measurements. Also, the 3-D effects on the oscillatory

pressures are identified.

The response of two thin shells under wind excitation
are studied experimentally, using the results from strain
gauge records.   The oscillatory pressures and the response
are analysed for the rms values by using analog methods.
Spectral analysis of these signals are carried out on the
Fourier Analyser HP5451-A which employs digital analysis
techniques.   Measured response spectra are compared with
those computed from the random vibration theory developed
here.

ACKNOWLEDGEMENTS

C O N T E N T S

PART A — THEORY

LIST OF TABLES

LIST OF PLATES

LIST OF FIGURES

NOTATION

a_i	Fourier pressure coefficients
a_{ij}	coefficients in the dynamic analysis
A, B, C, A_1, B_1, C_1	displacement coefficients
c	viscous damping coefficient, beam characteristic constant
C	characteristic velocity
C_p	pressure coefficient
D	diameter, drag force
$\mathcal{D}$	fatigue damage
E	Young's modulus
$E\{\cdot\}$	expected value of
F	force
F_{ij}	coefficients in the random analysis
f	frequency
f_s	Strouhal frequency
$g(i\omega)$	equivalent non-dimensional complex displacement coefficient
g	structural damping coefficient
h	thickness of the shell
$H(i\omega), H(\omega)$	transfer function
i	$\sqrt{-1}$
I_1 to I_6	integrals (see Appendix IV)
k	Weibull index, spring constants in Duffing's equation
l, L	length
L	lift force
m	slope of S-N curve, axial mode number

M	mass per unit length of the shell
M_x etc.	moment resultants
n	circumferential mode number
N	fatigue life in cycles
N_x etc.	force resultants
$p(\cdot)$	probability of occurance (probability density)
$p(t)$	pressure
$\rho(\omega)$	FT of pressure
P	force
$P(\cdot)$	probability of exceedence
q	dynamic pressure
Q	shear force
R	return period
Re	Reynolds number
R_j	equivalent Fourier pressure coefficients
$R_{xx}(\tau)$ etc.	correlations
St	Strouhal number
t	time variable
T	total time (sampling period), kinetic energy
u, v, w	displacements
U	strain energy
V	volume, velocity
W	work potential
$w(\omega)$	FT of w
x, y, z, θ	shell coordinates
α	index in ground wind distribution function

β	non-dimensional parameter $h^2/12a^2$
$\gamma^2(f)$	coherence function
δ	virtual increment, logarithmic decrement, Kronecker delta, determinant
Δ	increment, non-dimensional frequency parameter $\rho a^2 \omega^2 (1-\nu^2)/E$
ϵ_{xx} etc.	strains
θ	angular position, coordinate, inverse slope of S-N curve
λ	beam characteristic constant (Equation 3.8)
ν	Poisson ratio
ξ	non-dimensional axial separation distance
Π	continuous product
ρ	mass density of shell
ρ_a	mass density of air
$\sigma,\ \sigma_0,\ \sigma_{xx}$ etc.	stresses
σ_1	standard deviation
$\sigma_2,\ \sigma_3$	see Appendix XIII
τ	period, time delay
ϕ, ψ	beam functions
ψ_1^2	mean square value
ω	circular frequency
Ω	total potential

Additional Notation:

coordinate suffixes to displacements denote derivatives

(e.g. $u_x = \dfrac{\partial u}{\partial x}$, $v_{\theta\theta} = \dfrac{\partial^2 v}{\partial \theta^2}$)

suffix T denotes total quantities

suffix S denotes static component

suffix D denotes dynamic part

superscript (·) denotes time derivative

(e.g. $\dot{u} = \dfrac{\partial u}{\partial t}$)

superscript (*) stands for rms value, complex conjugate

superscript (') denote derivative with respect to x, on coordinates denotes different location

superscript (–) denotes mean values

PART   A

THEORY

1. INTRODUCTION.

1.1 Summary.

A comprehensive review of the literature in the thin
shell theory is presented including a detailed discussion
of non-linear effects. Importance of ground wind distri-
bution for loading actions on full scale structures is
briefly described. A review is also given of the measure-
ment and analysis techniques of oscillatory wind pressure
forces (lift and drag) on circular cylinders. The statis-
tical methods available for the response of thin cylindrical
shells to aerodynamic excitation are also considered. The
statement of the present problem and methods of analysis are
then briefly described.

1.2 General.

Cylindrical structures form one of the most basic
types of construction in the field of civil engineering and
in aerospace engineering practice. With current trends in
design and fabrication these structures increasingly tend to
be slender and thin and as such are amenable to large ampli-
tude response to fluctuating forces and consequent oscilla-
tory and divergent instabilities. Circular cylinders in
particular experience fluctuating forces with a narrow band
of frequencies in a uniform wind stream. This is a conse-
quence of the phenomenon of vortex shedding which may be
either stable or unstable depending upon the flow Reynolds
number. In the latter case and in the presence of free
stream turbulence the frequency band width increases. Thin
cylindrical shell type structures such as chimneys and
rockets on their launch pads in the ground shear flow of the

- 1 -

earth's boundary layer are thus subject to steady fluctuating forces where a definite harmonic is predominant or to a random pressure field with a number of harmonics, and both present a complicated dynamic response problem. This is particularly important in the estimation of fatigue life. It is then necessary (i) to develop a suitable shell theory to evaluate the stress levels accurately, which implies the solution of the deterministic vibration problem to obtain the transfer function of the structural system, (ii) to assess and adequately describe the nature of shear flow in earth's boundary layer, (iii) to measure the aerodynamic forces and moments on the structure in question and (iv) to obtain the response of the structure to the measured excitation inputs.

A large number of published works are cited in the literature covering one or more aspects of the problem outlined. Marris[1] and Johns[2] presented reviews of wind induced vibrations and their importance in structural design. In the following sections the present state of the art in the field is comprehensively reviewed.

1.3   Choice of the Thin Shell Theory.

1.3.1   Basic Thin Shell Theory.

A large number of different theories have been proposed by various investigators all purporting to describe the motion of a thin shell. The differences in these theories result from differences in the simplifying assumptions made and the exact stage in the derivation at which the assumptions are utilized. Rayleigh[3] evaluated the displacements of a point on the shell surface from an energy consideration assuming that the middle surface of the shell is inextensible.

This was shown by Love[4] to be inaccurate near the boundaries.

In the well known First Approximation theory, Love[4] obtained all deformations of the shell in terms of mid-plane deformations and the physical assumptions (see Appendix I) under which these are derived have long been accepted for sufficiently thin shells.

Love's[4] Second Approximation theory assumes that the extentional strains are small compared with the flexural strains and that the normal displacements are not completely independent of the normal coordinate. Later, Timoshenko[5] presented a detailed shell theory which is consistent with the First Approximation theory. Basset[6] pointed out the inconsistencies in the First Approximation theory and Vlasov[7] also pointed out that the above theories contradict the principle of conservation of energy and do not satisfy Betti's reciprocity condition.

Starting from three dimensional elasticity equations, several authors[8,9,10] deduced shell theories retaining terms to various degrees of accuracy but these were later found to be of little advantage. Flugge's[11] theory of thin shells retains terms of degree higher than those in Timoshenko theory, yet it is computationally tractable and satisfies the reciprocity condition. This theory has since been an accepted standard to which other theories are referred to for accuracy. Donnell[12] obtained by physical arguments equations which were uncoupled in the three displacement coordinates and hence simple to use but are limited in accuracy.

Free vibrations of cylindrical shells also were in-
vestigated by Rayleigh[13] considering the membrane stresses
only. Baron and Bleich[14] and Junger and Rosato[15]
accounted for bending stresses in addition to the membrane
stresses. Lin and Morgan[16] and Hermann and Mirsky[17]
included rotatory inertias and shear deformations in their
analyses. Yu[18] performed a similar analysis using
Donnell's theory. It was concluded that the effect of
shear deformations and rotatory inertia was to reduce the
propagation velocities and to lower the natural frequencies.

Naghdi[19] in an analysis based on a variational
method, considered the nonaxisymmetric motion of shells and
also included rotatory inertias. Hermann and Armenakas[20]
developed nonaxisymmetric forced motion of cylindrical
shells with initial stresses which forms a more realistic
approximation. Reismann[21] analysed this problem according
to Flugge's theory. Medige[22] has solved essentially the
equations of Reference (20) without initial stresses and has
applied them to the case of blast loading.

Recently, Leissa[23] has presented an extensive com-
pilation of published literature on the vibrations of shells
with an appraisal of various theories concerning complicating
effects such as large deformations, stiffeners etc. Sanders
[24] derived an improved form of Love's First Approximation
theory in which all strains vanish for rigid body motions.
This was achieved by considering the equilibrium equations and
the principle of virtual work in the definition of the strain
displacement relations.

In the present investigation, Flugge's[11] linear
theory is modified to include geometric non-linearities
arising due to large deformations and the derivations are
carried out ab initio.

1.3.2   Large Deformation Considerations.

When the deformations of the shell are large compared
to the thickness of the shell, the higher order terms in
the strain displacement relations are no longer negligible.
Considerable disagreement in the literature exists as to
the non-linear behaviour of the shell and whether it is
hardening or softening due to such geometric non-linearities
and also as to the effect of boundary conditions in such a
case. Reissner[25] in his pioneering work, reported that
the non-linearity may be either softening or hardening
depending on the number of circumferential waves in the mode
shape. The analysis was based on Donnell's theory and the
assumed modes were sinusoidal in both axial and circumfer-
ential directions but not necessarily in time. Chu's[26]
investigations indicated that the non-linearity is of the
hardening type. Nowinski[27] further confirmed Chu's results
but his attempt to satisfy the compatibility condition
resulted in satisfaction of a different set of boundary
conditions. Cummings[28] obtained a similar hardening be-
haviour.

Evensen[29] and Olson[30] observed through experiments
that the non-linearity was softening. The results of
Evensen[31] and Evensen and Fulton[32] indicated that for
certain geometries and certain ratios of axial wave number
to circumferential wave number the non-linearity is hardening

and for others it is softening. These studies were based on Donnell's theory and for simply supported boundary conditions but the end moments were non-zero because of the non-linear terms.

Matsuzaki and Kobayashi[33] solved the case with clamped ends and substantiated by experiments that the non-linearity is softening. It is interesting to note that Evensen's[29] and Olson's[30] experiments were also on clamped shells.

Some results in Reference (32) and more recently, those of Leissa and Kadi[34] indicated that the shell behaves like a soft spring initially and as the amplitude is further increased, it behaves like a hard spring. Mayers and Wrenn [35] using the "exact" theory of Sanders [24] concluded that the free non-linear vibration is nonperiodic and of the hard-ening type. Some results of the present investigation reported in Reference (36) indicate that the non-linearity is hardening as applied to a clamped - free thin circular cylin-drical shell.

1.4   Ground Wind Distribution.

Ground-fixed structures are immersed in the shear flow of earth's boundary layer. An assessment of the wind loads on them could only be obtained by measurements over long periods of time. Extensive data and literature are available on the subject. The basic wind speed records are maintained by the Meteorological Offices. However, complications in the data analysis arise due to statistical uncertainty in the distribution. An excellent account of wind data has been given in Reference (37) and of measurement techniques in Reference (38). Shellard[39] and Davenport[40] have discussed

the methods of interpretation of wind records as applied to structural design. References (41, 42, 43 and 44) have considered the variation of wind speeds with hight and averaging time. Methods of simulation of shear flow of earth's boundary layer in experimental investigations have been outlined by Cermak and Arya[45]. Design codes based on gust speeds of wind with a fifty year return period have been laid down in Reference (46). A comparison of various codes of practice is discussed by Pierce[47] and Sachs[38]. A detailed description of the ground wind distribution based on existing numerical data is given elsewhere in the present analysis (see Appendix X). However, the experimental investigation in the present analysis is based on "uniform" wind rather than on simulated shear flow.

1.5   Flow Field Round a Circular Cylinder.

A large number of researchers have contributed to the study of flow past circular cylinders, starting from the work of Strouhal[48] who showed that the frequency of shedding of a pair of complementary vortices increases linearly with flow velocity over a range of velocities yielding a constant value of the non-dimensional frequency – the Strouhal number. Rayleigh[49] established that the vortex shedding frequency, and hence the Strouhal number, is also a function of Reynolds number. Tritton[50], Roshko[51] and Gould[52] have presented experimental pressure distribution data covering a large range of Reynolds numbers. These results have been consolidated in Reference (53). Except for Reference (52) the others have referred to the time-average pressure distribution on rigid two dimensional cylinders while (52) has referred to three dimensional cylinders and has included root mean square

pressure measurements in addition to average pressure data.

Bishop and Hassan[54] measured fluctuating lift and drag forces on a rigid cylinder in the Reynolds number range of 3,600 - 11,000 in a water channel. The results indicated that the fluctuating lift forces were an order of magnitude greater than the fluctuating drag forces and that the lift frequency was equal to the frequency of shedding of a pair of vortices whilst the drag frequency was twice of that. Keefe[55], Fung[56], Chen[57], Schimdt[58] and Gerrald[59] are a few other investigators to have studied the fluctuating forces on a rigid cylinder at various Reynolds numbers. Surry[60] investigated the influence of the free stream turbulence on fluctuating pressure distributions around rigid cylinders at a Reynolds number of approximately 40,000. Increase in the free stream turbulence resulted in an increase in the fluctuating lift and a decrease in the fluctuating drag. Also detected was the presence of harmonics of Strouhal frequency. Gould's[52] tests were at high Reynolds numbers of 2.7×10^6 and 5.5×10^6 in the compressed air tunnel on 3" and 6" diameter models. From a correlation study of the pressure distributions on these rigid cylinders, it was found that due to three dimensional effects the flow characteristics near the top were so phased as to be more likely to cause in line bending oscillations, while away from the tip region ovalling was thought to be the more likely result.

Furguson and Parkinson[61] tested in airflow, a rigid cylinder on flexible supports and found that the maximum transverse amplitudes corresponded to $\frac{V}{fD} = 6.1$. Wootton[62]

conducted wind tunnel tests on model stacks and reported that
the response depends on aspect ratio, mass ratio, damping and
surface roughness. Maximum amplitudes occured at a Strouhal
number of S_t = 0.16. Both References (54) and (61) have
shown that there is a range of velocities over which "locking-
in" occurs characterized by transverse oscillations perpendi-
cular to the free stream at frequencies close to the struc-
tural natural frequencies. In a recent study on model piles,
King, Prosser and Johns[63] concluded that the critical $\frac{V}{fD}$
depends on a stability parameter (the product of mass and
damping) and that there are two regions of instability - viz.
unsymmetric and symmetric vortex shedding. Cincotta[64],
Toebes[65], Toebes and Ramamurthy[66] and Ukeguchi et al.[67]
have studied experimentally the unsteady forces and vortex
excitation of cylinders. It may be noted that in all these
cases, the cylinder considered was rigid but elastically
mounted to allow for the motion of the cylinder.

1.6   Transfer Function Evaluation.

Accurate measurements of the aerodynamic forcing func-
tion and of the response of the flexible structure should
lead naturally to a description of the input-output relation
between them in the form of the transfer function of the
system. Such an attempt has been reported by Campbell and
Etkin[68] for a cylindrical structure with idealized des-
cription of the structural stiffness. Response spectra for
bending of a cantilever was obtained by Cooper[69]. Novak[70]
also described response spectra for lateral vibrations of
cylindrical structures. Davenport[71] and Handa and
Clarkson[72] have derived a statistical description of the

response spectra for slender structures. To the author's knowledge there is no literature cited of the accurate measurement of unsteady aerodynamic pressures around a flexible circular cylindrical shell and of the consequent dynamic excitation particularly of the three dimensional kind.

A vast amount of literature is now available on the wind effects on buildings and structures through conference procedings (73, 74, 75, 76 and 77). Numerous studies on wind induced vibrations of structures are also presented in Reference (78). The methods for the theoretical evaluation of the random response of complicated structures and for fatigue analysis to some extent have been discussed in detail by Robson[79], Crandall[80] and Lin[81].

1.7   Statement of the Problem.

In the present investigation,

(i)   a generalized non-linear thin shell theory of cylindrical shells is developed, valid for any boundary condition and for any distribution of normal loading including wind loading,

(ii) the fluctuating aerodynamic pressure distribution is measured in real time on two dimensional rigid cylinders and on three dimensional rigid and flexible cylinders,

(iii) the response of flexible cylinders to various dynamic inputs is also measured,

and

(iv) theoretical and experimental transfer functions based

on a statistical energy method are evaluated and a method
of prediction of random fatigue life is also outlined.

1.8   Layout of the Dissertation.

Part A of the thesis is devoted to theoretical
analyses; Part B considers the experimental studies and
Part C contains the discussion of results. Information is
generously drawn in to the various sections of the disser-
tation from the expressions and ideas developed in the
thirteen Appendices.

In Chapter 2, a non-linear thin shell theory is
developed ab initio, following Flugge's description of
shell motion. An energy formulation is used. Various
types of surface tractions are considered. Energy for-
mulation of random response and fatigue problem based on
Miner's rule are also outlined.

In Chapter 3, the methods of dynamic analysis
incorporating method of averaging and Rayleigh-Ritz
procedure are described. Solution procedures are esta-
blished for free linear and free and forced non-linear
vibrations. The characteristic nature of the non-line-
arity is also qualitatively established.

In Chapter 4, the static analysis of the shell is
carried out for impressed time-average wind loading.

In Chapter 5, the more realistic problem of wind
excitation inclusive of static deformation is carried
out both as a deterministic and as a random process.

In Chapter 6, experimental concepts are developed
in a logical sequence. The various parameters involved in
the experimental procedure are identified and outlined,

including the statistical parameters.

In Chapter 7, a steady state vibration study of flexible shells is described with the shells in question being under single point excitation. The influence of transducer mass and cable stiffness on the natural frequencies are accounted for. The response is also obtained for various magnitudes of the forcing function.

In Chapter 8, fluctuating pressure measurement and analysis techniques, instrumentation and data processing equipment are detailed. For accurate measurements of fluctuating pressures the use of DISA 51F32 low pressure transducers is outlined. Techniques of spectral analysis of the analogue data carried out on HP 5451A Fourier Analyzer is described. Analogue procedure for the evaluation of root mean square pressures is also discussed.

In Chapter 9, the results of various cases of deterministic analysis are presented.

In Chapter 10 are described the results of experimental measurements and data analysis. The overall effects of pressure distribution on the shell and the distribution functions are also discussed.

In Chapter 11, the results of response analysis utilizing statistical methods are described.

In Chapter 12 the conclusions of this extensive integrated study are listed.

It is believed that the list of thirteen Appendices adequately describes their contents.

2. FORMULATION.

2.1 Introduction.

Deformations encountered in modern cylindrical shell type of structures such as chimneys, missiles and launch vehicles are comparable in order of magnitude to the thickness of the shell. This implies that the higher order terms in the strain displacement relations are no longer negligible. Further, accurate evaluation of stress levels is necessary from the point of view of estimation of fatigue life. For the purpose, an accurate shell theory and non-linear analysis are required. In the literature Flugge's theory[11] and Sanders theory[24] are looked for whenever accuracy is important. However, it was demonstrated by Sharma and Johns[82] from a comparison with the exact solution of Forsberg[83] that Flugge's theory gives acceptable estimates of natural frequency in a vibration problem when used in conjunction with beam functions[84] for displacement description. Also from a physico-geometrical stand point, the strain-displacement relations and the subsequent vibration analysis may be easily derived.

In the present analysis Flugge's theory is hence followed and is modified to include non-linearities arising from large deformations. For ease of comparison the non-linear terms in the analysis are identified throughout in the notation with chain brackets { }. Expressions for strain energy, kinetic energy, work potential, stress resultants are all derived from first principles in this section.

The derivations are subject to approximations assumed in Flugge's theory (see Appendix I) excepting that the

second order terms arising due to large radial deformations are not negligible in the strain displacement relations.

2.2   Strain-Displacement and Stress-Strain Relations.

The geometry of the shell and the coordinate system are shown in Figure (2.1). For end boundary conditions corresponding to a fixed-free configuration, the circumferential full waves relating to circumferential mode numbers n and axial mode shapes associated with the axial mode numbers m are sketched in Figure (2.2). The displacements of a point A on the shell element are shown in Figure (2.3). In terms of mid-plane displacements the general expressions for strains at any point on the shell volume derived in Appendix I are

$$\epsilon_{xx} = u_x - zw_{xx} + \left\{ 1/2 \; w_x^2 \right\} ,$$

$$\epsilon_{\theta\theta} = \frac{v_\theta}{a} + \frac{w}{a+z} - \frac{zw_{\theta\theta}}{a(a+z)} + \left\{ 1/2 \; \frac{w_\theta^2}{(a+z)^2} \right\} ,$$

$$\epsilon_{x\theta} = \frac{u_\theta}{a+z} + \frac{a+z}{a} v_x - \left(\frac{z}{a} + \frac{z}{a+z} \right) w_{x\theta} + \left\{ \frac{w_x \, w_\theta}{a+z} \right\}$$
$$2.1$$

The non-linear terms enclosed in chain brackets are assumed to be due to _moderate_ rotations corresponding to large displacement w in the radial direction. It is to be noted that the displacement relations themselves are linear as a consequence of this assumption. Equations (2.1) are the same as those of Flugge[11] except for the additional non-linear terms.

It is assumed that the stress strain law is linear. In addition, consistent with the conventional thin shell

theory a state of plane stress is assumed. Under these assumptions,

$$\sigma_{zz} = \sigma_{xz} = \sigma_{yz} \approx 0 \qquad\qquad 2.2$$

and

$$\sigma_{xx} = \frac{E}{1-\nu^2} (\epsilon_{xx} + \nu\,\epsilon_{\theta\theta})\,,$$

$$\sigma_{\theta\theta} = \frac{E}{1-\nu^2} (\epsilon_{\theta\theta} + \nu\,\epsilon_{xx})\,,$$

$$\sigma_{x\theta} = \frac{E}{2(1+\nu)} \epsilon_{x\theta}$$

or

$$\begin{Bmatrix} \sigma_{xx} \\ \sigma_{\theta\theta} \\ \sigma_{x\theta} \end{Bmatrix} = \frac{E}{1-\nu^2} \begin{bmatrix} 1 & \nu & 0 \\ \nu & 1 & 0 \\ 0 & 0 & \frac{1-\nu}{2} \end{bmatrix} \begin{Bmatrix} \epsilon_{xx} \\ \epsilon_{\theta\theta} \\ \epsilon_{x\theta} \end{Bmatrix}$$

$$2.3$$

2.3   Strain Energy.

There exists a system of infinitesimally small virtual strains $\delta\epsilon_{xx}$, $\delta\epsilon_{\theta\theta}$ and $\delta\epsilon_{x\theta}$ corresponding to a set of assumed infinitesimally small virtual displacements δu, δv and δw. Assuming a quasi-steady state of stress, the incremental virtual strain energy due to these displacements is

$$\delta U = \int_{vol} (\sigma_{xx}\,\delta\epsilon_{xx} + \sigma_{\theta\theta}\,\delta\epsilon_{\theta\theta} + \sigma_{x\theta}\,\delta\epsilon_{x\theta})\,dvol$$

$$2.4$$

For a Hookean material substitution of Equations (2.3) into (2.4) yields

$$U = \frac{E}{2(1-\nu^2)} \int_{-h/2}^{h/2} \int_0^{2\pi} \int_0^1 [\epsilon_{xx}^2 + \epsilon_{\theta\theta}^2 + 2\nu\epsilon_{xx}\epsilon_{\theta\theta} + \frac{1-\nu}{2}\epsilon_{x\theta}^2] \cdot (a+z)\,d\theta\,dx\,dz$$

$$2.5$$

- 15 -

where $(a+z)\, d\theta\, dx\, dz$ is an elemental volume at a distance z from the median surface. Since the strains contain linear and non-linear parts, for convenience the total strain energy may be written as

$$U \;=\; U_{linear} + U_{non\text{-}linear} \qquad\qquad 2.6$$

2.3.1 Linear Strain Energy.

The strain energy obtained by the substitution of linear part of Equation (2.1) into Equation (2.5) is termed here as linear strain energy. Integrating (2.5) with respect to z and retaining terms up to the order of h^3/a^3 in the expansion of $\ln \dfrac{1 + h/2a}{1 - h/2a}$, the linear strain energy is

$$U_{lin} = \frac{Eah}{2(1-\nu^2)} \int_0^{2\pi} \int_0^1 \Big[\, u_x{}^2 + \frac{1}{a^2}\,(\,w + v_\theta\,)^2 + \frac{2\nu}{a}\, u_x\,(v_\theta + w)$$

$$+ \frac{1-\nu}{2a^2}\,(\,u_\theta + a v_x\,)^2 + \beta\,\Big[a^2 w_{xx}{}^2 + \frac{1}{a^2}\,(\,w + w_{\theta\theta}\,)^2$$

$$- 2a u_x w_{xx} + 2\nu\, w_{xx}\,(\,w_{\theta\theta} - v_\theta\,) + \frac{1-\nu}{2}\Big(\frac{u_\theta{}^2}{a^2} + 3 v_x{}^2 \Big)$$

$$+ 4 w_{x\theta}{}^2 + \frac{2}{a}\, u_\theta w_{x\theta} - 6 v_x\, w_{x\theta}\,\Big]\,\Big]\; dx\, d\theta\;,$$

$$\qquad\qquad 2.7$$

where $\quad \beta = \dfrac{h^2}{12a^2}\,.$

This expression is identical to the one that is derived in Reference (82).

2.3.2 Non-Linear Strain Energy.

That part of the total strain energy which arises due to non-linear terms and the product of linear terms with

non-linear terms in the integral (2.5) is referred to here as the non-linear strain energy. Integration of this part of (2.5) with respect to z and rearranging like terms results in

$$U_{non-linear} = \frac{Eah}{2(1-\nu^2)} \int_0^{2\pi} \int_0^1 \left\{ \frac{w_x^4}{4} + u_x w_x^2 + \frac{w_\theta^4}{4a^4} + \frac{v_\theta w_\theta^2}{a^3} + \frac{w w_\theta^2}{a^3} \right.$$

$$+ \frac{\nu}{a} w_x^2 (v_\theta + w) + \frac{\nu u_x w_\theta^2}{a^2} + \frac{w_x^2 w_\theta^2}{2a^2}$$

$$+ \frac{1-\nu}{a^2} w_x w_\theta (u_\theta + av_x) + \beta \left[-aw_{xx}w_x^2 \right.$$

$$+ \frac{6w_\theta^4}{4a^4} + \frac{v_\theta w_\theta^2}{a^3} + \frac{2w_{\theta\theta}w_\theta^2}{a^3} + \frac{3w w_\theta^2}{a^3}$$

$$+ \frac{\nu w_x w_\theta^2}{a^2} + \frac{\nu}{a} w_{xx} w_\theta^2 + \frac{w_x w_\theta^2}{2a^2}$$

$$\left. + (1-\nu) w_x w_\theta (u_\theta + aw_{x\theta}) \right] \left. \right\} dx \; d\theta \qquad 2.8$$

where terms up to the order of h^3/a^3 only are retained in the logarithmic expansion of $\ln \left[\frac{1+h/2a}{1-h/2a} \right]$. It is seen later in Section (3.3) that this seemingly complex integral leads to a very simple algebraic expression in the characteristic equation under the single mode response assumption.

2.4   Kinetic Energy.

The kinetic energy of an element at point O on the median surface (see Figure 2.3) is given by

$$(\delta T)_{VO} = \frac{1}{2} \; \rho \left[(\dot{u})^2 + (\dot{v})^2 + (\dot{w})^2 \right] dx \; dz \; ad\theta \qquad 2.9$$

An elemental volume at point A at a distance z from the median surface has kinetic energy

$$(\delta T)_{VA} = \frac{1}{2} \; \rho \left[(\dot{u}_A)^2 + (\dot{v}_A)^2 + (\dot{w}_A)^2 \right] (a+z)d\theta \; dx \; dz$$

$$2.10$$

Integration over the volume gives

$$\int_V \delta T = T = \frac{\rho}{2} \int_0^1 \int_0^{2\pi} \int_{-h/2}^{h/2} [(\dot{u} - z\dot{w}_x)^2 + (\frac{a+z}{a} \dot{v} + \frac{z}{a}\dot{w}_\theta)^2$$

$$+ (\dot{w})^2] (a+z) \, d\theta \, dx \, dz.$$

or

$$T = \frac{\rho a h}{2} \int_0^1 \int_0^{2\pi} [\dot{u}^2 + \dot{v}^2 + \dot{w}^2 + \beta [a\dot{w}_x(a\dot{w}_x - 2\dot{u})$$

$$+ (\dot{w}_\theta - \dot{v})(\dot{w}_\theta - 3\dot{v})]] \, d\theta \, dx \qquad\qquad 2.11$$

where terms in the first parentheses are due to rotatory inertias and those in the second set of parentheses are contributed by in-plane inertias. It is observed that within the frame work of assumptions (1) and (2) in Appendix I the non-linearity due to large deformations does not affect the kinetic energy.

2.5   Work Potential.

The work done by surface tractions is evaluated in Appendix II for arbitrary normal loading distribution. It is assumed that the external loads are harmonic functions in θ direction and in time. The specific types of distribution are considered below.

2.5.1   Concentrated Load at the Tip.

A concentrated load P is considered at the free end x = 1 and θ = 0 acting radially inwards on the shell and is assumed to be harmonic in time with frequency ω, defined by

$$P(t) = - P \cos \omega t \qquad\qquad 2.12a$$

If $w(1) = w_1$ is the tip deflection, the work done is

$$W(t) = (-P)w_1 \cos \omega t. \qquad\qquad 2.13a$$

- 18 -

The negative sign of P implies that the load is acting radially inwards and the z coordinate is positive radially outwards.

2.5.2   Line Load - Beam Function Distribution.

In this hypothetical case, the load is assumed to be distributed spatially along a generator at $\theta = 0$ with the distribution function proportional to the clamped-free beam function (see Appendix III) and to be a single harmonic in time. The functional form is

$$p(x,t) = -p_0 \phi(x) \cos \omega t . \qquad 2.12b$$

The work done is then,

$$W(t) = -p_0 \int_0^1 \phi(x) w(x,t) \cos \omega t \, dx$$

i.e.,

$$W(t) = -p_0 \cos \omega t \int_0^1 \phi(x) w(x,t) \, dx. \qquad 2.13b$$

where $w(x,t)$ is the displacement distribution function along a generator at $\theta = 0$ of the form

$$w = \phi(x) f(t) = \phi(x) \cos \omega t$$

2.5.3   Distributed Load - Harmonic Distribution.

The load is distributed uniformly in the axial direction and harmonically in the circumferential direction in the form

$$p(x,\theta,t) = p(\theta,t) = -p_0 \cos n\theta \cos \omega t \qquad 2.12c$$

The work potential is

$$W(t) = \int_0^1 \int_0^{2\pi} -p_0 \cos n\theta \; w(x,\theta,t) \cos \omega t \; dx d\theta$$

or

$$W(t) = -p_0 \cos \omega t \int_0^1 \int_0^{2\pi} \cos n\theta \; w(x,\theta,t) \, dx \, d\theta$$

$$2.13c$$

where $w(x,\theta,t)$ is the displacement distribution function (see Section 3, Equation 3.1).

2.5.4   Wind Load Distribution.

The more realistic case of wind load distribution considering the variation with height of the structure (axial direction in the present analysis) is discussed in detail in Appendix XII. The coefficient and the index in the power law are derived on the basis of the 3-second gust data given in Reference (46). The circumferential pressure distribution may be expressed in the form of a truncated Fourier series. For the purposes of analysis, the total pressure may be resolved into two components namely the time-average pressure distribution producing static deformations and the root mean square (rms) value of the fluctuating pressures with a characteristic frequency equal to the predominant frequency in the average power spectrum. Symbolically, the sectional total pressure at a point is

$$p_T (x,\theta,t) = p_S (x,\theta) + p (x,\theta,t) \qquad\qquad 2.14$$

such that
$$p_S (x,\theta) = \overline{p_T (x,\theta,t)} \qquad\qquad 2.15$$

and
$$\overline{p (x,\theta,t)} = 0 \qquad\qquad 2.16$$

where a "bar" indicates a time-average value. Considering the fluctuating part to be a single frequency component,

$$p (x,\theta,t) = - p_0 \, f(x) \, g(\theta) \cos \omega t \qquad\qquad 2.12d$$

where
$$f(x) = K \, x^{\alpha} \qquad\qquad 2.18$$

with K and α as defined in Appendix XII.

and

$$g (\theta) = \sum_{i=0}^{N} a_i \cos i\theta \qquad\qquad 2.19a$$

The work done by these fluctuating forces could be written (see Appendix II) as

$$W (t) = \int_0^1 \int_0^{2\pi} - p_0 \, f(x) \, g (\theta) \left[w + \frac{1}{2} \left\{ \frac{w^2}{a} - \frac{2vw_\theta}{a} \right. \right.$$

$$+ \frac{v^2}{a} + u_x w - uw_x \} \;] \quad \cos \omega t \; dx \; d\theta$$

$$2.13d$$

Similarly the work done by the time-average pressures could be written including the non-linear terms as

$$W_S = \int\limits_0^1 \int\limits_0^{2\pi} - P_{SO} \; f \; (x) \; g_S (\theta) \; [\; w + \frac{1}{2} \{ \frac{w^2}{a} - \frac{2vw_\theta}{a} + \frac{v^2}{a}$$

$$+ u_x w - uw_x \} \;] \; dx \; d\theta \qquad 2.13e$$

where $\qquad P_S \; (x,\theta) \; = \; P_{SO} \; f \; (x) \; g_S \; (\theta) \qquad 2.12e$

with f (x) defined by (2.18) and

$$g_S \; (\theta) \; = \; \sum_{i=0}^{N} \; a_{iS} \; \cos i\theta \qquad 2.19b$$

In the above expressions the axial distribution of fluctuating and time-average pressures is assumed to be of the same form, as given by Equation (2.18).

The concepts developed here are utilized later in the dynamic and static analyses, once the displacement functions are chosen so as to satisfy the kinematic boundary conditions.

2.6 <u>Derived Stresses.</u>

It is essential to know the peak stress levels in the shell in order to estimate the fatigue life. The dynamic stresses, clearly, are functions of displacements and mode shapes. Expressions are derived here for the stress resultants in terms of the mid-plane displacements. Knowing the stress resultants the stresses could be computed. Alternately the stresses may be obtained by substituting Equations. (2.1) into Hooke's law given by Equations (2.2).

The stress resultants on a cylindrical shell element from Figure (2.4) are

$$N_x = \int_{-h/2}^{h/2} \sigma_x \left(1 + \frac{z}{a} \right) dz$$

$$N_\Theta = \int_{-h/2}^{h/2} \sigma_\Theta \, dz$$

$$N_{x\Theta} = \int_{-h/2}^{h/2} \sigma_{x\Theta} \left(1 + \frac{z}{a} \right) dz$$

$$N_{\Theta x} = \int_{-h/2}^{h/2} \sigma_{\Theta x} \, dz \, . \qquad \text{2.20a}$$

It is seen that for a cylindrical shell equality of shear stresses does not imply equality of shear stress resultants. The moments may be similarly written as

$$M_x = -\int_{-h/2}^{h/2} \sigma_x \left(1 + \frac{z}{a} \right) z dz$$

$$M_\Theta = -\int_{-h/2}^{h/2} \sigma_\Theta \, z dz$$

$$M_{x\Theta} = -\int_{-h/2}^{h/2} \sigma_{x\Theta} \left(1 + \frac{z}{a} \right) z dz$$

$$M_{\Theta x} = -\int_{-h/2}^{h/2} \sigma_{\Theta x} \, z dz \qquad \text{2.20b}$$

As in the case of "shear forces" the "twisting moments" are not equal. In thin shells this difference is

- 22 -

small and is often neglected. It is, however, very important in the exact formulation and is considered in the present analysis. It should be noted that in the derivation of Equations (2.20) no particular law of stress distribution is implied. Hence these definitions of "forces" and "moments" are always valid. The transverse "shear forces" Q_x and Q_θ have been omitted in accordance with the plane stress assumption. Assuming a linear stress distribution, the stresses are given by

$$\sigma_x = \frac{N_x}{h} - \frac{12\ M_x\ z}{h^3}$$

$$\sigma_\theta = \frac{N_\theta}{h} - \frac{12\ M_\theta\ z}{h^3}$$

$$\sigma_{x\theta} = \frac{N_{x\theta}}{h} - \frac{12\ M_{x\theta}\ z}{h^3}$$

$$\sigma_{\theta x} = \frac{N_{\theta x}}{h} - \frac{12\ M_{\theta x}\ z}{h^3} \qquad 2.21$$

In general, $\sigma_{x\theta} \neq \sigma_{\theta x}$ which implies that linear stress distribution assumption is not correct.

For a Hookean material, substitution of Equations (2.1) and (2.2) into Equation (2.20), and integration over the thickness yields, in terms of mid-plane displacements, the stress resultants as

$$N_x = \frac{Eh}{1-\nu^2}\ [\ u_x + \{\tfrac{1}{2}\ w_x^2\} + \frac{\nu v_\theta}{a} + \frac{\nu w}{a} + \frac{1}{2}\ \{\frac{\nu\ w_\theta^2}{a^2}\} +$$

$$\beta (\ - aw_{xx} + \frac{1}{2}\ \{\frac{\nu w_\theta^2}{a^2}\ \}\ )\ ]$$

- 23 -

$$N_\theta = \frac{Eh}{1-\nu^2} \left[\frac{v_\theta}{a} + \frac{\beta w_{\theta\theta}}{a} + \frac{w}{a}(1+\beta) + \left\{ \frac{1}{2} \frac{w_\theta^2}{a^2}(1+3\beta) \right\} + \nu u_x \right.$$

$$\left. + \left\{ \frac{1}{2} \nu w_x^2 \right\} \right]$$

$$N_{x\theta} = \frac{Eh}{2(1+\nu)} \left[\frac{u_\theta}{a} + v_x(1+\beta) - \beta w_{x\theta} + \left\{ \frac{w_x w_\theta}{a} \right\} \right]$$

$$N_{\theta x} = \frac{Eh}{2(1+\nu)} \left[\frac{u_\theta}{a}(1+\beta) + v_x + \beta w_{x\theta} + \left\{ \frac{w_x w_\theta}{a}(1+\beta) \right\} \right]$$

<div align="right">2.22a</div>

$$M_x = \frac{Eh\beta}{1-\nu^2} \left[-au_x + a^2 w_{xx} - \left\{ \frac{1}{2} a w_x^2 \right\} - \nu(v_\theta + w_{\theta\theta}) \right.$$

$$\left. + \left\{ \frac{1}{2} \frac{\nu w_\theta^2}{a} \right\} \right]$$

$$M_\theta = \frac{Eh\beta}{1-\nu^2} \left[w_{\theta\theta} + w + \left\{ \frac{w_\theta^2}{a} \right\} + \nu a^2 w_{xx} \right]$$

$$M_{x\theta} = \frac{Eh\beta}{2(1+\nu)} \left[-2a v_x + 2a w_{x\theta} \right]$$

$$M_{\theta x} = \frac{Eh\beta}{2(1+\nu)} \left[u_\theta - av_x + 2a w_{x\theta} + \left\{ w_x w_\theta \right\} \right]$$

<div align="right">2.22b</div>

In the above equations the contributions due to geometric non-linearities are identified by chain brackets. Omission of these terms result in expressions identical to those given in Reference (11).

2.7   Random Loading.

2.7.1   General.

The wind loading on chimney like structures covers a wide range of Reynolds numbers. This implies that the nature of the fluctuating aerodynamic loading may be of the broad band type in the Reynolds number region where there is no regular vortex shedding and of the narrow band random type elsewhere. The study of both types of loading is important, from the structural response point of view, because the loads are of larger magnitudes (due to higher wind velocities) in the former case while the resonance effects are predominant in the latter case. A simple procedure is developed herein purely in terms of the power spectrum of the input and the mechanical admittance (frequency response function) of the structure.

2.7.2   Work Potential.

The total pressure may be recalled to be given by

$$p_T(t) = p_S + p(t)$$

where $\overline{p_T(t)} = p_S$

and $\overline{p(t)} = 0,$ 2.23

with the functional dependence on (x, θ) suppressed for convenience in writing. In the following analysis only $p(t)$ is considered which implies that the mean value is zero. In terms of the Laplace transform, $p(t)$ may be written as

$$p(t) = \frac{1}{2\pi} \int_0^\infty \overset{\lambda}{p}(i\omega) e^{i\omega t} d\omega \qquad 2.24$$

where

$$\overset{\lambda}{p}(i\omega) = \int_0^\infty p(t) e^{-i\omega t} dt \qquad 2.25$$

is the Laplace transform of p (t). The power spectrum of the pressure can then be obtained by conjugate multiplication as

$$S(\omega) = \rho(i\omega) \; \rho^*(i\omega). \qquad 2.26$$

One could now look at the problem in the frequency domain instead of in the time domain. The work potential for a line element of load (see Figure 2.5)

$$\rho(i\omega) \; e^{i\omega t} \Delta\omega = 2\pi \Delta p(t)$$

acting along a generator at θ' is

$$\Delta W = \int_0^1 \Delta p(t) \; w \Big|_{\theta=\theta'} a \, d\theta' \qquad 2.27$$

In the limit,

$$2\pi \, dp(t) = \rho(i\omega) \; e^{i\omega t} \, d\omega$$

$$\therefore \int dW = W = \frac{1}{2\pi} \int_0^{\infty} \rho(i\omega) \; e^{i\omega t} d\omega \int_0^1 w(x)_{\theta=\theta'} a \, d\theta' \, dx$$

$$2.28$$

The work done due to distributed wind loading which is a function of θ only is then obtained by carrying out integration over $d\theta$. However, this involves cross-correlation effects of pressure. These are explained in Section (5.6) where the analysis procedure is discussed in detail.

2.8   Fatique Considerations Under Wind Loading.

2.8.1   General.

The importance of the accurate description of the load levels or, equivalently, the stress levels in the dynamic design of wind-excited structures is clear. The wind speed distribution in time which causes these stresses follows the statistical variations and hence introduces uncertainties in

the prediction of the fatigue life. As a first step in the dynamic design it is therefore necessary to ascertain the nature of the wind loading in the earth's shear flow. This depends on the turbulence characteristics of the free stream and the shape of the structure. The free wind spectrum (Figure 2.6) indicates that the wind fluctuations could be classified as (1) gust fluctuations and (2) mean wind fluctuations depending on the averaging time. Davenport[85] has suggested an averaging time of 10-20 minutes for the mean wind fluctuations. These fluctuations may be diurnal, cyclonic or seasonal.

Even in the absence of resonance effects of the structure, the response spectrum does not necessarily follow the mean wind spectrum. This is because of the influence of vortex shedding and aerodynamic stability on the response. The geometry of the structure and the free stream turbulence affect the vortex shedding and the spectral distribution of the fluctuating pressures.

From the point of view of fatigue analysis, therefore, the complicated load-response problems could be divided into two categories:

(1)   Mean response fluctuations where the resonance effects are negligible due to either high structural stiffness or damping,

(2)   The dynamic response fluctuations which are characterized by the presence of resonance peaks in the response spectrum due to free wind or/and vortex shedding.

The first of these two problems provides an idealization

implying a "one-to-one" relation between the loading and the response. A probabilistic analysis of the wind speeds can be directly translated to that of the stress levels and forms a special case of the general approach developed by Davenport (86,87) and as such is not considered here.

The second problem is mathematically tractable only if the response spectrum is known either from a theoretical analysis or from experimental measurements on models. There would still be a considerable uncertainty, typical of many probabilistic phenomena, as to the choice of representative averaging time and its influence on the overall response effects. Since one is concerned with the estimation of the expected life of the structure the combined effect of both static and dynamic stresses over the design life period should be evaluated. For want of a complete mathematical description, the method outlined in the References (86,87) relies on a semi-graphical procedure. In the present analysis a theoretical method based on a probabilistic-deterministic approach is developed within the frame work of the assumptions of Palmgren-Miner cumulative damage rule. The ideas utilised here have already been applied in other related fields. A more detailed discussion of the statistical properties of the wind is dealt with in Appendix X. Though the analysis in the text is confined to the circular cylindrical chimney structure, the procedure is completely general and can be easily extended to any structure under random wind or earthquake loading. The procedure is similar to that of the Reference (86) to a certain extent.

2.8.2   <u>Wind Distribution Function.</u>

The probabilistic distribution of the wind speeds, ideally, should be considered over the entire design period. This is not always possible due to the fact that the data are too extensive for the purposes of reduction. From the map of isopleths (equal wind speeds), the maximum wind speed with a 50 year return period could be obtained. It is proposed to assume a Rayleigh distribution with the standard deviation σ_1 equal to 25% of this maximum wind speed or a Weibull function with the characteristic velocity C equal to 35% of this maximum wind speed. It should be noted that these hypotheses provide viable alternatives and that the wind speeds referred to are 3-sec. gust values. If, however, the typical wind speed data over a long period, of the order of a year, are available the standard deviation σ_1 or the characteristic velocity C can be obtained from a plot of the data on extremum probability graph type I (see Figure 2.7).

The Weibull distribution is given by

$$P (V) = \exp - (\frac{V}{C})^k \qquad\qquad 2.31$$

The value of the index k is approximately 2, in general, and is obtained graphically (Figure 2.7). On the other hand, the Rayleigh distribution for this problem is represented by

$$P (V) = \exp - (\frac{V^2}{2\sigma_1^2}) \qquad\qquad 2.32$$

Once the distribution is known a step by step procedure outlined below is followed.

2.8.3   Method of Approach.

Figure (2.8a) shows a typical wind-structure configuration. The typical free wind speed variation is shown in Figures (2.8b,c) and the wind pressure variation at any point on the structure is shown in Figure (2.8d). The Aerodynamic Transfer Function, which depends on the geometry of the structure and the flow Reynolds number, relates the Figures (2.8b,c) to (2.8d). Figure (2.8e) illustrates the response – displacements, bending moments or stresses – at a point on the structure. Evidently, the Structural Transfer Function, also called the mechanical admittance or the frequency response function, relates the transformation of Figure (2.7d) to (2.8e). For a theoretical analysis, therefore, these two functions viz. the aerodynamic admittance and the mechanical admittance should be evaluated. Then, a fatigue analysis based on derived stresses is a possible proposition.

The analysis procedure is illustrated in Figure (2.9). The wind velocity distribution which may be assumed to be a Gaussian distribution reduces to the Rayleigh distribution in the wind speeds in an isotropic atmosphere. Since the local winds are directional to some extent, the Weibull distribution is more likely, as explained previously. Figure (2.9a) illustrates the probability density function given by

$$p(V) = \frac{d\,P(V)}{d\,V} \qquad\qquad 2.33$$

The "locking-in" range of velocities, $2\Delta_i V$, corresponding to the known natural frequencies, f_i, can be obtained from simple wind tunnel tests on representative flexible shell models.

If R is the design life in years, the number of years over which one of the critical velocities is experienced by the structure is

$$R_i = R \int p(V) \, dV = R \int_{V_i - \Delta_i V}^{V_i + \Delta_i V} \frac{d P(V)}{d V} \, dV \qquad 2.34$$

Using the formulation developed earlier and following the solution procedure given later in Section (5), the overall stress distribution in the shell could be evaluated at the critical velocity for a known value of structural damping. The following procedure is adapted for the purpose. The aerodynamic admittance functions are shown in Figures (2.9b) and (2.9c) for mean and rms distribution of pressures respectively. These functions are chosen at the flow Reynolds number under consideration. The overall peak stress distribution in the shell evaluated from a non-linear analysis of single mode response levels for these pressures, is shown in Figure (2.9d). It is now assumed that only tensile stress peaks contribute to the fatigue damage. From isotropy considerations of the wind, and due to the axisymmetry of the shell it is seen that there is equal (or approximately equal for the Weibull distribution) probability that a given stress peak level occurs. It is then probably a reasonable approximation to reality to consider for fatigue stress levels an average positive stress level $\overline{\sigma}_{xx}$ defined by

$$\overline{\sigma}_{xx}(f_i) = \frac{1}{2\pi} \int_0^{2\pi} \sigma_{xx}(\theta, f_i) d\theta, \quad \sigma_{xx} > 0. \qquad 2.35$$

The non-resonance effects are ignored in the present analysis.

Now the material fatigue behaviour can be represented[81]
by the equation

$$N_i \quad \sigma_{xx}^{\ominus} \quad = \quad C \qquad\qquad 2.36$$

based on experimental data, where N_i is the number of cycles
to failure (or fatigue life) at a stress level σ_{xx}. Figure
(2.9e) shows the graphical representation of the above
equation. The values of $\ominus$ and C are $\ominus = \frac{1}{m}$, is a positive
number $C = \sigma_0^{\ominus}$ where $\log \sigma_0$ is the ordinate intercept and
(- m) is the slope of the S-N diagram on the log-log plot.
It should be borne in mind that the above equation is in
general based on alternating stress fatigue tests on stand-
ard fatigue specimens.

The Palmgren-Miner cumulative damage rule states that
the total damage $\mathfrak{D}$ is given by

$$\mathfrak{D} = \quad \Sigma_i \quad \mathfrak{D}_i \quad = \quad \Sigma_i \quad \frac{n_i}{N_i} \qquad\qquad 2.37$$

where n_i is the number of cycles of stress peaks at a level
$(\sigma_{xx})_i$. In the present case, the expected number of cycles
of stress at a level $(\overline{\sigma}_{xx})_i$ is

$$n_i \quad = \quad f_i \quad R_{is}$$

where R_{is} is the expected number of seconds of duration of a
critical velocity V_i.

Substitution for n_i in the Equation 2.37 yields

$$\mathfrak{D} = \quad \Sigma_i \quad \frac{f_i}{N_i} \quad R_{is} \quad .$$

Together with Equations (2.31) and (2.34) the result is

$$\mathcal{D} = \Sigma_i \frac{f_i}{N_i} R_s \int_{V_i - \triangle_i V}^{V_i + \triangle_i V} k \frac{V^{k-1}}{C^k} \exp - (\frac{V}{C})^k \, dV \; .$$

2.38

Now the total damage $\mathcal{D}$ at failure is given by

$$\mathcal{D} = 1$$

2.39

from which, the design life R_s in seconds is

$$R_s = 1/ \; [\; \Sigma_i \frac{f_i}{N_i} \int_{V_i - \triangle_i V}^{V_i + \triangle_i V} k \frac{V^{k-1}}{C^k} \exp - (\frac{V}{C})^k \, dV \;]$$

2.39

This in essence is the "semi-probabilistic" analysis of fatigue and once the expected values of the duration of the critical velocities are known from probabilistic estimates, the remaining analysis follows a straight forward deterministic approach. It is to be noted that the mean velocity and hence mean stress effects are inherent in the analysis thus developed.

In this proposed method of analysis, the stresses are evaluated utilizing the nonlinear deterministic procedure (as in Section 5.3). It is implied that the superposition of the stresses is valid. However, an experimental verification of the theory is not undertaken. Further, the flexible models tested displayed amplitudes which were within the scope of a linear solution, as will be seen later. Hence, a linear multimode random response analysis technique is developed in the sections 5.5 and 5.6.

Further discussion of the fatigue analysis outlined above is omitted in the text that follows.

3. DYNAMIC ANALYSES.

3.1 Introduction.

Using the energy expressions derived in Section (2), the characteristic equations for the non-linear single mode vibration problem are obtained in this section. The displacements are assumed in beam function form for axial modes and as harmonic functions for circumferential modes. The response is assumed to be periodic and of a single mode type, though in general, the non-linear problem has a number of periodic and aperiodic solutions. The unknown coefficients in the assumed displacements are evaluated using the Rayleigh-Ritz technique. Due to non-linearity, the resulting equations are time dependent. One method of "eliminating" this difficulty is by "averaging" the total potential over one cycle (88,89). This results in a set of three algebraic equations which, by an elimination process, could be reduced to a cubic characteristic equation in a single unknown. In this equation the response frequency appears as a parameter. The real roots of this equation for various values of the frequency parameter constitute a frequency response plot. The nature of the plot indicates the type non-linearity. For the geometries and modes considered the geometric non-linearity has a definite hardening effect in agreement with the result found in References (26,27,35) but unlike that of References (31,33). This is further substantiated by a novel comparison drawn with the Duffing's equation (89) for a single-degree-of-freedom system.

3.2 Assumed Displacement Functions.

In the absence of damping (see Appendix VI for damping

considerations), and as a first approximation, a single harmonic (in the time domain) of the response function could be assumed to be either in phase or out of phase with the forcing function. This assumption is justified by the fact that the non-linearity is caused by moderate rotations and that the shell is thin, and that large response may be expected near the linear natural frequency. In other words, this assumption is equivalent to linearity of displacement functions and no coupling between the harmonics in the response (weak non-linearity). The displacement functions (82) are then written as

$$u/l = [A \phi'(x) + A_1 \psi'(x)] \cos n\theta \cos \omega t$$

$$v/l = [B \phi(x) + B_1 \psi(x)] \sin n\theta \cos \omega t$$

$$w/l = [C \phi(x) + C_1 \psi(x)] \cos n\theta \cos \omega t$$

$$3.1$$

where $\phi(x)$ and $\psi(x)$ are the beam functions. Prime (') denotes a derivative of the beam with respect to the axial coordinate x. Linear combinations of ϕ and ψ are introduced above to permit any set of edge conditions such as stiffening edge ring etc., to be approximated. Without loss of generality, in the analysis that follows the function ψ is omitted.

3.3 Characteristic Equations.

The total potential of the shell volume is

$$\Omega(t) = U - (T + W) \qquad 3.2$$

where U, T and W are also functions of time. Application of the method of averaging[88,89] to the Equation (3.2) yields

$$\frac{1}{\tau} \int_0^\tau \Omega \, dt = \frac{1}{\tau} \int_0^\tau U \, dt - \frac{1}{\tau} \int_0^\tau T \, dt - \frac{1}{\tau} \int_0^\tau W \, dt$$

where τ is the time interval between two successive displacement positions of the shell motion in time which have the same of velocity (the period of oscillations, were the motion periodic). It is not a necessary condition for the validity of the method of averaging that the motion is periodic. In the present analysis, however, the motion is assumed to be periodic for simplicity.

Substitution of the displacements (3.1) into the Equation (3.3) in conjunction with the Equations (2.7, 2.8, 2.11 and 2.13) on applying the Rayleigh-Ritz procedure results in the three characteristic equations

$$(U_{11} - \Delta T_{11}) A + (U_{12} - \Delta T_{12}) B + (U_{13} - \Delta T_{13}) C = 0,$$

$$(U_{21} - \Delta T_{21}) A + (U_{22} - \Delta T_{22}) B + (U_{23} - \Delta T_{23}) C = 0$$

$$(U_{31} - \Delta T_{31}) A + (U_{32} - \Delta T_{32}) B + (U_{33} - \Delta T_{33}) C$$

$$+ \{ U_{34} \, C^3 \} - W_{30} = 0 \qquad\qquad 3.4$$

where the coefficients U_{ij} are defined as

$$U_{11} = \lambda_m^2 + (1 + \beta) \left(\frac{1-\nu}{2} \right) n^2 I_2 ,$$

$$U_{22} = n^2 + \left(\frac{1-\nu}{2} \right) \lambda_m^2 (1 + 3\beta) I_2 ,$$

$$U_{33} = 1 + \beta [\lambda_m^4 + (n^2-1)^2 - 2\nu\lambda_m^2 n^2 I_1 + 2(1-\nu)n^2\lambda_m^2 I_2] ,$$

$$U_{12} = U_{21} = \nu\lambda_m n I_1 - \left(\frac{1-\nu}{2} \right) n \lambda_m I_2 ,$$

$$U_{23} = U_{32} = n + \beta n \lambda_m^2 \left[-\nu I_1 + \frac{3}{2} (1-\nu) I_2 \right] ,$$

$$U_{13} = U_{31} = \nu \lambda_m I_1 + \beta \lambda_m \left[-\lambda_m^2 + \left(\frac{1-\nu}{2} \right) n^2 I_2 \right] ,$$

$$U_{34} = \frac{9}{32} \frac{l^2}{a^2} \{ \lambda_m^4 I_3 + n^4 I_4 (1+6\beta) + \frac{2}{3} \lambda_m^2 n^2 (1+\beta) I_5 \}$$

3.5

and the coefficients T_{ij} are

$$T_{11} = I_2$$

$$T_{22} = 1 + 3\beta$$

$$T_{33} = 1 + \beta(\lambda_m^2 I_2 + n^2)$$

$$T_{12} = T_{21} = 0 ,$$

$$T_{23} = T_{32} = 2n\beta ,$$

$$T_{13} = T_{31} = - \beta\lambda_m I_2$$

3.6

with

$$W_{30} = \eta I_6$$

$$\eta = \frac{1}{\pi} \frac{a(1-\nu^2)}{Eh} (-\frac{p}{l^2}) \qquad \text{for point load,}$$

$$\eta = \frac{1}{\pi} \frac{a(1-\nu^2)}{Eh} (-\frac{p}{l}) \qquad \text{for line load}$$

and

$$\eta = \frac{a(1-\nu^2)}{Eh} (-\frac{pa}{l}) \qquad \text{for distributed load.}$$

3.7

It may be noted that the characteristic Equations (3.4) are non-dimensional by virtue of the fact that all the coefficients (3.5, 3.6 and 3.7) are non-dimensional. In the above equations, the following definitions are employed for simplicity in the notations:

$$\Delta = \frac{\varrho a^2 (1-\nu^2) \omega^2}{E} ,$$

$$\lambda_m = p_m \, a$$

$$\beta = h^2/12 \, a^2 \quad , \tag{3.8}$$

$$I_1 = \int_0^1 \phi\phi'' \, d\bar{x}$$

$$I_2 = \int_0^1 \phi'^2 \, d\bar{x}$$

$$I_3 = \left\{ \int_0^1 \phi'^4 \, d\bar{x} \right\}$$

$$I_4 = \left\{ \int_0^1 \phi^4 \, d\bar{x} \right\}$$

$$I_5 = \left\{ \int_0^1 \phi^2 \phi'^2 \, d\bar{x} \right\} \tag{3.9}$$

$$I_6 = \phi_1 \quad \text{for point load at the tip,}$$

$$I_6 = \int_0^1 \phi^2 \, d\bar{x} = 1 \quad \text{for beam function distribution}$$

$$\tag{3.10}$$

and

$$\bar{x} = x/1$$

I_6 for harmonic distribution forms a special case of wind loading which is described in detail in Section (5).

The formulation up to this stage has been completely general. The boundary conditions are for the first time introduced in the choice of the beam functions ϕ_m which are given in Appendix III for the clamped-free case. For any other boundary conditions, it is only required to evaluate the integrals I_1 to I_6 making use of the orthogonality properties of the beam functions. The evaluation of these

integrals is discussed in Appendix IV for the clamped-free boundary conditions.

3.4   Solution Procedure.

Whilst confining to the study of periodic and approximately periodic vibrations, it is recalled that the formulation is easily extendible to aperiodic forced and free motion of the shell. Also, the method of averaging permits in the analysis subharmonic and multimode response. Only single mode analysis under a point load at the tip and a distributed load in the beam function form are considered in this section.

3.4.1   Free Linear Vibrations.

Equating the coefficients of the non-linear terms and the external load function to zero (i.e., $U_{34} = 0$ and $W_{30} = 0$), the Equations (3.4) reduce to three homogeneous simultaneous equations in the unknowns A, B and C. This set represents the eigen value problem of free linear vibrations where the frequency parameter Δ is still unknown. The zeros of the determinant of the coefficients of A, B and C yield the frequency cubic

$$K_3 \Delta^3 + K_2 \Delta^2 + K_1 \Delta + K_0 = 0 \qquad 3.11$$

where,

$$K_3 = T_{11} T_{22} T_{33} - T_{11} T_{23}^2 - T_{22} T_{13}^2$$

$$K_2 = -(U_{11}T_{22}T_{33} + U_{22}T_{33}T_{11} + U_{33}T_{11}T_{22} - U_{11}T_{23}^2$$
$$- 2U_{23}T_{11}T_{23} + 2U_{12}T_{13}T_{23} - U_{22}T_{13}^2 - 2U_{13}T_{22}T_{13})$$

$$K_1 = U_{11}U_{22}T_{33} + U_{22}U_{33}T_{11} + U_{33}U_{11}T_{22} - 2U_{11}U_{23}T_{23}$$

$$- U_{23}^2 \, T_{11} - U_{12}^2 \, T_{33} + 2U_{12} \, U_{23} \, T_{13} + 2U_{12} \, U_{13} \, T_{23}$$

$$- 2U_{22} \, U_{13} \, T_{13} - U_{13}^2 \, T_{22}$$

$$K_0 = - (U_{11} \, U_{22} \, U_{33} - U_{11} \, U_{23}^2 - U_{12}^2 \, U_{33}$$

$$+ 2U_{12} \, U_{23} \, U_{13} - U_{22} \, U_{13}^2)$$

This cubic equation is evaluated for the values of Δ
(90)
following the Newton's method. Of the three roots, the
lowest represents the predominantly w mode and is the only
one of significance at the excitation levels of interest.
The other two – predominantly u and v modes, are ignored.
The effect of omission of rotatory and inplane inertias is
easily checked by putting the coefficients T_{ij} of the
kinetic energy, for $i \neq j$, to zero. In this case the
characteristic equations obtained are identical to those
in Reference (82). Table (9.1) compares the two results,
one with and the other without rotatory and inplane
inertias with those of Reference (82) and the "exact"
results of Reference (83). The comparison substantiates
the conclusion drawn in Reference (82), namely, that the
beam functions provide good approximations to the dis-
placements in the frequency analysis. The small differ-
ences between the present results and those of (82) are
due to the omission in (82) of a constant in the evalu-
ation of integral I_4 which has now been included.

3.4.2   Free Non-Linear Vibrations.

If the forcing function W_{30} is put to zero in the
Equations (3.4), of the resulting set of equations only the

last one is non-linear. With Δ as a parameter, the equations may be written as

$$a_{11} \; A + a_{12} \; B + a_{13} \; C = 0$$

$$a_{21} \; A + a_{22} \; B + a_{23} \; C = 0$$

$$a_{31} \; A + a_{32} \; B + a_{33} \; C + a_{34} \; C^3 = 0 \qquad 3.12$$

where $a_{ij} = (U_{ij} - \Delta \; T_{ij})$ $i, j = 1, 2, 3$ and $a_{34} = U_{34}$. Using Cramer's rule in the first two of these equations and eliminacting A and B in the third equation,

$$(a_{13} \; \delta_1 + a_{23} \; \delta_2 + a_{33} \; \delta) \; C + a_{34} \; C^3 = 0$$
$$3.13$$

where

$$\delta_1 = \begin{vmatrix} a_{12} & a_{13} \\ a_{22} & a_{23} \end{vmatrix} \quad ,$$

$$\delta_2 = - \begin{vmatrix} a_{11} & a_{13} \\ a_{12} & a_{23} \end{vmatrix}$$

and

$$\delta = \begin{vmatrix} a_{11} & a_{12} \\ a_{12} & a_{22} \end{vmatrix} .$$

Neglecting the trivial solution at $C = 0$, the other two roots are given by the quadratic solution

$$C_1, C_2 = \pm \sqrt{ \frac{-(a_{13} \; \delta_1 + a_{23} \; \delta_2 + a_{33} \; \delta)}{a_{34} \; \delta} }$$

$$3.14$$

It is recalled that the Equation (3.13) contains the non-dimensional frequency Δ as parameter. A response

curve sketched in Figure (3.1a) may be constructed for various values of frequency ratio $\Delta_{non} / \Delta_{lin}$. It will be seen later (Section 9.3) that the numerical value of the radix is negative for $\Delta_{non} / \Delta_{lin} < 1$, giving imaginary roots. The real roots correspond to

$\Delta_{non} / \Delta_{lin} > 1$, indicating that the non-linearity is hardening. The more familiar form of the response curve with the magnitude of the amplitude $|C|$ plotted against the frequency ratio is sketched in Figure (3.1b). This in fact forms the "back bone" of the forced non-linear response as will be seen in the next section.

3.4.3 Forced Non-Linear Vibrations.

The forcing function W_{30} appears only in the third of the Equations (3.4) for the cases of loading (2.6.1) and (2.6.2), since the force is applied only in the z direction. As in the previous case substitution for A and B in terms of C gives a cubic in C

$$(a_{13} \delta_1 + a_{23} \delta_2 + a_{33} \delta) C + a_{34} \delta c^3 - W_{30} = 0$$

3.15

which may be written for simplicity as

$$K_3 C^3 + K_1 C + K_0 = 0,$$ 3.16

with $\quad K_3 = a_{34} \delta$,

$$K_1 = a_{13} \delta_1 + a_{23} \delta_2 + a_{33} \delta$$

and $\quad K_0 = - W_{30}$

where δ_1, δ_2 and δ are defined in Equation (3.13). Equation (3.16) contains the non-dimensional frequency Δ

implicitly. The cubic in C is solved for various values

of $\Delta_{non} / \Delta_{lin}$ with the excitation force as a parameter

using Newton's method to construct a response curve

(Figure 3.2).

Only the real roots of Equation (3.16) constitute

the response curve. An elegant extention of the formu-

lation to include structural damping is described in

Appendix VI.

3.4.4   Comparison with the Duffing's Equation.

Duffing's equation for a single-degree-of-freedom

system forms probably the simplest example of a non-

linear system with viscous damping and with a cubic non-

linear spring system. The governing differential equation

may be written, in general, for a spring-mass-damper

system under sinusoidal excitation as

$$m\ddot{x} + c\dot{x} + k(x) = F\cos\omega t \qquad\qquad 3.17$$

The functional form of k (x)

may be assumed to be a combination of linear and cubic

terms and then

$$m\ddot{x} + c\dot{x} + (k_1 x + k_3 x^3) = F\cos\omega t \qquad\qquad 3.18$$

This equation is often called the Duffing's

equation and possesses a number of periodic and aperiodic

solutions (89). In the absence of damping an assumed

harmonic solution for the displacement of the form

$$x = x_0 \cos\omega t \qquad\qquad 3.19$$

in the above equation yields, on integration over one

cycle (method of averaging), a cubic which has the same

form as the Equation (3.15). The sign of the coefficient of the third degree term in the Equation (3.18) for positive k_1 indicates the type of non-linearity:

if $k_3 > 0$, the non-linearity is hardening i.e.,
the frequency increases with amplitude,

$k_3 < 0$, the non-linearity is softening i.e.,
the frequency decreases with increase
in amplitude and

$k_3 = 0$, the problem is linear.

In the present formulation (where the sign of the strain energy is positive in the derivations, $\equiv k_1$ positive in Duffing's equation) the sign of K_3 in the Equation (3.16) determines the nature of the non-linearity. The present problem has, in fact, reduced to a single-degree-of-freedom system under the assumption of a single harmonic in the response. For the range of geometries studied, K_3 is found to be positive and hence it is clear that the non-linearity has a hardening effect which is in agreement with the solution obtained for the response plots in the previous section. Since the perturbation method for stability analysis is applicable to the Duffing's equation, it directly follows from the comparison drawn above, that the same method could be used here for stability considerations.

4. STATIC ANALYSIS.

4.1 Introduction.

The formulation given in Section (2) is applicable to the static problem also provided that the assumed displacement functions, in the steady state, are independent of time. In other words $\omega = 0$ yields the static problem. The kinetic energy identically vanishes and the applied loads are time-average or static loads. The total potential is then

$$\Omega = U - W \qquad 4.1$$

and there is no need for method of averaging. The unknown coefficients in the shell displacements are evaluated in the usual manner using Rayleigh-Ritz technique. The linear analysis of the static displacement of the shell is developed here, which is employed in the subsequent section for the solution of a more general dynamic analysis including the deformations due to static loads.

4.2 Characteristic Equations and Their Solution.

4.2.1 Assumed Displacements.

The assumed displacements of the median surface of the shell for N radial modes and M axial modes in the general case may be written as

$$u/l = \sum_{m=1}^{M} \sum_{n=0}^{N} A_{mn} \; \phi'_m(x) \cos n\theta$$

$$v/l = \sum_{m=1}^{M} \sum_{n=0}^{N} B_{mn} \; \phi_m(x) \sin n\theta$$

$$w/l = \sum_{m=1}^{M} \sum_{n=0}^{N} C_{mn} \; \phi_m(x) \cos n\theta \qquad 4.2$$

where prime (') denotes a derivative of the beam function with respect to the axial coordinate x. As in the dynamic case, the function ϕ_m is chosen so as to satisfy the boundary conditions. Linear displacement relations are assumed. As a consequence of thin shell assumptions, initial state of loading and orthogonality of beam functions, the coupling between the modes may be assumed to be a weak one, so that each mode could be solved independently of the other. General expressions are derived in the following section for the quasi-steady state but only the initial state is used in the combined analysis.

4.2.2   Work Potential under Steady Wind.

The variations in sectional flow properties are negligible except in the vicinity of the top (as a result of three dimensional effects); axial variations of pressure are not considered here. The circumferential pressure distribution may be expressed in the form of a truncated Fourier series as

$$p_S(\theta) = p_0 \sum_{i=0}^{N} a_i \cos i\theta \qquad 4.3$$

The Fourier coefficients a_i are evaluated from existing data based on wind tunnel tests. The work done by the external forces in the quasi-steady state is given (in Appendix II) by

$$W = \int_0^1 \int_0^{2\pi} (-p_S) \, a \left[w + \frac{1}{2} \left\{ \frac{w^2}{a} - \frac{2vw_\theta}{a} + \frac{v^2}{a} + u_x w - uw_x \right\} \right] dx d\theta \qquad 4.4$$

From equations (4.2), (4.3) and (4.4)

- 46 -

since the order of summation and integration are inter-changeable,

$$W = - p_0 \, \pi \, a^2 \, l \, \sum \frac{2c_m}{\lambda_m} \, a_i \, C_{mn} \, \delta_{i,n}$$

$$- p_0 \, \frac{\pi}{4} \, l^3 \, \{ \sum a_i \, C_{mj} \, C_{mn} \, (\delta_{i+j,n} + 2\delta_{i-j,n} + \delta_{i+j+n,0})$$

$$+ 2 \sum a_i \, B_{mj} \, C_{mn} \, n \, (\delta_{i+j,n} + 3\delta_{i+j+n,0})$$

$$+ \sum a_i \, B_{mj} \, B_{mn} \, (\delta_{i+j,n} + 3\delta_{i+j+n,0})$$

$$+ \sum a_i \, A_{mj} \, C_{mn} \, (\delta_{i+j,n} + 2\delta_{i-j,n} + \delta_{i+j+n,0}) \, \lambda_m I_1$$

$$- \sum a_i \, A_{mj} \, C_{mn} \, (\delta_{i+j,n} + 2\delta_{i-j,n} + \delta_{i+j+n,0}) \, \lambda_m I_2 \}$$

$$4.5$$

where

$$\sum = \sum_{m=1}^{M} \quad \sum_{i=0}^{N} \quad \sum_{j=0}^{N} \quad \sum_{n=0}^{N}$$

and I_1 and I_2 are defined in Appendix IV.

4.2.3   Governing Equations.

The linear strain energy (2.7) on substitution of displacements (4.2) reduces to

$$U_{lin} = \frac{Ehl^3 \, \pi}{2a(1-\nu^2)} \, [\sum_{mn} A_{mn}^2 \, U_{11} + \sum_{mn} B_{mn}^2 \, U_{22}$$

$$+ \sum_{mn} C_{mn}^2 \, U_{33} + 2 \sum_{mn} A_{mn} \, B_{mn} \, U_{12} + 2 \sum_{mn} B_{mn} \, C_{mn} \, U_{23}$$

$$+ \quad 2 \sum_{mn} A_{mn} \, C_{mn} \, U_{13} \qquad\qquad 4.6$$

where $\quad \sum_{mn} = \sum_{m=1}^{M} \sum_{n=0}^{N}$

and U_{11} etc., are defined in the Equations (3.5).
Application of the Rayleigh-Ritz method to the Equation
(4.1), where W and U are defined by the Equations (4.5)
and (4.6), results in a set of 3M(N+1) simultaneous equations
in the unknowns A_{mn}, B_{mn} and C_{mn}. However, these equations
are coupled due to the fact that Equation (4.5) contains
higher order terms arising from quasi-steady work.

In the simplified analysis the coupling is <u>ignored</u>
on the basis of the initial state and the orthogonality of
beam functions and trigonometric functions and hence the
work potential is

$$W = 2 \, p_0 \, \pi \, a^2 \, 1 \quad \sum_{mn} \frac{c_m}{\lambda_m} \, a_n \, C_{mn} \qquad 4.7$$

(i.e., first term only in Equation (4.5)). Application of
the Rayleigh-Ritz method to the total potential (4.1) with
U and W given by the Equations (4.6) and (4.7) yields a
set of uncoupled equations of the form

$$U_{11} \, A_{mn} + U_{12} \, B_{mn} + U_{13} \, C_{mn} = 0 \, ,$$

$$U_{21} \, A_{mn} + U_{22} \, B_{mn} + U_{23} \, C_{mn} = 0 \, ,$$

$$U_{31} \, A_{mn} + U_{32} \, B_{mn} + U_{33} \, C_{mn} - (W_{30})_{mn} = 0$$

where $(W_{30})_{mn} = \left[\frac{-p_0}{E} \, \frac{a}{h} \, \frac{a^2}{1^2} \, (1 - \nu^2) \right] \frac{2c_m}{\lambda_m} \, a_n$

$$4.8a$$

The suffixes mn may be omitted and the equations may be solved for A, B and C for all the modes independently. Writing Equations (4.8a) as

$$U_{11} A + U_{12} B + U_{13} C = 0$$

$$U_{21} A + U_{22} B + U_{23} C = 0$$

$$U_{31} A + U_{32} B + U_{33} C - W_{30} = 0 \qquad 4.8b$$

and solving for A, B and C yields

$$A = \frac{\delta_{S1}}{\delta_S} C$$

$$B = + \frac{\delta_{S2}}{\delta_S} C$$

$$C = + W_{30} / \left(U_{13} \frac{\delta_{S1}}{\delta_S} + U_{23} \frac{\delta_{S2}}{\delta_S} + U_{33} \right)$$

$$4.9$$

where

$$\delta_{S1} = \begin{vmatrix} U_{12} & U_{13} \\ U_{22} & U_{23} \end{vmatrix} ,$$

$$\delta_{S2} = - \begin{vmatrix} U_{11} & U_{13} \\ U_{12} & U_{23} \end{vmatrix}$$

$$\delta_S = \begin{vmatrix} U_{11} & U_{12} \\ U_{12} & U_{22} \end{vmatrix} .$$

Since all these displacements are linear, super-position of displacements and stresses holds good in this linear static analysis.

4.3   Stress Resultants.

The stress resultants given by the linear parts of Equations (2.22) on substitution of displacements (4.2) in single mode reduce to

$$N_x = \frac{Eh}{(1-\nu^2)} \frac{1}{a} [\ A \phi'' \lambda + \phi \nu (nB+C) - \beta \lambda^2 \ \phi'' \ C\ ] \cos n\theta$$

$$N_\theta = \frac{Eh}{(1-\nu^2)} \frac{1}{a} [\ nB\phi - n^2 \beta C \phi + (1+\beta)\ C\phi + \nu \phi'' \lambda A\ ] \cos n\theta$$

$$N_{x\theta} = \frac{Eh}{2(1+\nu)} \frac{1}{a} [\ - nA \phi' + B \phi' \lambda (1+\beta) + C \phi' n \beta \lambda\ ] \sin n\theta$$

$$N_{\theta x} = \frac{Eh}{2(1+\nu)} \frac{1}{a} [\ - nA \phi' (1+\beta) + B \phi' \lambda - C \phi' n \beta \lambda\ ] \sin n\theta$$

4.10a

$$M_x = \frac{Eh}{1-\nu^2} \beta 1 [\ - \lambda A \phi'' + \lambda^2 C \phi''' - \nu n \phi B + \nu n^2 \phi C\ ] \cos n\theta$$

$$M_\theta = \frac{Eh}{1-\nu^2} \beta 1 [\ - n^2 C \phi + C \phi + \lambda^2 \nu \phi''\ ] \cos n\theta$$

$$M_{x\theta} = \frac{Eh}{2(1+\nu)} \beta 1 [\ - 2\lambda \phi' B - 2\lambda \phi' n C\ ] \sin n\theta$$

$$M_{\theta x} = \frac{Eh}{2(1+\nu)} \beta 1 [\ - n A \phi' - \lambda \phi' B - 2\lambda \phi' n C\ ] \sin n\theta$$

4.10b

The suffix m denoting the axial mode number has been suppressed in the above equations from λ and ϕ.

Each of these stress resultants may be summed over all the modes to evaluate the corresponding total force and moment resultants.

4.4 Median Stresses.

The mid-plane stresses are obtained by substituting the linear part of the strain displacement relations (2.1) for $z = 0$ and the assumed displacements (4.2) into Hooke's laws (2.3). Again, the stresses are evaluated separately for each mode and then summed over all the modes to get the total stresses:

$$\frac{\sigma_{xx}}{E} = \frac{1}{a} \frac{1}{1-\nu^2} \left[A \lambda \phi'' + \nu(B\phi n \frac{1}{a} + C \phi \frac{1}{a}) \right] \cos n\theta ,$$

$$\frac{\sigma_{\theta\theta}}{E} = \frac{1}{a} \frac{1}{1-\nu^2} \left[\nu A \lambda \phi'' + B\phi n \frac{1}{a} + C\phi \frac{1}{a} \right] \cos n\theta$$

$$\frac{\sigma_{x\theta}}{E} = \frac{1}{a} \frac{1}{2(1+\nu)} \left[B \phi' \lambda - A \phi' n \right] \sin n\theta$$

4.11

As before, the suffix m has been suppressed from λ and ϕ in the above equations.

- 51 -

5. COMBINED METHOD OF ANALYSIS: STATIC PLUS DYNAMIC.

5.1 Introduction.

The analysis of the non-linear multi-degree-of-freedom system presents considerable difficulty in the solution of many simultaneous coupled non-linear equations. In the present analysis, these equations are reduced to non-linear algebraic equations. Approximate methods like Newton's iterative method[90], with known trial solutions, provide an answer to the problem but at the expense of considerable computational time; even then, there is no guarantee that the method converges. The solution is not easily tractable if the trial solutions are not known and if the static deformations also are to be included. Fortunately, the physics of the problem provides a basis in the form of a single frequency dominance at or near the natural frequency (which is in fact the basis of deterministic analysis). It is then, probably, justified to consider a single frequency deterministic response even if the loading function contains a number of harmonics. In the random vibration problem, however, the spectrum of the input and the corresponding response spectrum are considered. It should be noted that a linear single mode solution is assumed for the static loading also. When considering the superposition of the displacements and surface tractions, no restriction is imposed on the strains and stresses.

5.2 Modified Displacement Functions.

Subject to the assumption of a single mode response, the assumed displacements are given by

$$u/l = (A_S + A \cos \omega t) \; \varphi' \; \cos n\theta$$

$$v/1 = (B_S + B \cos \omega t) \quad \phi \quad \sin n\theta$$

$$w/1 = (C_S + C \cos \omega t) \quad \phi \quad \cos n\theta \qquad 5.1$$

where the coefficients A_S, B_S and C_S are known from the linear static solution (Section 4). That such an assumption for the displacements (5.1) is valid follows from the fact that the oscillatory motion does occur over the deformed mean position as indicated by wind tunnel tests on flexible shells. Single mode analysis for the separate static solution is, strictly speaking, not justifiable. However, since a weak coupling is expected due to orthogonality of the assumed displacement functions, it is believed that the present method yields a better approximation to the real situation, at the same time, providing a model amenable to the solution.

5.3   <u>Combined Characteristic Equations</u>.

The total potential may be now written as

$$\Omega = U_{1in} + U_{non} - (T + W_S + W_D + W_{SD}) \qquad 5.2$$

where W_S is the work done by the static loading

         W_D is that by dynamic loading and

         W_{SD} is the work done by the static loads due to components of dynamic displacements.

From the Equations (2.7, 2.8 and 5.1), method of averaging and integration over x and θ yield

$$U_{1in} = \frac{E\ h\ 1^3\ \pi^2}{a(1-\nu^2)} \ \left[U_{11} \left(A_S^2 + \frac{A^2}{2} \right) + U_{22} \left(B_S^2 + \frac{B^2}{2} \right) \right.$$

$$\left. + U_{33} \left(C_S^2 + \frac{C^2}{2} \right) + 2 U_{12} \left(A_S\ B_S + \frac{AB}{2} \right) \right.$$

$$+ 2 U_{23} (B_S C_S + \frac{BC}{2}) + 2 U_{13} (A_S C_S + \frac{AC}{2})]$$

<div align="right">5.3</div>

where U_{ij} are defined by the Equations (3.5).

Similarly,

$$U_{non} = \frac{E h \pi^2 1^3}{a(1-\nu^2)} \quad \frac{2}{3} \{ U_{34} (C_S^4 + \frac{3}{8} C^4 + 3 C_S^2 C^2)\}$$

where U_{34} is defined by the Equation (3.5).

The kinetic energy does not change and is the same as in Section (3.3) and is given by

$$T = \frac{E h 1^3 \pi^2}{a(1-\nu^2)} \quad [T_{11} \frac{A^2}{2} + T_{22} \frac{B^2}{2} + T_{33} \frac{C^2}{2} + T_{12} AB$$

$$+ T_{23} BC + T_{13} AC] \triangle \qquad 5.5$$

The work done by the external forces in each mode of excitation could be written as

$$W_S = 2(-p_S) \pi a^2 1 \frac{2c}{\lambda} a_{nS} C_S ,$$

$$W_D = (-p_D) \pi a^2 1 \frac{2c}{\lambda} a_n C$$

and $\quad W_{SD} = 0.$

<div align="right">5.6</div>

The total work potential is therefore

$$W = \pi a^2 1 \frac{2c}{\lambda} (- 2p_S a_{nS} C_S - p_D a_n C)$$

<div align="right">5.7</div>

Applying the Ritz technique to the Equation (5.2) one arrives at

$$(U_{11} - \triangle T_{11})A + (U_{12} - \triangle T_{12})B + (U_{13} - \triangle T_{13})C = 0,$$

<div align="center">- 54 -</div>

$$(U_{21} - \triangle T_{21})A + (U_{22} - \triangle T_{22})B + (U_{23} - \triangle T_{23})C = 0,$$

$$(U_{31} - \triangle T_{31})A + (U_{32} - \triangle T_{32})B + (U_{33} + 4U_{34}\, c_S^2 - \triangle T_{33})C$$
$$+ U_{34}\, c^3 - W_{30} = 0. \qquad 5.8$$

where $W_{30} = \eta\, I_6$.

U_{ij} and T_{ij} are defined in the Equations (3.5) and (3.6) and I_6 is given by the Equation (IV.16c) and η is given by (3.7c). Within the limitations of the assumptions made it is observed that the effect of static deformations in a single mode appears only in the last of the Equations (5.8) which are themselves similar to the Equations (3.4).

5.4   Solution Procedure.

Because of the similarity between the Equation sets (3.4) and (5.8) one would naturally expect the solution procedure to be similar. Eliminating A and B a cubic is obtained in C from the Equations (5.8), of the form

$$K_3\, c^3 + K_1\, C + K_0 = 0, \qquad 5.9$$

where K_3, K_1 are defined as before in which

$$a_{33} = U_{33} + 4\, U_{34}\, c_S^2 - \triangle T_{33}.$$

The Equation (5.9) contains the frequency parameter implicitly. The cubic is solved for the displacement coefficient C for various values of $\triangle_{non}/\triangle_{lin}$ with the magnitude of the force p_D as the parameter. Only the real roots are of significance. The results are discussed in detail later in a separate section.

5.5   <u>Random Response Technique.</u>

In continuation with Section(2.7)it is noted that the random analysis will be carried out over a linear model. In addition, structural damping is introduced to obtain bounded amplitudes in the response (otherwise there are as many singularities as the degrees-of-freedom). The structural damping force is proportional to the displacements and is in phase with the velocities. It follows then that the damping energy is proportional to the strain energy. In other words, one could write

$$D.E. \ = \ igU \hspace{4cm} 5.10$$

where g is the damping factor(hysteretic type).
The total potential is therefore

$$\Omega = U (1 + ig) - T - W. \hspace{3cm} 5.11$$

At this stage,the assumed displacements are introduced in the form

$$u/l \ = \ \Sigma_{mn} \ A_{mn} \ \Phi'_m \ \cos n\theta \ \exp i\omega t$$

$$v/l \ = \ \Sigma_{mn} \ B_{mn} \ \Phi_m \ \sin n\theta \ \exp i\omega t$$

$$w/l \ = \ \Sigma_{mn} \ C_{mn} \ \Phi_m \ \cos n\theta \ \exp i\omega t \hspace{2cm} 5.12$$

Ignoring coupling between the modes, minimization of the total potential by the Ritz technique leads to three simultaneous linear equations for each of the (m, n) modes. These equations are

$$F_{11} A_{mn} \ + \ F_{12} B_{mn} \ + \ F_{13} C_{mn} \ = \ 0$$

$$F_{21} A_{mn} \ + \ F_{22} B_{mn} \ + \ F_{23} C_{mn} \ = \ 0$$

$$F_{31} A_{mn} + F_{32} B_{mn} + F_{33} C_{mn} = W_{3R} \qquad 5.13$$

where

$$F_{jk} = U_{jk} (1 + ig) - \Delta T_{jk} \qquad 5.14$$

and for a line load element,

$$W_{3R} = \frac{a(1-\nu^2)}{E h \pi l^2} \int_0^1 \Phi_m \, dx \int_0^{2\pi} \cos n\theta' \, ad\theta'.$$

$$\cdot \frac{1}{2\pi} \cdot \int_0^\infty p(i\omega) \, d\omega . \qquad 5.15$$

A_{mn}, B_{mn} and C_{mn} in the above equations are complex.

The integral over the circular frequency ω, $0 \leqslant \omega < \infty$, indicates that the above set of equations is to be solved for all values of ω in the range prescribed. The solution for the nondimensional coefficients C_{mn} could be written as

$$2\pi C_{mn} = g_m \, p(i\omega) \, d\omega \, \cos n\theta' \, ad\theta' \qquad 5.16$$

where $g_m = g_m(i\omega)$.

Hence the deflection for all the frequencies is given by

$$w = \frac{1}{2\pi} \Sigma_{mn} \, ad\theta' \, \Phi_m \cos n\theta \cos n\theta' \int_0^\infty p(i\omega) \, g_m \exp(i\omega t) . d\omega$$

or

$$w = \frac{1}{2\pi} \int_0^\infty \Sigma_{mn} \, ad\theta' \, \Phi_m \cos n\theta \cos n\theta' \, g_m \, p(i\omega) \exp(i\omega t) . d\omega$$
$$5.17$$

The mean square value of w is therefore

$$\overline{w^2} = \frac{1^2}{4\pi^2} \lim_{T\to\infty} \frac{1}{T} \int_0^\infty \left| \Sigma_{mn} \, ad\theta' \, \Phi_m \cos n\theta \cos n\theta' \, g_m \, p(i\omega) \right|^2 d\omega$$
$$5.18$$

- 57 -

Also, the response power spectrum is given by

$$S_{ww} (\omega) = (\Sigma_{mn} \, ade' \, \phi_m \, \cos n\theta \, \cos n\theta' |g_m|)^2 \, S_{pp}$$

5.19

where

$$S_{pp} (\omega) = \lim_{T \to \infty} \frac{1}{T} \, |h(i\omega)|^2$$

5.20

is the power spectral density of the excitation pressure.

5.6   Response to Distributed Wind Pressure.

The technique developed in the previous section is extended to distributed random wind loading in this section. Due to the complexity of the problem, the response spectra inclusive of resonance effects could be obtained on imposition of another assumption viz. the excitation is fully correlated. Wind tunnel tests in uniform free stream substantiate the validity of such an assumption over a large part of the surface of the cylindrical shell (see Section 11). This is also true in the ground shear flow where the correlation length of the flow turbulence are of the order of the characteristic dimension(height)of the chimney structure. However, for a more exact analysis measurement of cross-correlations particularly in the absence of axi-symmetry is essential, though time consuming. The analysis technique developed follows the simplification on the cross-correlations and assumes that there is no variation of pressure in the axial direction.

The deflection w for the distributed pressure may be written as

$$w = \frac{1}{2\pi} \int_0^\infty \int_0^{2\pi} \Sigma_{mn} \, \phi_m \, \cos n\theta \, \cos n\theta' \, g_m \, h(i\omega) \, \exp(i\omega t).d\omega \, ade$$

5.21

- 58 -

or

$$w = \frac{1}{2\pi} \int_0^\infty \hat{w}(i\omega) \exp(i\omega t) \, d\omega \qquad 5.22$$

where

$$\hat{w}(i\omega) = 1 \, \Sigma_{mn} \, \Phi_m \cos n\theta \, g_m \, a \int_0^{2\pi} \cos n\theta' \, p'(i\omega) \, d\theta' \qquad 5.23$$

is the Laplace transform of the displacement w

and

$$p'(i\omega) = p(i\omega)\big|_{\theta = \theta'}$$

Therefore the squared displacement in the frequency domain
is given by

$$|\hat{w}(i\omega)|^2 = 1^2 [\, \Sigma_{mn} \, \Phi_m \cos n\theta \, g_m \, a \int_0^{2\pi} \cos n\theta' \, p'(i\omega) \, d\theta' \, .$$

$$\cdot \, \Sigma_{rs} \, \Phi_r \cos s\theta \, g_r^* \, a \int_0^{2\pi} \cos s\theta'' \, p''^*(i\omega) \, d\theta''$$

or

$$|\hat{w}(i\omega)|^2 = \Sigma_{mnrs} \, \Phi_m \, \Phi_r \, g_m \, g_r^* \cos n\theta \cos s\theta \, a^2 .$$

$$\cdot \int_0^{2\pi} \int_0^{2\pi} \cos n\theta' \cos s\theta' \, p'(i\omega) \, p''^*(i\omega) \, d\theta' \, d\theta''$$

$$5.24$$

where (*) indicates the complex conjugate.

As a first approximation, for circular cylindrical
chimney of uniform section, the power spectrum of the pressure
could be assumed to be similar both axially and circumfer-
entially so that

$$p'(i\omega) = R(\theta') \, p(i\omega)$$

and $\qquad \mu''^{*}(i\omega) = R(\theta) \; \mu^{*}(i\omega)$ $\qquad\qquad$ 5.25

Hence

$$|w(i\omega)|^2 = l^2 \sum_{mnrs} \Phi_m \; \Phi_r \; g_m \; g_r^{*} \cos n\theta \cos s\theta \; a^2 \cdot$$

$$\cdot \int_0^{2\pi} \int_0^{2\pi} R(\theta') \; R(\theta'') \cos n\theta' \cos s\theta'' \; d\theta' \; d\theta'' \; |\mu(i\omega)|^2$$

$$5.26$$

$R(\theta)$ could be expanded in a Fourier series given by

$$R(\theta) = \sum_{j=0}^{J} R_j \cos j\theta. \qquad\qquad 5.27$$

Then the integral

$$\int_0^{2\pi} \int_0^{2\pi} R(\theta') \; R(\theta'') \cos n\theta' \cos s\theta'' \; d\theta' \; d\theta''$$

$$= \int_0^{2\pi} \int_0^{2\pi} \sum_{jk=0}^{JK} R_j \; R_k \cos j\theta' \cos n\theta' \cos k\theta'' \cos s\theta'' \; d\theta' \; d\theta''$$

$$= \pi^2 \sum_{n,s=0}^{N=S} R_n \; R_s \qquad\qquad 5.28$$

$$\therefore \quad |w(i\omega)|^2 = |H(i\omega)|^2 \quad |\mu(i\omega)|^2 \qquad\qquad 5.29$$

where the frequency response function $H(i\omega)$ is given by

$$|H(i\omega)|^2 = \sum_{mnrs} \Phi_m \Phi_r \; g_m \; g_r^{*} \cos n\theta \cos s\theta \; a^2 \pi^2 \; R_n R_s$$

$$5.30$$

The Equation (5.29) can also be written as

$$S_{ww}(\omega) = |H(i\omega)|^2 \; S_{pp}(\omega) \qquad\qquad 5.31$$

The analysis developed above is linear and hence the displacement spectra in u and v are similar to that in w. Therefore, from Equations (2.1) and (3.1), following a procedure similar to that in Equation (5.29) the squared strains can be written as

$$
|\epsilon_{xx}|^2_h = \sum [Rl\{ g_{mnA} - g_{mnC} \frac{h}{l}(p_m l)\} \cdot Rl\{g_{rsA} - g_{rsC} \frac{h}{l}(p_r l)\}
$$

$$
+ Im\{ \ \} \cdot Im\{ \ \}] \cdot \phi_m'' \phi_r'' \cos n\theta \cos s\theta \ R_n R_s (\frac{a}{l})^2 |H(i\omega)|^2 ;
$$

and

$$
|\epsilon_{\theta\theta}|^2_h = \sum [Rl\{ g_{mnB} \cdot n + g_{mnC}(1 + \frac{h}{a} n^2)\} \cdot Rl\{g_{rsB} \cdot s + g_{rsC}(1 + \frac{h}{a} s^2)\}
$$

$$
+ Im\{ \ \} \cdot Im\{ \ \}] \ \phi_m \phi_r \cos n\theta \cos s\theta \ R_n R_s \ |H(i\omega)|^2
$$

$$5.32$$

where g_{mn} is defined earlier and

$$
\sum = \sum_{mnrs} = \sum_{m=1}^{M} \sum_{n=0}^{N} \sum_{r=1}^{M} \sum_{s=0}^{N}
$$

Clearly, the computer analysis of the spectral description of the response (strain or displacement) can be easily carried out at various chosen frequencies such that the natural frequencies of the shell also are included.

This elegant mathematical model thus gives the aggregate of the response over a _finite_ number of modes, accounting for both axial and circumferential deformations.

PART B

EXPERIMENTATION

6. EXPERIMENTAL CONCEPT.

6.1 Introduction.

Bluff bodies experience fluid dynamic forces of oscillatory nature when in a flow field. These oscillatory forces are due to ͟an instability in the flow field caused by one or more reasons of which the study of stable and unstable vortex shedding behind circular cylinders has been a problem in basic aerodynamics. From the structural dynamics point of view thin and slender structures may experience resonance effects under such loading in adverse wind conditions. Aeroelastic models provide useful information in ͟an experimental investigation. It is not often convenient to scale all the non-dimensional parameters to represent the full scale[91]. A knowledge of the nature of the aerodynamic forces, oscillatory or otherwise, is very useful information to the designer. A number of investigators have studied the distribution of time averaged pressures round circular cylinders[50,51,52] covering a wide range of Reynolds numbers. Figure (6.1) shows the summary of these investigations, wherein a graph of the mean pressure coefficient is plotted against the position on the cylinder surface. The vortex shedding phenomenon is not generally restricted to low Reynolds number, but extends over a large range. Figure (6.2) shows the dependence of the Strouhal number on the Reynolds number where the Strouhal frequency f_S is defined as the frequency of shedding of a pair of vortices. It is seen from the figure that the Strouhal number is almost a constant at 0.2 over a large range of Reynolds numbers though values as high as 0.4 are observed

in the transition region of critical to trans-critical region. In these investigations on rigid circular cylinders, the measurement of mean (time-average) pressures through a set of static tappings was a simple matter. Measurement of oscillatory pressures on vibrating cylinders on the other hand presents many problems as would be clear in the subsequent discussion.

The experimental methods adapted in a majority of studies regarding the nature of oscillatory forces on circular cylinder may then be classified as

(i)   measurement of cylinder motion,

(ii)   measurement of lift and drag acting on a rigid cylinder and

(iii)   the study of wake conditions behind the cylinder. The first of these methods gives only a partial picture dominated by the natural frequencies of the cylinder model and not the true nature of the oscillatory forces. The results are also affected by the associated aerodynamic damping. The second method has the inherent disadvantage that it gives rather an overall state of the forces over a finite length regardless of the force distribution function. The third technique is not really suitable for obtaining the fluctuating lift and drag forces and the results depend on the distance in the wake from the cylinder. Extrapolation to model location is somewhat doubtful. Thus the technique of local surface pressurements is the only reliable method for evaluating the fluctuating pressures and may be classified as the fourth category.

However, the literature in this aspect is scarce - Bishop and Hassan[54], Ferguson and Parkinson[61], Surry[60], Gould[52] and Novak and Fischer[92] to cite most of them. These reports however do not consider the flexible fixed-free circular cylinder configuration. It is important to consider this configuration since the harmonic component in the pressure spectrum has strong influence on the cylinder response and consequently ovalling modes of oscillation. In this investigation, the experimental work refers to fixed-free flexible shell of finite length with open top and no efflux. The investigation is supplemented by measurements on rigid cylinders and these details are discussed in Section 8.

6.2   Vibration Characteristics.

In any work involving aeroelastic behaviour or dynamic stress analysis, the characteristic (i.e. the natural) frequencies of the structure are important. A knowledge of the natural frequencies and of the damping in the system are adequate to describe the system transfer function provided that the system is linear. For small amplitude vibrations one might assume linearity and the natural frequencies can be measured experimentally by the single point excitation method. The damping constant can be evaluated by a study of the decay of free oscillations. These studies form the initial investigation in the present aerodynamic excitation study.

6.3   Flow Properties Around   Rigid Cylinder.

The distribution of time-average pressures round rigid cylinders has been entensively investigated. The

effects of free stream turbulence, surface roughness of the model and Reynolds number on this distribution have also been established. The frequency of vortex shedding and its dependence on the Reynolds number are well known. However, due to the upstream effects, the instantaneous pressures are expected to be modified. The dominance of the vortex frequency on these pressures is clear. The influence of free stream turbulence and the magnitude of the fluctuating pressures are, however, not so obvious. Also the effect of end conditions and the Reynolds number effects can be evaluated only by experimental measurements. These studies were hence conducted on rigid circular cylinders as preliminary studies at various Reynolds numbers in the region $0.4 \times 10^5 < Re < 2.9 \times 10^5$. It is desirable to study the correlation effects for various axial separation distances and circumferential separation angles. This is rather time consuming and the model design would be more complicated so as to allow for various (i) axial separation distances and (ii) circumferential angles. In the present case, however, the pressure correlation study is attempted only for two axial separations and two circumferential separations.

6.4   Flow Properties Around Flexible Cylinder.

A cylindrical shell is considered as flexible when the first few of its natural frequencies (or more exactly, the natural frequencies in the service frequency range) could be excited in the flow field under consideration. Two flexible shells were designed so that the natural frequencies with n=1,2 and 3 modes could be excited within the

capacity of the wind tunnel. One of them (F4) is an approximate scale model of a full scale chimney. The vortices that are shed excite the model, at its natural frequency, at the critical velocities. The excitation frequency is expected to influence the vortex frequency. In other words, there is an interaction between the two. This aeroelastic interaction can be brought out experimentally by comparison with rigid model studies at exactly the same Reynolds numbers. The details are discussed in Sections 10 and 11.

6.5   Methods of Analysis of Analogue Signals.

The instantaneous pressures and the shell response signals are recorded in analogue form on a FM tape recorder. The methods of analysis of such analogue signals may be classified into two categories (93,94):

(1)   analogue analysis, and

(2)   digital analysis.

In both cases, the data are assumed to be stationary and ergodic and that the methods of analysis of random variables hold good in the present case though there are predominant characteristics which make the variables deterministic at certain Reynolds numbers. The methods of analysis described here are well established and are described in many text books on the subject. The objective here is to familiarise with the notations and to lay the foundation relevant to the discussion given in Section 11. The limitations of the digital techniques are elaborated in Appendix VII.

6.5.1   Power Spectrum.

The power spectral density gives the frequency decomposition of the variable in terms of its mean square

values. The average squared value will approach an exact

mean square value as the observation time approaches infinity.

Symbolically, for a variable x (t, ω), with one-sided power

spectral density $S_{xx}(\omega) = 2G_{xx}(\omega)$, the positive half of the

symmetric spectrum in the region $0 < \omega < \infty$ is given by

$$G_{xx}(\omega) = \lim_{\Delta\omega \to 0} \frac{1}{\Delta\omega} \left[\lim_{T \to \infty} \frac{1}{T} \int_0^T x^2(t, \omega, \Delta\omega) \, dt \right] \qquad 6.1$$

The power spectral density is always a positive real function.

The mean squared value of the variable is the expected value

of the square of the variable given by

$$\psi_x^2 = 2 \int_0^\infty G_{xx}(\omega) \, d\omega = E\{x^2(t)\} \qquad 6.2$$

where the notation $E\{\cdot\}$ stands for the "expected value of".

If the mean value is zero the above expression gives the

variance σ_1^2.

For non-zero mean values, the variance σ_1^2 is

$$\sigma_1^2 = E\{(x(t) - \bar{x})^2\} \qquad 6.3$$

where

$$\bar{x} = E\{x(t)\} = \lim_{T \to \infty} \frac{1}{T} \int_0^T x(t) \, dt \qquad 6.4$$

is the mean value. If $x(t)$ represents white noise, its

power spectrum has a constant magnitude over the entire

frequency range. The principal application of power

spectrum is in establishing the frequency response charac-

teristics if the transfer function of the system is known.

Symbolically,

$$S_{yy}(\omega) = |H(\omega)|^2 \, S_{xx}(\omega) \qquad\qquad 6.5$$

where $H(\omega)$ is the modulus of the transfer function. In this relation, the phase information is lost.

On the other hand the cross power spectrum which is, in general, complex gives the phase information as well:

$$S_{xy}(\omega) = C_{xy}(\omega) - iQ_{xy}(\omega) \qquad\qquad 6.6$$

and

$$H(\omega) = \frac{S_{xy}(\omega)}{S_{xx}(\omega)} = |H(\omega)| \, e^{-i\theta(\omega)} \qquad 6.7$$

Both these methods can be used for the evaluation of the transfer function and in the present analysis it is the latter method that is followed.

6.5.2   Correlation and Coherence Functions.

These are equivalent descriptions in time and frequency domains respectively. The autocorrelation function describes the general dependence of the values of the data at one time on the values at another time. Symbolically, the autocorrelation function

$$R_{xx}(\tau) = \lim_{T \to \infty} \frac{1}{T} \int_0^T x(t)\, x(t+\tau)\, dt \qquad\qquad 6.8$$

where τ is the time delay. Typical plots of autocorrelation functions are shown in the Figure (6.3). The following information can be obtained from a study of autocorrelations:

(i) The nature of the variable as to its randomness, and

harmonic content and their relative magnitudes.

(ii)   The period of the fundamental frequency content is given by 4 times the time delay for the first zero crossing of the autocorrellogram.

(iii)   Non-linearity and damping in the system if the variable is a response data. The autocorrellogram would be similar to the Figure (6.3c) if the system is heavily damped or non-linear. The decay is proportional to twice the logarithmic decrement (log dec). This has the advantage of bringing out the aeroelastic (flutter) characteristics since, in wind excitation, the overall damping is zero or negative if the structure is in "bounded" flutter instability and the autocorrellogram indicates divergence with time delay. This is a very important property of the correlation functions but has been hardly exploited till now.

(iv)   The mean value $\bar{x}$ is given by

$$\bar{x} = \sqrt{R_{xx}(\infty)} \qquad\qquad 6.9$$

and the mean square value is given by

$$\psi_x^2 = R_{xx}(0) \qquad\qquad 6.10$$

Also,

$$R_{xx}(0) \geqslant |R_{xx}(\tau)| \qquad \text{for all } \tau$$

for a purely random variable and for a positively

damped system and R_{xx} is an even and real valued function.

From cross correlation function one can obtain also (v) the velocity of propagation of a disturbance measured at two points if the spatial separation is known: the time delay for the first peak in the cross correllogram gives the propagation time.

Perhaps the most important property is its relation to spectral density function:

$$S_{xx}(f) = 2 \int_{-\infty}^{\infty} R_{xx}(\tau) e^{-i2\pi f\tau} d\tau$$

and

$$R_{xx}(\tau) = \int_{-\infty}^{\infty} S_{xx}(f) e^{i2\pi f\tau} df$$

or

$$S_{xx}(f) = 4 \int_{0}^{\infty} R_{xx}(\tau) \cos 2\pi f\tau \, d\tau$$

and

$$R_{xx}(\tau) = \int_{0}^{\infty} S_{xx}(f) \cos 2\pi f\tau \, d\tau \qquad 6.11$$

It should be noted that throughout this work, the power spectrum S_{xx} is one sided spectrum defined in the region $0 \leqslant f < \infty$ and $S_{xx} = 0$ elsewhere.

The following relations also exist between the cross correlation and the cross spectral density:

$$R_{xy}(\tau) = \int_{-\infty}^{\infty} S_{xy}(f) e^{i2\pi f\tau} df$$

and
$$S_{xy}(f) = 2 \int_{-\infty}^{\infty} R_{xy}(\tau) \, e^{-i 2 \pi f \tau} \, d\tau$$

6.12

In the digital analysis, however, only the positive half of the symmetric spectrum is computed and hence factor $(\frac{1}{2})$ appears on all those computed power spectral plots where the normalising factor is different from the mean square value.

The autocorrelation can also be directly computed from

$$R_{xx}(\tau) = \lim_{T \to \infty} \frac{1}{T} \int_{0}^{T} x(t) \, x(t + \tau) \, dt$$

6.13

The coherence function between the input $x(t)$ and the response $y(t)$ is a real valued function defined by

$$\gamma_{xy}^{2}(f) = \frac{|S_{xy}(f)|^2}{S_{xx}(f) \, S_{yy}(f)}$$

6.14

and satisfies the relation $0 \leqslant \gamma_{xy}^{2}(f) \leqslant 1$ provided that the mean value is zero. For a linear system with well defined "one-to-one" relation between the input and the response, $\gamma_{xy}^{2}(f) = 1$ over all frequencies. The coherence function is less than unity if

(i)   extraneous noise is present

(ii)   the system is non-linear

(iii) $x(t)$ does not describe completely the excitation loads.

6.5.3   Transfer Function.

The transfer function in the frequency domain, also called the frequency response function $H(f)$ is given by Equations 6.5 and 6.7. The frequency response function is generally a complex function

$$H(f) = |H(f)| e^{-i\theta(f)} \qquad\qquad 6.15$$

The modulus $|H(f)|$ is called the gain factor and the phase angle $\theta(f)$ is called the phase factor.

For physically realizable linear systems, $H(f)$ possesses the following symmetry properties:

$$H(-f) = H^*(f)$$

$$|H(-f)| = |H(f)|$$

and

$$\theta(-f) = -\theta(f). \qquad\qquad 6.16a$$

Also, for multi-degree-of-freedom systems provided that there is no modal coupling, the overall response function is

$$H(f) = \prod_n H_n(f)$$

$$|H(f)| = \prod_n |H_n(f)|$$

and

$$\theta(f) = \sum_n \theta_n(f) \qquad\qquad 6.16b$$

where $\prod_n$ stands for product over n and $\sum_n$ represents summation over n.

This property of the transfer function provides a powerful tool in the random response analysis of multi-degrees-of-freedom systems using normal mode approach

It should be noted that such normal modes are defined only for linear systems.

6.5.4   Probability Density Function.

The probability of occurance of a value x such that $x_i < x < x_i + \Delta x$ is $p(x) \Delta x$. The function $p(x)$ is called the probability density function. Random processes in most physically realizable cases follow a Gaussian or normal distribution where the probability density is given by

$$ p(x) = \frac{1}{\sqrt{2\pi}\,\sigma_1} \exp - \frac{(x - \bar{x})^2}{2\sigma_1^2} \qquad 6.17 $$

where σ_1^2 is the variance and $\bar{x}$ is the mean value. The following are some of the useful properties of probability density function:

$$ \bar{x} = \int_{-\infty}^{\infty} x\, p(x)\, dx \qquad 6.18 $$

and

$$ \sigma_1^2 = \int_{-\infty}^{\infty} (x - \bar{x})^2\, p(x)\, dx \qquad 6.19 $$

i.e. the first and second moments of the probability density function are, respectively, the mean value and variance of the variable. Figure (6.4) shows some of the typical probability density functions. Related discussions are given in detail in Appendix XIII.

7.   EXPERIMENTAL INVESTIGATION OF VIBRATION RESPONSE.

7.1   General.

Experiments have been performed to obtain the linear

forced natural frequencies of cantilever shell. Attempts to

obtain the non-linear response were not successful due to,

probably, the "jump" phenomenon and the limitations in the

instrumentation particularly in controlling the frequency.

Attempts to measure the modal amplitude distribution also

were not very successful. These are hence omitted in further

discussion and only the forced vibration analysis of the

flexible shell models (see Chapter 8) are considered herein.

Experiments conducted to evaluate the influence of pressure

transducer inertia and stiffness of the connecting cables

indicated no significant change in the natural frequencies.

7.2   The Apparatus.

The apparatus consisted of a rig to fix the shell in

the cantilever configuration, an electrodynamic exciter

suspended at the top of the shell with a radial excitation

axis, a power amplifier and an oscillator to drive the exciter.

The response levels were measured from strain gauges fixed to

the shell and the excitation force levels were measured using

a strain gauge type proving ring. A strain gauge bridge was

used to resolve the signals to measurable levels and a FM

tape recorder was used to record the response and force levels.

Figure (7.1) shows a schematic diagram of the apparatus.

7.2.1   The Models.

Ideally, the thin shell models should be seamless

which is possible in the thickness range of interest only

by electroforming. This is a very expensive proposition.
The next best is to construct shells with welded or adhesive
bonded seam or seams. The latter of the two was resorted to
in preference to spot welded construction since welding
alters the material elastic properties. Also adhesive
bonding is inexpensive and could be *effec*ted easily. The
shells, $4\frac{7}{8}$" and 6" in diameter, were rolled out of 10 thou
thick commercial aluminium sheet stock. For ease in con-
struction and uniformity in bonding, the shells were formed
with a half inch wide lap joint along a generatrix. The
width of the lap joint was then carefully reduced to $\frac{1}{4}$" by
cutting out the excess material which was then peeled off.
The joints thus produced were strong enough to endure all
the wind tunnel and vibration tests performed on the shells.

The vibration tests were conducted with the
base fixture which was later used in wind excitation studies.
The base fixture consisted of a steel plate to which a ring
of height 1" and thickness $\frac{3}{8}$" was fixed. The base of the
shell was then slipped over this ring and another 1" wide
ring clamp with a rubber lining on the insides was tightened
so as to *clamp* the base of the shell. The exciter was
suspended in contact with the shell, from a bracket by means
thick elastic cords so that the excitation was through the
proving ring on an initial deformed position of the shell
(see Figure 7.1). This ensured a minimum of inertia effects
of the exciter on the shell, though excitation at the base
would have been ideal. In the present case, single point
excitation at the base was abandoned because of the local
effects; for excitation forces large enough to induce

perceptible deformation levels, the shell being thin, localized failure occured in the vicinity of the excitation point. The shell being slender, it is believed that the end condition is adequately represented as fully fixed at the base.

7.2.2   The Excitation System.

The excitation system consisted of a shaker, an oscillator, a power amplifier and a proving ring together with a strain bridge. The shaker has ± 3 mm displacement amplitude and ± 7.5 lbs force amplitude at full load. The oscillator is a variable frequency sine wave generator. The output power of the power amplifier is 50 watts at full load. The proving ring was machined out of mild steel bar stock to a ring of 1" OD, 1/16" thick and 1/4" wide. 4 single-axis strain gauges were fixed and the ring was statically calibrated in tension and compression (see Figure 7.2). The entire proving ring could be screwed onto the armature of the exciter. As explained before, the exciter was then suspended at the top of the shell so as to excite radial modes, transmitting the force to the shell through the proving ring.

7.2.3   Sensor and Recording System.

The natural frequencies can be measured accurately by identifying those frequencies at which a circle is obtained as the Lissoujas figure on the CRO corresponding to the input signal from the proving ring and output or response signal from one of the strain gauges fixed on the shell. Four strain gauges were used for the purpose of

measuring the response, two of them to measure the ovalling modes and two for bending modes. Alternately, the natural frequencies may be taken to be those at which there is a peak response in a frequency band. Within the limits of experimental errors both methods identified the same values of natural frequencies, and the latter method was used more extensively in the present case.

With the objective of accounting for inertia effects of the pressure transducer on the pressure measurements with values proportional to strains (as a first approximation), transducer response was also recorded at various strain levels. The different levels of strain were achieved by varying the excitation force. To measure the logarithmic decrement the natural frequency was excited and at steady state condition the power to the exciter was cut off and the exciter itself was disengaged from the shell. The strain gauge response was then recorded. All the signals were recorded on a FM tape recorder - Sangamo model 3562 described later (see Section 8.5).

7.3   Experimental Procedure.

(i)   Natural Frequencies.

With the shaker in position, the output of the oscillator through the power amplifier was connected to the shaker at chosen excitation levels. The strain gauge response from the proving ring and the shell were monitered on an oscilloscope. The oscillator frequency was gradually in-creased starting from a low frequency. When the response signal on the scope was a maximum, the frequency indicated by

the oscillator was taken as the natural frequency. The mode
shape was identified by using a stroboscope. The experiment
was repeated at higher frequencies. As a check, the natural
frequencies were obtained also from a Fourier analysis of the
recorded maximum signals. The experiments were repeated with
the pressure transducers in position.

(ii)   Response Measurements.

At the lowest natural frequency for one position of
the shaker relative to the reference transducer T_6 position,
the signals from the strain gauges, the pressure transducer
and the proving ring were recorded at various force levels.
These were then analyzed on the level recorder (see Section
8.6) to obtain the transducer signal rms levels due to "g"
loads. Proportional rms component were intended to be
employed to "eliminate" the inertia effects from the pressure
distribution on oscillating cylinder. Figure (7.3) shows
the force-response plot for the shell F5.

(iii)   Measurement of Structural Damping.

The exponential decay of the free vibrations gives
a measure of damping. The shell was excited at a natural
frequency and at steady state the excitation was cut off
simultaneously disengaging the shaker from the shell. The
shell response then decays under its damping (in air). The
strain signals were recorded and later analysed on the level
recorder, this time for peak (not rms) levels, to obtain the
logarithmic decrement as

$$\delta = \frac{1}{n} \ln \frac{A_i}{A_{i+n}} \qquad\qquad 7.1$$

where A_i is the amplitude of ith peak ln is the natural logarithm. The method is highly inadequate at higher frequencies due to structural and aerodynamic coupling between the modes.

7.4   Limitations of the Experimental Analysis.

It is difficult to estimate the effect of the shaker on the natural frequency in the present method of excitation. The two influences viz. the shaker inertia and amplitude contraint imposed by the shaker (the shaker acts as a partial support) are compensating to some extent. At the lowest frequency the overall effect was not noticeable as observed from the frequency derived during damping measurement.

It was difficult to identify the modes particularly $n > 4$ and $m > 2$. This was not considered as a setback since wind tunnel excitation modes were generally in the same range of $1 < n < 4$ and $m = 1$ or 2. It is emphasized that the frequencies and the damping were measured in air and not in vacuum.

8.   FLUCTUATING PRESSURES AND DYNAMIC RESPONSE.

8.1   Introduction.

Pressure measurements on circular cylinders were
conducted in the open jet wind tunnel in a uniform wind
stream. All pressure data and response signals were
recorded on an analogue tape recorder. Digital analyses
of the data acquired were performed on the special purpose
computer for Fourier analysis.

8.2   Description of the Wind Tunnel.

The present investigations were conducted in the
uniform wind stream of the Open Jet Return Circuit tunnel
which has an ejector section of 43" x 30". The maximum
free stream velocity attainable is 94 fps at atmospheric
pressure. Figure (8.1) indicates the velocity distri-
bution and the turbulence levels at approximate location
of the model[95]. It is assumed that the effect of free
stream turbulence is negligible and that the velocity
distribution could be idealized to a uniform wind stream.
For convenience in the experiments the control panel dial
gauge connected between the settling chamber static and
atmosphere was calibrated over the range of test velocities
against a standard pitot tube located at the representitive
position in the tunnel with the model in position. The
pitot tube was then taken out of the way so as to ensure
interference - free flow.

8.3   Description of the Models.

Extensive studies were conducted on the three
models R_1, R_2 and R_3 and the two flexible models F_4 and
F_5. Details of the geometry of the models are shown in

the Figure (8.2). R_1 and R_2 were rigid circular cylinders of diameter $3\frac{1}{2}$" and $8\frac{1}{2}$" respectively and of $\frac{1}{4}$" thick PVC plastic. The cylinders were mounted on wooden base fixtures which fitted onto a turntable. The turntable could be clamped at any desired incidence of the reference generatrix with respect to the free stream. The cylinders were open at the top. The transducers and the oscillators were clamped to the turntable so as to rotate with the cylinder. The cylinder R_2 was tested in the "2-D" configuration also, by fixing a large end plate at the top.

The rigid cylinder R_3, 6" in diameter, was fabricated in two parts the top section being of $\frac{1}{4}$" thick perspex and the lower part made of wood. The cylinder was of open top and the wooden base fixture was fixed to a steel turntable. Top 27" of the cylinder R_3 was exposed to the free stream in the test section. The transducer and the oscillator were fixed to a traverse which could be lowered into the cylinder through the open top (see Figure 8.3) and clamped in position. The traverse and the turntable could be rotated independently for selecting the angle of incidence. The connecting wires and the transducer back pressure tube were taken out from the top along the traverse.

The shells F4 and F5 were made of 10 thou aluminium sheet as described in Section (7.2). Base fixity of both shells was effected by clamping rings and the shells were mounted on the steel turntable. Top 27" of shell F4 and top 28" of shell F5 were exposed to the free stream in the wind tunnel. The transducers were

located at 13" from the top in both shells. The transducers

and the oscillators were lowered into the shell with the

traverse mechanism at the top of the shell (see Plate 8.1).

Connecting wires and transducer back pressure tubes were

taken out from the top of the shell. The traverse was

designed to have an additional degree of freedom in rotation.

To minimise the influence of transducer - cable stiffness,

the mechanism, after locating the transducer in the rubber

gaskets fixed to the shell, was allowed to find itself an

equilibrium position of least influence of the cable stiff-

ness and then locked in that position. For other angles

of the shell, the traverse was rotated by the same angle as

the turntable and locked. This ensured minimization of

influence of the cable stiffness and maintained it to the

same degree for all angular positions of the shell.

8.4   The Transducer System.

The local static pressure at any point on the

shell surface could be expressed as a resultant of the

time-average pressure and oscillatory component (see

Equation 2.14). Clearly, better resolution in oscillatory

component is achieved by biasing the time-average (or non-

zero mean) pressure from the total pressure signals. The

requirements of the pressure transducer, then, are:

(i)   sensitive as to pick up small fluctuations with
        a bias facility

(ii)   small in size so that the measured pressure can
        be approximated to that at a point

(iii)   light in weight so that the inertia in dynamic
        measurements does not influence the structure

(iv)   little acceleration sensitivity

(v)   "instantaneous" and linear static and dynamic

         response

(vi)   convenient to handle.

The DISA Type 51 F 32 low pressure transducer seemed to meet these requirements and was the best available at the time. In conjunction with the DISA Type 51 E 32 oscillator, the DISA Type 51 E 01 reactance converter, a digital dc voltmeter read out and monitoring oscilloscope, the transducer was calibrated (see Appendix VIII) as a unit and referred to herein as the transducer system. The system can measure pressures from 0.1 to 700 mm of water with an over pressure of one atmosphere and in the dynamic range 0 to 100 KHz. The mean pressure bias may be applied by a "back pressure" (see Section 8.4.1) or electronically by an appropriate choice of the carrier frequency (see Section 8.4.3). A brief description of the relevant individual instruments is given in the following sections.

8.4.1   The Transducer.

The DISA Type 51 F 32 low pressure transducer is a capacitive microphone, in which a change in capacitance is caused by the deformation of a diaphragm due to impressed pressure. A $\frac{1}{4}$" condenser microphone B & K Type 4135 has been adapted for the purpose. A schematic diagram of the microphone cartridge is shown in the Figure (8.4). The diaphragm and the back plate separated by an insulator form the two plates of the capacitor ($\approx$ 6.4 PF). A pressure tight enclosure is provided behind the diaphragm by means of an adapter, of the DISA Type 51 F 33. Any reference

static pressure may be impressed on the backside of the diaphragm by a length of PTFE tubing connected to a variable pressure source. Though the diaphragm can withstand an over pressure of one atmosphere, it is prone to be damaged if touched. To facilitate ease in handling a modification was made to the adapter incorporating an integral protective cap (see Figure 8.5). The weight of the microphone together with the modified adapter was just over 8 gms.

In the pressure range of the present application, the effects of temperature changes, relative humidity and the changes in ambient pressure on transducer sensitivity are negligible. Also, the response is omnidirectional to the pressure field. The microphone in its basic (B & K) configuration has an acceleration sensitivity of $\approx$ 88 dB $(0.5N/M^2)$ pressure level at 1 g acceleration in a direction perpendicular to the plane of the diaphragm. In the present configuration the inertia of the air column seems to _damp out_ con- siderably   the acceleration sensitivity. Signal to noise ratios of better than 30 dB were observed in the worst case. Hence, no corrections to account for the vibratory motion were applied in the final analysis.

8.4.2   The Oscillator.

The DISA Type 51 E 32 oscillator is connected to the transducer via a special double shielded cable, the capacitance of which is greatly reduced by a special circuit. Capacitance changes due to temperature variations or due to mechanical forces applied to the cable are consequently greatly reduced. The sensitivity can be selected in four ranges: 0.1 PF, 1 PF, 10 PF and 100 PF. These values

indicate transducer capacitance change for a full scale variation of 6 V of the reactance converter (corresponding to a 0.5% variation of the operating frequency).

The oscillator consists of a Clapp oscillator coupled to the tuning circuit C_{2a} and C_{2b} (Figure 8.6). The sensitivity of the oscillator is determined by the value of C1 in parallel with the transducer capacitance while L1 determines which frequency band is being used. The selector plug has four different positions one corresponding each L1 and C1. The transducer is connected in parallel with C1 through the double-shielded cable. The inner shield carries a voltage which equals the oscillator voltage in amplitude and phase. This is accomplished by amplifier A1 which has a very high input reactance. Transformer Tr corrects the phase shift produced by the amplifier and the capacitive load imposed by the cable. In addition Tr delivers a voltage, approximately twice the oscillator voltage, to one stator of a differential capacitor Cp. The rotor connects to the tuning circuit. The other stator connects to the ground. Amplifier A2 drives the cable connecting the oscillator to the converter. DC power for A1 and the oscillator is obtained from the cable through an RC circuit.

8.4.3   The Reactance Converter.

The DISA Type 51 E 01 reactance converter is designed for detecting and linearizing the signal from a capacitive device. The system of measurement is based on frequency modulation of a carrier wave by means of a reactance change in the transducer. The frequency-sensitive

detector rectifies the signal following which the DC voltage variation will be proportional to the mechanical influence on the transducer system. The detector covers the frequency range 4.4 - 5.6 MHz. The converter tuning control facilitates matching with transducer capacitance in the system working range. This may be effectively utilised in compensating for the time-average pressure signal, so that a resultant signal has a zero mean value. Figure (8.7) shows the working range of the instrument. There is also facility for the correction of non-linearity and upper frequency limiting filters of 0.2 KHz , 2 KHz and 20 KHz. The sensitivity of the detector in the normal working range is approximately ±6 volts for ±9.5 PC frequency swing around detector zero frequency. The detector sensitivity is somewhat dependent on the zero frequency but the variation does not exceed 10% at 4.4 and 5.6 MHz, respectively. In the present tests, this zero frequency was within 5.0 ±0.05 MHz and the results are expected to be within 1%. The non-linearity in the most sensitive 0.1 PF range is 0.5% and is corrected for in the reactance converter. The maximum permissible length of the cable between the converter and read out or record divice is of the order of 200 meters.

8.5   The Analogue Tape Recorder.

The pressure and response signals are recorded on the FM channels of a 14 channel Sangamo Type 3562 recorder/ reproducer. The recorder is bidirectional with two tape speeds of 15 ips and 7½ ips. Accuracy of tape speed is

± 0.25% of the nominal speed. Input sensitivity is 0.1 to 2.5 volts rms, adjustable by input attenuator for ±40% deviation. The frequency response on FM channels is 5 KHz at 15 ips and 2.5 KHz at 7½ ips. Signal to noise ratio is better than 46 dB. All signals were recorded for later analysis, at 7½ ips tape speed with a nominal input level of 1.4 peak and a centre frequency of 13.5 KHz. DC linearity is within ±0.5% of peak to peak deviation and AC distortion is less than 1.5% total harmonic distortion at all speeds. No additional dynamic calibrations were therefore required and only a reference calibration was performed to obtain absolute levels. Since the gain control is not externally possible, the record-replay was set to unity gain at 1V rms at 50 Hz. Throughout the experiment, the signals were monitored on standard oscilloscopes.

8.6   The Level Recorder.

The rms levels were obtained as a first step in the analysis using the B & K Type 2315 level recorder. The paper speed and writing speed were selected such that the low cut frequency was 2 Hz and by replaying the tape at 15 ips (double the recording speed) this frequency was reduced to 1 Hz. This analogue analysis not only provided a check on the accuracy of the digital process but also provided a useful guide to the selection of data for further analysis from a large set of experiments.

8.7   The Digital Data Reduction System.

8.7.1   The Fourier Analyser.

The analogue data acquired on the tape recorder

was further analysed using the Fourier analyser system HP 5451 A. The system performs analyses of time and frequency data over a frequency range of 0-25 KHz by means of keyboard programming. The analogue data can be entered through a 10-bit 2 channel analogue-to-digital converter (ADC). Results of all operations are displayed on the oscilloscope. The output could be plotted on a x-y plotter or an on-line digital plotter. The flexibility of the system is greatly enhanced by the magnetic tape system and the facility to generate overlays suitable for individual requirements. The system, thus, comprises of 2100A digital computer, type 180 AR/DR oscilloscope, 5460A display plug-in unit, 5465A ADC plug-in unit, 5475A control unit, a teleprinter, HP 200A high speed punch, HP 5600A magnetic tape system and an on-line digital plotter. Only the salient features of the system pertaining to the present work are explained below in the following sections.

The Fourier analyser transforms any time domain data into the components in the frequency domain using a Finite Fourier Transform. It is more flexible than analogue machines for the purpose. Since the data processing is done digitally, it is more accurate and faster. All the mathematical operations involved in the data processing here are available as keyboard functions and no knowledge of the software is required.

8.7.2   The Analogue-to-Digital Converter.

The HP 5465A analogue-to-digital converter is a plug-in unit forming a part of the Fourier analyser system.

The digitization parameters could be selected either in the time domain or in the frequency domain using "mode" and "multiplier" selecting switches. With the choice in one domain, the parameters in the other are automatically fixed. The frequency resolution and the maximum frequency were chosen as the frequency domain parameters in the present analysis. The ADC is a 10 bit two channel unit with a digitization constant of 17 μ seconds. In dual channel operation, there is a 13 μ second gap between the two signals. Whilst the "free-run" mode provides instantaneous starting of digitization, a combination of "external-trigger" mode, "trigger level" and "slope" of trigger signal facilitate sychronous digitization if required. The "over load volts" switches determine the initial scale factors and the scale factors are automatically adjusted within if the signal levels exceed the set levels. No data are lost in the process. The ADC could be used with an "external clock" as well, in which case "multiplier" sets the proportional values of the parameter. The digitized data may be entered into any data block of the computer memory or may be stored in the ADC through-put file on a configured magnetic tape. The modes of operation corresponding to particular analyses such as PSD, correlations etc., are dealt with later in Section 11.

8.8   Experimental Procedure.

The experimental procedure and analyses techniques are briefly described here. Unless otherwise mentioned the procedure is identical in all the test runs-1 through 34.

(1)   The model is installed in the tunnel and the con-
       trol panel dial gauge (connected between settling
       chamber static tapping and atmosphere) is cali-
       brated for tunnel dynamic pressure over the range
       of velocities of the experiment. A pitot tube is
       used for the purpose which is removed after cali-
       brations.

(2)   The calibration signals are put on each of the
       record channels - 1V signal on pressure channels
       and set calibration signal ($\equiv$ 120 μ strains),
       provided in the strain gauge bridge, on the strain
       channels.

(3)   The model at a selected angular position and the
       traverse at an identical angular position are
       clamped in position in the wind tunnel.

(4)   The pressure transducer calibrations (Appendix VIII)
       and strain gauge calibrations are then checked.

(5)   The test velocity is attained by adjusting the fan
       speed, the dynamic pressure being read out on a
       betz manometer which is connected in parallel with
       the dial gauge.

(6)   When steady state is reached, the required bias
       (see Section 8.4.3) on pressure signals is applied
       by a choice of the RC centre frequencies and the
       signals are recorded over a predetermined period.

(7)   Steps (5) and (6) are repeated for all test speeds
       for a given model.

(8)   The wind tunnel is then stopped and "transducer
       sensitivities" are checked.

(9)   Steps (3) to (8) are repeated for other angular

positions at 15° increment of angles in the

interval 0° - 180°.

The procedure is repeated for all the five models.

Throughout the experiment signals were monitored

on oscilloscopes. The sensitivity levels were checked

using a digital DC voltmeter. Ambient conditions at the

beginning and end of the experiments were also noted down.

As a first step in the analysis, the analogue rms

levels were obtained from a level recorder at a later time.

10 seconds averaging time and 15 ips replay speed were used.

The low frequency limit was 1 Hz. From this study, runs

were selected for further digital analysis.

The ADC settings were adjusted corresponding to a

total time T of 1 sec. and frequency resolution of 1 Hz

for dual channel digitization. 20 blocks of size 1024

samples were recorded on a digital magnetic tape with the

analogue replay at the same speed (7$\frac{1}{2}$ ips) as record speed.

The rest of the analysis followed systematically standard

digital signal analysis procedures (Appendix VII).

8.9   Limitations.

Apart from the possible human errors, the experi-

mentation and analyses are subject to the following limit-

ations. (A more complete treatment is given in Appendix IX.)

(1)   The signals are not corrected for instrument noise

levels since the signal to noise ratios were

better than 40 dB (with the exception of oscill-

ating shell tests).

(2)   In general, no drift in the sensitivities of trans-
        ducers was observed as a consequence of steps (4)
        and (8) of Section (8.8).

(3)   Over the period of test runs, the changes in
        ambient conditions were observed to be small.

(4)   No corrections to account for the acoustic noise
        levels in the wind tunnel laboratory (reverberent
        field) were applied. The noise levels measured
        (Appendix IX) were less than -30 dB ref 1V.

(5)   Analog analysis of 1 second averaging time had
        a maximum deviation of $\pm$ 2 dB in some cases and
        the quoted results are the mean of the rms values.

(6)   Correlations were obtained from signals from which
        the DC levels were eliminated by performing a
        forward and inverse FT. Correlations being real
        time analyses, the unaveraged data set is a random
        set.

(7)   PSD are scaled to account for the interval centred
        Hanning that was employed. The scale factors
        obtained were based on those from the spectra of
        single frequency signals of known levels at ≈ 100
        hz and ≈ 200 hz from a sine wave generator and
        proportional variances.

(8)   The values of total damping (Structural and Aero-
        dynamic) obtained from half power values are
        corrected for loss of frequency resolution due to
        Hanning but are not filtered to eliminate other
        modes. The results are stress (strain) amplitude
        dependent as expected and are believed to be

accurate particularly in lower modes. At higher

modes, even the "unfiltered damping" is consider-

ably small.

PART   C

RESULTS AND DISCUSSIONS

9. RESULTS AND DISCUSSION OF DETERMINISTIC ANALYSES

9.1   Introduction

In this section the results of the theoretical deter-
ministic analyses are discussed. Rotatory and inplane in-
ertias are included in the results quoted. Axial variation
of pressures is not considered in the combined solution
consistent with the wind tunnel tests. Static solutions
are not discussed since the static analysis is straight
forward. However, the solutions from single mode static
analysis have been incorporated in the combined solution.

9.2   Linear Solution

The free linear vibration solution is obtained here
as a special case of the general solution and also to as-
sess the effect of rotatory and inplane inertias. The
frequency determinant, described in Section 3.4.1, is
identical to that of Reference (82). In Table 9.1 the
non-dimensional frequency $\sqrt{\Delta}$ is compared with the exact
solution of Forsberg[83] and that of Reference (82). It
is seen that the present analysis overestimates the fre-
quency, consistent with the Ritz technique employed. It
is observed that the beam function provides a reasonable
approximation to the axial displacements. The difference
between the present results and those of (82) are due to
the omission of a constant of integration in the latter.
The effect of rotatory and inplane inertias reduces with
increase in radius to thickness ratio and likewise with
increase in the axial mode number m and increase in slen-
derness ratio. The effect increases with increase in the

frequency. In general, while the results improve with the inclusion of these inertias, the overall effect on the frequency is still negligible for the geometries considered.

9.3 Free Non-Linear Vibrations

Figures 9.1 to 9.4 illustrate the non-linear response in the absence of excitation force and zero damping corresponding to the analysis described in Section 3.4.2. The free-non-linear response forms the 'back bone' of the forced response and is sufficient to describe the characteristic nature of the non-linearity. It is clear from the figures that the geometric non-linearity introduced in the analysis is of hardening type wherein an increase in the magnitude of the response amplitude is associated with an increase in the frequency ratio $(\Delta/\Delta_{lin})^{\frac{1}{2}}$. The multiplication factors associated with the amplitude $|C|$ do not convey any special significance; these factors were arrived at by trial and are for convenience in presentation of the data. However, for the mode (m = 1, n = 1) the 'reduced amplitude' ($|C|\ l^3/a^3$) is coincident over a large number of slenderness ratios and radius to thickness ratios (see Figure 9.1.a). Also, for the mode (2,1) the influence of the geometry on the reduced amplitude is negligible (see Figure 9.2.a). Considering the absolute amplitude $|C|$, it is clear from the Figures 9.1 and 9.2 that the influence of geometric non-linearity increases with increase in the magnitude of slenderness ratio. The influence of radius to thickness ratio is negligible for the modes (1,1) and (2,1) as indicated by Figures 9.1a and 9.2a. Figures 9.3 and 9.4

show the reduced response $(|C|a^2/h^2)$ curves with a/h as parameter. Consideration of absolute amplitude $|C|$ indicates that the geometric non-linearity increases with the radius to thickness ratio (shown by an increase in the curvature of the response plot). Figure 9.5 which is the solution of the linear frequency determinant (Equation 3.11) indicates that for the geometries considered (l/a = 15 to 50 and a/h = 50 to 600), the lowest frequency is in either (1,1) or (1,2) mode.

Figure 9.6 shows typical amplitudes in various modes for a given ratio of corresponding non-dimensional frequency and also the frequency ratio for a given amplitude corresponding to a typical shell geometry l/a = 20 and a/h = 250. Though the representation does not provide any absolute measure, it indicates that the dependance of absolute amplitude $|C|$ tends to be identical for higher values of circumferential wave numbers. Also, from the figure it is observed that for the given geometry n = 2 mode has the lowest frequency and that the influence of geometric non-linearity is to a larger extent in n = 1 mode as indicated by a higher frequency ratio required to achieve a given amplitude. Such a diagramatic representation can be employed in a suitable definition of the 'reduced amplitude.'

9.4   Forced Non-Linear Vibrations

Figure 9.7 illustrates the solution of forced non-linear vibration problem in which the parameter is the absolute value of the peak forces applied at the tip, acting

radially inwards. It is observed from the figure that the effect of increase in loading is to broaden the frequency range over which a given amplitude is exceeded,similar to that in the linear case. As described earlier, for larger values of frequency ratio, theoretically, the amplitude has three possible values. In practice, however, due to the associated damping, there occurs a 'jump' from a higher energy state (see Appendix VI, Fig. VI.1) to a lower energy state with the excitation frequency increasing and from a lower energy state to a higher energy state with the excitation frequency decreasing. The response curves in Figure 9.7 are constructed by solving the characteristic cubic for various values of the frequency ratio.

9.5   Natural Frequencies from Vibration Tests.

The comp.u ted natural frequencies of the shells F4 and F5, obtained from the solution of frequency determinant (see Section 3.4.1), are given in Table 9.2. It is clear from the Table that the lowest frequency of the shell F4 is in mode (1,1) and that of the shell F5 is in mode (1,2). This result can also be interpolated from the frequency envelope given in Figure 9.5 (which in fact is the solution of the same frequency determinant). Table 9.3 compares the theoretical results with the measured resonance frequencies. The measured values of the frequencies show better agreement at higher frequencies than at lower frequencies (contrary to the expectations). This may be, probably, due to the fact that the method of *clamping* at the base does not ensure 100% fixity; the shell being thin the effect of imperfect boundary condition diminishes as the frequency increases. The frequencies

obtained from the wind tunnel tests are generally lower than those from the vibration tests. This is attributed to the wind effects, perhaps, due to an interaction between the vortex shedding frequencies and the structural natural frequencies, rather than the 'added mass effects'. The observed results are in close agreement with those of Reference 97 for a shell geometry 'almost' the same as that of F4. The interchange of the mode shape for lowest frequency given by Reference 97 is, probably, because the frequencies in mode (1,1) and (1,2) are very close and also, 1/a for that shell is slightly higher than 1/a for the shell F4.

9.6   Measurements of Damping

Table 9.5 gives the values of logarithmic decrement evaluated from response decay plots. Also, the overall damping coefficients (structural damping + aerodynamic damping) are given, which were obtained from the ratio of half power values of the strain spectra to the bandwidth, corrected for the effect of single Hanning employed in the spectral evaluation. The structural damping coefficients agree with those of Reference 97, in which, half power method was used on oscilloscope traces of the response.

The negative values of the aerodynamic damping coefficients indicate the onset of the aeroelastic phenomenon though no instability was observed (since overall damping is still positive). In some of the intermediate modes, the aerodynamic excitation was slightly away from the corresponding resonance frequency and as such the damping coefficients are not reliable. It should be noted in this context, that

the damping coefficients are defined by the ratio of the band width to the centre frequency, only at the natural frequency; the ratio is a minimum when resonance occurs. The values quoted in the Table, consequently, are the lowest values.

10. RESULTS AND DISCUSSION OF OSCILLATORY PRESSURE AND RESPONSE MEASUREMENTS

10.1 Introduction

In this section the experimental data are analyzed for rms values. The time-average (mean) pressure distributions are taken from other references. The rms pressure distributions quoted are obtained by an analysis with an averaging time of 1 sec., low frequency cut of 1 Hz and high frequency limit of 2.5 KHz. The spectral analyses and probabilistic analyses both give results which are derived from digital analyses techniques. The relevant details are described in the following sections. The arrows in the Figure (6.2) indicate the range of Re covered in the study. Spectral analysis described later confirms that the present study does not extend into the transcritical regime.

10.2 Mean Pressure Distribution

In the present investigations the mean pressures were not studied for reasons described below. A large quantity of reliable information covering a whole range of Re is readily available on the subject. Also, better resolution of the oscillatory pressures implies the elimination of the mean pressures from the measurements. Further, the level recorder is limited by a low frequency cut of 2 Hz and the digital spectral analysis requires that the mean values are zero.

Figure (6.1) shows the distribution of mean pressure coefficient C_p (53) based on Gould's work (52). It is seen

from the figure that the C_p values are numerically lower for finite aspect ratio rigid cylinders than for a 2-D cylinder because of 3-D (tip) effects. This is clearly illustrated in Figure (10.1) wherein the axial variation of C_p is depicted (53). Likewise the tip effects are expected to decrease the magnitude of the oscillatory pressures (see Plate 10.1) due to the presence of tip vortices, though detailed pressure measurements were not conducted.

10.3 Rigid 'Two Dimensional' Cylinder Surface Pressures

Table (10.1) lists the cylinder geometries and the test runs conducted at various Reynolds numbers. Figure (10.2) shows the distribution of RMS pressure coefficient

$$c_p^* = \left[\frac{1}{T} \int_0^T p^2(t) \, dt \right]^{\frac{1}{2}} / \frac{1}{2} \rho \, v_\infty^2 \quad \text{at Re} = 1.63 \times 10^5 \text{ in}$$

comparison with the results of Surry[60] at Re = 0.4 $\times$ 10^5. The 2-D effect was achieved in the present case by fixing a top end plate on the shell R_2 as described in Section (8.3). Figure (10.3) depicts a typical pressure level record. The C_p^* levels are correct to $\pm$ 1dB ref unity. Not withstanding that the test conditions were different in the two cases good agreement is seen at 'zero' turbulence. Figure (10.4) shows the C_p^* distribution at two other Reynolds numbers. It is clear from these figures that the magnitude of C_p^* decreases with increase in Reynolds number. Attention is drawn to the high value of C_p^* in the 2-D configuration tests particularly at low Re. It is also noted that though the aspect ratio of the cylinder is comparatively small (= 3.3) for the configuration to be of a purely two-dimensional nature, never the less, the flow field is uniform

- 101 -

along the axis of the cylinder as will be later seen in the correlation studies (Section 11.3).

10.4   Rigid 'Three Dimensional' Cylinder Surface Pressures

A large number of experiments (Runs 1-5 and 9-20) were conducted on shells R_1, R_2 and R_3 in order to bring out scale effects. The distribution of the pressure coefficients is shown in Figures 10.5, 10.6 and 10.7. Clearly, from Figures 10.1 and 10.5,   the C_p^* nearer the tunnel wall (as recorded by T_3) is considerably lower than that at the top for the two Re $(0.4-1.62 \times 10^5)$ Comparison of Figures 10.5 and 10.6 at Re ≃ 1.63 for the response of T_1 indicates that the oscillatory pressure depends on the axial position of measurement. It is also clear from the Figure (10.5) that the present investigation shows good agreement with the results of Reference (52). Perusal of Figures 10.6 and 10.7 leads to the conclusion that for small aspect ratios, the C_p^* is very much dependent on the axial position of measurement and on the Reynolds number and   exhibits no   regular pattern. However, it is clear from Figure (10.8) that for large aspect ratios, the variation of C_p^* with Re is less drastic at any given circumferential position.   This suggests that excepting in the vicinity of the tip and the base, a mean C_p^* can be employed which is independent of the Reynolds number for the purposes of Fourier series representation.

10.5   Flexible 'Three Dimensional' Shell Surface Pressures

Great care had to be exercised to measure the surface

pressures on a flexible cylinder though the transducer acceleration sensitivity is within acceptable limits (see Appendix VIII). Comparison of Figures 10.8, 10.9 and 10.10 indicates that the C_p^* values are generally higher on the flexible shells. Clearly there are no apparent acceleration induced signals in the pressure measurements on the shell F4 (see Figure 10.9) though high values of C_p^* are experienced in the vicinity of 165° and 180° angles. A consistent distribution pattern is exhibitted in the Figure (10.10) for the shell F5, excepting in the vicinity of 45° and 135° incidence at lower values of Re (see also Section 11.5). These pressure rises are believed to be due to favourable phasing of the pressure and motion of the transducers, possibly in the sway mode for the shell F4 and the ovalling mode for the shell F5, rather than acceleration sensitivity for reasons stated elsewhere. The general consistent pattern of distribution of C_p^* apparent from both the Figures 10.9 and 10.10 suggests that a mean distribution can, probably, be employed to describe the aerodynamic admittance mathematically.

10.6 Aerodynamic Admittance Function for Oscillatory Pressures

Table 10.2 gives the rms fluctuating pressure coefficients round rigid cylinders for typical runs. A thirteen term Fourier Series expansion for this data was fitted and the coefficients are given in the Table 10.3. The coefficient a_o representing the uniform distribution round the cylinder is predominant. No special significance to this need be attached, since, the distribution represents rms values, which are always positive. The coefficients

generally decay with increasing number of terms. A smaller number terms in the expansion can be justified for certain distributions.

The rms fluctuating pressure coefficients, evaluated as a graphical mean, are given in the Table 10.4 for runs 9 to 20 and runs 21 to 34 and the corresponding Fourier coefficients are given in the Table 10.5. These coefficients of the describing function are later used in the random response analysis.

10.7 The Coefficients of Fluctuating Lift and Drag

The rms values of the fluctuating lift and drag coefficients can be easily derived by integrating the inline and transverse components of C_p^* respectively. Thus, the rms drag coefficient C_D^* is given by

$$C_D^* = \int_0^{2\pi} C_p^* \cos \theta \, d\theta$$

$$= \int_0^{2\pi} p_n \cos n\theta \cos \theta \, d\theta$$

or $\quad C_D^* = p_1 \pi$

and the rms lift coefficient C_L^* is given by

$$C_L^* = \int_0^{\pi} C_p^* \sin \theta \, d\theta$$

$$= \int_0^{\pi} p_n \cos n\theta \sin \theta \, d\theta$$

- 104 -

or $\quad C_L^* \quad = \quad - 2 \quad \sum\limits_{n=0,2,4\cdots}^{N} P_n / (n^2 - 1)$

It is noted that the lift coefficient is over estimated due to the assumption of alternate vortex shedding. The location of the centre of pressure (rms) can be also evaluated easily. Table 10.6 gives typical values of the lift and drag coefficients and the corresponding location of the centre of oscillatory pressure. From the Table, it is seen that there is a wide variation in the location of oscillatory C.P. (118° to 148°). It is generally expected that C_L^* will be less than C_D^* for cylinders and that the C.P. will be in the vicinity of 135°. With the exception of runs 3, 4, and 8, $C_L^* < C_D^*$ and the C.P. is located such that there is a greater tendency for the shell to oscillate with an ovalling (mode 1,2) axis at 135°, rather than with the axis in line. Such a conclusion will be, however, *erroneous* unless supported by pressure correlation studies.

11.   RESULTS AND DISCUSSION OF SPECTRAL ANALYSES

11.1   Introduction

In this section typical, measured pressure and response data are analyzed using digital spectral analysis techniques. Continuous analogue data (4 min duration at $7\frac{1}{2}$ ips record speed) are digitized and stored on a digital magnetic tape. A block size of $N = 1024$ samples with a frequency resolution of $\Delta f = 1$ Hz and a total time $T = 1$ sec. are employed in general. A Hewlett-Packard HP 5451 A Fourier Analyser system was employed for the analyses described here.

11.2   Pressure Spectra (Rigid Cylinders)

Typical pressure power spectra for selected cases are shown in Figures (11.1 to 11.4). The spectra are corrected averages of 10 set estimates subject to a single Hanning. Both the ordinate and abscissa in Figures 11.1 to 11.3 are in log scales. It is clear from Figure (11.1) for the rigid '2-D' cylinder R2, at Re = 2.26 x 10^5 (Run No.7), that there exists predominant vortex shedding with a Strouhal number of 0.18. In the region of attached flow of 0° to 60° angular position the higher harmonics are not apparent. At higher angles however, the first and second harmonic of the Strouhal frequency also are discernible. The factor $\frac{1}{2}$ in the ordinate description is because the spectrum obtained from the computer is only one half of the symmetric spectrum.

The spectra at various angular positions for the rigid 3-D cylinder R3, at the same Re = 2.26 x 10^5 (Run No.4), at

two axial positions corresponding to $\xi = 0.965$ and $\xi = 1.75$ are shown in Figures 11.2 and 11.3. It is seen that the Strouhal number is 0.17. In contrast with Figure (11.1) the higher harmonics are not clearly identifiable and the magnitude of the squared pressure is two orders of magnitude lower in the predominant frequencies compared with '2-D' results. In 3-D case there is a tendency for a more uniform distribution over the frequency band as also broadening of the peak frequency. It should be noted that the vortex influence has propagated up stream including the vicinity of the stagnation line, in contrast with the observations of Surry[60] wherein no such Strouhal peak was identified at this position. This broadening of the spectra in the 3-D case suggests that the wind load in a steady wind should also be treated as a random load, provided it is confirmed by a probability distribution function (see Section 11.4). In all these cases the spectra were plotted in linear scale also, to identify the frequency band as a check against aliasing. Figure (11.4) represents these spectra for the rigid cylinder R3 at a Re = 1.9×10^5 (Run No. 19). It is observed from the figure that, excepting at the stagnation point, there is virtually no spectral energy at higher frequencies implying that there is no apparent need for filtering high frequencies. The analyses up to a maximum frequency of 512 Hz are generally adequate.

11.3 Correlation Studies

The auto-correlations were obtained as real time functions for an effective period of 0.5 sec. The mean value

was eliminated from the signal by a forward and inverse transform, clearing the zero frequency component in an intermediate step. Wrap-around errors were eliminated as explained in Appendix VII. The cross correlations were normalized with respect to the product of zero time delay auto-correlations. Typical symmetric correlograms and correlation coefficients of pressures are illustrated in Figures 11.5 to 11.13. It is seen from Figures 11.5 and 11.6 for a '2-D' cylinder that there is strong influence of vortex shedding as seen by the cosine form of the curves. Higher frequencies also are present at the stagnation point due to free stream turbulence, at 105° due to turbulent separation and at 180° due to wake turbulence caused by vortices. In general, the correlograms exhibit a slow decay indicating that the physical process is a combination of sine-random variation (see Figure 6.3). Figure (11.7) indicates the axial cross-correlation of pressures at various angles and Figure (11.8) gives the axial correlations coefficient (zero time delay cross correlation). In general, the first zero crossing and the peaks are approximately at the corresponding time delays for various angles (excepting 60°, 75° and 180°) indicating that the flow field is independent of the axial location on the cylinder. At 105°, probably due to separation effects the correlations are not good.

Figures 11.9 and 11.10 display the auto-correlations at the same Re for the 3-D configuration. It is seen that though the influence of vortex shedding is still present there are higher frequencies throughout the flow field.

Only at 45° where the boundary layer is purely laminar and the free stream turbulence influence is negligible, is the vortex influence strikingly predominant. From Figure (11.11) it can be said that the flow field has no variation in the direction of cylinder axis. In conjunction with Figure (11.12), poor cross-correlations are observed at angular positions greater than 45°. This implies that the flow field is highly turbulent at these positions due to the influence of tip vortices in the 3-D case.

Figure (11.13) illustrates the auto-correlations for the cylinder R3 (Run No. 19). Here again the behaviour is somewhat erratic and the presence of higher frequencies also can be observed. It can be concluded that in this case the vortex shedding is not stable. These discussions agree with the conclusions drawn from the spectral study but also provide more information about the flow field.

11.4   Probability Description

The probability density function provides information about the mean values and peak excursions in addition to establishing the nature of a random process. Figures 11.14 to 11.16 illustrate the density of occurrences of a value of C_p. The analysis was carried out on 'raw' signals. Comparing with Figure (6.4) one can deduce that the spikes in the density function indicate the presence of higher frequencies. However, the mean curve may be considered as a narrow band random process. If the observation time and the number of samples are large, the process could be approached as purely random with Gaussian distribution. Figure (11.14) shows the probability density functions of pres-

sures at various angular position for Run No.7. The mean value of the signals is seen to be zero as indicated by the symmetry about the ordinate at zero.

Similar observations can be inferred from Figure (11.15) for Run No. 7 and Figure (11.16) for Run No. 19. As in the case of the rms values previously considered, the peak values also are smaller in the 3-D case compared to the 2-D case. The scale of the abscissa in Figure (16) is, however, arbitrary. The integral of the probability density which yields the probability distribution is illustrated in Figure (11.17) for Run No. 19. It is concluded that the distribution function can be considered as Gaussian provided that the observation time is large, as would be the case in wind effects on ground structures.

11.5 Flexible Shell Analysis

Extensive experiments were conducted on the flexible shells F4 and F5 to establish the (wind) force-response characteristics. The complexity of the experimental study, involving multimode response, can be seen in that there are a number of critical velocities. So also, there are many possible locations on the shell at which the strain or the displacement response is a maximum, depending on the mode of oscillation. Ideally, critical velocities should be established from simple, qualitative tests in the wind tunnel and the quantitative measurements should be carried out at and in the neighbourhood of these velocities. In the present study, however, a number of runs were conducted at regular intervals on an arbitrary dynamic pressure scale.

The critical velocities measured in preliminary tests were close to the velocities of these runs. This will be clear from the explanation that follows.

Figures 11.18, 11.19 and 11.20 illustrate the progressive development of strains as the test velocity increases. The spectra shown are normalized spectra, so that the area under the curve is unity. It is clear from the Figure 11.18 that shell F4 exibits a change in mode of oscillation as the test velocity increases. The mode $(1,1)$ is not clearly identified due to the fact that the strain gauge at $(66",60^{\circ})$ produces little axial strain signals, the gauge being at the top end. The next four lowest modes are clearly discernible from these spectra. The progressive growth of mode $(2,3)$ at 122 Hz from runs 21 to 27 has masked in growth of the response in $(2,2)$ mode at 114 Hz, with the gauge located at $(66",60^{\circ})$.

Figures 11.19 and 11.20 indicate that the shell F5 is excited at the frequencies and modes given in Table 9.4. Because of the location of the strain gauges the response at 70 Hz is missing in Figure 11.19 and two other modes can not be identified in Figure 20. It is clear that the excitation is at different natural frequencies as the test velocity varies.

The frequency-weighted power spectra $(f\,S_{pp})$ of the oscillatory pressures are given in Figure 11.21 for the two shells F4 and F5, at various velocities. The measurement point was at 90° angular position to the free stream direction. The arrows indicate the Strouhal (vortex shedding) frequency. Due to rather an unfortunate choice

of the location of the transducer, the locking-in phenomenon is not clearly brought out, since at this location due to laminar separation, the vortex frequency is masked in the turbulent pressure signals. The arrows in the figures indicate the Strouhal frequencies. The response of the transducer to the natural frequencies of the shell is predominant at certain velocities at this location (90°) as shown by the peaks in the spectra.

The weighted power spectra of the strains given in the Figures 11.22, 11.23 and 11.24 convey essentially the same information, as was discussed with respect to the Figures 11.18, 11.20 and 11.19 respectively. In these figures, the non-dimensionalizing factor is the square of the dynamic pressure. Frequency-weighting brings out characteristic higher frequencies which are otherwise lost in the noise. The various modes and the corresponding frequencies have been identified and marked on these figures.

Figures 11.25, 11.26, 11.27 and 11.28 indicate the rms values of the fluctuating strains at various angular positions. Comparison of Figures 11.25 and 11.26 for the shell F4 and Figures 11.27 and 11.28 for the shell F5 indicate that the breathing mode strains are more critical than the sway mode strains, for these geometries.

11.6   Results of Random Response Analysis

The response to white noise excitation, evaluated for unit value of the non-dimensional coefficient

$(a/h)(1-\nu^2)(a/l)(q/E)$ (see Equation 5.15), where q is the dynamic pressure, is shown in the Figures 11.29, 11.30 and 11.31. These results were obtained from the program

RANDOM. Figure 11.29 illustrates the strain power spectra for three values of the structural damping coefficient, for the shell F4 at a location $(66", 60^{\circ})$. For simplicity, the effect of damping is shown only at the structural natural frequencies. At the other points on the graph, the spectral values very nearly coincide. Comparison of the Figures 11.22 and 11.29 indicates that the results of the theoretical analysis closely follow those of the experiments. Unfortunately, it is difficult to compare the exact magnitudes since the evaluated input spectra in Figure 11.21 are not representative of the total pressure field. It can be seen, however, that the above non-dimensional constant yields a factor of $(3.45 \times 10^{-9}/\text{mm}$ of water$)$ for the shell F4 and multiplication of smoothed spectra in Figure 11.21 by q times the spectra in Figure 11.29 yields the spectra of magnitude comparable to those in Figure 11.22.

Figures 11.30 and 11.31 illustrate the reduced strain spectra computed for the shell F5 at the three locations $(2", 0^{\circ})$, $(66", 45^{\circ})$ and $(66", 0^{\circ})$. Comparison of the computed spectra for the first two locations with the measured spectra given in the Figures 11.24 and 11.23 repsectively, brings out the ability of the present multimode analysis to evaluate the strain levels at any given location. The magnitudes of the computed strain spectra, in conjunction with Figure 11.21 and the new non-dimensional constant $(5.22 \times 10^{-9}/\text{mm}$ of water$)$ for the shell F5, compare well with the measured spectra. The effect of structural damping is illustrated in the figures at the spectral peaks corresponding to the natural frequencies of the shell F5. It is

observed that the effect of increasing g from 0.01 to 0.03 is to reduce the spectral peaks by one order of magnitude.

The output/input relations evaluated from the measured signals at arbitrary locations are illustrated in the Figures 11.32, 11.33 and 11.34. However, since the input is not representative of the total pressure field, which is causing the excitation, the figures should be treated to be as qualitative in nature. It is noted that the response characteristic of the multi-mode type are brought out in these figures also, with the peaks clearly located at the natural frequencies of the shells.

11.7   Notes on the Scales of the Power Spectra

and Run Numbers

The ordinates of the power spectra in the Figures 11.1 to 11.3 and 11.21 to 11.24 are such that for any intermediate point a linear interpolation is to be carried out between each multiples of 10. The number read out should be multiplied by 2 so that the result is of the form f. S_{pp}/q^2 or f S_{ee}, as the case may be. This is as a consequence of replacing the dB ordinates in the figures by multiples of 20: e.g. 10^{-2} stands for $10 \log 10^{-2} = -40$dB. The ordinates in the Figures 11.29 to 11.31 should be interpolated logarithmically. The abscissa in all these figures are in log scale.

Throughout the text, the data are identified by the run number of the tests. For convenience, the conditions of tests at these runs are listed separately in the Table 11.1.

12   CONCLUSIONS

The linear deterministic analysis indicates that the beam functions provide reasonably accurate description of the displacements, in evaluating the natural frequencies. The non-linear analysis incorporating large deformation leads to a "hardening" effect. The energy method formulation, in the form that is adapted, is elegant in that the extentions to the analyses of single-mode-static-collapse, non-linear response in the presence structural damping and probabilistic-deterministic fatigue inclusive of mean or initial deformations, can be easily carried out as have been developed here.

The multimode random response analysis technique developed from energy methods, gives results which show good agreement with the response measurements carried out in the wind tunnel tests. Increase in damping coefficient from 0.01 to 0.03 will reduce the strain (power) spectral peaks to one tenth the original peak.

The oscillatory pressure measurements indicate that these pressures are larger in magnitude in 2-D configuration than in the 3-D configuration and the energy in the latter extends over higher frequencies. It is also observed that the harmonics of the Strouhal frequency are identified in the pressure spectra. In the Re region of (1.6 to 2.85)x 10^5, the vortex shedding is unsteady indicating that a probabilistic analysis needs to be followed, if the observation times are large; this will be the case in wind effects on earth-borne structures where the Re number extends to the transcritical regime and beyond.

The study of oscillatory pressures on <u>flexible</u> shells
(first of its kind to the author's knowledge) indicates
that these pressures are larger in magnitude, than those
on rigid cylinders. Due to the complexity and the cost of
instrumentation, a more extensive study involving space-
time correlations than attempted here will, probably,
not be justified. It is observed from the experiments that
there is locking-in phenomenon over a range of velocities,
at each natural frequency of the structure. Also, the
strains in the breathing modes are more severe than in the
sway modes.

There is a need for further work, in the measurement
of pressures on full scale structures over long periods of
time, such that the statistical methods of evaluating wind
loads, which are at present based on velocity measurements,
can be applied with confidence. The current codes of
practice on wind loading should be modified to incorporate
dynamic effects to a greater detail.

REFERENCES.

1. Marris, A.W.
A Review of Vortex Streets, Periodic Wakes and Induced Vibration Phenomena.
ASME 62 - WA - 106, 1962.

2. Johns, D.J.
Wind Excited Behaviour of Cylindrical Structures: Its Relevance to Aerospace Design.
Paper 25, AGARD CP 48, 1969.

3. Rayleigh, J.W.S.
On the Infinitesimal Bending of Surfaces of Revolution. London Math. Soc. Proc., 13, 1881, p.4.

4. Love, A.E.H.
A Treatise on Mathematical Theory of Elasticity. Dover Publ., Fourth Ed., 1944, Ch. 24.

5. Timoshenko, S.
Theory of Plates and Shells. McGraw-Hill, N.Y., 1940.

6. Basset, A.B.
On the Extention and Flexure of Cylindrical and Spherical Thin Elastic Shells. Phil. Trans. Roy. Soc., A, 181, 1890, pp. 433-480.

7. Vlasov, V.Z.
Basic Differential Equations in General Theory of Elastic Shells. NACA TN 1241, Translation from Russian, 1951.

8. Hildebrand, F.B.
Notes on the Foundations of the Theory of Small Displacements of Orthotropic Shells. NACA TN 1833, 1949.

9. Kennard, E.H.   The New Approach to Shell Theory:
                                  Circular Cylinders. J. Ap. Mech.
                                  Trans. ASME, 75, 1953, pp. 33-40.

10. Epstein, P.S.   On the Theory of Elastic Vibrations
                                  in Plates and Shells. J. Maths.
                                  Phys., 21, 1942, pp. 198-208.

11. Flugge, W.   Stresses in Shells. Springer-Verlag,
                                  Berlin, 1967.

12. Donnell, L.H.   Stability of Thin-Walled Tubes under
                                  Torsion. NACA TR 479, 1933.

13. Rayleigh, J.W.S.   The Theory of Sound, (1894), Dover
                                  Publ., N.Y., 1945, Vol. I.

14. Baron, M.L.   Table of Frequencies and Modes of
    and   Free Vibration of Infinitely Long
    Bleich, H.H.   Thin Cylindrical Shells. J. Ap.
                                  Mech. Trans. ASME, 76, 1954,
                                  pp. 178-18.

15. Junger, M.C.   The Propagation of Elastic Waves
    and   in Thin-Walled Cylindrical Shells.
    Rosato, F.J.   J. Acou. Soc. Am., 26, 1954,
                                  pp. 709-713.

16. Lin, T.C.   A study of Axisymmetric Vibrations
    and   of Shells as Affected by Rotatory
    Morgan, G.W.   Inertia and Transverse Shear.
                                  J. Ap. Mech. Trans. ASME, 78, 1956,
                                  pp. 255-261.

17. Herrmann, G.   Three Dimensional Shell Theory and
    and   Analysis of Axially Symmetric
    Mirsky, I.   Motions of Cylinders. J. Ap. Mech.,

23, 1956, pp. 563-568.

18. Yu, Y.Y. Vibrations of Thin Cylindrical Shells Analyzed by Means of Donnell-Type Equations. J. Aero. Sc., 25, 1958, pp. 699-715.

19. Naghdi, P.M. On the Theory of Thin Elastic Shells. Quart. Ap. Maths., 14, 4, 1957, pp. 369-380.

20. Herrmann, G. and Armenakas, A.E. Dynamic Behaviour of Cylindrical Shells under Initial Stress. Proc. Fourth U.S. Nat. Cong. Ap. Mech., June 1966, pp. 203-213.

21. Reismann, H. Forced Motion of Cylindrical Shells. Fourth U.S. Nat. Cong. Ap. Mech., June 1966, P. 159.

22. Medige, J. Dynamic Response of Cylindrical Shells. Ph.D. Thesis, I.I.T., Illinois, 1966.

23. Leissa, A.W. Vibration of Shells. NASA SP 288, 1973.

24. Sanders, J.L., Jr. An Improved First Approximation Theory for Thin Shells. NASA TR-R24, 1959.

25. Reissner, E. Non-Linear Effects in the Vibration of Cylindrical Shells. Report No. AM 5-6, Guided Missiles Res. Div., The Ramo-Wooldridge Corp., Sept. 1955.

26. Chu, H. — Influence of Large Amplitudes on Flexural Vibrations of a Thin Cylindrical Shell. J. Ae. Sc., 28, 8, Aug. 1961, pp. 602-609.

27. Nowinski, J.L. — Non-Linear Transverse Vibrations of Orthotropic Cylindrical Shells. AIAA, 1, 3, March 1963, pp. 617-620.

28. Cummings, B.E. — Some Non-Linear Vibration and Response Problems of Cylindrical Panels and Shells. AFOSR 3123, CIT, Aeroel. Str. Dyn. SM 62-32, N62-16248, June 1962.

29. Evensen, D.A. — Some Observations on the Non-Linear Vibration of Thin Cylindrical Shells. AIAAJ, 1, 12, Dec. 1963, pp. 2857-2858.

30. Olson, M.D. — Some Experimental Observations on the Non-Linear Vibration of Cylindrical Shells. AIAAJ, 3, 9, Sept. 1965, pp. 1775-1777.

31. Evensen, D.A. — Non-Linear Flexural Vibrations of Thin-Walled Circular Cylinders. NASA TN-D 4090. Langley Res. Centre, 1967.

32. Evensen, D.A. and Fulton, R.E. — Some Studies on the Non-Linear Dynamic Response of Shell-Type Structures. Int. Conf. Dyn. Stability of Str., Evanston, 1965, also, Dynamic Stability of

Structures, Ed. G. Herrmann,

Pergamon Press, N.Y., 1966,

pp. 237-254.

33. Matsuzaki, Y. A Theoretical and Experimental
and Study of the Non-Linear Flexural
Kobayashi, S. Vibrations of Thin Circular

Cylindrical Shells with Clamped

Ends. Trans. Jap. Soc. Ae. Sp.

Sc., 12, 21, 1970, pp. 55-62.

34. Leissa, A.W. Curvature Effects on Shallow
and Shell Vibrations. JSV, 16, 2,
Kadi, A.S. May 1971, pp.

35. Mayers, J. On the Non-Linear Free Vibrations
and of Thin Cylindrical Shells. Dev.
Wrenn, B.G. in Mech. Proc. Tenth Midwestern

Mech. Conf. 4, 1967, Johnson Publ.

Co. pp. 819-846.

36. Nataraja, R. Non-Linear Vibrations of Circular
and Cylindrical Shells with Various
Johns, D.J. Boundary Conditions. Symp. on

Non-Linear Dyn. LUT, March 1972.

37. Anon. Characteristics of Wind Speed in

the Lower Layers of the Atmosphere

near the Ground: Strong Winds

(Neutral Atmosphere). ESDU 72026,

Publ. Eng. Sc. Data Unit, London,

Nov. 1972, Amendment A, July 1973.

38. Sachs, P. Wind Forces in Engineering,

Pergamon Press, 1972.

39. Shellard, H.C.   Wind Records and their Application to Structural Design. Met. Mag., 96, 1141, 1967, pp. 235-243.

40. Davenport, A.G.   Wind Loads on Structures, NRC, Canada, Div. Building Res. Tech. Paper 88, Rep. NRC 5576, March 1960.

41. Harris, R.I.   The Nature of the Wind, Paper 3, The Modern Design of Wind-Sensitive Structures, Proc. CIRIA Seminar, London, 1970.

42. Pasquill, F.   Wind Structure in the Atmospheric Boundary Layer. Phil. Trans. Roy. Soc., London, A, 169, Feb. 1971, pp. 439-456.

43. Thompson, N.   The Variation of Mean Wind Speed with Height for Strong Winds. ESDU Memor. No. 6, 1972.

44. Thompson, N.   The Variation of Mean Maximum Wind Speeds with Averaging Time for Strong Winds. ESDU Memor. No. 7, 1972.

45. Cermak, J.E.
    and
    Arya, S.P.S.   Problems of Atmospheric Shear Flows and their Laboratory Simulation. Paper 12, AGARD Conf. Proc. No. 48, Feb. 1970.

46. Anon.   British Standard Code of Practice CP3: Chapter V: Part 2, Wind Loads. BSI, 1972.

47. Pierce, R.W.   The Case for a Harmonisation of
                            National Codes. Proc. Chimney
                            Design Symp. Vol. 1, CICI, Univ.
                            Edinburgh, April 1973.

48. Strouhal, V.   Über eine Besondere art der
                            Tonerregung. Annalen der Physik
                            und Chemie, 5, 1878, pp. 216-251.

49. Rayleigh, J.W.S.   The Theory of Sound, (1896),
                            Dover Publ. N.Y. 1945, Vol. II.

50. Tritton, D.J.   A Note on Vortex Streets Behind
                            Circular Cylinders at Low Reynolds
                            Numbers. JFM 45, 1971, pp. 203-208.

51. Roshko, A.   Experiments on the Flow Past a
                            Circular Cylinder at Very High
                            Reynolds Numbers. JFM, 10, 3,
                            1961, pp. 345-356.

52. Gould, R.W.F.   Wind Tunnel Tests on Chimneys of
    et al.   Circular Section at High Reynolds
                            Numbers. Symp. on Wind Effects on
                            Buildings and Structures, LUT, 1968.

53. Anon.   Fluid Forces Acting on Circular
                            Cylinders for Application in General
                            Engineering. Part 1: Long Cylinders
                            in Two Dimensional Flow. 70013.
                            Part 2: Finite Length Cylinders.
                            70014 ESDU, London, 1970.

54. Bishop, R.E.D.   The Lift and Drag Forces on a
    and   Circular Cylinder Oscillating in a
    Hassan, A.Y.   Flowing Fluid. Proc. Royal Soc.

A, 277, 1964.

55. Keefe, R.T.   An Investigation on the Fluctu-
ating Forces Acting on a
Stationary Circular Cylinder
in a Subsonic Stream and Asso-
ciated Sound Field, UTIAS Rept.
76, Sept. 1961.

56. Fung, Y.C.   Fluctuating Lift and Drag
Acting on a Cylinder in a Flow
at Supercritical Reynolds
Numbers. J.Ae. Sc., 27, 11,
Nov. 1960, pp. 801-814.

57. Chen, Y.Y.   Influence of the Von Karman
Vortex Behaviour upon the
Strouhal Number and the Drag
and Lift Coefficients for a
Circular Cylinder with Smooth
or Rough Surface in a Turbulent
Cross Flow up to the Trans-
critical Reynolds Number. Res.
Lab. for Vibration and Acoustics,
Sulzer Bros. Ltd., Winterthur,
Switzerland, Nov. 1967.

58. Schmidt, L.V.   Measurements of Fluctuating
Air loads on a Circular Cylinder.
JA/C, 2, 1, 1965, pp. 49-55.

59. Gerrald, J.H.   Measurements of the Fluctuating
Pressure on the Surface of a
Circular Cylinder, Part I;

Cylinder of 1" Diameter.   ARC 19,
844, Jan. 1958.

60. Surry, D.   The Effect of High Intensity
Turbulence on the Aerodynamics of
a Rigid Circular Cylinder at Sub-
critical Reynolds Number.   UTIAS
Rept. 142, Oct. 1969.

61. Ferguson, N.   Surface and Wake Flow Phenomena
     and   of the Vortex-Excited Oscillation
     Parkinson, G.V.   of a Circular Cylinder.   Paper 57,
ASME Vibrations Conf. Boston, 1967.

62. Wootton, L.R.   The Oscillations of Large Circular
Stacks in the Wind.   Proc. Inst.
Civil Eng. 43, 1969, pp. 573-598.

63. King, R.,   On Vortex Excitation of Model
     Prosser, M.J.   Piles in Water.   JSV, 29, 2, July
     and   1973, pp. 169-198.
     Johns, D.J.

64. Cincotta, J.J.   Experimental Investigation of
     et al.   Wind Induced Oscillation Effects
on Cylinders in Two Dimensional
Flow at High Reynolds Numbers.
Ref. 76, 1966.

65. Toebes, G.H.   Fluid-Elastic Features of Flow
Around Cylinders.   Paper 37, Ref.
77, Vol. II, 1967, pp. 323-341.

66. Toebes, G.H.   Fluid-Elastic Force on Circular
     and   Cylinders.   Proc. ASCE, J. Eng.
     Ramamurthy, A.S.   Mech. 93, 1967, pp.

67. Ukeguchi, N. et al. — Study on Unsteady Aerodynamic Forces Acting on an Oscillating Circular Cylinder. Proc. of 1st Symp. on Wind Effects on Structures, Japan, 1970.

68. Campbell, A.C. and Etkin, B. — The Response of Cylindrical Structure to a Turbulent Flow Field at Subcritical Reynolds Number. UTIAS TN-115, July 1967.

69. Cooper, K. — Bending Response of a Cantilever Cylinder to Turbulent Shear Flow. UTIAS TN-139, Aug. 1969.

70. Novak, M. — On Problems of Wind-Induced Lateral Vibrations of Cylindrical Structures. Ref. 77, 1967, pp. 429-457.

71. Davenport, A.G. — The Application of Statistical Concepts to the Wind Loading of Structures, Proc. Inst. Civil Eng., 19, 1961.

72. Handa, K.N. and Clarkson, B.L. — Response of Tall Structures to Atmospheric Turbulence. Paper 14, Ref. 74, 1968.

73. Anon. — Wind Effects on Buildings and Structures. 2 Vols. Proc. of Conf. at NPL, Teddington, June 16-28, 1963.

74. Anon. — Wind Effects on Buildings and Structures. 2 Vols. Proc. of

Symp. at LUT, Loughborough,
April 2-4, 1968.

75. Anon.
Wind Effects on Buildings and Structures. Proc. of Third Int. Conf. at Tokyo, 1971.

76. Anon.
Meeting on Ground Wind Load Problems in Relation to Launch Vehicles. Compilation of Paper Presented at NASA Langley Res. Centre, June 7-8, 1966.

77. Anon.
Wind Effects on Buildings and Structures. Proc. Int. Res. Sem. at Ottawa, 2 Vols., Sept. 11-15, 1967.

78. Anon.
Vibration Problems in Industry. Int. Symp. April 10-12, 1973, Keswick, England. (Preprints).

79. Robson, J.D.
Random Vibrations, Edinburgh, 1963.

80. Crandall, S.H.
Random Vibrations, Wiley, 1958.

81. Lin, Y.K.
Probabilistic Theory of Structural Dynamics. McGraw-Hill Book Co., 1967.

82. Sharma, C.B.
and
Johns, D.J.
Vibration Characteristics of Clamped Free and Clamped Ring Stiffened Circular Cylindrical Shells: A Theoretical Analysis. LUT, TT-7001, Jan. 1970.

83. Forsberg, K.
Exact Solution for Natural Frequencies of Ring Stiffened

		Cylinders. AIAA/ASME 10th Str., Str. Dyn. and Materials Conf. New Orleans, April 14-16, 1969.
84.	Bishop, R.E.D. and Johnson, D.C.	The Mechanics of Vibration. Cambridge Univ. Press, 1960.
85.	Davenport, A.G.	On the Statistical Prediction of Structural Performance in the Wind Environment. Proc. of Sem. Wind Loads on Structures, Hawaii, 19-24 Oct., 1970.
86.	Davenport, A.G.	The Estimation of Load Repititions on Structures with Application to Wind Induced Fatigue and Overload. RILEM Int. Symp. on the "Effects of Repeated Loading of Materials and Structures", Mexico City, Sept. 15-17, 1966, Vol. I.
87.	Davenport, A.G.	Structural Safety and Reliability Under Wind Action. Int. Conf. on Structural Safety and Reliability, April 9-11, 1969, Ed. A.M. Freudenthal, Pergamon Press, 1972. pp. 131-145.
88.	Minorski, N.	Nonlinear Oscillation. Van Nostrand Co. Inc., N.Y. 1962.
89.	Stoker, J.J.	Nonlinear Vibrations in Mechanical and Electrical Systems. Interscience Publ. Inc., 1950.

90. Conte, S.D.

Elementary Numercial Analysis:
An Algorithmic Approach,
McGraw-Hill Inc. 1965.

91. Walshe, D.E.J.

Wind Excited Oscillations of
Structures: Wind-Tunnel Tech-
niques for their Investigation
and Prediction. H.M.S.O.,
London 1972.

92. Novak, M.
and
Fischer, O.

On the Lift Forces on a Cylinder
Vibrating in Air Flow. ACTA
Technica CASV, 6, 1969,
pp. 719-737.

93. Bendat, J.S.
and
Piersol, A.G.

Random Data: Analysis and Measure-
ment Procedures. Wiley-Inter-
science, 1971.

94. Otnes, R.K.
and
Enochson, L.

Digital Time Series Analysis,
John Wiley and Sons, 1972.

95. Boyd, R.

The Study of Turbulence and
Velocity Profiles Behind an
Aerofoil.Undergraduate Project
Report, LUT, 1971.

96. McLachlan, N.W.

Ordinary Non-Linear Differential
Equations in Engineering and
Physical Sciences. Second Ed.,
The Clarendon Press, Oxford, 1956.

97. Sharma, C.B.
and
Johns, D.J.

Wind-Induced Oscillations of
Circular Cylindrical Shells: An
Experimental Investigation.
TT 7008, L.U.T. July 1970.

APPENDICES

APPENDIX I.

STRAIN DISPLACEMENT RELATIONS FOR A GENERAL SHELL.

Expressions are derived here for the strain-displacement relations purely from a consideration of the geometry, for a cylindrical shell in cylindrical coordinates. The following assumptions are made here though in the derivation at this stage not all of them are used:

(1)   The thickness of the shell is small compared with the radius of curvature of the middle surface of the shell.

(2)   Displacements, not necessarily strains, are large so that the strain-displacement relations are non-linear, this non-linearity being proportional to the consequent <u>moderate</u> rotations corresponding to the radial displacements.

(3)   The transverse normal stress is small compared with the other normal stress components and may be neglected.

(4)   Normals to the median surface before deformation remain so after deformation and undergo no extension.

These are essentially the assumptions of Love's First Approximation theory with the exception of assumption (2) where second order terms are now included.

The displacements of a point 0 (see Figure 2.3) in the median plane are given by u, v and w corresponding to a deformed state of the shell. The displacements of another point A at a distance z from the median surface on the normal at 0 are given by

$$u_A = u - zw_x ,$$

$$v_A = \frac{a+z}{a} v - \frac{z}{a} w_\theta ,$$

$$w_A = w .$$ 1

In accordance with the assumption (2) the median surface strains are

$$e_{xx} = u_x + \frac{1}{2}\{w_x^2\} ,$$

$$e_{\theta\theta} = \frac{v_\theta}{a} + \frac{w}{a} + \frac{1}{2}\{\frac{w_\theta^2}{a^2}\}$$

$$e_{x\theta} = v_x + \frac{u_\theta}{a} + \{\frac{w_x w_\theta}{a}\}$$ 2

Expressions 1, 2 are identical to those of Evensen[31]. The strains at a point A can be evaluated by substituting the displacements (1) into the expressions (2) for strains and by replacing the operator $\frac{1}{a} \frac{\partial}{\partial\theta}$ by $\frac{1}{a+z} \frac{\partial}{\partial\theta}$. This results in

$$\epsilon_{xx} = u_x - z\, w_{xx} + \frac{1}{2}\{w_x^2\}$$

$$\epsilon_{\theta\theta} = \frac{v_\theta}{a} - \frac{z}{a(a+z)} w_{\theta\theta} + \frac{w}{a+z} + \frac{1}{2}\{\frac{w_\theta^2}{(a+z)^2}\}$$

and

$$\epsilon_{x\theta} = \frac{u_\theta}{a+z} + \frac{a+z}{a} v_x - (\frac{z}{a} + \frac{z}{a+z}) w_{x\theta} + \{\frac{w_x w_\theta}{a+z}\} .$$

3

These expression form the basis for the non-linear analysis developed in the text. The terms in the chain brackets are the non-linear terms arising due to moderate rotations in accordance with the assumption (2) and the second and higher order terms in the derivatives of u and v have been ignored.

APPENDIX II.

GENERAL EXPRESSION FOR THE WORK POTENTIAL.

Here, a general expression for the work done is developed considering a quasi-steady state of the surface tractions. For the purpose, an area element $ad\theta dx$ on the surface of the shell is considered. Under the thin shell assumption no distinction is drawn between the outer surface and median surface of the shell. Due to a displacement state u, v and w the dimensions of this median surface element would change to $(1 + u_x)$ dx and $(1 + \frac{v_\theta}{a})$ $ad\theta$ (Figure II.1). The projected areas in the coordinate directions are

x: $- a\,d\,\theta\,d\,x\,(1+u_x)\,w_x \simeq - a\,d\,\theta\,d\,x\,\,w_x$

y: $a\,d\,\theta\,d\,x\,(1+\frac{v_\theta}{a})\,(-\frac{w_\theta}{a}+\frac{v}{a}) \simeq a\,d\,\theta\,d\,x\,(\frac{v}{a}-\frac{w_\theta}{a})$

z: $a\,d\,\theta\,d\,x\,(1+u_x)\,(1+\frac{v_\theta}{a})\,(1+\frac{w}{a}) \simeq a\,d\,\theta\,d\,x\,(1+u_x+\frac{v_\theta}{a}+\frac{w}{a})$

$\hspace{12cm}$ 1

The work done by external distributed load p acting radially inwards is

$\delta W_{steady} \quad = \quad - p\,w \quad a\,d\,\theta\,d\,x$ $\hspace{5cm}$ 2

The incremental work done due to the shell motion is

$\delta W_{inc} \quad = \quad - \frac{p}{2}\,\{ - w_x\,u + (\frac{v}{a} - \frac{w_\theta}{a})\,v + (u_x + \frac{v_\theta}{a} + \frac{w}{a})\,w \}\,a\,d\,\theta\,d\,x$

$\hspace{12cm}$ 3

The total work done over the shell volume is

$$W \quad = \int_0^1 \int_0^{2\pi} - pa[\,w + \frac{1}{2}\,\{ - w_x\,u + \frac{v^2}{a} - \frac{w_\theta}{a}\,v + u_x\,w$$

$$+ \frac{v_\theta}{a}\,w + \frac{w^2}{a} \}\,]\,d\,\theta\,d\,x$$

or

$$W = -a \int_0^1 \int_0^{2\pi} p\left[w + \frac{1}{2}\left\{ \frac{w^2}{a} - 2\frac{vw_\theta}{a} + \frac{v^2}{a} + u_x w - uw_x\right\} \right] dx d\theta$$

4

since

$$\int_0^{2\pi} \frac{v_\theta}{a} w \, d\theta = v w \Big|_0^{2\pi} - \int_0^{2\pi} v w_\theta \, d\theta$$

$$= - \int_0^{2\pi} v w_\theta \, d\theta$$

In the derivations given here no assumption has been made as to the load distribution function except that the load is assumed to act radially inwards and the rotations are small so that the products of rotations are negligible.

APPENDIX III.

CLAMPED-FREE BEAM FUNCTION.

The beam function and its properties (84) for clamped-free boundary conditions are given below: The beam function satisfies the differential equation,

$$\frac{d^4 \Phi_m}{dx^4} = p_m^4 \Phi_m \quad \text{or} \quad \Phi_m^{iv} = \Phi_m \qquad\qquad 1$$

and the orthogonality conditions,

$$\frac{1}{l} \int_0^1 \Phi_r \Phi_s \, dx = \frac{1}{l} \int_0^1 \Phi_r'' \Phi_s'' \, dx = \delta_{rs} \qquad\qquad 2$$

where δ_{rs} is the Kronecker delta.
The characteristic function and its derivatives are

$$\Phi_m(x) = \cosh p_m x - \cos p_m x - c_m (\sinh p_m x - \sin p_m x)$$

$$\Phi_m'(x) = \frac{1}{p_m} \frac{d\Phi_m}{dx} = \sinh p_m x + \sin p_m x - c_m (\cosh p_m x - \cos p_m x)$$

$$\Phi_m''(x) = \frac{1}{p_m^2} \frac{d^2\Phi_m}{dx^2} = \cosh p_m x + \cos p_m x - c_m(\sinh p_m x + \sin p_m x)$$

$$\Phi_m'''(x) = \frac{1}{p_m^3} \frac{d^3\Phi_m}{dx^3} = \sinh p_m x - \sin p_m x - c_m(\cosh p_m x + \cos p_m x)$$

$$3$$

The boundary values are

$$\Phi_m(0) = \Phi_m'(0) = \Phi_m''(1) = \Phi_m'''(1) = 0 \qquad\qquad 4$$

The values of p_m and c_m for the mode m are given by the transcendental equations

$$\cos p_m l \, \cosh p_m l + 1 = 0 \, . \qquad\qquad 5$$

$$c_m = \frac{\sinh p_m l - \sin p_m l}{\cosh p_m l + \cos p_m l} \qquad 6$$

Table III.1 gives the values of p_m and c_m for

$m = 1, 2, \ldots 5$.

APPENDIX IV.

EVALUATION OF INTEGRALS.

The integrals $I_1, I_2 \ldots\ldots\ldots I_6$ which involve beam function have been evaluated using the following procedure and the orthogonality properties.

Considering the integral

$$I = \int_0^1 \cos(p\, x)dx \qquad\qquad 1$$

if

$$x = 1\,\bar{x}$$
$$dx = 1\, d\,\bar{x} \qquad\qquad 2$$

then,

$$I = 1. \int_0^1 \cos(p\, 1.\, \bar{x})\, d\,\bar{x}$$

$$\bar{I} = I/1 = \int_0^1 \cos(p1.\, \bar{x})\, d\,\bar{x} \qquad\qquad 3$$

A change of variable similarly can be used to define the non-dimensional integrals, I_1 to I_6.

Now,

$$I_1 = \int_0^1 \phi\phi'' \, d\,\bar{x}$$

is written as

$$I_1 = \int_0^1 \phi\phi'' \, d\, x$$

omitting bar (—) here and henceforth in this section.

Thus,

$$I_1 = \int_0^1 \phi\phi'' \, dx \qquad\qquad 4$$

Integrating by parts,

$$I_1 = \left[\ \phi\phi'/p1\ \right]_0^1 - \int_0^1 (\phi')^2 \, dx \qquad\qquad 5$$

Also, $\quad I_1 = \left[\ (\int\phi dx)\phi''\ \right]_0^1 - \int_0^1 (\int\phi dx)\, p1\, (\phi''') \, dx$

$$\qquad\qquad 6$$

From III.1,

$$\phi^{iv} = \phi$$

Integrating on both sides,

$$\frac{\phi'''}{p1} = \int\phi\, dx \qquad\qquad 7$$

Substituting (7) in (6)

$$I_1 = \left[\ \frac{\phi'''}{p1}\ \phi''\ \right]_0^1 - \int_0^1 (\phi''')^2 \, dx \qquad\qquad 8$$

Adding 5 and 8, from III.3,

$$I_1 = (k_1 + k_2)/2 - \int_0^1 (A^2 + B^2) \, dx \qquad\qquad 9$$

where $\quad k_1 = \left[\ \phi\phi'/p1\ \right]_0^1 \quad ,$

$$k_2 = [\ \Phi''\ \ \Phi'''\ /\ pl\ ]\ _0^1\ ,$$

$$A\ =\ \sinh\ px\ -\ c\ \cosh\ px$$

$$B\ =\ \sin\ px\ +\ c\ \cos\ px\ .$$

$$\therefore\ I_1\ =\ \frac{1}{4\ pl}\ \ 2(1-c^2)\sin\ pl-2(1+c^2)\cos\ pl\ \sinh\ pl-4\ plc^2$$

10

Now, from (5),

$$I_2\ =\ k_1\ -\ I_1$$

From (9),

$$\therefore\ I_2\ =\ (k_1\ -\ k_2)/\ 2\ +\ \int_0^1\ (A^2\ +\ B^2)\ d\ x \qquad 11$$

Hence

$$I_2 = \frac{1}{2pl}\ [-4c\ -\ 2c\ (\cosh\ 2pl\ +\ \cos\ 2pl)\ -\ (1+c^2)\ \sin\ 2pl$$

$$-(1-c^2)\sin\ 2pl\ -(1+c^2)\sinh\ pl\ \cos\ pl\ +(1-c^2)\cosh\ pl\ \sin\ pl]$$

12

The integrals

$$I_3\ =\ \int_0^1\ (\Phi')^4\ d\ x\ ,\qquad\qquad 13$$

$$I_4\ =\ \int_0^1\ (\Phi)^4\ d\ x\qquad\qquad 14$$

and

$$I_5 = \int_0^1 (\phi\phi')^2 \, dx \qquad\qquad 15$$

have been evaluated numerically using a Simpson rule routine with self adjusting step length in double precision on the ICL 1904 A computer. It is the evaluation of these integrals that takes a large computational time even in single precision due to the oscillatory nature of the function but these are needed to be evaluated only once. The following integrals I_6 are met with in the work potential for various cases:

$$I_6 = \phi_1 \qquad\qquad \text{for point load,} \qquad 16\text{ a}$$

$$I_6 = 1 \qquad\qquad \text{for line load} \qquad 16\text{ b}$$

$$I_6 = \int_0^1 \phi \, dx = \frac{2ca}{\lambda 1} \qquad \text{for distributed load.} \qquad 16\text{ c}$$

The integral

$$I_6 = \int_0^1 x^\alpha \phi \, dx \qquad\qquad 16\text{ d}$$

can only be evaluated numerically. These values of integrals for the mode numbers m = 1 to 5, I_1 to I_5 are given in the Table IV.1.

The other integrals

$$\int_0^1 \phi^2 \, dx = \int_0^1 \phi''^2 \, dx = 1 \qquad\qquad 17$$

also are met within the analysis and follow from orthogonality

properties.

The trigonometric integrals involved are listed
below:

$$\frac{1}{\tau} \int_0^\tau \cos^2 \omega t \; dt \; = \frac{1}{2\pi} \int_0^{2\pi} \cos^2 \omega t \; d\omega \; = \; \frac{1}{2} \qquad\qquad 18$$

$$\int_0^{2\pi} \cos^2 n\theta \; d\theta = \int_0^{2\pi} \sin^2 n\theta \; d\theta \; = \pi \qquad\qquad 19$$

$$\int_0^{2\pi} \cos^3 n\theta \; d\theta = \int_0^{2\pi} \sin^3 n\theta \; d\theta = \int_0^{2\pi} \sin\theta \cos^2\theta d\theta = \int_0^{2\pi} \cos\theta \sin^2\theta \; d\theta = 0$$
$$20$$

$$\int_0^{2\pi} \cos^4 n\theta \; d\theta = \int_0^{2\pi} \sin^4 n\theta \; d\theta = \; \frac{3\pi}{4} \qquad\qquad 21$$

$$\int_0^{2\pi} \cos^2 n\theta \sin^2 n\theta \; d\theta = \frac{\pi}{4} \qquad\qquad 22$$

The values of the following integrals for various cases are
given in the Table IV.2:

$$(i) \qquad \int_0^{2\pi} \cos i\theta \cos j\theta \cos n\theta \; d\theta \qquad\qquad 23$$

$$(ii) \qquad \int_0^{2\pi} \cos i\theta \sin j\theta \sin n\theta \; d\theta \qquad\qquad 24$$

$$(iii) \qquad \int_0^{2\pi} \cos n\theta \cos j\theta \cos n\theta \; d\theta \qquad\qquad 25$$

(iv) $\displaystyle\int_0^{2\pi} \sin i\theta \, \sin j\theta \, \cos n\theta \, d\theta$ 26

APPENDIX V

STATIC STABILITY CONSIDERATIONS

Analogous to the dynamic analysis outlined in Section 3, a non-linear static analysis is investigated here. The displacements are written in single mode form and the coupling between the modes is neglected. Essentially, the non-linear dynamic analysis reduces to the non-linear static one if the frequency Δ is put to zero. The assumed displacements are therefore written as

$$u/l = A \quad \phi'(x) \quad \cos n\theta$$
$$v/l = B \quad \phi(x) \quad \sin n\theta$$
$$w/l = C \quad \phi(x) \quad \cos n\theta \qquad\qquad 1.$$

Minimization of the total potential Ω with respect to A, B and C using Ritz procedure yields

$$U_{11} A + U_{12} B + U_{13} C = 0$$

$$U_{21} A + U_{22} B + U_{23} C = 0$$

$$U_{31} A + U_{32} B + U_{33} C + U_{34} C^3 - W_{30} = 0 \qquad\qquad 2.$$

where U_{11} etc., are given by the Equations (3.5). The Equations (2) are identical to the Equations (3.4) with $\Delta = 0$. Elimination of A and B yields a cubic in C of the form (similar to Equation (3.16)),

$$K_3 C^3 + K_1 C + K_0 = 0, \qquad\qquad 3.$$

with
$$K_3 = U_{34} \delta$$

$$K_1 = U_{13} \delta_1 + U_{23} \delta_2 + U_{33}\delta$$

and $\qquad K_0 = - W_{30}$

where δ are defined in Section 3 provided that $a_{ij} = U_{ij}$. In the present case K_3 is always positive and the bifurcation point which corresponds to static collapse (in single mode) is given by that value of the impressed wind pressure for which

$$K_1^3 + \frac{27}{4} K_0^2 = 0 \qquad\qquad 4.$$

where the mean wind pressure is expressed in a Fourier series expansion. The shell is statically stable for all those values external wind load for which the LHS of Equation (4) is positive. Though, this analysis is a crude mathematical model, it is very useful in selecting the modal combination for a refined static collapse analysis.

APPENDIX VI

INFLUENCE OF STRUCTURAL DAMPING

The analysis of non-linear vibrations with damping is more difficult due to the introduction of another unknown, namely the phase of the response, in each of the assumed modes. The structural damping model provides a useful concept which can be easily incorporated in a modification of the present analysis. Since the structural damping coefficient is proportional to the displacement, it is clear that the energy dissipation is indeed proportional to the strain energy. Also, non-linearity in strain-displacement relations implies non-linear structural damping force but the damping coefficient g is linear. Application of analysis technique similar to that in Section (3) yields the three characteristic equations

$$a_{11} A + a_{12} B + a_{13} C = 0$$

$$a_{21} A + a_{22} B + a_{23} C = 0$$

$$a_{31} A + a_{32} B + a_{33} C + a_{34} C^3 + W_{30} = 0 \qquad 1.$$

where $a_{ij} = U_{ij} (1 + ig) - T_{ij}$ $i, j = 1, 2$ and 3

and $a_{34} = U_{34}$

with W_{30} defined in the Equations (3.7).

In the above equations the arbitrary constants A, B and C in the assumed displacements (3.1) are complex. Elimination of A and B in terms of C results in the cubic

$$K_3 C^3 + K_1 C + K_0 = 0 \qquad\qquad 2.$$

where K_3, K_1 and K_0 also are complex.

The above equation can be solved numerically using Newton-Raphson iteration technique. Unless the assumed initial root is sufficiently close to an actual root the convergence is not guaranteed. An iteration technique is developed here based on the physics of the problem namely the phase and amplitude relations. An approximate method of solution making use of these relations but different from the present is cited in Reference (97). Thus writing

$$K_j = p_j + iq_j \qquad j = 0, 1 \text{ and } 3$$

and $\qquad C = x + iy$

Equation (2) reduces to two coupled real algebraic cubic equations in x and y, on putting real and imaginary parts separately to zero, of the form:

$$F(x, y) = 0$$

and $\qquad G(x, y) = 0. \qquad\qquad 3.$

The real roots of Equations (3) are such that the amplitude

$$C = \sqrt{x^2 + y^2}$$

and the phase

$$\theta = \tan^{-1}\left(\frac{y}{x}\right) \qquad\qquad 4.$$

From physical considerations, $\theta = 0$ when $\Delta = 0$ which

implies $y = 0$ and the amplitude is given by x. For a neighbouring point which has a finite value of Δ, the phase is nearly zero and the approximate amplitude is given by x from the second equation with $y = 0$. Knowing x, y is evaluated from the first equation. The procedure is repeated, alternately evaluating x and y till the desired accuracy is achieved. The response curve is constructed point by point using this procedure. Convergence is not satisfactory in the region where the phase is nearly $\frac{\pi}{2}$. In the subsequent regions the phase is nearly π and the amplitude is again given predominantly by x. This procedure is found to converge with in a few iterations. Figure (VI.1) shows a typical response plot.

In the experimental study of non-linear vibrations, the part of response curve DE is not traced bcause of the "jump" phenomenon. With the frequency increasing, the response curve is traced along ABD when a jump to a lower energy state F occurs at D along DD_1F. With the frequency decreasing, the response curve is traced along GFE when a jump to a higher energy state B occurs along EE_1B and the curve BA is followed for further decrease in frequency. In many experiments, where a careful continuous control of frequency is not possible, the curve traced tends to be ABE_1EG even for increasing frequency.

DIGITAL SPECTRAL ANALYSIS TECHNIQUES.

The digital analysis techniques are now well established and special purpose computers for spectral analysis are commercially available. One such is the Fourier Analyzer HP 5451 A and was extensively used throughout this work. The objective here is to recapitulate the method of analysis rather than to propose any new technique. The Fourier analyzer software comprises of a fast Fourier transform which utilises the fact that the sampling is at uniform intervals and that the number of samples N is an even number.

The Fourier transform (FT) of variable x(t) could be written as

$$X(f) = \int_{-\infty}^{\infty} x(t) \; e^{-i2\pi ft} \; dt \; . \qquad\qquad 1$$

For digital operations, the continuous function x(t) must be replaced by a series of discrete data samples. This is accomplished by sampling the input x(t) at certain uniform intervals of time Δt. In order to perform the above integral $\Delta t \to dt$ should be small. Due to the physical constraints on the analogue to digital converter (ADC), a compromise has to be sought. As a discrete sum, the integral now is the summation,

$$X_D(f) = \Delta t \sum_{n=-\infty}^{+\infty} x(n\Delta t) \; e^{-i2\pi fn\Delta t} \; , \qquad\qquad 2$$

where $x(n\Delta t) = x_n(t)$ is the nth sample value, the suffix D denotes discrete function. The FT computed by this summation

no longer contains accurate magnitude and phase information

at all frequencies contained in X (f). However, X_D (f)

accurately describes the spectrum of x(t) up to some maximum

frequency, f_{max} which is dependent upon the sampling interval

Δ t and the number of samples N.

Due to the time limitations, the total time of

sampling T is finite such that T = N Δt. The discrete Fourier

transform (DFT) is thus

$$X_D \ (m \ \Delta f) = \Delta t \sum_{n=0}^{n-1} x \ (n \ \Delta t) \ e^{-i2\pi m \Delta f n \Delta t} \qquad\qquad 3$$

only periodic functions have such a discrete frequency spectra

and the DFT can be interpretted as a sampled Fourier series.

Now, to fully describe a frequency in the spectrum it is

observed that two values viz. magnitude and phase are to be

computed. As a result N time domain data define N/2 complex

quantities in the frequency domain. Symbolically,

$$f_{max} = \Delta f \ \frac{N}{2} \qquad\qquad 4$$

where Δf is defined as the frequency resolution. The summa-

tion(3) is one sided and hence the actual linear spectra is

obtained by multiplying the above by 2 and the power spectra

has a factor 4.

It is observed that f_{max} given by the Equation (4)

is actually the Shannon limiting frequency. This would be

clear from the following explanation. Shannon's sampling

theorem states that slightly more than two samples per period

are required to define uniquely a sinusoid. In sampling a

time function this implies that $f_{max} < \frac{1}{2\Delta t}$. In the limit $f_{max} = \frac{1}{2\Delta t}$ in which it is understood that the maximum frequency which can be accurately resolved is $f_{max} - \Delta f$. It follows from the sampling theorem that $\Delta f = \frac{1}{T}$.

Since the starting point of sampling is in general arbitrary, the DFT implies periodicity of the sample set itself with a period equal to the total sampling time T (see Figure VII.1). The DFT will then be erroneous due to the side lobes introduced as a result of step input at the beginning and end of sampling. A weighted function called the "window" function is generally used to eliminate this error introduced in digital process.

In the present analysis an interval centred Hanning function given by $\frac{1}{2} \left| 1 - \cos \frac{2\pi t}{T} \right|$ is employed (see Figure VII.2). Table VII.1 gives the theoretical correction factor on the main lobe and measured correction factor on the rms value. It should be noted that the correction factor given should be applied on the linear spectrum. On the power spectrum, the dB corrections should be doubled and multiplication factor should be squared. The increased side lobe roll-off due to Hanning window enhances the resolution of other frequencies. Though the exact values of the primary frequencies is coarse, with each Hanning the statistical uncertainty error reduces considerably (e.g. four Hannings reduces this error to less than $\frac{1}{2}$ dB).

The finite transform introduces another error due to limitation on the maximum frequency (Shannon limit). The frequency contents higher than the set maximum frequency fold back over the maximum frequency and then over the zero

frequency, in other words, the value at any given frequency

is $\sum\limits_{n=0}^{\infty} X_D (2nf_{max} \pm f)$. This effect is called aliasing.

One way of eliminating this effect is to filter the signal with an upper

frequency cut equal to f_{max}. The other method is to make

f_{max} large enough to contain all frequencies of significant

levels. The latter implies larger core size. In the present

case however, analysis up to f_{max} of 2500 Hz indicated neglig-

ible levels of signal above 200 Hz. An f_{max} of 512 Hz is

hence believed to be adequate in the absence of analog filter-

ing.

The DFT introduces an error called the wrap-around

error in the correlations (as well as in the convolution).

This error is eliminated by adding half as many zeros as the

number of samples in the time domain on either side of the

sample set and computing the correlations for this new set

of 2 N samples. In the present case, a sample set of N values

was effectively reduced to N/4 zeros in the beginning and N/4

zeros at the end with N/2 sample values in the middle unaltered.

After the correlations are performed the first and last quarter

represent the +ve and -ve time delay correlation values.

The rounding off errors introduce numerically high

values (> 1) of coherence function at high frequencies. This

is due to the computational procedure employed in the software,

wherein the square of the modulus of the cross spectrum is

divided by the product of the input and output power spectra,

to obtain the coherence function. The denominator then at

higher frequencies has very low values of either the input or

the output as compared to the cross spectral values. The

"block calibrator" in the Fourier Analyzer "masks" the meaningful range of the coherence function. This is easily overcome by setting the higher values of the coherence function to zero in which case the "block calibrator" resolves the range of interest to the one with a scale which could be directly used on the graph plotter.

APPENDIX VIII

CALIBRATION OF PRESSURE TRANSDUCER

The low pressure transducer DISA Type 51 F 32 is
an ingeneous adaption of the B & K Type 4135 condenser
microphone well known in acoustical practice. However,
the present investigation was its maiden application in
the measurement of low pressures. The transducer being a
capacitive device microphone—oscillator—reactance converter
was used as integral with the connecting cables. Extensive
calibrations were, therefore, performed to gain confidence
in the instrumentation. The effect of modification to the
adapter was also established in the transducer dynamic
response studies. Lateral oscillations of double—shielded
cable induced noise levels of comparable order. The trans-
ducer was sensitive to some extent to accelerations perpen-
dicular to the diaphragm. These "noise" levels were estab-
lished in the single point excitation vibration tests. The
transducer is operational at the impressed carrier frequency
($\approx$ 5MHz) only if the total capacity of the system is less
than 15 pF in the high sensitivity (0.1 PF) range. Consid-
erable difficulty was experienced in the initial stages
since in three out of three cases the double—shielded cables
had dry joints. The transducers were normally stored in a
desiccator. On drying the tranducers (T_1 and T_3) in an oven
for two hours at $80^{\circ}C$ the sensitivity of T_1 increased from
90mv/mmH$_2$O to 104mv/mmH$_2$O and that of T_3 increased from
94mv/mmH$_2$O to 275mv/mmH$_2$O. The calibration tests conducted,
therefore, were in the following categories:

(i)   static calibration

(ii)   dynamic calibration

(iii) acceleration sensitivity

(iv)   in-situ static calibration check.

(i)   Static Calibration

The calibration set up is shown in Plate (VIII.1)
and also in the schematic diagram (VIII.1). The pressure
transducer is enclosed in a PVC capsule with the back
pressure connected to atmosphere through a U tube to damp
out the atmospheric fluctuations. The capsule pressure
was adjusted by a micro-manometer and read out on a Betz
manometer. Transducer output was indicated on a digital
voltmeter type Wier Electronics 500 MK2. Capacitance of
the system was tuned to the working range in the 0.1 PF
($\equiv$ 0-70 mm H_2O) range using the oscillator tuning capacitor.
Typical calibration plots in the full scale range 0-6V of
the system are shown in Figure (VIII.2) and are found to
be linear within the experimental tolerance.

(ii)   Dynamic Calibration

In the original (B & K) configuration the micro-
phone has a flat response in the frequency range of 0-5000Hz.
However, the adapter and the cavity between the adapter and
the shell wall were expected to produce cavity resonance
affecting the high frequency response. The transducer was
hence calibrated dynamically against a B & K $\frac{1}{4}$" microphone.
The calibration set up is shown in Figure (VIII.3). The
transducer was fixed by means of a rubber gasket to a flat
aluminium plate of thickness same as the shell thickness.

- 152 -

The standard microphone was fixed side by side with the transducer. Acoustic pressures of approximately 110 dB were impressed on the microphones at a distance of about 18" from a loud speaker. The loud speaker and the level recorder (B & K Type 2305) were driven by a Sine-Random generator B & K Type 1024. A typical sweep time of 10 minutes over 0-50 KHz was employed. Figure (VIII.4) shows the dynamic calibration curve , observed to be linear up to 1500 Hz. Since the initial investigations for the frequency spectrum did not show any significant energy content at higher frequencies no filters were used to limit to this frequency (1500 Hz).

(iii) Acceleration Sensitivity

This, as per specifications, is negligible — 88 dB/ 1 g acoustic pressure level $\equiv$ 0.5 N/M^2 $\equiv$ 0.051 mm of water at 20°C. As remarked earlier, the lateral oscillations produced some noise levels. Also oscillations of the transducer along with the shell, with the pressure tapping sealed indicated very high levels so that wind-on and wind-off test comparisons could not be interpretted to obtain the acceleration effects. At the strain levels of the order of those in wind excitation tests, pressure transducer response levels in vibration tests indicated a maximum of -30dB ref 1V in the worst case (see Figure VIII.5). This is thought to be within experimental errors and no corrections to the fluctuating pressures were hence applied.

(iv) In-Situ Calibration Checks

A simple technique was devised to ensure that the pressure seals were in order and no errors due to drift,

if any, in the electronics were carried over. This consisted of a three way (T) pressure connection, one limb of which was connected to a Betz manometer, the other limb held pressure tight around the transducer pressure tapping on the shell and the third to impress any disired pressure. The transducer response was indicated on a digital voltmeter. In general no drift was observed and pressure leakage was detected in the transducer in only one experiment which was then set right and the experiment itself was repeated.

APPENDIX IX

ERROR ANALYSIS

Experimental measurements of fluctuating pressures, are subject to the following sources of errors; however, it is difficult to estimate the contribution of each of these sources:

1. calibration errors

2. variability of ambient conditions

3. error due to acoustic pressures

4. statistical variability of r.m.s. pressures

5. errors due to spectral distortion

6. error due to acceleration sensitivity

The pressure transducer static calibration error was found to be within $\pm$ 2 percent over the entire range of the experiments. The dynamic calibrations were performed only to establish the linearity of the response and hence, do not contribute to the errors. However, no attempt was made to establish the errors in the level recorder. The tape recorder calibration errors were found to be within $\pm$ 2.5 percent.

A maximum variation of $\pm$ 3°C and $\pm$ 0.9" Hg were recorded in the ambient conditions over the duration of the experiments. However, neither were the experiments performed in a continuous stretch, nor were these ambient changes sudden and consequently no attempt was made to account for these variations in evaluating the free stream velocity. Also, it is observed from Figure (8.1a) that there is approximately a 5 percent variation of velocity in a typical cross section of the wind tunnel. The results are, therefore, expected to be

within $\pm$ 5%.

The acoustic pressure levels were measured at two locations in the wind tunnel laboratory. The results are shown in Figure (IX.1) and also are given in Table IX.1. No definite trend in the noise distribution can be established from these data, but a rough indication of the noise levels at the tunnel centre line can be obtained by the assumption of reverberation conditions (uniform noise levels). It is seen from the measurements that, at the test velocities, the error due to acoustic pressure is less than + 5 percent except at 0° angular position. Further, it is noted that the acoustic pressure levels are in the lower end of the transducer sensitivity and hence, are considered as too small to be of any significance.

The statistical variability error in the r.m.s. readings is approximately $1/\sqrt{\Delta f_e T}$ where Δf_e is the effective band width of the spectra. In the analogue analysis, the results presented are as averaged over approximately 4 minutes and as such the errors are negligible.

The spectral analysis performed, extends from 1 Hz to 512 Hz and as such, there is no truncation error on the low frequency end. On the high frequency end, there is negligible energy, in general, beyond 100 Hz as seen from Figure 11.4, though detailed computations of percentage contributions of various band widths were not carried out. It is therefore inferred that the truncation errors are not significant.

The effect of acceleration sensitivity has been discussed in Appendix VIII.

It is concluded that the pressure measurements are subject to a maximum error of ± 5%.

APPENDIX X

GROUND WIND DISTRIBUTION

1. General

The mechanism of generation of wind is a complex phenomenon. Pressure gradients resulting from temperature gradients and earth's rotation are the main contributing factors in this process. In the study of wind effects on many earth-borne structures, it is only the horizontal winds that cause concern to a design engineer. Meteorological Offices throughout the world keep a record of these horizontal winds which are measured using anemometers. The interpretation of these data should be attempted with great caution since the local effects and the error in the instrument are often difficult to estimate. Also the response of the instruments for winds less than 10 m/sec is not reliable A map of isopleths (contours of equal wind speeds) is more reliable since it provides a space-time average representing the extreme mean hourly speeds over 50 years, derived from records at various stations and reduced to a reference height of 10 m.

Due to the atmospheric boundary layer effects, the wind speed varies with height up to the gradient height (where the viscosity effects are neglible). Above the gradient height (200 m to 2000 m) the winds are generated purely by the pressure gradients and unaffected by local terrain. A power law model following Davenport[71] has been adopted in the BSCP3: Wind Loads[46] where in 3-sec. gust speeds at a height of 10 m are introduced as basic wind speeds.

Correction factors S_1, S_2 and S_3 (see Appendix XII) are incorported to account for topography, dimensions of the structure and expected life respectively. This greatly simplified model is useful in the design based on the extreme expected wind loads, but is inadequate in fatigue and random response analyses.

2. Statistical

The statistical properties[77] required in a refined analysis of wind effects are discussed here. The turbulence scales in the atmosphere are generally large implying that correlation heights in free wind are of the same order of magnitude as the size of the structure in question. Under the assumption of isotropic atmosphere, the statistical distribution of wind speeds forms a two-degrees-of-freedom system and the distribution function can be assumed to be Gaussian. If u and v are the components of velocity in two orthogonal directions in an isotropic plane, the probability density can be written as

$$p(u)\,du = \frac{1}{\sqrt{2\pi}\,\sigma_{1u}}\ \exp - [\,(u - \bar{u})^2/2\sigma_{1u}^2\,]\ du$$

$$p(v)\,dv = \frac{1}{\sqrt{2\pi}\,\sigma_{1v}}\ \exp - [\,(v - \bar{v})^2/2\sigma_{1v}^2\,]\ dv \qquad 1.$$

Without loss of generality, $\bar{u}$ and $\bar{v}$ may be omitted, and also,

$$\sigma_{1u}^2 = \sigma_{1v}^2 = \sigma_1^2 \qquad \text{due to isotropy.}$$

Hence, the joint probability of occurance is

$$p(u, v)\, du\, dv = \frac{1}{2\pi\sigma_1^2} \exp - [\, (u^2 + v^2)/2\sigma_1^2\,] \; .$$

Writing $\quad u^2 + v^2 = V^2$

$$p(V)\, dV = \frac{1}{2\pi\sigma_1^2} \int_0^{2\pi} \exp - (V^2/2\sigma_1^2).V\, dV\, d\theta$$

or

$$p(V)\, dV = \frac{V}{\sigma_1^2} \exp - (V^2/2\sigma_1^2)\, dV$$

The probability of exceedence is given by

$$P(>V) = \exp - (V^2/2\sigma_1^2) \qquad\qquad\qquad 2.$$

This is the well known Rayleigh distribution.

However, the assumption of isotropy is not strictly valid since the maximum winds are, in addition to being subjected to local effects, geostrophic and hence directional. Further, the winds normally have a steady variation as consequence of which the sample set of records is not an independent set. Weibull distribution function seems to best fit the yearly distribution of maximum winds and the probability of exceedence in this case is given by

$$P(>V) = \exp - (V/C)^k.$$

The characteristic wind speed C and the exponent k may be obtained from a plot of the numerical data of wind speeds. In general, $k \simeq 2$ and the distribution is identical to

Rayleigh distribution if $C = \sqrt{2}\ \sigma_1$.

The probability of exceedence of an extreme wind V_{max} in any year is given by

$$P(V_{max}) = \exp[\exp - \alpha(V_{max} - \hat{v})] \qquad \text{3.}$$

In this expression, for a Weibull distribution the mode $\hat{v}$ is

$$\hat{v} = C(\ln N)^{1/k} \qquad \text{4.}$$

and the dispersion factor $1/\alpha$ is

$$\frac{1}{\alpha} = \frac{d\hat{v}}{d\ln N} = \frac{C}{k}(\ln N)^{\frac{1-k}{k}} \qquad \text{5.}$$

where N is the number of independent data points in a given sample period, say one year. The maximum wind speed with a return period R years may be evaluated from the expression

$$V = \hat{v} + \frac{1}{\alpha}f(R) \qquad \text{6.}$$

where the function

$$f(R) = \ln[-\ln(1 - \frac{1}{R})] \qquad \text{7.}$$

From Equations (3, 6 and 7) it is clear that

$$P(V_{max}) = 1 - \frac{1}{R} \qquad \text{8.}$$

and the modal probability is

$$P(\hat{v}) = \frac{1}{N} \qquad \text{9.}$$

In a purely random process with the Rayleigh distribution, the mode

$$\hat{v} = \sigma_1 \sqrt{2 \ln N} \qquad\qquad 4a.$$

and the dispersion

$$\frac{1}{\alpha} = \sigma_1 / \sqrt{2 \ln N} \cdot \qquad\qquad 5a.$$

If the sample set is not an independent set, the variation of velocity may be considered as a continuous random process. The effective number of samples can then be obtained from

$$N_{eff} = \nu_1 T \qquad\qquad 10.$$

where T is the total time of sampling and the effective frequency (or the number of zero crossing per unit time) is given by

$$\nu_1 = \frac{\sigma_2}{\sigma_1} = \left[\frac{\int f^2 S(f) \, df}{\int S(f) \, df} \right]^{\frac{1}{2}} \qquad\qquad 11.$$

and the power spectrum of the velocity should necessarily be known. These statistical properties of wind together with Palmgren-Miner rule form the basic entities in the estimation of fatigue life.

APPENDIX XI

COMPUTER PROGRAM

The flow charts of the main program SHELL ANALYSIS, subroutine CNONLINEAR and the other main program RANDOM are given below. SHELL ANALYSIS gives the free linear natural frequencies, nonlinear response and stress resultants for prescribed loading. The integrals I1 to I5 are evaluated separately (in INTEGRALS) in double precision, using a self-adjusting step length Simpson rule (DSIMPSON). For (m=) 5 modes the execution time for the evaluation of the integrals was approximately 800 seconds on ICL 1905A Computer, with the higher modes requiring longer times. The rest of the analysis needs very little computer time.

RANDOM evaluates the random vibration response - displacements and strains at any prescribed point. Using the principle of superposition, the components of the response in the first (m,n) normal modes are summed to obtain the total response at any prescribed excitation frequency. The solution vector ($\{6\}$) is evaluated (m x n x j) times and as such the execution times are large. Typically, for the evaluation of the w and ϵ_θ for (j=) 20 spectral points, with (m x n x j = 5 x 6 x 20), at one prescribed point (x,θ) and for a given value of damping, the execution times required were approximately 60 seconds on ICL 1905A Computer and 150 seconds on ICL 1903T Computer.

- 163 -

SHELL ANALYSIS

```
┌─────────┐
│  START  │
└─────────┘
     │
┌──────────────────┐
│  Nonlin. Rot.    │
│ Inertia, Struc   │
│    Damping       │
└──────────────────┘
     │
┌──────────────┐
│  Max. Iter.  │
│     Acc.     │
└──────────────┘
     │
┌──────────────┐
│   Ncases     │
│   Naspect    │
│   Nmodes     │
└──────────────┘
     │
┌──────────────┐
│   Geometry   │
└──────────────┘
     │
┌──────────────┐
│   Co-ordi.   │
└──────────────┘
     │
┌──────────────┐
│  Load Type,  │
│  Dyn., Mom., │
│  Deflec.,    │
│  Stress      │
└──────────────┘
     │
┌──────────────┐
│   Fourier    │
│  Coefficient │
│  Rms & Mean  │
└──────────────┘
     │
     ▼
```

```
                              ┌──────┐
                              │      │
                              └──┐ ┌─┘
                                 │ │
                                 └─┘
                                  │
                                  │
                                 ╱ ╲
                               ╱     ╲
    ┌───┐    ╱────────╲      ╱         ╲
    │ 1 │───│ Output   │◀─1─│ Moments?  │
    └───┘    ╲────────╱      ╲         ╱
                               ╲     ╱
                                 ╲ ╱
                                  │
                                  │2
                                  │
    ┌──────────┐      ┌──────────────┐
    │  YNORM   │───▶──│  Normalize   │
    └──────────┘      └──────────────┘
                              │
                              │
                              │
                         ╱─────────╲
                        │  Graph    │
                        │  Outputs  │
                         ╲─────────╱
                              │
                              │
                             ┌───┐
                             │ 1 │
                             └───┘
   end loop                    │
         Nmodes     ◀──────────┤
         Naspect              │
         Ncases             ┌─────┐
                            │ END │
                            └─────┘
```

- 167 -

CNONLINEAR

```
    (5)                    ⌂
     │                     │
     │              ┌──────────────┐
     │              │  Amp.        │
     │              │  Phase       │
     │              └──────────────┘
     │                     │
     │              ┌──────────────┐
     │              │  Increment   │
     │              │  Freq.       │
     │              │  Y = ───     │
     │              └──────────────┘
     │                     │
end loop  j frequency ──◄──(4)
                           │
                         (END)
```
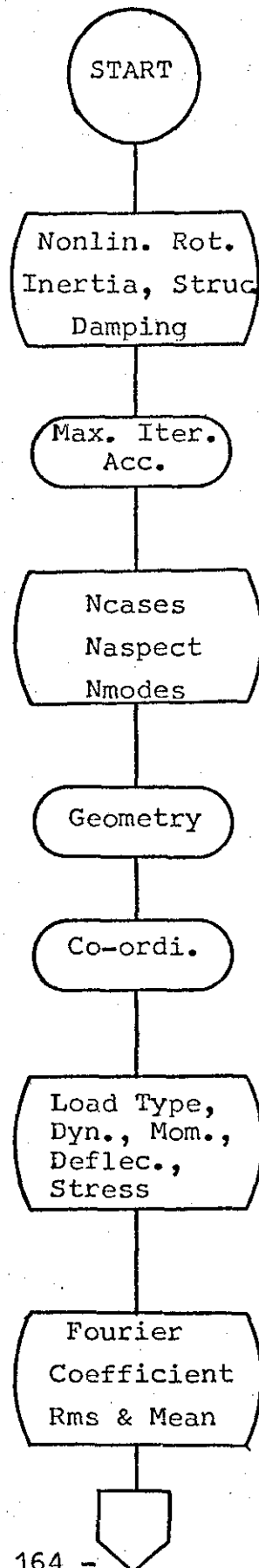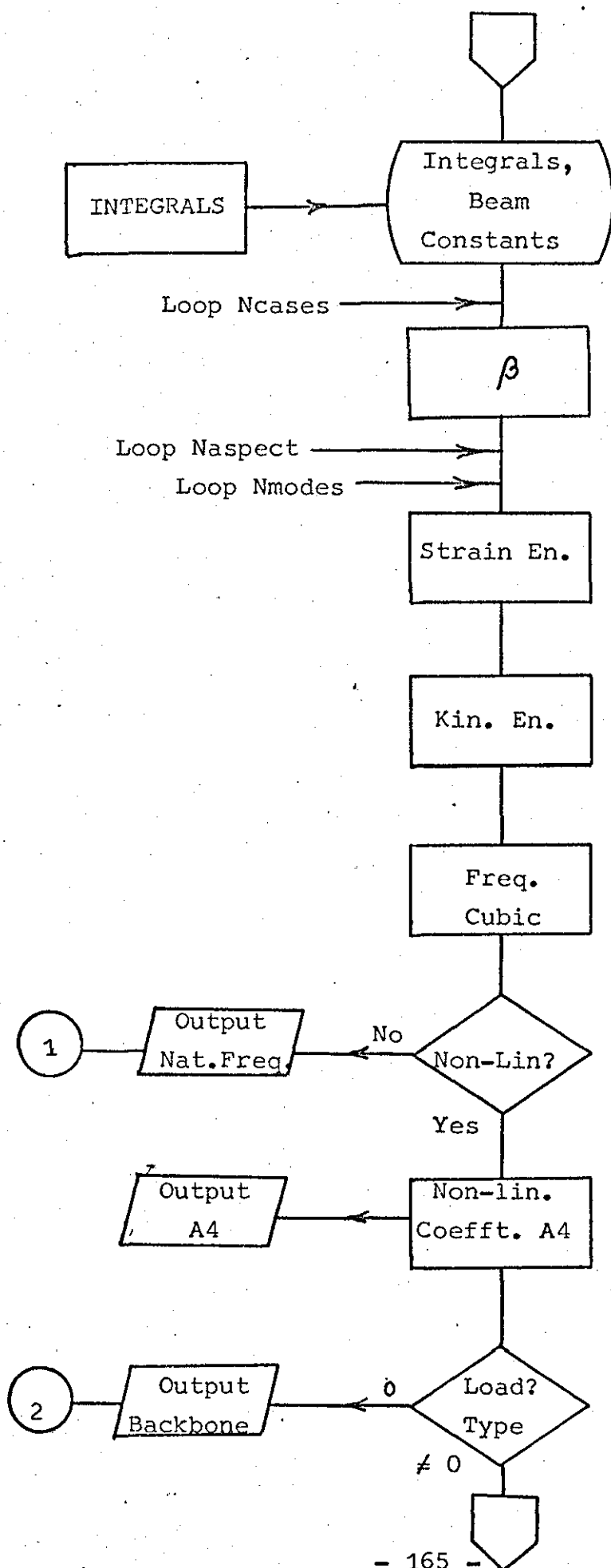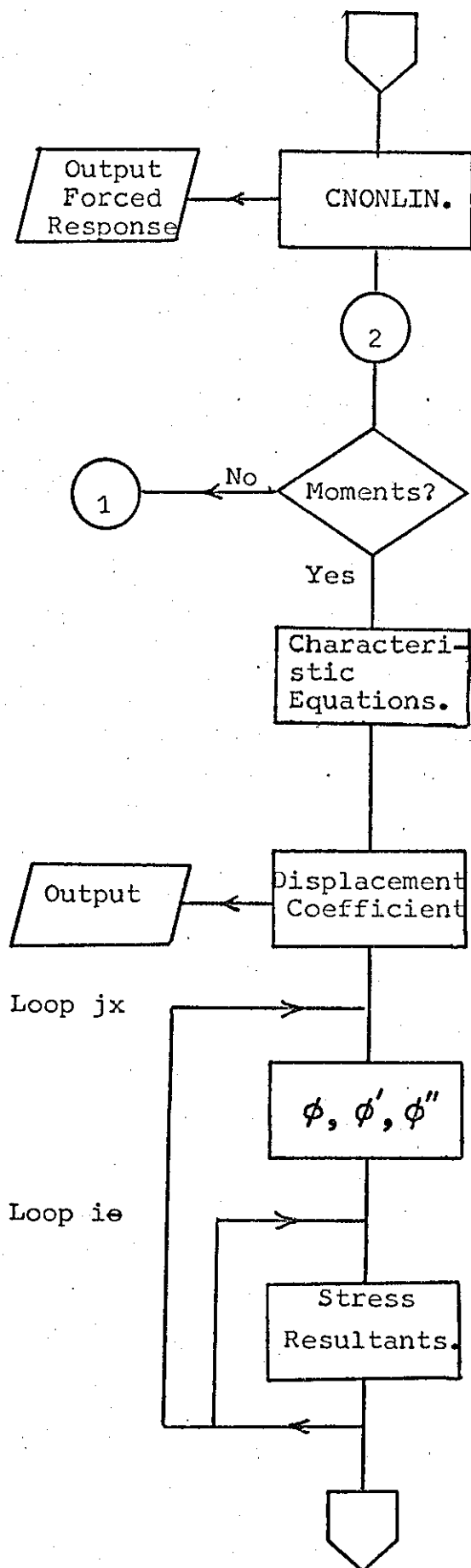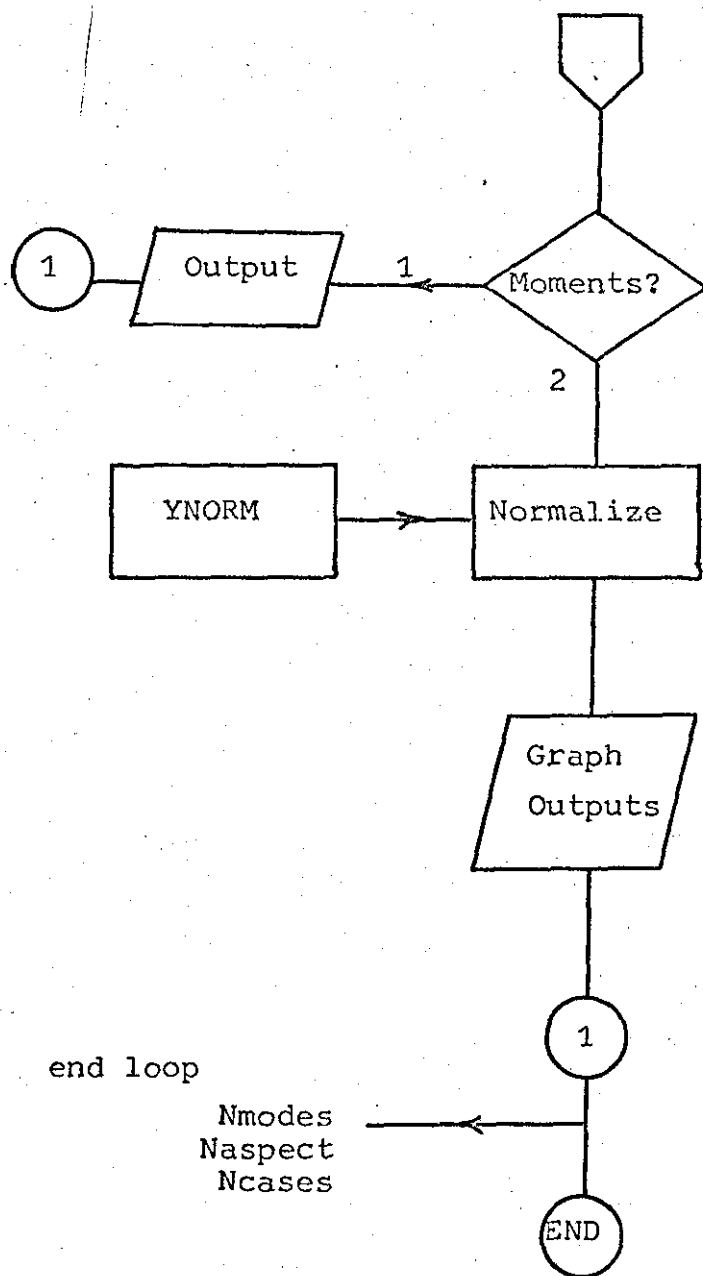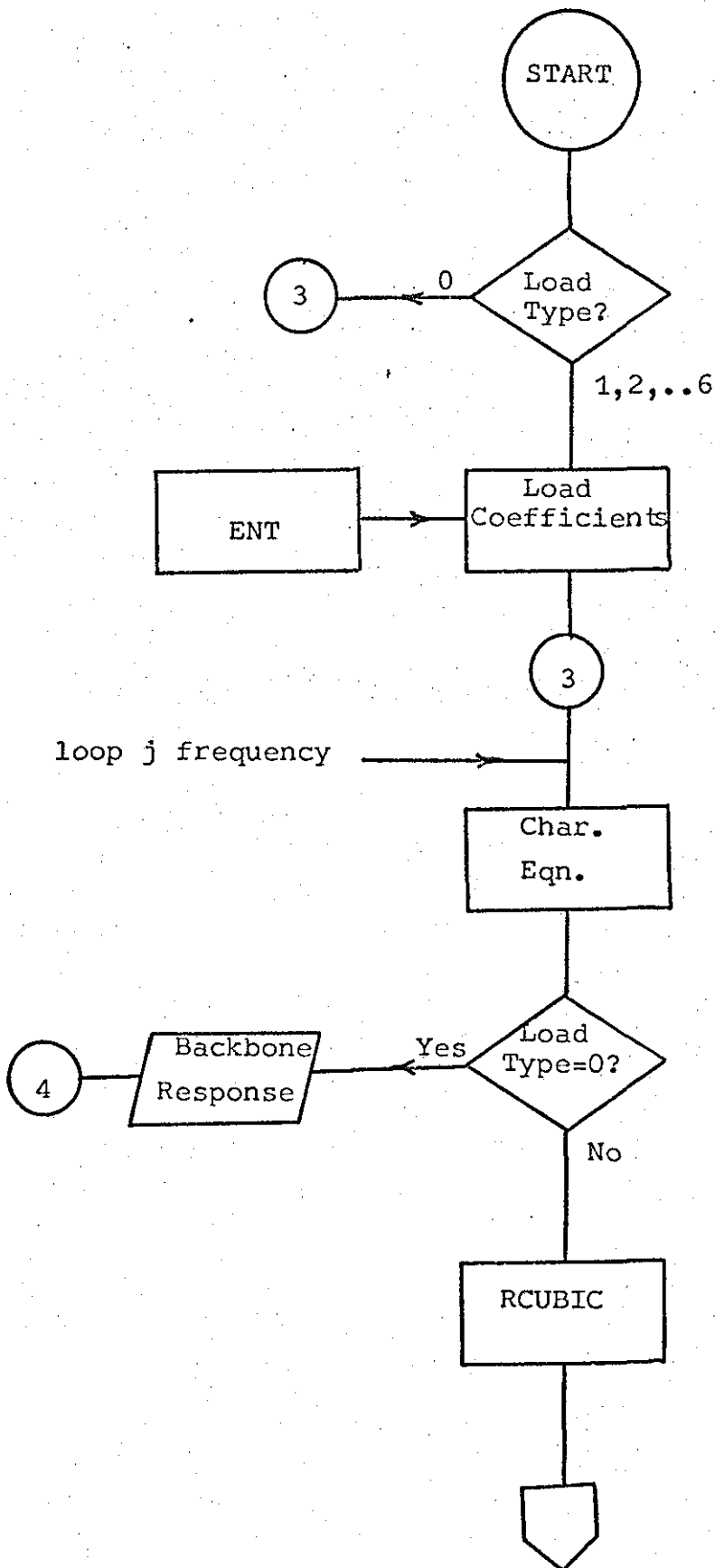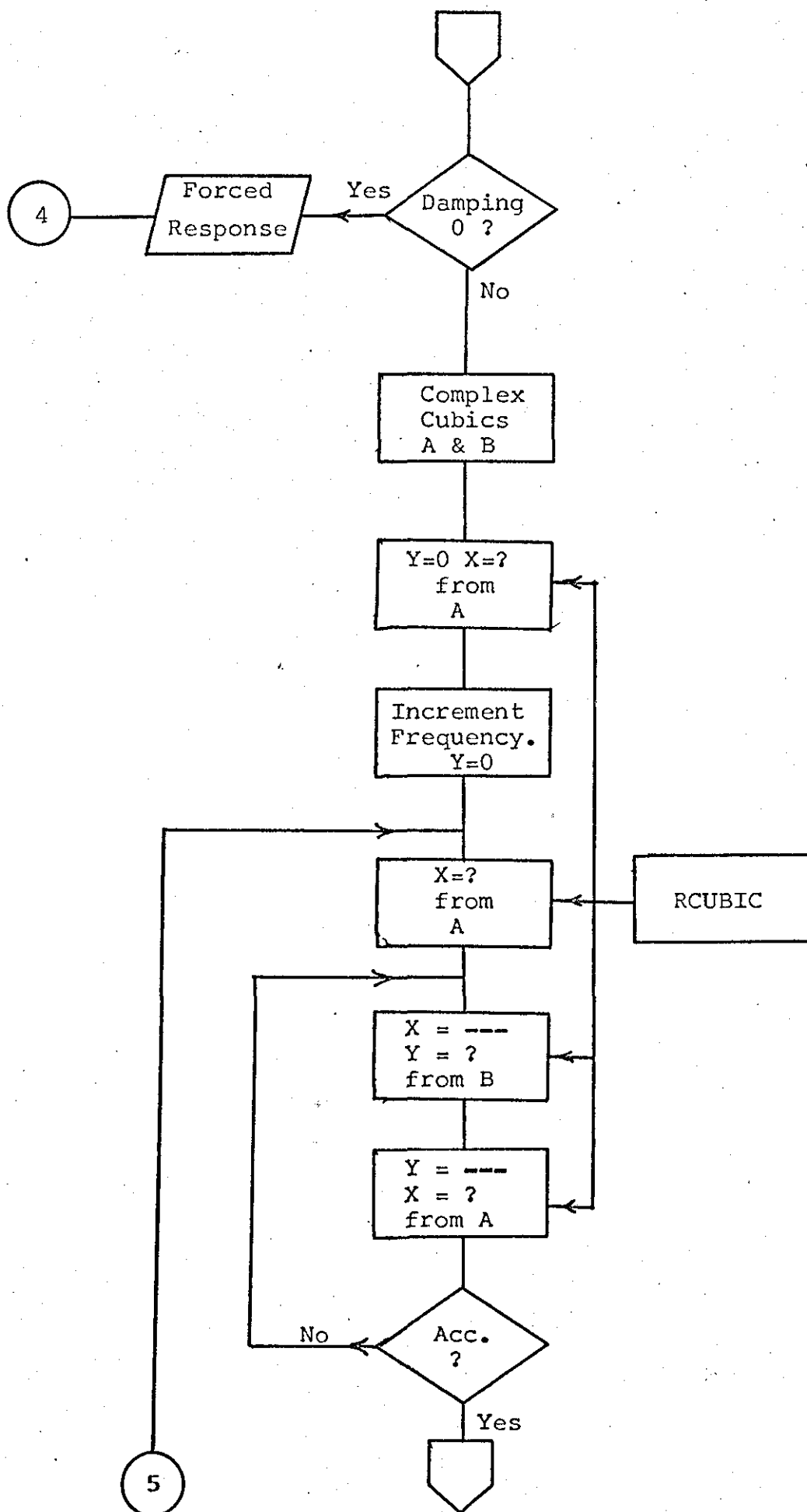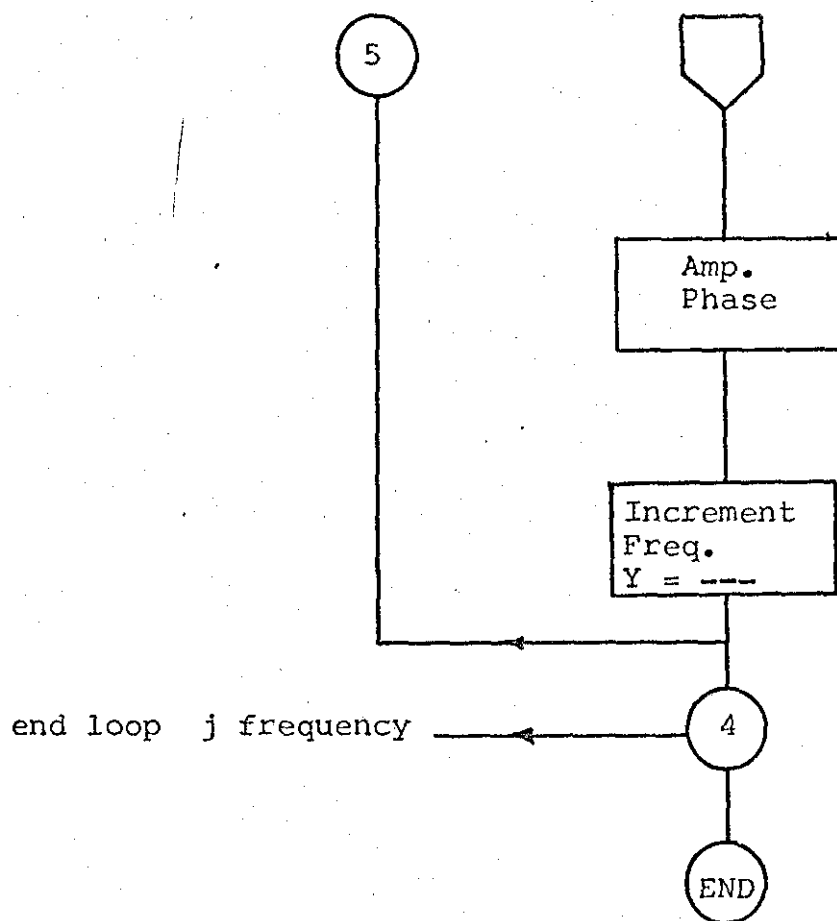
0 : Free Nonlinear

1 : Tip Load

2 : Line Load (∅)

3 : Line Load (uniform)

4 : Osci. Wind Load

5 : Comb. Wind Load

6 : Harmonic Distrib.

START

l,a,h,E, ϱ , μ Geometrical Constants

PRDIST $\Rightarrow$ RF(n) n=0,..5   Fourier Coefficients of RMS pressure distribution

PR(m),CR(m) m=1,..5   Fixed-free beam constants

INTEGRALS $\Rightarrow$ I1(m), I2(m) m=1,..5   Integrals

SHELL ANALYSIS $\Rightarrow$ FREQ. (j)   j frequencies including the shell natural frequencies

SPECTRAL ANALYSIS $\Rightarrow$ SF (j)   Load Spectrum j = convenient no. of points

DC, (x,θ)   Damping coefft., co-ordi. of pt. at which the strain spectrum is reqd.

Loop j
Loop m

$\int$ Integral for external loading

Loop n

```
┌─────────────┐
│ F11, F12,..  │     Coefficients of strain
│ ....F33     │     energy
└─────────────┘

┌─────────────┐
│ T11,...T33  │     Coefficients of Kinetic
│             │     energy
└─────────────┘

┌─────────────┐
│  D(3,7)     │     External load
│             │
└─────────────┘

┌─────────────┐
│  MATPAC     │
│             │
└─────────────┘

Evaluate over loop j
determinant to check
frequencies.

┌─────────────┐
│  MATPAC     │     Solution of Characteristic
│             │     equation
└─────────────┘

┌─────────────┐     Solution vector (real parts
│ A(m, n, i)  │     i = 1,2,3 imaginary parts
│             │     i = 4,5,6)
└─────────────┘

end loop m,n

loop m

┌─────────────┐
│   φ, φ″     │
│             │
└─────────────┘

loop r

┌─────────────┐
│   φ, φ″     │
│             │
└─────────────┘
```

loop n
loop s

SUMW, SUM $\epsilon_\ominus$

SUM ϵ_x

end loop n,s

end loop m,r

Spectra
SW, S$\epsilon_\ominus$

Sϵ_x

end loop j

Output

END

THE IMPLICATIONS OF CODES OF PRACTICE ON STRUCTURAL DESIGN OF STEEL CHIMNEYS.

Authors: D.J. Johns & R. Nataraja.

Analyses are presented which consider the most recent wind loading code and the requirements of the current British Standard for the design of free-standing steel chimneys.

The wind loading takes account of the local topography, surface roughness and design life of the chimney as well as its height and a power law is used to define the variation of wind velocity with height.

The design criteria for allowable stress, allowable deflection and for swaying and charts are obtained for a wide range of chimney geometries of the design wind speed to satisfy these criteria.

The allowable deflection criterion is in general the more critical of the two static criteria and the authors question its validity.

The two dynamic criteria may also be critical but other factors may preclude such oscillations from occurring. These factors are not considered and quantified in the current codes of practice.

Department of Transport Technology,
University of Technology,
Loughborough.

Notation.

A_e — frontal area (projected area on a plane normal to wind direction).

C — defined in the text.

C_f — force coefficient of steel chimney.

d — diameter of chimney

E — Young's modulus.

f_s, f_o — frequency in sway and ovalling respectively.

f_b — bending stress.

g — acceleration due to gravity.

h — height at which slope changes (see fig. 1.)

H — height variable

I — second moment of area

K — coefficient in equation (3)

k — radius of gyration $= d/2\sqrt{2}$

L — height of the shell.

m — pressure exponent ($= 2\alpha$)

m_o — mass per unit length.

N — life span in years

P — probability

q — dynamic pressure.

R — return period in years

$S_1 S_2 S_3$ — factors defined in the text

S_t — Strauhal number

t — thickness of chimney shell

V — basic wind speed.

V_H — wind speed and height H in the velocity profile.

V_L, V_s — design wind speed.

V_{cr} — critical windspeed in dynamic instability

W_o — weight/unit length of chimney.

α — velocity index

β — mode constant

σ — mass density of basic shell material

ρ — density of air.

1.   Introduction.

British Standard 4076:1966 (Reference A1) includes four design requirements for free-standing steel chimneys:

(i)   allowable stress.
(ii)   allowable deflection.
(iii)   swaying oscillations.
(iv)   ovalling oscillations.

Although consideration is given to dead weight loadings the major loadings are usually those due to the action of the wind.

A previous study (Reference A2) presented design charts based on Reference A1 from which the designer of free-standing steel chimneys, could at a glance determine the chimney dimensions to satisfy the above static and dynamic design criteria. These charts were based on the wind loading code then current.

The wind loading requirements have recently been revised (Reference A3) and it is the purpose of the present paper to consider the implications of the new codes in an analytical treatment of the chimney design process. A fuller treatment is presented in Reference A4.

It is assumed throughout that the steel chimney is unlined, unclad, unstiffened and uniform. The implications of alternative assumptions are considered in Reference A4.

2.   Wind Loads.

2.1. General.

Reference A3 contains a map of isopleths (lines of equal wind speed, V) which relate to the maximum gust speeds at a height 10 m above ground which are likely to be exceeded not more than once in 50 years in open level country.

To obtain the local design wind speed, V_s, the map wind speed V is multiplied by the following three factors:-

S_1 for local topographic influences.
S_2 for surface roughness at the chimney location, for gust duration appropriate to chimney size and for various chimney heights.
S_3 for the chimney design life.

Thus $V_s = V.S_1 S_2 S_3$ (1)

2.2. S_1 Factor for Topography

It is advisable that S_1 should always lie within the range $0.85 \leqslant S_1 \leqslant 1.2$ and generally within the range $0.9 \leqslant S_1 \leqslant 1.1$. A value of $S_1 = 1.0$ relates to level, open country and the higher and lower values relate to exposed and sheltered regions respectively.

2.3. S_2 Factor for Surface Roughness, Gust Duration and Chimney Height (Table A1.)

The variation of wind velocity with height depends upon the type of terrain and surface roughness (see Fig.XII.1) and upon the averaging time of the gust duration. For chimney heights less than 50 m. the S_2 factor is given by the 5 second gust data and for heights greater than 50 m. by the 1^5 second data.

Although this sudden change in data to be used may appear inconsistent and a progressive change could be proposed it is believed that this is not necessary since the given approach should provide a slightly conservative design.

Reference A3 tabulates S_2 but for present purposes an empirical relation of the form

$$S_2 = KH^\alpha \qquad (2)$$

is obtained. Table A1 gives the values of K and α so obtained for the four categories of local conditions considered in Reference A3.

It is seen that for conditions 2, 3 and 4 the values of K and α in equation (2) vary from below to above a given height.

Reference A3 should be consulted for cases where the chimney is to be built on a cliff or escarpment since the effect then generally is to effectively increase the values of S_2 which should be applied and to make them thereby more uniform over the given chimney height. Such effects are considered in Reference A4. They generally lead to a more critical design.

2.4. S_3 Factor for Design Life

The basic wind speeds, V, in Reference A3 have a return period, T of 50 years. It can easily be shown that the probability of a given speed V_x exceeding V i.e. $S_3 > 1.0$, occurring in a period of N years is

$$P = 1 - (1 - \frac{1}{R})^N \qquad (3)$$

Therefore for $R = N = 50$ years $P = 0.63$ and $S_3 = 1.0$.
Plots of S_3 are given in Reference A3 for different values of P and N and these should not be extrapolated for $N < 2$.

Normally $S_3 = 1.0$ but lower values may be taken for temporary structures and higher values for those with an anticipated life longer than 50 years or for those where additional safety is required.

2.5. Design Wind Forces.

The design dynamic pressure is given by

$$q = \frac{1}{2}\rho V_s^2 \qquad (4)$$

where V_s is given by equation (1).

In S.I. units equation (4) becomes

$$q = 0.613 \, V_s^2 \qquad (5)$$

where V_s is in m/s and q is in N/m^2.

The design force is given by

$$F = A_e \cdot C_f \cdot q \qquad (6)$$

where Ae is the projected frontal area normal to the wind, and for most chimney geometries it is realistic to assume that $C_f = 0.6$. For smooth structures of a diameter greater than 0.25 m. this value is slightly conservative. Only for smaller diameters or for roughness levels untypical of chimney construction in general would higher values of C_f be used. Thus if a chimney has roughness greater than 8% of the diameter e.g. longitudinal ribs, a value of C_f up to 1.2 to 1.3 might apply as is shown in Reference A3.

3. Static Analysis based on Allowable Stress.

For a uniform cantilever of diameter d subjected to such a distributed load, engineer's theory of bending gives

$$E \, I \, w^{iv} = d \cdot C_f \cdot q.$$

Substituting for q,

$$EI \, w^{iv} = \tfrac{1}{2} \rho \, d \, C_f \, S_1^2 \, S_3^2 \, K^2 \, H^m \, v^2 \qquad (7)$$

where $m = 2\alpha$.

For category 1 in Table A1 this yields

$$M = \tfrac{1}{2} \, d \, C \, K^2 \, v^2 \left[\frac{H^{m+2}}{(m+1)(m+2)} - \frac{HL^{m+1}}{m+1} + \frac{L^{m+2}}{m+2} \right] \qquad (8a)$$

where $C = C_f \rho S_1^2 S_3^2$.

The maximum bending stress f_b at the base of the cantilever chimney is

$$f_{b \, max} = \frac{r \, M_{H=0}}{I} = \frac{S_{2L}^2 \, C \, v^2}{(m+2) \, \pi} \left(\frac{L}{k} \right)^2 \left(\frac{d}{t} \right) \qquad (9a)$$

and $f_{b \, allowable} \geqslant f_{b \, max}$. (See values of $f_{b \, allowable}$ in Reference A1). L is the height of the chimney at which S_{2L} applies and $k = d/2\sqrt{2}$. It should be noted that $CV^2 S_{2L}^2 \equiv C_f \cdot \rho \, V_{sL}^2$ where V_{sL} is the design wind speed at height L.

For categories (2), (3) and (4) in Table A1 the values of S_2 are given by K_1 and m_1 for heights above h and by K_2 and m_2 for $H < h$. The bending moment is given by

$$M = \frac{Cd}{2} K_1^2 V^2 \left(\frac{L^{m_1+2} - h^{m_1+2}}{m_1 + 2} - \frac{L^{m_1+1} - h^{m_1+1}}{m_1+1} \cdot H \right)$$

$$+ \frac{Cd}{2} K_2^2 V^2 \left[\frac{H^{m_2+2}}{(m_2+1)(m_2+2)} - \frac{Hh^{m_2+1}}{m_2 + 1} + \frac{h^{m_2+2}}{m_2+2} \right]$$

for $0 < H < h$

$$= \frac{Cd}{2} K_1^2 V^2 \left(\frac{H^{m_1+2}}{(m_1+1)(m_1+2)} - \frac{HL^{m_1+1}}{m_1+1} + \frac{L^{m_1+2}}{m_1+2} \right)$$

for $h < H < L$

(8b)

The maximum bending moment and hence the maximum bending stress occurs at $H = 0$ and is given by

$$f_b = \frac{C}{\pi} \frac{V^2 S_{2L}^2}{m_1 + 2} \left[1 - \left(\frac{h}{L} \right)^{m_1+2} \frac{m_2 - m_1}{m_2+2} \right] \left(\frac{L}{k} \right)^2 \left(\frac{d}{t} \right)$$

(9b)

and f_b allowable $\geqslant f_b$.

Equations (9) give the values of V satisfying the allowable stress criterion when f_b is the allowable stress and the height of the chimney is given by other considerations. Since the basic wind speed is known, the geometric parameter t can be calculated from equation (9).

4. Static Analysis based on Allowable Deflection.

Further integrations of equation (8a) yield the deflection, the maximum of which at $H = L$ is given by

$$EI \dot{w}_L = \frac{dC K^2 V^2}{2} L^{m+4} \left[\frac{1}{(m+1)(m+2)(m+3)(m+4)} - \frac{1}{6(m+1)} + \frac{1}{2(m+2)} \right]$$

or $EI w_L = \frac{dC K^2 V^2}{2} L^{m+4} f(m)$

(10a)

where the function in square brackets is written as $f(m)$. Equation (10a) can be written as

$$\frac{w_L}{L} = \frac{C\sqrt{2}}{E} V^2 S_{2L}^2 f(m) \left(\frac{L}{k} \right)^3 \left(\frac{d}{t} \right)$$

(11a)

The allowable maximum deflection as stipulated in Reference 4 is that

$$\frac{w_L}{L} \not> \frac{1}{200}$$

(12)

The corresponding equation for categories (2), (3) and (4) is

$$\frac{w_L}{L} = \frac{C\sqrt{2}}{E} V^2 S_{2L}^2 f(m_1, m_2) \left(\frac{L}{k} \right)^3 \left(\frac{d}{t} \right)$$

(11b)

where

$$f(m_1, m_2) = \frac{1}{(m_1+1)(m_1+2)(m_1+3)(m_1+4)} - \frac{1}{6(m_1+1)} + \frac{1}{2(m_1+2)}$$

$$- \frac{(h/L)^{m_1+3}(m_2-m_1)}{2(m_1+3)(m_2+3)} + \frac{(h/L)^{m_1+4}(m_2-m_1)}{6(m_1+4)(m_2+4)}.$$

Equations (11) together with equation (12) set the criterion for allowable deflection and as before the geometric parameter t may be evaluated.

5. Dynamic Analysis based on Sway Oscillations

In the sway mode of oscillation the entire chimney oscillates in the cantilever beam modes. The structural natural frequencies are calculated using a simplified model approximating to a single degree of freedom system in any one normal mode of vibration. The sway mode natural frequencies of a chimney shell are given in Reference A1 by

$$f_s = \frac{\beta}{2\pi L^2} \sqrt{\frac{EIg}{W_o}}. \tag{13}$$

where W_o is weight per unit length and frequency f is in Hz. The constant β depends on the mode. For the fundamental Mode $\beta = 3.515$.

The critical wind speed at which the fundamental frequency is excited can be calculated by using the formula

$$V_{cr} = \frac{f_s \, d}{S_t} \tag{14}$$

where $S_t = 0.2$, is the Strouhal number.
For a simple uniform steel shell of material density σ, equation 13 becomes

$$f_s = \frac{2.5}{2\pi} \frac{d}{2L^2} \left(\frac{E}{\sigma}\right)^{\frac{1}{2}} = 2010 \frac{d}{2L^2}$$

where d, L are in metres.
Equation (14) then becomes

$$V_{cr} = 40200 \left(\frac{k}{L}\right)^2 \tag{15}$$

where V_{cr} is in m/s.
The criterion to avoid sway oscillations is therefore

$$V_{cr} > V_L$$

It should be noted that equation (15) is independent of thickness t. Hence the only way to increase V_{cr} is by decreasing (^{L}/k). In cases where this is not permissible one should either increase damping or increase the stiffness by using guys or destroy the effectiveness of vortex induced forces by means of helical strakes, perforated shroud etc.

6. Dynamic Analysis based on Ovalling Oscillations.

The ovalling modes of oscillation, also called the breathing modes, could be critical for a range of values of t/d ratios encountered in modern design practice. A formula for the simplest ovalling mode given in Reference A1 is

$$f_o = 622 \; t/(d/2)^2 \qquad (16)$$

with t and d in metres.
The critical wind speed at which ovalling may occur is given in Reference A1 by

$$V_{cr} = \frac{f_o d}{2 \; S_t} \qquad (17)$$

The value of Strouhal number $S_t = 0.2$ is again taken and

$$V_{cr} = 6220 \; \frac{t}{d} \qquad (18)$$

with V_{cr} in m/s.
The ovalling criterion therefore is

$$V_{cr} > V_L$$

In cases where a change of design is not feasible, an end ring would considerably increase f_o and hence V_{cr}, particularly for smaller values of (L/k) ratios used in design practice. Though it is difficult to substantiate quantitively chimney lining should have some beneficial effects on ovalling instability due to increased t/d (in proportion to modular ratio) and due to increased damping.

7. Dynamic Stability Parameter.

It has been shown that vortex induced swaying and ovalling oscillations are most unlikely when the chimney has a value of $2 \; m_o \delta / \rho d^2 > 17 \cdots 23$ where m_o = mass per unit length = W_o/g; δ = logarithmic decrement. The existing codes do not point out this fact and since δ for steel chimneys should be at least of the order of .03 it may be possible to preclude instability by increasing m_o and/or δ.

8. Design Charts.

Using the previous analyses it is possible to construct design charts which give chimney dimensions necessary to satisfy the four basic design criteria listed in Section 1 and analysed in Sections 3 - 6. The most critical of the cases are presented in Tables A2 to 5. It is found that the allowable stress criteria is most critical for category 1 for heights less than 50 metres (Table A2) with that for category 4 (Table A4) for heights less than 50 metres being at the other extreme. All the other classifications fall within these two cases. It is observed that the difference in design wind speeds for the two extreme cases above is so small that the error in using the corresponding conservative values given by category 1 is less than 5% over a wide range of geometries. Thus considerable simplification is achieved in the preliminary design stages

by selecting a suitable geometry from TableA2, immaterial of the category under consideration.

Similar observation is made for allowable deflection criterion. The results for allowable deflection are given in TablesA3 and A5 and it is seen that the allowable deflection criterion is at all times more critical than the allowable stress criterion. This suggests to the authors that the present deflection criterion which has, apparently, no precise logical basis, be re-appraised by the British Standards Institution and possibly removed or replaced.

The deflection criterion appears to be even more severe than the swaying mode oscillation criterion (TableA6) for certain practical geometries. However TableA6 suggests that the top value of L/k to be considered is about 30 unless remedial measures are taken to prevent swaying oscillations.

Likewise TableA7 for ovalling mode oscillations suggests that d/t should not exceed 150. However since TableA7 is for an un-stiffened shell it would be relatively easy to increase the critical design wind speed for such a shell by the addition of ring stiffeners particularly near to the top of the chimney.

It is therefore clear that to simultaneously satisfy the four design criteria would restrict the range of geometries available to the designer. In fact TableA6 suggests $L/k \not> 30$ and Table A7 suggests $d/t \not> 150$. Tables 4(a), 4(b) give corresponding pairs of values of L/k and d/t to prevent V_s exceeding, say, 42 m/s and it may be seen that $L/k \not> 30$ and $d/t \not> 150$ would give a safe design.

The simplified ovalling oscillation criterion used considered the chimney as a simple ring element and neglected the effects of chimney length. It has been shown for shorter shells that this criterion is quite conservative and should then be used with caution.

9. Alternative Method of Calculation.

It is found that the two dynamic criteria are generally more critical than the static criteria. Hence the design procedure is, as follows.

(i)   Select the height L of the chimney such that it satisfies the minimum height requirement for efflux considerations.

(ii) Select factor S_1 and also choose S_3 (Section 2).   Calculate S_{2L} from values of K and α from TableA1 and L from step (i) obtain the value of basic wind speed from Figure 3 of reference A3, and calculate V_L. Calculate the diameter, d from k from equation (15).

(iii) Check for efflux rate and consider forced draught if d is inadequate.

(iv) Obtain t from equation (18).

(v)   Obtain the design stress f_b from equation (9). Also obtain

$\frac{W_L}{L}$ from equation (11). If the allowable deflection criterion is not satisfied, increase d and/or t such that the allowable stress criterion is also satisfied.

(vi)   In case the allowable stress is much larger than design stress due consideration should be given to reducing t and using stiffeners to satisfy the ovalling criterion.

(vii) If, in the structure built based on thes design procedure, any dynamic instability is found, which is highly unlikely, consideration should be given to increasing damping by lining or cladding or by added foundation damping and/or incorporating devices such as helical strakes (patented) or perforated shrouds etc, which minimise the effectiveness of the vortices being shed.

10. Conclusion.

A simplified procedure for the design of steel chimneys is described. A method of obtaining the wind loading amenable to integration over the height of the structure and conforming to the wind loading code is given. Static and dynamic structural design criteria were considered. Of the two static criteria, the allowable deflection criterion seems to be the more critical and its validity is questioned. The geometry is probably dictated most by the dynamic criteria and hardly at all by static strength requirements.

There is a need for a more logical design code which takes full account of static strength and fatigue considerations and of possible dynamic instabilities due to vortex shedding. There is increasing knowledge of the unsteady nature (gustiness) of the wind and the random pressure fluctuations on the chimney structure and a corresponding simple analysis for designers to apply should be introduced as soon as possible.

If a deflection criterion is to be retained it should be one which relates the transverse (wind) and dead weight loads when acting simultaneously to the possibility of static instability and/or combined stresses due to compression and bending of the chimney cross-section.

References.

A1.   Specification for Steel Chimneys; British Standard Institute, B.S. 4076 (1966)

A2.   D.J. Johns and   The Structural Design of Self-Support-
      C.B. Sharma.   ing Steel Chimneys Deduced from B.S.4076 1966, Loughborough University of Technology. Report TT.6915.

A3.   Loading, Part 2, Wind Loads, B.S. Code of Practice CP3: Chapter V: Part 2: 1970.

A4.   D.J. Johns and   The Design of Self-Supporting Steel
      R. Nataraja.   Chimneys. Loughborough University of Technology, Report TT7301 , Feb.. 1973.

STATISTICS OF RANDOM PROCESSES

1.   Introduction

In this section, some   probability parameters pertaining to random fatigue analysis are introduced. These can be found in many text books on the subject; the objective here is to write these parameters in consistent notations and to derive the expressions using an engineering approach.

2.   Normal Distribution

A random process $x(t)$ is said to have a normal or Gaussian distribution when its probability of occurance (i.e., probability density) is given by

$$p(x) = \frac{1}{\sqrt{2\pi}\ \sigma_1} \exp \left[-\frac{(x-\bar{x})^2}{2\sigma_1^2} \right] \qquad 1.$$

where σ_1 is the standard deviation and $\bar{x}$ is the mean values given respectively by

$$\sigma_1^2 = E\{x^2\} - [E\{x\}]^2 = \frac{1}{2T} \int_{-T}^{T} x^2(t)\, dt$$

and $\quad \bar{x} = E\{x\} = \frac{1}{2T} \int_{-T}^{T} x(t)\, dt \qquad 2.$

Without loss of generality, the discussion that follows assumes that the process has a zero mean value. Also, station-

arity and ergodicity of the process are assumed.

The probability distribution function which gives the probability of occurance of all values less than a given value can be written, in general, as

$$P(<x) = \int_{-\infty}^{x} p(x)\,dx \qquad\qquad 3.$$

3.   Correlations

The correlation function $R(\tau)$ is defined as

$$R(\tau) = E\{x(t)\,x(t+\tau)\} = \frac{1}{2T}\int_{-T}^{T} x(t)\,x(t+\tau)\,dt$$

$$4.$$

where τ is the time delay. Since the mean value is zero, the zero time delat correlation gives the variance, i.e.,

$$R(0) = \sigma_1^2.$$

For a continuous random process with continuous derivatives, the correlation of $j^{th}|_t$ derivative with $k^{th}|_{(t+\tau)}$ derivative can be written as

$$(-1)^{j+k}\, R^{j+k}(\tau) = E\{x^j(t)\,x^k(t+\tau)\} \qquad 5.$$

4.   Derivatives of a Random Process

The random process $x(t)$ is assumed to possess higher order derivatives. In a purely random process , the derivatives also are random processes and are completely independent (uncorrelated).

Let N_{xi} be the expected number of crossings of a level x_i per unit time. Then the probability of an x_i crossing in an infinitesimally small time dt is given by N_{xi} dt. If there is such a crossing, it corresponds to either of the two conditions

$$x_i - |\dot{x}(t)| \, dt < x(t) < x_i \quad \text{when} \quad \dot{x}(t) < 0$$

or

$$x_i + |\dot{x}(t)| \, dt > x(t) > x_i \quad \text{when} \quad \dot{x}(t) > 0 \, .$$

The joint probability density function of x and $\dot{x}$ can be written as

$$p(x_i, \dot{x}_i) \, dx \, d\dot{x} \quad \text{where}$$

$$x_i < x(t) < x_i + dx \quad \text{and} \quad \dot{x}_i < \dot{x}(t) < \dot{x}_i + d\dot{x} \, .$$

The probability of an x_i crossing can therefore be written as

$$N_{xi} \, dt = \int_0^\infty \int_{x_i - |\dot{x}|dt}^{x_i} p(x_i, \dot{x}_i) \, dx \, d\dot{x}$$

$$+ \int_{-\infty}^0 \int_{x_i}^{x_i + |\dot{x}|dt} p(x_i, \dot{x}_i) \, dx \, d\dot{x} \qquad 6 \text{ a}$$

As $\quad dt \rightarrow 0$,

$$N_{xi} = \int_{-\infty}^\infty |\dot{x}_i| \, p(x_i, \dot{x}_i) \, d\dot{x}$$

- 186 -

Since x and $\dot{x}$ are completely uncorrelated, the joint probability density function can be written as a product of the individual probabilities.
Thus,

$$N_{xi} = p(x_i) \int_{-\infty}^{\infty} |\dot{x}_i| \; p(\dot{x}_i) \; d\dot{x}$$

or $\quad N_{xi} = p(x_i) \; E\left\{|\dot{x}_i|\right\}$ $\qquad\qquad$ 6 b

Therefore, the number of zero crossings per unit time can be written as

$$N_0 = p(x=0) \; E\left\{|\dot{x}|_{x=0}\right\}$$

or simply,

$$N_0 = p(x=0) \; E\left\{|\dot{x}|\right\}$$ $\qquad$ 7

The expected number of peaks per unit time is given by the number of zero crossings of $\dot{x}(t)$ as

$$N_e = p(\dot{x}=0) \; E\left\{|\ddot{x}|\right\}$$ $\qquad$ 8

In general, the expected number of zero crossings of kth derivative can be written as

$$N_0^k = p(x^k=0) \; E\left\{|x^{k+1}|\right\}$$

For a Gaussian random process with zero mean value the following relations between the probability density function and zero time delay correlations exist:

$$p(x) = \frac{1}{\sqrt{2\pi R(0)}} \exp [-x^2/2 R(0)]$$

$$p(\dot{x}) = \frac{1}{\sqrt{-2\pi R''(0)}} \exp [-\dot{x}^2/-2 R''(0)]$$

$$p(\ddot{x}) = \frac{1}{\sqrt{2\pi R^4(0)}} \exp [-\ddot{x}^2/2 R^{iv}(0)] \qquad 9$$

In terms of correlations, the expected values can be written as

$$E\{|\dot{x}|\} = \int_{-\infty}^{\infty} |\dot{x}| \, p(\dot{x}) \, d\dot{x} = \sqrt{\frac{-2}{\pi} R''(0)}$$

$$E\{\ddot{x}\} = \int_{-\infty}^{\infty} |\ddot{x}| \, p(\ddot{x}) \, d\ddot{x} = \sqrt{\frac{2}{\pi} R^{iv}(0)} \qquad 10$$

Hence

$$N_{xi} = \frac{1}{\pi} \frac{\sigma_2}{\sigma_1} \exp(-x_i^2/2\sigma_1^2)$$

$$N_0 = \nu_1 = \frac{1}{\pi} \frac{\sigma_2}{\sigma_1}$$

$$N_e = \nu_2 = \frac{1}{\pi} \frac{\sigma_3}{\sigma_2}$$

$$\vdots$$

$$N_0^k = \frac{1}{\pi} \frac{\sigma_{k+2}}{\sigma_{k+1}} \qquad 11$$

where

$$\sigma_1^2 = \frac{1}{2\pi} \int_{-\infty}^{\infty} s(\omega) \, d\omega$$

$$\sigma_2^2 = \frac{1}{2\pi} \int_{-\infty}^{\infty} \omega^2 s(\omega) \, d\omega$$

$$\sigma_3^2 = \frac{1}{2\pi} \int_{-\infty}^{\infty} \omega^4 \, s(\omega) \, d\omega$$

$$\vdots$$

$$\sigma_{k+2}^2 = \frac{1}{2\pi} \int_{-\infty}^{\infty} \omega^{2k+2} \, s(\omega) \, d\omega \qquad\qquad 12$$

The number of zero crossings provides an equivalent entity, in a random loading, where a definite frequency of loading in a fatigue analysis is not easily discernible.

TABLE 9.1   COMPARISON OF FREQUENCY PARAMETER ($\sqrt{\triangle} \times 10^2$), $\frac{a}{h}$ = 250

	l/a = 9				l/a = 12			
	m = 1							
	Present				Present			
n	A	B	Ref.82	Forsberg (83)	A	B	Ref.82	Forsberg (83)
1	2.9358	2.9358	2.7001	2.6660	1.6828	1.6828	1.5465	1.5530
2	1.0113	1.0113	0.9382	0.9510	0.6263	0.6263	0.5886	0.5971
3	0.9925	0.9925	0.9761	—	0.9161	0.9161	0.9105	0.9101
4	1.7065	1.7065	1.7034	—	1.6901	1.6901	1.6891	—
5	2.7289	2.7288	2.7281	—	2.7225	2.7225	2.7223	—
6	3.9945	3.9944	3.9942	—	3.9905	3.9905	3.9905	—
7	5.4939	5.4908	5.4938	—	5.4906	5.4905	5.4906	—
8	7.2252	7.2249	7.2251	—	7.2221	7.2218	7.2221	—
9	9.1877	9.1872	9.1877	—	9.1848	9.1843	9.1848	—
10	11.3814	11.3806	11.3814	—	11.3785	11.3777	11.3785	—
	m = 2							
1	15.5100	15.5100	14.2590	12.4200	9.4605	9.4605	8.6181	7.9980
2	5.7739	5.7738	5.2647	5.1780	3.3361	3.3336	3.0220	3.0660
3	2.9486	2.9486	2.6969	2.7510	1.8279	1.8279	1.6933	1.7400
4	2.3699	2.3699	2.2632	2.2950	1.9365	1.9365	1.8944	1.9080
5	2.9561	2.9561	2.9200	2.9260	2.8058	2.8058	2.6936	2.7910
6	4.0977	4.0976	4.0849	4.0760	4.0327	4.0326	4.0286	4.0790
7	5.5582	5.5580	5.5530	—	5.5204	5.5204	5.5187	5.5100
8	7.2753	7.2750	7.2730	—	7.2475	7.2472	7.2467	—
9	9.2321	9.2317	9.2310	—	9.2084	9.2079	9.2080	—
10	11.4232	11.4225	11.4226	—	11.4013	11.4006	11.4011	—

A: No rotatory inertia   B: With rotatory inertia

1/a = 9   1/a = 12

	m = 1							
	Present				Present			
n	A	B	Ref.82	Forsberg (83)	A	B	Ref.82	Forsberg (83)
1	2.9358	2.9358	2.7001	2.6650	1.6828	1.6828	1.5465	1.5520
2	0.9702	0.9702	0.8937	0.9074	0.5584	0.5584	0.5157	0.5258
3	0.5854	0.5854	0.5571	0.5635	0.4474	0.4474	0.4358	0.4384
4	0.7500	0.7500	0.7428	0.7434	0.7169	0.7169	0.7145	0.7143
5	1.1475	1.1475	1.1455	1.1320	1.1377	1.1377	1.1371	—
6	1.6679	1.6679	1.6672	—	1.6638	1.6638	1.6636	—
7	2.2905	2.2905	2.2903	—	2.2882	2.2882	2.2881	—
8	3.0111	3.0111	3.0110	—	3.0094	3.0094	3.0094	—
9	3.8285	3.8285	3.8285	—	3.8271	3.8270	3.8271	—
10	4.7424	4.7424	4.7424	—	4.7411	4.7410	4.7411	—
	m = 2							
1	15.5100	15.5100	14.2589	12.2400	9.4605	9.4605	8.6180	—
2	5.7656	5.7656	5.2556	5.1060	3.3241	3.3241	3.0074	3.0170
3	2.8293	2.8293	2.5658	2.5950	1.6358	1.6358	1.4839	1.5240
4	1.7802	1.7802	1.6353	1.6720	1.1630	1.1630	1.0915	1.1150
5	1.5632	1.5632	1.4938	1.5130	1.2891	1.2891	1.2623	1.2700
6	1.8356	1.8356	1.8068	1.8130	1.7227	1.7227	1.7129	1.7140
7	2.3688	2.3688	2.3566	2.3560	2.3172	2.3172	2.3132	—
8	3.0554	3.0554	3.0498	3.0460	3.0274	3.0274	3.0257	—
9	3.8586	3.8586	3.8558	3.8500	3.8406	3.8406	3.8397	—
10	4.7660	4.7660	4.7645	—	4.7525	4.7525	4.7521	—

A: No rotatory inertia   B: With rotatory inertia

TABLE 9.2   NATURAL FREQUENCIES OF SHELL F4 (in Hz)
a=2.4375", L=69", E=10.0x10^6 PSI, h=0.01"
=0.000259 lb-sec^2/in^4

Mode No. m / n	0	1	2	3	4	5
1	606.21	41.24	44.88	121.53	232.71	376.28
2	1600.98	248.42	91.44	127.58	234.13	376.97
3	2472.23	652.05	225.04	161.43	241.58	379.51
4	3361.76	1182.53	424.51	237.97	268.83	386.24
5	4104.18	1780.70	679.87	354.99	305.44	400.21

TABLE 9.3   NATURAL FREQUENCIES OF SHELL F5 (in Hz)
a=3", L=69", E=10x10^6 PSI, h=0.01",
=0.000259 lb-sec^2/in^4

Mode No. m / n	0	1	2	3	4	5
1	606.21	50.76	32.56	80.24	153.19	247.62
2	1600.98	301.98	103.19	93.01	155.91	248.66
3	2472.23	774.3	271.47	152.64	171.46	253.49
4	3361.76	1368.80	512.32	262.30	212.45	267.10
5	4104.18	2004.20	811.15	412.80	284.26	295.09

TABLE 9.4. MEASURED RESONANCE FREQUENCIES (Hz) OF THE SHELLS

Sl No.	SHELL F4					SHELL F5			
	Mode No. m,n	Theory	Vib.Tests[@]	W.T.Tests[£]	Ref.96[×]	Mode No. m,n	Theory	Vib.Tests[@]	W.T.Tests[£]
1	1,1	41.24	33.0	32.3	(1,2) 33.0	1,2	32.56	32.5	27.32
2.	1,2	44.88	36.8	38.0	(1,1) 43.0	1,1	50.76	48.5	46.0
3	2,2	91.44	87.0	84.0	—	1,3	80.24	79.0	70.0
4	1,3	121.53	122.0	114.0	—	2,3	93.01	88.0	86.0
5	2,3	127.58	126.0	122.0	—	2,2	103.19	101.5	93.0

@ — Single point sinusoidal excitation at the tip.

£ — Spectral Analysis of Strain Signals, see Figs. 11.18,11.19,11.20.

× — W.T. Tests on a = 2.4", L = 71", h = 0.01" Aluminium Shell.

TABLE 9.5. MEASURED DAMPING COEFFICIENTS

	S1 No.	Mode No.	δ @	$g = \dfrac{\delta}{\pi}$	$\dfrac{\Delta\omega}{\omega} = g + g_a$ £	$g_a = \dfrac{\Delta\omega}{\omega} - \dfrac{\delta}{\pi}$	Ref.97 ξ
Shell F4	1	1,1	0.066	0.021	0.03	0.09	0.02-0.025
	2	1,2	0.079	0.025	0.026	0.001	
	3	2,2	0.072	0.023	0.003	− 0.020	
	4	1,3	0.073	0.023	*	−	
	5	2,3	0.063	0.020	0.007	− 0.013	
Shell F5	1	1,2	0.069	0.022	0.011	− 0.011	0.02-0.025
	2	1,1	0.065	0.021	*	−	
	3	1,3	0.072	0.023	*	−	
	4	2,3	0.078	0.025	0.008	− 0.017	
	5	2,2	0.066	0.021	*	−	

@   − Logarithmic decrement from response decay over 10 peaks

£   − Half power method from resonance strain spectra (W.T.Tests) − only lowest values are quoted

§   − Half power method from oscilloscope observations (tests on aluminium shells)

*   − Very high overall damping, data not reliable

g − Structural damping

g_a − Aerodynamic damping

TABLE 10.1 DETAILS OF MODELS

Shell Number	R1	R2	R3	F4	F5
Configuration	Rigid 3-D Fully immersed	Rigid 3-D, 2-D Fully immersed	Rigid 3-D Partially immersed	Flexible 3-D Partially immersed	Flexible 3-D Partially immersed
Wetted length (inches)	28	28	27	27	28
Run Numbers *	1-2	3-5, 6-8	9-20	21-27	28-34
Material	PVC	PVC	Perspex	Al	Al
Diameter D (inches)	3.5	8.5	6.0	4.875	6.0
Thickness h (inch)	0.25	0.25	0.25	0.01	0.01
Height L (inches)	28	28	69	69	69
Aspect ratio L/D	8	3.3	11.5	14.15	11.5
a/h	-	-	-	244	300
No. of Pressure Trans.	2	3	1	2	2

* See Table 11.1 for details

195

TABLE 10.1 (cont'd.)   DETAILS OF MODELS
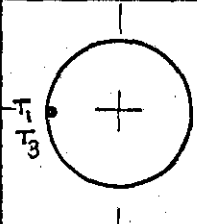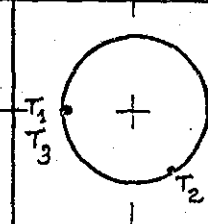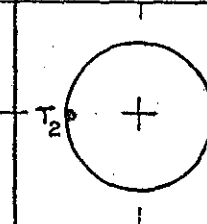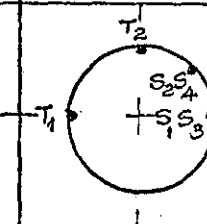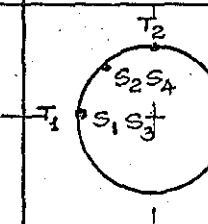
Shell Number		R1	R2	R3	F4	F5
Transducer Location	T_1	8.2, 0°	8.2, 0°	–	13.0	13.0
		(2.35)	(0.965)		(2.72)	(2.16)
Inches from top, angle from T_1	T_2	–	8.2, 120°	13.0	13.0	13.0
		–	(0.965)	(2.16)	(2.72)	(2.16)
(x/D)	T_3	22.0, 0°	14.10, 0°	–	–	–
		(6.3)	(1.75)	–	–	–
Location of Strain Gauges	S_1	–	–	–	1,-90°	2, 0°
Inches from base, angle w.r.t. T_2	S_2	–	–	–	1,-45°	2, 45°
	S_3	–	–	–	66,-90°	66, 0°
	S_4	–	–	–	66,-45°	66, 45°
Re Range ($\times 10^5$)		0.4-1.62	1.63-2.85, 1.63-2.85	0.78-2.09	0.85-1.79	0.78-2.09

196

TABLE 10.2   TYPICAL VALUES OF C_p^*

Angle Degrees \ Run No.	1 T1	2 T1	3 A	4 A	6 A	7 A	8 A	19
0	0.019	0.034	0.014	0.013	0.013	0.010	0.006	0.005
15	0.021*	0.036*	0.014	0.015	0.067	0.022	0.012	0.007
30	0.027	0.040	0.015	0.024	0.122	0.044	0.030	0.011
45	0.046*	0.05 *	0.019	0.035	0.115	0.064	0.058	0.018
60	0.077	0.068	0.037	0.059	0.164	0.091	0.095	0.029
75	0.136	0.096	0.031	0.091	0.365	0.200	0.158	0.050
90	0.108	0.096	0.034	0.069	0.334	0.182	0.160	0.044
105	0.108	0.101	0.040	0.075	0.325	0.154	0.110	0.056
120	0.108	0.091	0.034	0.059	0.290	0.150	0.090	0.040
135	0.128	0.102	0.030	0.049	0.305	0.163	0.073	0.038
150	0.115	0.108	0.029	0.043	0.315	0.159	0.090	0.040
165	0.136	0.115	0.031	0.046	0.265	0.129	0.073	0.045
180	0.145	0.119	0.032	0.043	0.240	0.115	0.053	0.048

* - Extrapolated,   A - Average of T1 and T3

TABLE 10.3　FOURIER COEFFICIENTS OF FLUCTUATING (RMS) PRESSURE DISTRIBUTION

Run No. ⟶ Coefficient	1	2	3	4	6	7	8	19
a_0	0.09100	0.08162	0.02808	0.04942	0.23279	0.11838	0.08154	0.03371
a_1	-0.05276	-0.03788	-0.00769	-0.01119	-0.10982	-0.05717	-0.02168	-0.01742
a_2	-0.02047	-0.01081	-0.00784	-0.02624	-0.08767	-0.05238	-0.05358	-0.01221
a_3	-0.01252	-0.00584	-0.00165	-0.00639	-0.00357	-0.00528	-0.01583	-0.00316
a_4	0.00883	0.00683	0.00142	0.00567	0.01767	0.00800	0.01375	0.00558
a_5	0.00883	0.00273	-0.00012	0.00313	0.01873	0.01739	0.01202	-0.00056
a_6	0.00283	-0.00142	0.00267	0.00167	-0.03175	-0.01358	-0.01092	0.00008
a_7	-0.00959	-0.00110	0.00166	-0.00265	-0.02185	-0.01152	-0.00170	-0.00007
a_8	-0.00000	-0.00050	-0.00158	-0.00417	-0.01267	-0.00050	-0.00142	-0.00208
a_9	0.00186	-0.00066	-0.00235	0.00139	0.00774	0.00745	0.00633	-0.00034
a_{10}	0.00464	0.00247	-0.00033	0.00407	0.01567	0.00622	-0.00075	0.00338
a_{11}	0.00119	0.00025	0.00115	0.00071	-0.00473	-0.00336	-0.00264	0.00005
a_{12}	-0.00483	-0.00171	0.00058	-0.00242	-0.00754	-0.00362	-0.00875	-0.00196

198

TABLE 10.4   VALUES OF C_p^* IN THE DESCRIBING FUNCTION

Angle	Runs 9 — 20	Runs 21 — 34
0	0.005	0.010
15	0.007	0.015
30	0.012	0.020
45	0.018	0.025
60	0.027	0.040
75	0.047	0.055
90	0.042	0.047
105	0.047	0.055
120	0.040	0.050
135	0.035	0.053
150	0.040	0.058
165	0.044	0.062
180	0.047	0.084

TAB:E 10.5   FOURIER COEFFICIENTS OF THE OSCILLATORY PRESSURE
DESCRIBING FUNCTION

Coefficient	Run Nos. 9 – 20	Run Nos. 21 – 34
a_0	0.032083	0.043917
a_1	–0.016585	–0.023351
a_2	–0.010123	–0.005763
a_3	–0.003690	–0.006739
a_4	0.004667	0.004250
a_5	0.000134	–0.000243
a_6	–0.000167	0.002000
a_7	–0.000949	–0.002788
a_8	–0.001833	–0.000917
a_9	0.001024	–0.002261
a_{10}	0.002290	0.003763
a_{11}	0.000665	–0.001619
a_{12}	–0.000917	–0.000250

TABLE 10.6 C_D^* , C_L^* and Location of Centre of
Pressure (RMS) at Various Run Numbers

Run No.	C_D^*	C_L^*	C.P. Degrees from Stagnation
1	0.166	0.102	148.5
2	0.119	0.087	143.8
3	0.0242	0.033	126.2
4	0.0352	0.065	118.5
6	0.345	0.292	139.8
7	0.180	0.153	139.6
8	0.067	0.115	120.2
19	0.055	0.040	144.0
9-20	0.052	0.038	139.8
21-34	0.073	0.046	147.8

TABLE 11.1 DETAILS OF TEST RUNS

Run No.	Velocity f p s	Dyn. Pressure mm water.	Re (x 10^5)	Remarks.
1	21.8	2.75	0.4	3D R1
2	86.7	43.5	1.62	"
3	36.0	7.5	1.63	3D R2
4	49.8	14.4	2.26	"
5	63.0	23.0	2.85	"
6	36.0	7.5	1.63	2D R2
7	49.8	14.4	2.26	"
8	63.0	23.0	2.85	"
9	26.24	4.0	0.84	3D R3
10	38.44	8.6	1.23	"
11	43.69	11.1	1.40	"
12	52.28	15.9	1.67	"
13	56.15	18.3	1.79	"
14	24.50	3.5	0.78	"
15	32.7	6.2	1.04	"
16	40.87	9.7	1.31	"
17	47.90	13.3	1.53	"
18	54.05	17.0	1.73	"
19	59.43	20.5	1.9	"
20	64.2	23.9	2.09	"
21	32.9	6.3	0.846	3D F4
22	41.46	9.9	1.06	"
23	45.79	12.1	1.18	"
24	54.45	17.1	1.40	"
25	59.83	20.7	1.54	"
26	65.07	24.5	1.67	"
27	69.67	28.1	1.79	"
28	24.5	3.5	0.78	3D F5
29	32.67	6.2	1.04	"
30	40.87	9.7	1.31	"
31	47.89	13.3	1.53	"
32	54.05	17.0	1.73	"
33	59.43	20.5	1.90	"
34	64.16	23.9	2.09	"

TABLE III.1.   BEAM CONSTANTS.

m	$p_m l$	c_m
1	1.8751 0410	0.7340 955 000
2	4.6940 9113	1.0184 664 400
3	7.8547 5743	0.9992 245 000
4	10.9955 4074	1.0000 335 530
5	14.1371 6839	0.9999 985 501

For m > 5 , $p_m l \simeq (2m-1)\pi/2$ and $c_m \simeq 1.0$.

TABLE IV.1   INTEGRALS INVOLVING BEAM FUNCTIONS.

m I	1	2	3	4	5
I_1	0.24409556	−0.60334863	−0.74403279	−0.81795540	−0.79261289
I_2	1.32188804	1.47117873	1.25288109	1.18174873	1.0659110
I_3	2.32964076	4.25876876	2.95369377	2.54627272	2.2627730
I_4	2.34865697	1.78057208	1.69284372	1.63632881	1.5929542
I_5	2.03117982	1.49488963	1.07167611	0.90929765	0.79507604

TABLE IV.2   OTHER INTEGRALS.

case I	$n = i+j$	$n = i-j$	$n = j-i$
(i)	$\pi/2$	$\pi/2$	$\pi/2$
(ii)	$\pi/2$	$-\pi/2$	$\pi/2$
(iii)	$\pi/2$	$\pi/2$	$-\pi/2$
(iv)	$-\pi/2$	$\pi/2$	$\pi/2$

TABLE V11.1.   CORRECTION FACTORS FOR HANNING
ON <u>LINEAR</u> SPECTRUM

NO. OF HANNINGS	THEORETICAL *			MEASURED @
	CORRECTION FACTOR. dB	MULTIPLICATION FACTOR.	FREQUENCY RESOLUTION	MULTIPLICATION FACTOR.
1	6.02	2.00	2 Δ f	1.631
2	9.52	2.67	3 Δ f	1.910
3	10.10	3.20	4 Δ f	2.102
4	11.26	3.66	5 Δ f	−

*   As referred to the main lobe

@   Derived from rms values of 100 Hz and 200 Hz signals

TABLE IX.1   NOISE LEVELS IN THE WIND TUNNEL LABORATORY

Free Stream Velocity fps	Dyanmic Pressure mm of water	Equivalent Acoustic Pressure mm of water	
		Location 1	Location 2
36.0	7.5	0.025	0.020
51.0	51.0	0.061	0.042
65.0	65.0	0.074	0.078
92.0	92.0	0.211	0.260

Values of K and α for Evaluating $S_2 = KH^{\alpha}$

Table A1.

SL No.	Surface Category.	Height above Reference datum	Class A 3 sec. (Basic data)		Class B 5 sec. (for $L < 50m$)		Class C 15 sec. (for $L > 50m$)	
			K	α	K	α	K	α
1.	Open country with no shelter.	All heights	0.832	0.080	0.782	0.087	0.721	0.098
2.	Open country with scattered wind breaks	$> 5m$ $(K_1 \, \alpha_1)$	0.792	0.087	0.724	0.101	0.682	0.108
		$\leqq 5m$ $(K_2 \, \alpha_2)$	0.615	0.178	0.578	0.183	0.506	0.216
3.	Country with many wind breaks: small towns, outskirts of large cities.	$> 7.6m$	0.724	0.101	0.653	0.116	0.601	0.128
		$\leqq 7.6m$	0.412	0.275	0.389	0.279	0.352	0.293
4.	Surface with numerous obstructions e.g. city centres.	$> 14m$	0.600	0.130	0.536	0.154	0.488	0.168
		$\leqq 14m$	0.355	0.274	0.316	0.293	0.278	0.316

Design Wind Speed Satisfying Allowable Stress Criterion. Height less than 50 metres.

Table A2. (Category 1).

Design wind speed V_s m/s

L/k \ d/t	25	30	35	40	45	50	60	70	80	90	100	125
50	*	*	*	*	*	*	*	*	*	*	*	67.68
60	*	*	*	*	*	*	*	*	*	68.08	64.59	56.40
80	*	*	*	*	*	68.51	62.54	57.90	54.16	51.06	48.44	42.30
100	*	*	65.5	61.27	57.77	54.81	50.03	46.32	43.33	40.85	38.75	33.84
120	64.59	58.96	54.59	51.06	48.14	45.67	41.69	38.60	36.11	34.04	32.29	28.20
140	54.33	49.59	45.91	42.95	40.90	38.41	35.07	32.47	30.37	28.63	27.16	24.17
160	45.35	41.40	38.33	35.85	33.80	32.07	29.28	27.10	25.35	23.90	22.68	20.28
180	38.54	35.18	32.57	30.47	28.73	27.25	24.88	23.03	21.55	20.31	–	–
200	32.78	29.92	27.70	25.91	24.43	23.18	21.16	–	–	–	–	–
220	29.18	26.63	24.66	23.07	21.75	20.63	–	–	–	–	–	–
240	26.18	23.90	22.13	20.70	–	–	–	–	–	–	–	–
260	23.83	21.75	20.14	–	–	–	–	–	–	–	–	–
280	21.79	–	–	–	–	–	–	–	–	–	–	–
300	20.01	–	–	–	–	–	–	–	–	–	–	–

Table A3. (Category 4).

L/k \ d/t	25	30	35	40	45	50	60	70	80	90	100	125
50	*	*	*	*	*	*	*	*	*	*	*	*
60	*	*	*	*	*	*	*	*	*	*	68.18	59.53
80	*	*	*	*	*	*	66.01	61.12	57.17	53.90	51.13	44.65
100	*	*	69.14	64.68	60.98	57.85	52.81	48.89	45.73	43.12	40.91	35.72
120	68.18	62.24	57.62	53.90	50.82	48.21	44.01	40.74	38.11	35.93	34.09	29.77
140	57.35	52.35	48.47	45.34	42.74	40.55	37.02	34.27	32.06	30.22	28.67	25.51
160	47.87	43.70	40.46	37.85	35.68	33.85	30.90	28.61	26.76	25.23	23.94	21.41
180	40.68	37.14	34.38	32.16	30.32	28.77	26.26	24.31	22.74	21.44	20.34	–
200	34.60	31.59	29.24	27.35	25.79	24.47	22.33	20.68	–	–	–	–
220	30.80	28.11	26.03	24.35	22.95	21.78	–	–	–	–	–	–
240	27.64	25.23	23.36	21.85	20.60	–	–	–	–	–	–	–
260	25.15	22.96	21.26	–	–	–	–	–	–	–	–	–
280	23.00	21.00	–	–	–	–	–	–	–	–	–	–
300	21.12	–	–	–	–	–	–	–	–	–	–	–

* $V_s > 70$ m/s   – $V_s < 20$ m/s

Design Wind Speed Satisfying Allowable Deflection Criterion.   Height less than 50 metres

Table A4.   (Category 1).

d/t L/k	25	30	35	40	45	50	60	70	80	90	100	125
					Design Wind Speed V_s m/s							
40	*	*	*	*	*	*	*	*	*	66.83	63.40	56.70
50	*	*	*	*	67.62	64.15	58.56	54.22	50.72	47.82	45.36	40.57
60	69.02	63.00	58.33	54.56	51.44	48.80	44.55	41.25	38.58	36.38	34.51	30.87
80	44.83	40.92	37.89	35.44	33.41	31.70	28.94	26.79	25.06	23.63	22.41	20.05
100	32.08	29.28	27.11	25.36	23.91	22.68	20.71	−	−	−	−	−
120	24.40	22.28	20.62	−	−	−	−	−	−	−	−	−
140 and over	−	−	−	−	−	−	−	−	−	−	−	−

Table A5.   (Category 4).

L/k	25	30	35	40	45	50	60	70	80	90	100	125
40	*	*	*	*	*	*	*	*	*	69.30	65.74	58.80
50	*	*	*	*	*	66.52	60.73	56.22	52.59	49.58	47.04	42.07
60	*	65.33	60.49	56.58	53.34	50.61	46.20	42.77	40.01	37.72	35.78	42.07
80	46.49	42.44	39.29	36.75	34.65	32.87	30.01	27.78	25.99	24.50	35.78	32.01
100	33.26	30.36	28.11	26.30	24.79	23.52	21.47	−	−	−	23.24	20.79
120	25.30	23.10	21.39	20.00	−	−	−	−	−	−	−	−
140	20.08	−	−	−	−	−	−	−	−	−	−	−
160 and over	−	−	−	−	−	−	−	−	−	−	−	−

* $V_s > 70$ m/s

− $V_s < 20$ m/s

Table A6.	Design Wind Speed Satisfying Sway Oscillation Criterion.

L/k	V_s m/s
10	402.0
20	100.5
30	44.6
40	25.1
50	16.1
60 and over	Less than 15

Table A7.	Design Wind Speed Satisfying Ovalling Oscillations Criterion.

d/t	V_s m/s
25	248.8
50	124.4
75	83.0
100	62.2
125	50.0
150	41.5
175	35.5
200	31.1
225	27.6
250	25.0
300	20.7
350	17.7
400	15.5
450 and over	Less than 15
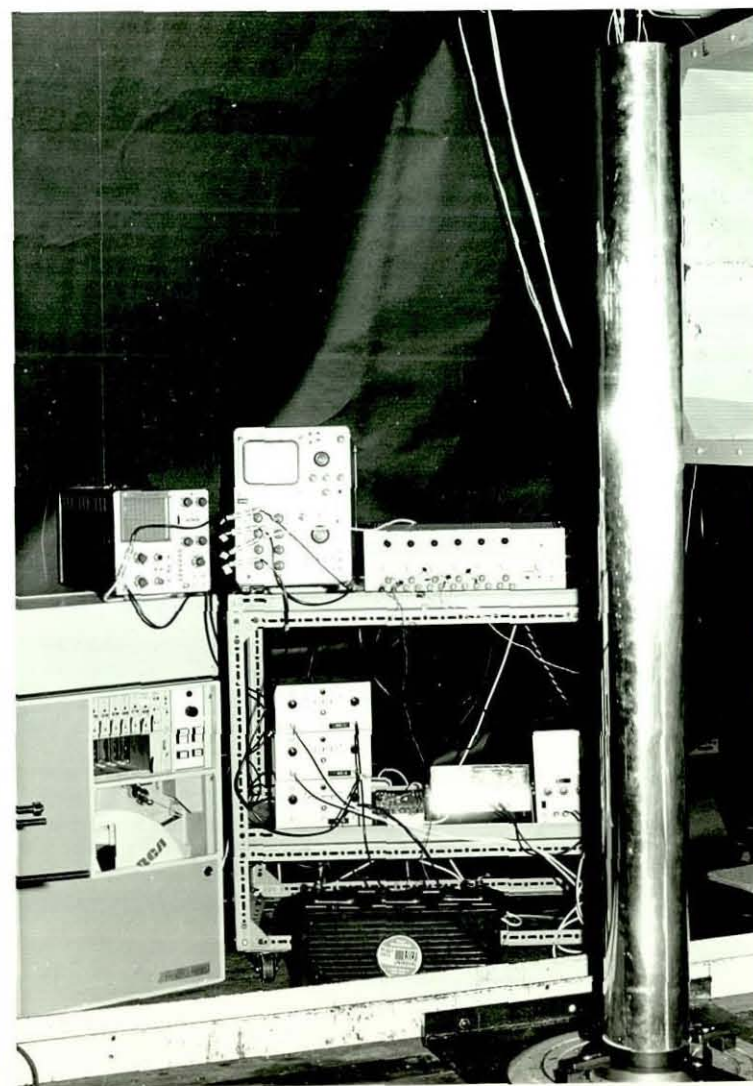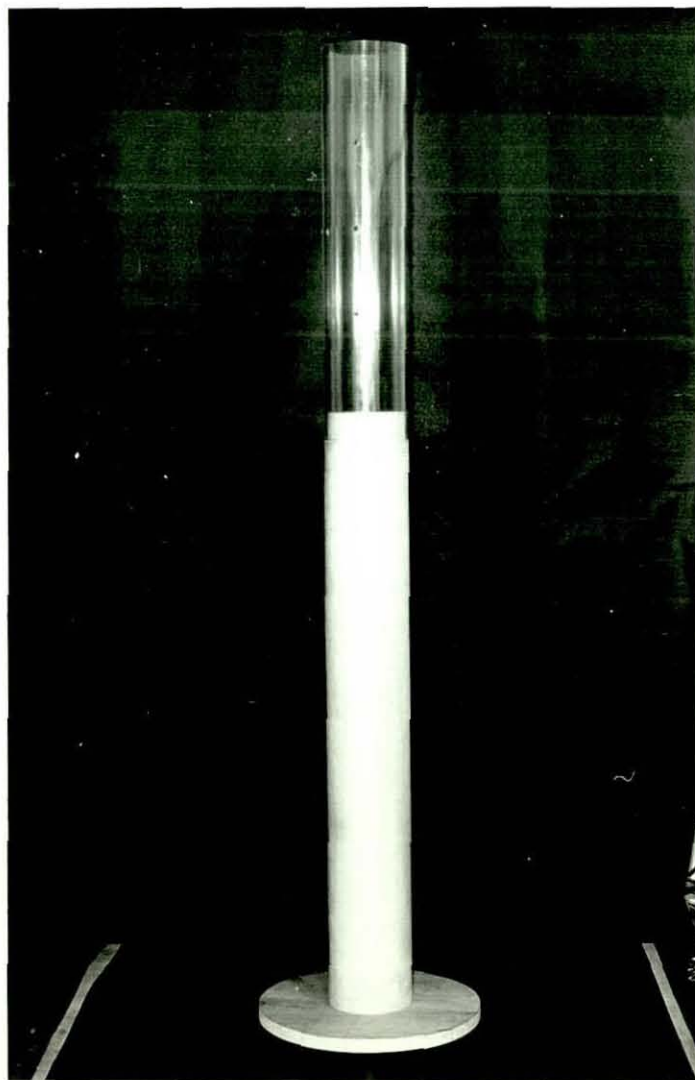
PLATE 8.1   MODELS & EXPERIMENTAL   SET-UP
a. rigid cylinder R3,   b. shell F5
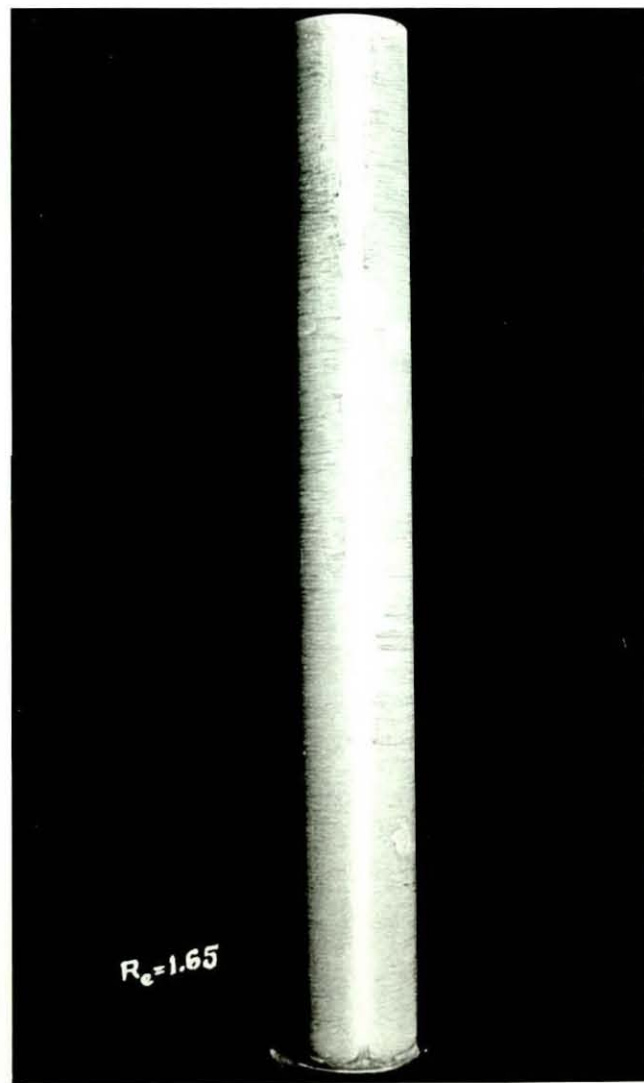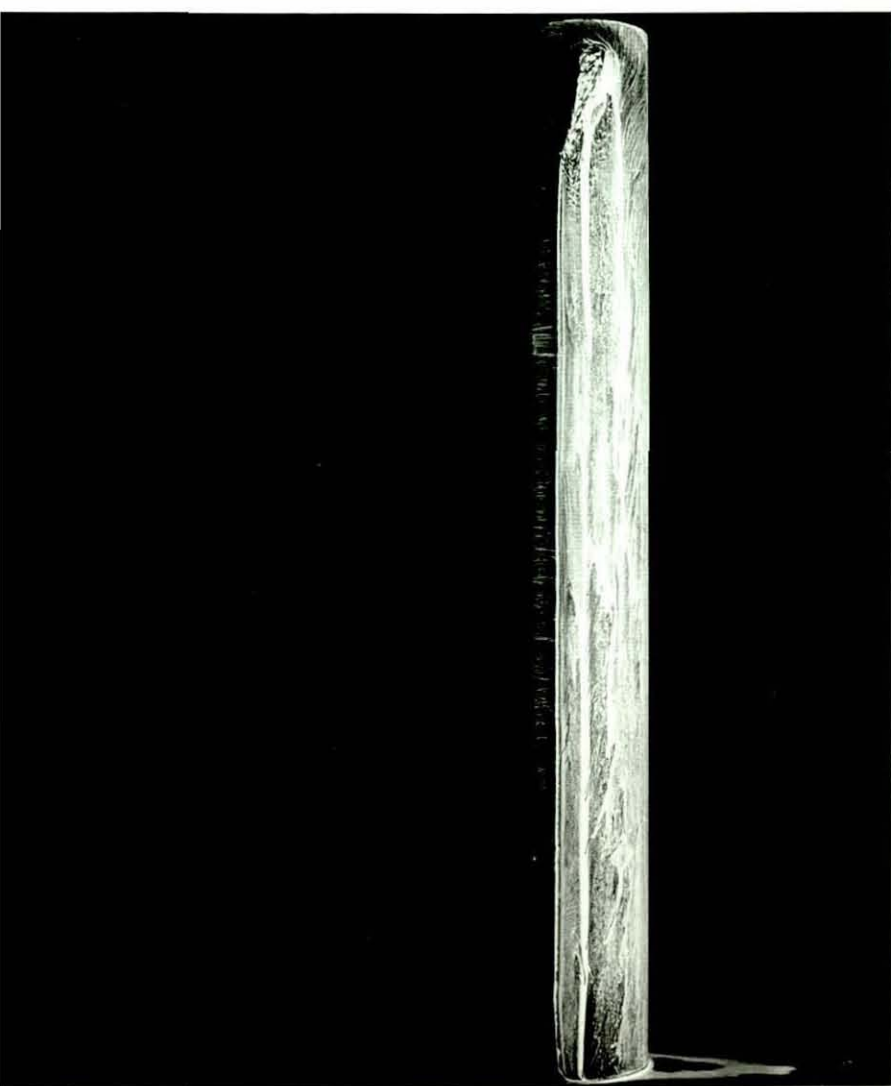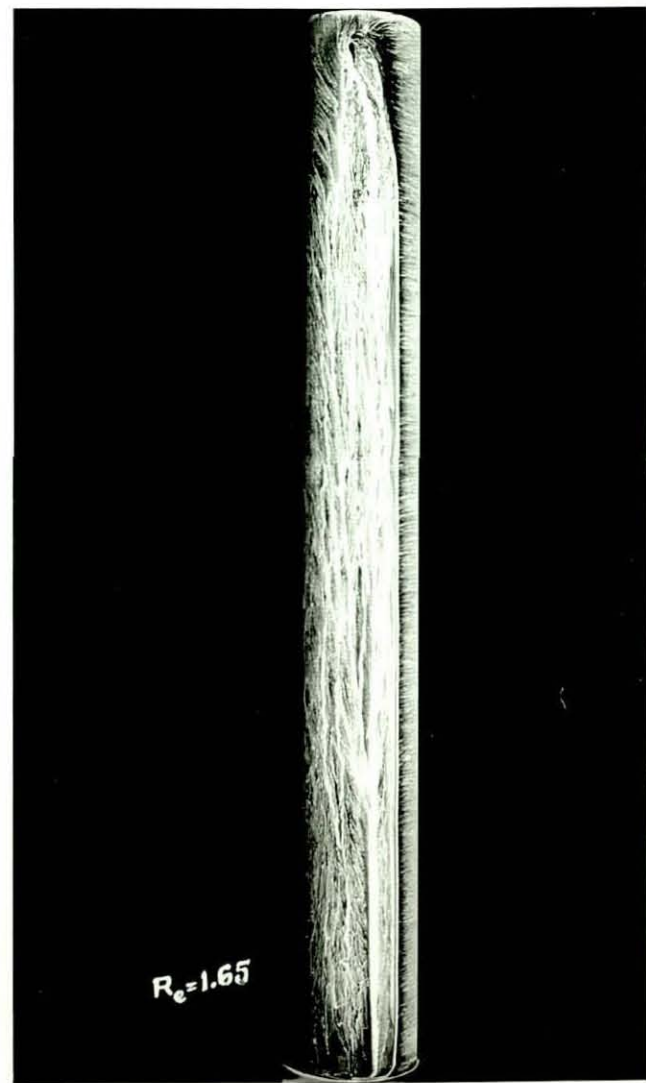
PLATE 101   SURFACE FLOW PATTERN ON RIGID CYLINDER, Re=1.65X10^5
a & c. side views,   b. front stagnation
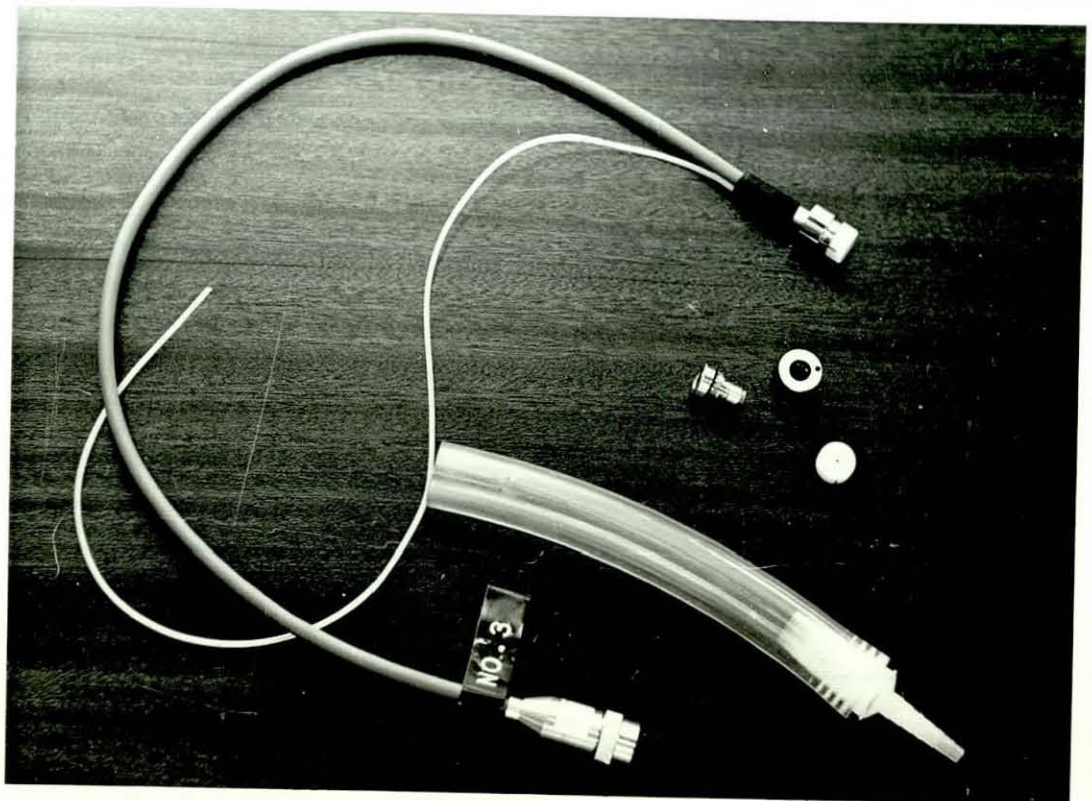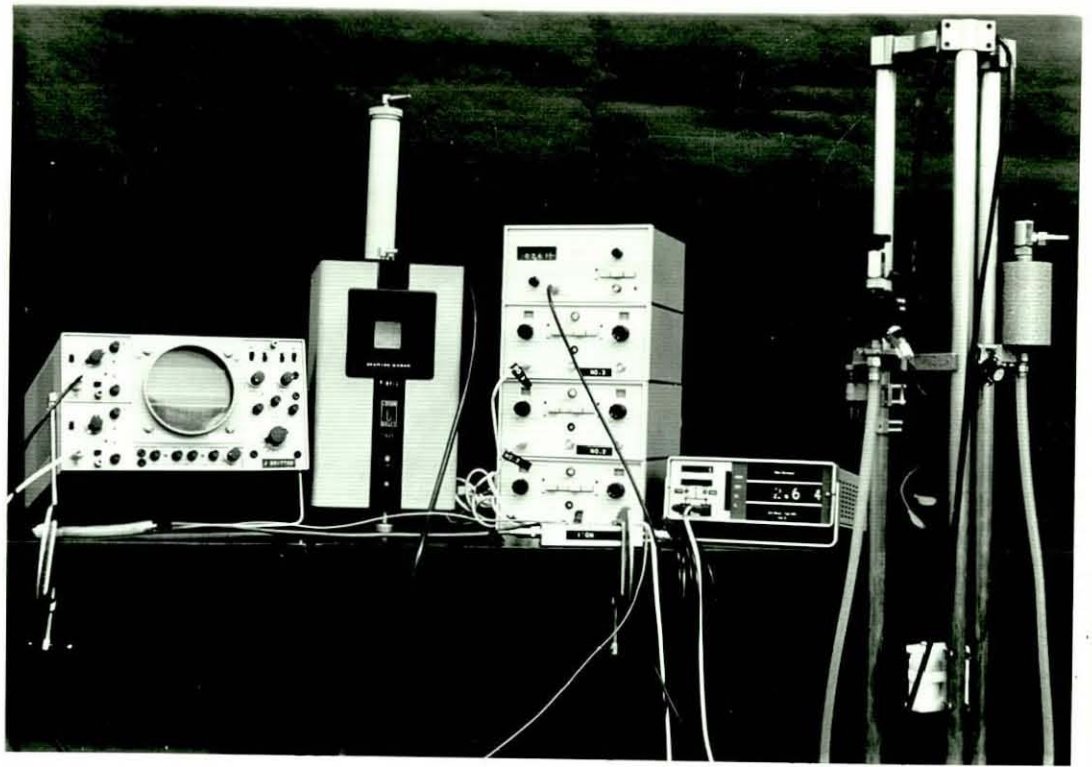
PLATE VIII.1 STATIC CALIBRATION SET-UP
& DETAILS OF TRANSDUCER
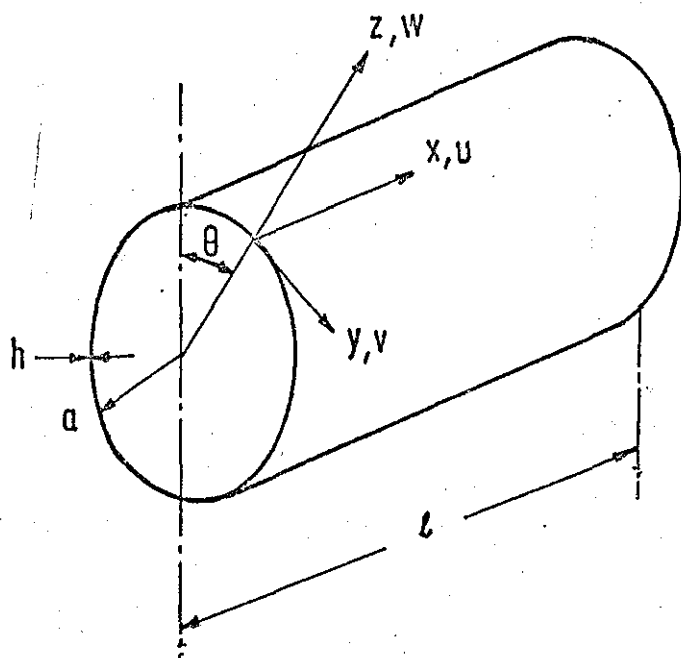
FIG. 2.1. COORDINATE SYSTEM

n=1   n=2   n=3

m=1   m=2
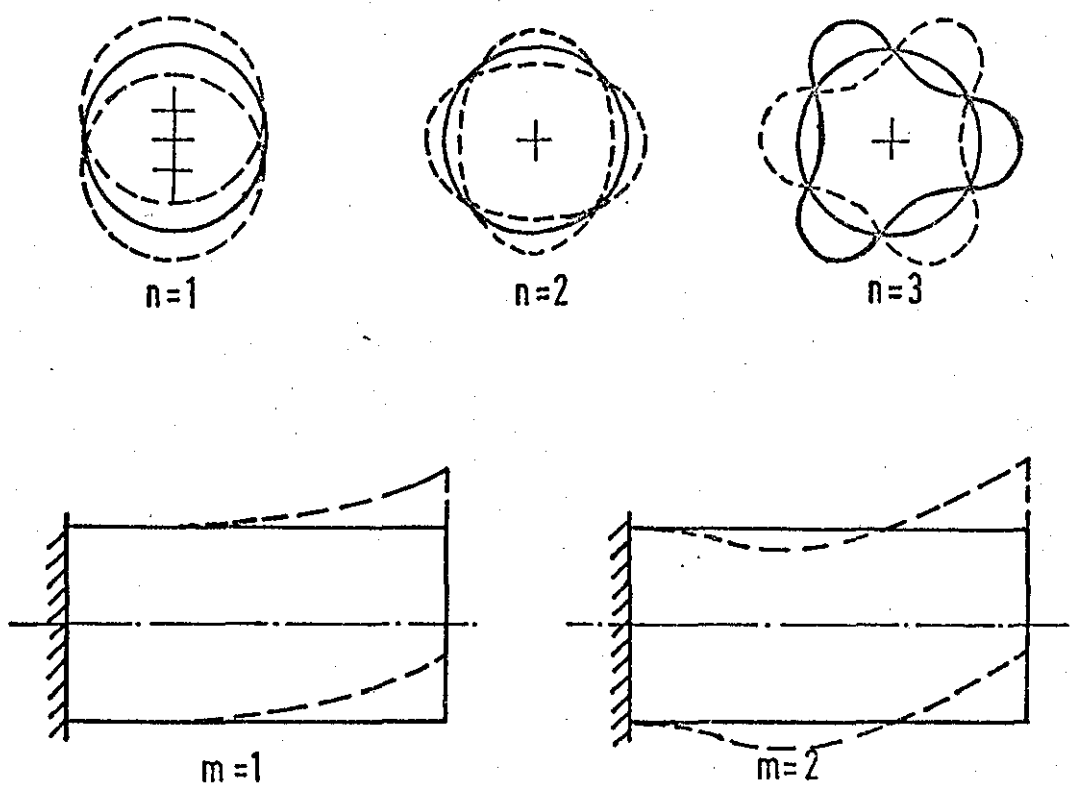
FIG. 2·2   TYPICAL MODE SHAPES

x-z   Plane

θ-z   Plane
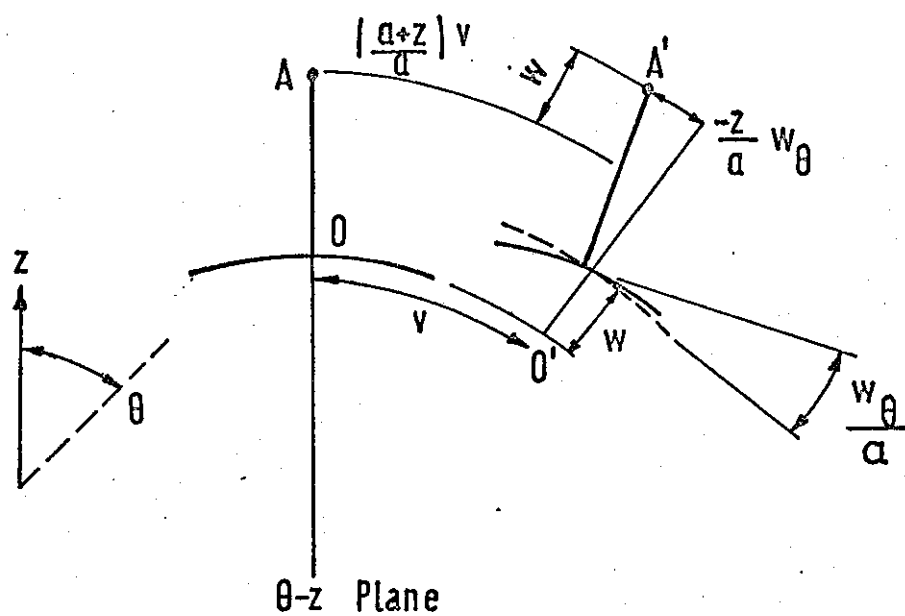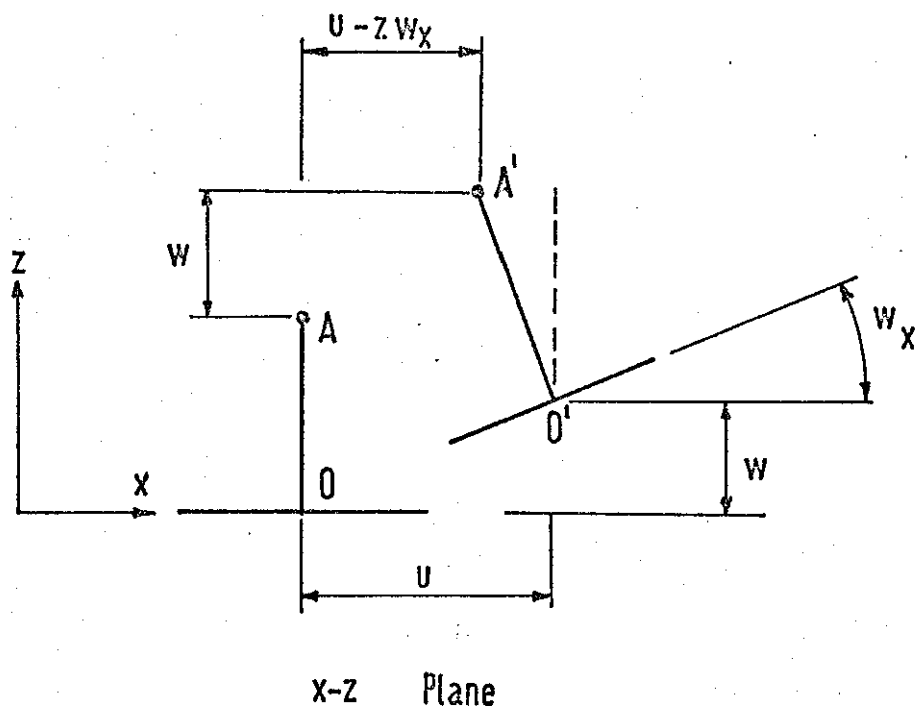
FIG. 2·3   DISPLACEMENTS
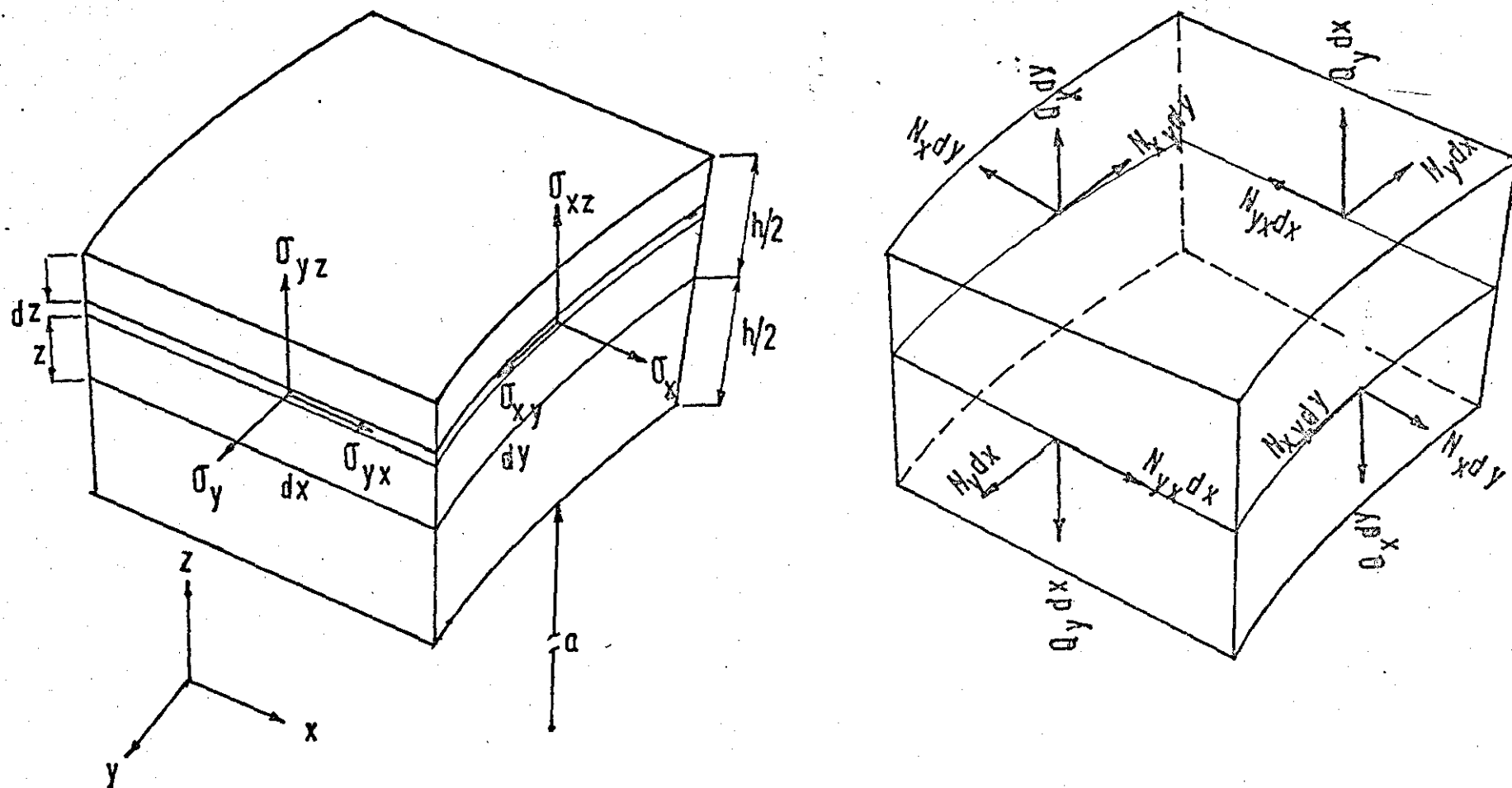
FIGURE 2·4 STRESSES AND STRESS RESULTANTS
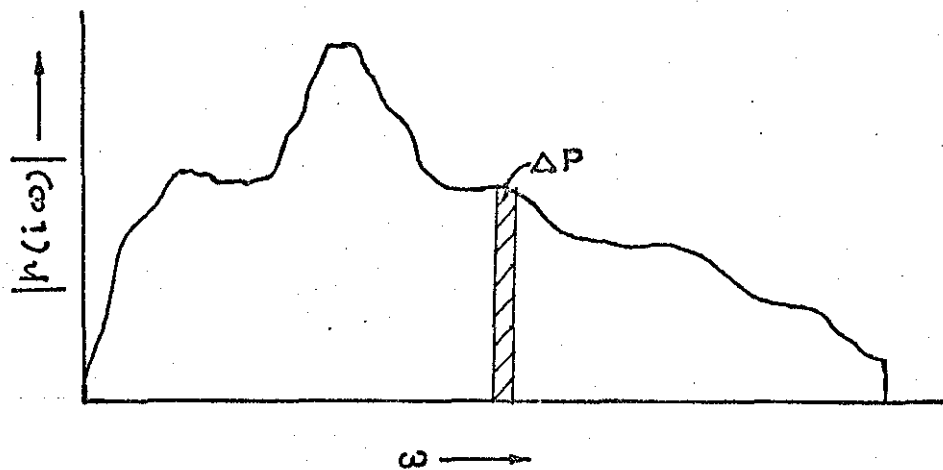
FIGURE 2·5   LINEAR PRESSURE SPECTRUM
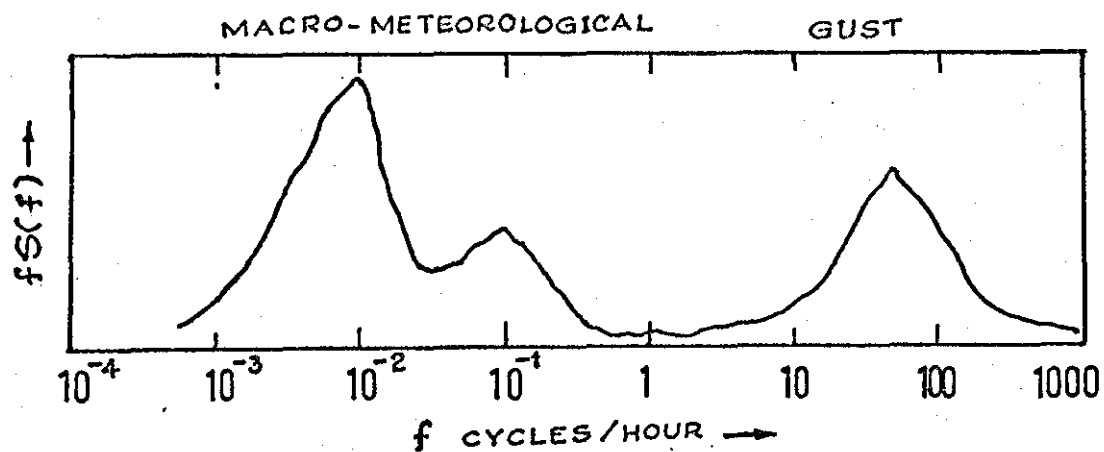
FIGURE 2·6   WIND SPECTRUM   (REF.85)
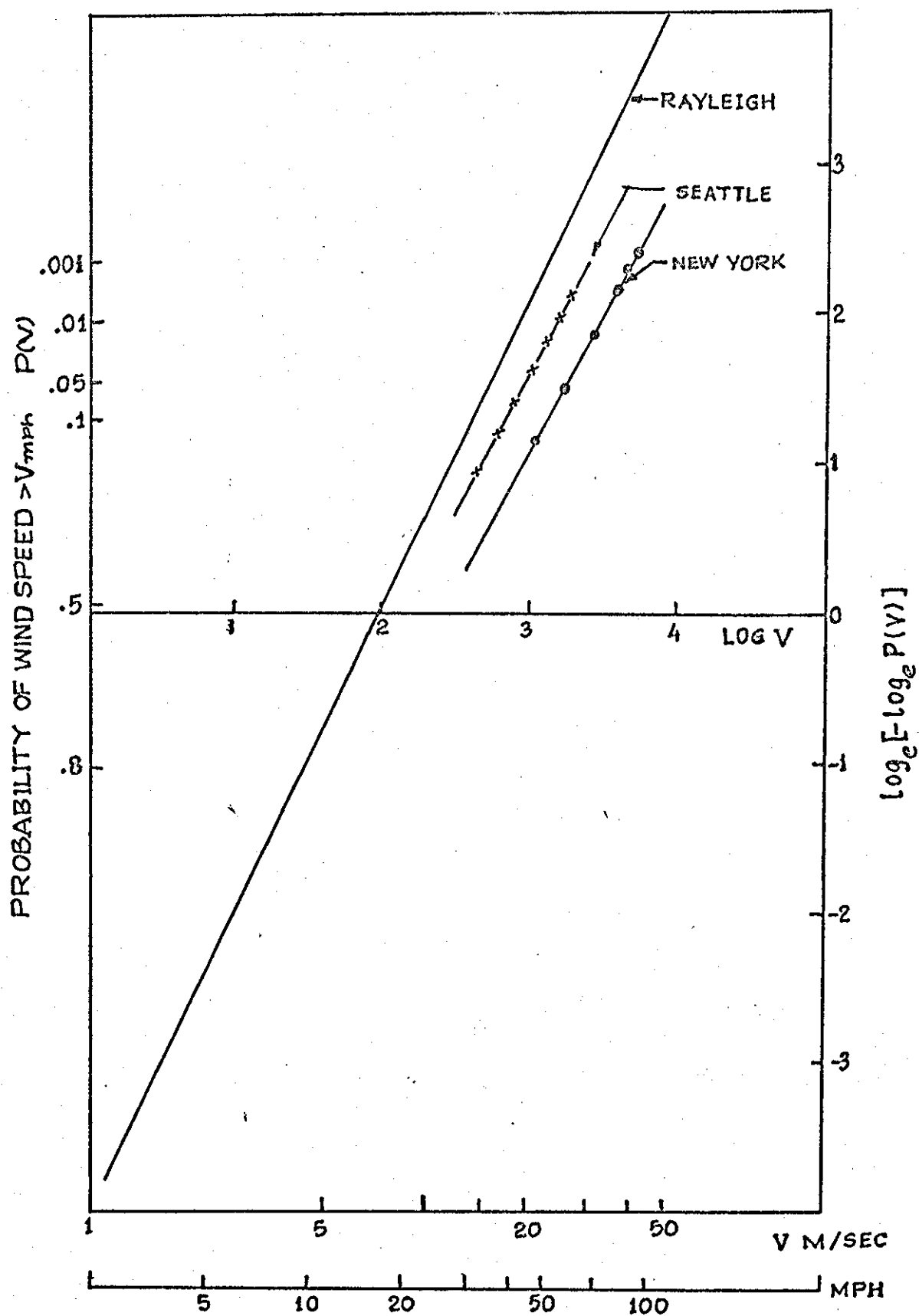
FIGURE 2·7   PROBABILITY OF WIND SPEEDS (REF.77)
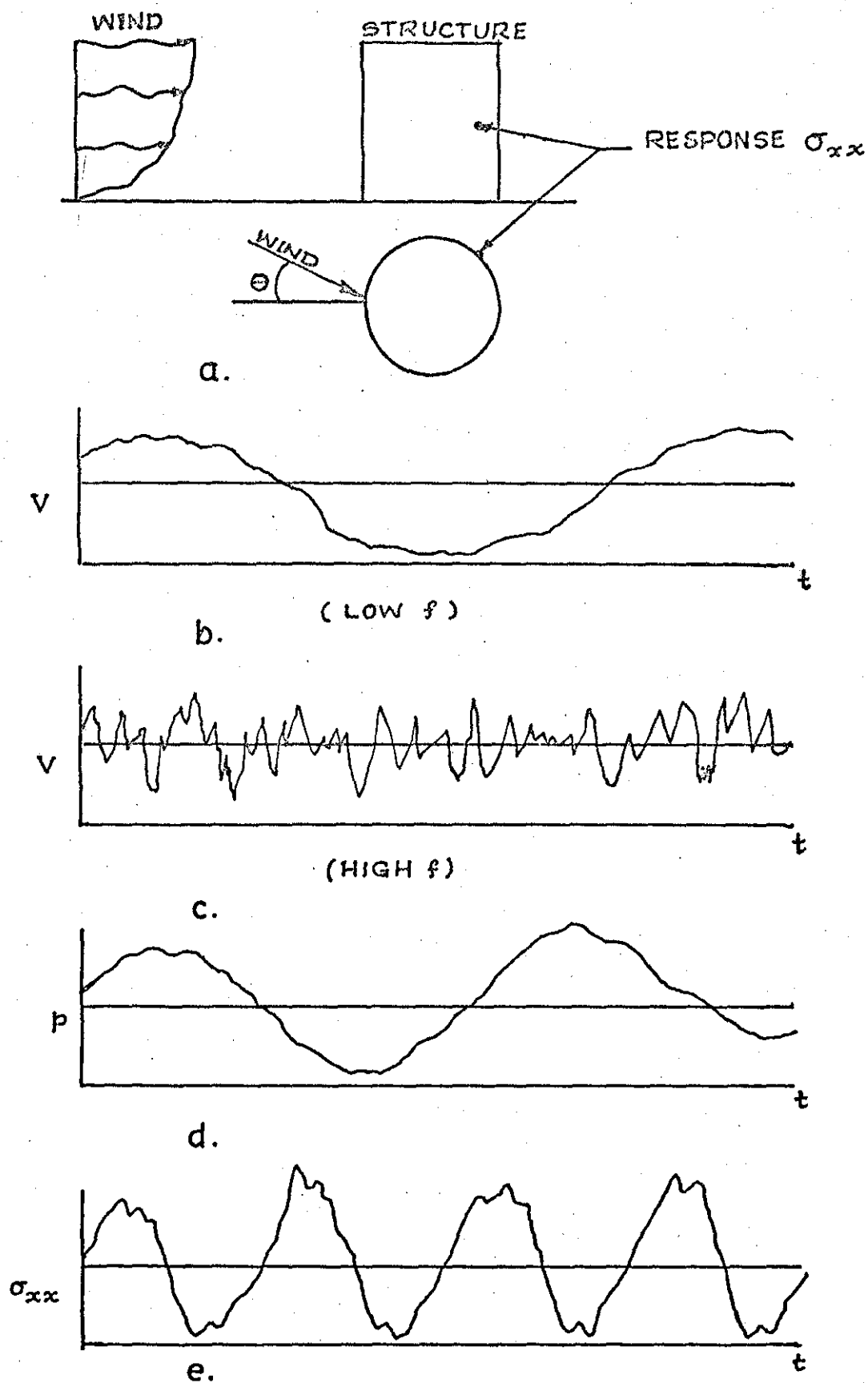
FIGURE 2·8 a. WIND-STRUCTURE CONFIGURATION
  b &c FREE WIND VARIATION - LOW & HIGH FREQUENCY
  d. LOCAL PRESSURE VARIATION
  e. RESPONSE
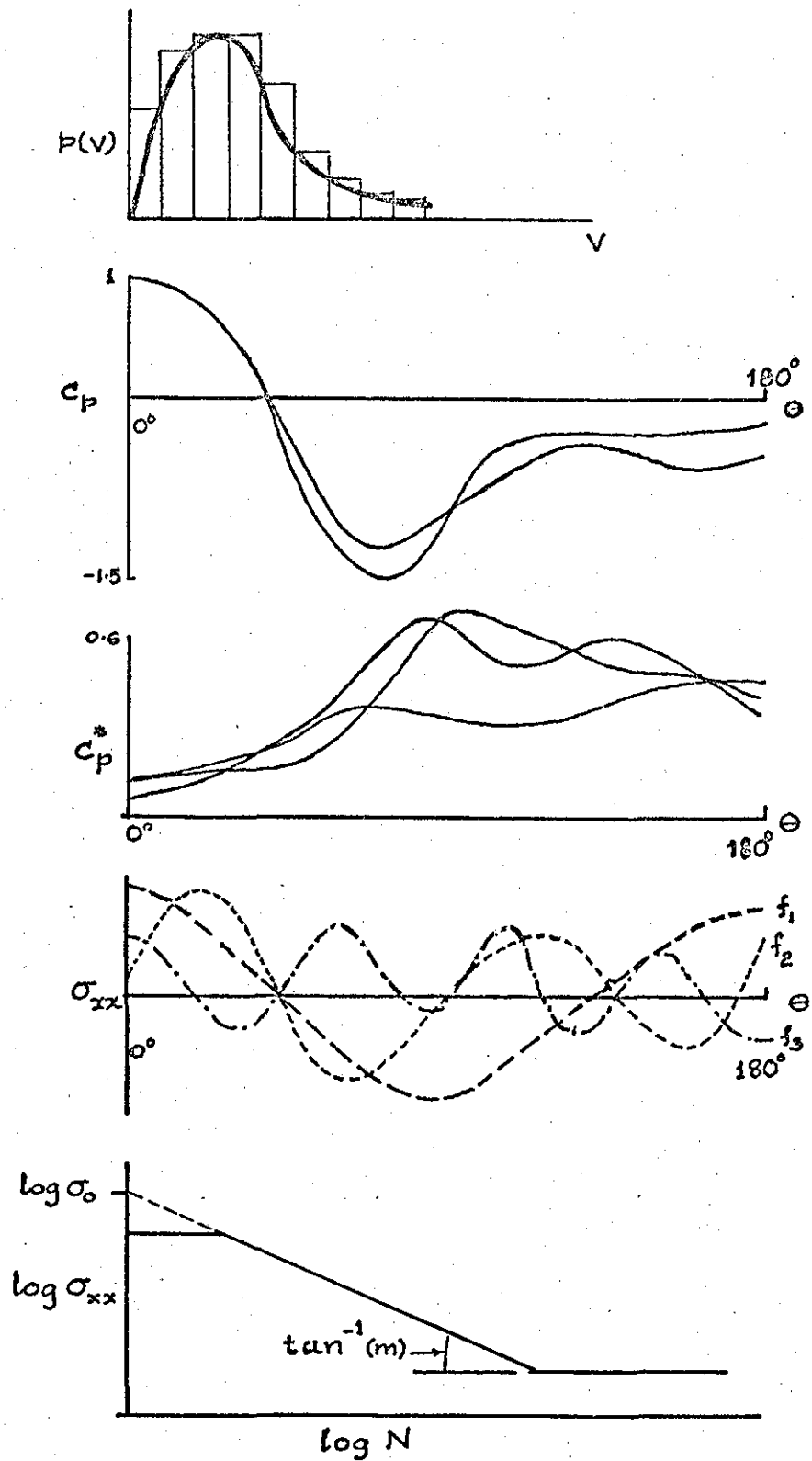
2·9 a PROBABILITY DENSITY OF WIND SPEED
     b MEAN PRESSURE COEFFICIENT c. RMS VALUE OF C_p
     d MODAL STRESS DISTRIBUTION
     e "S-N DIAGRAM"

FREE NON-LINEAR

FREE LINEAR

FORCED VIBRATIONS

AMPLITUDE C

f_n

f

$|C|$

f_n

f
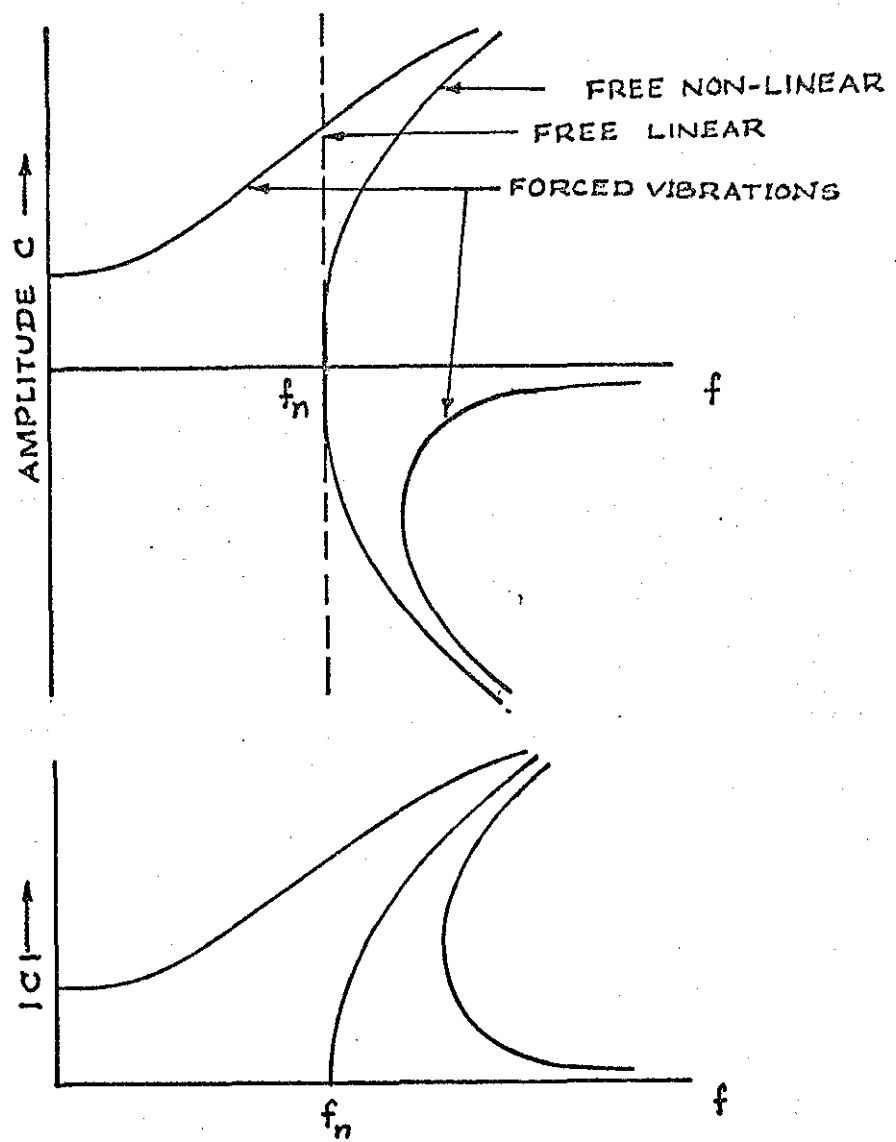
FIG. 3·1   SOLUTION   OF   CUBIC

$|C|$

FORCE

f_n

f
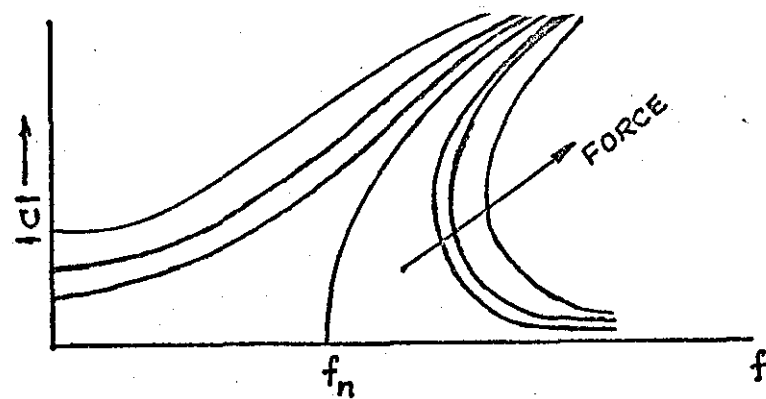
FIG. 3·2   RESPONSE   VARIATION   WITH   FORCE
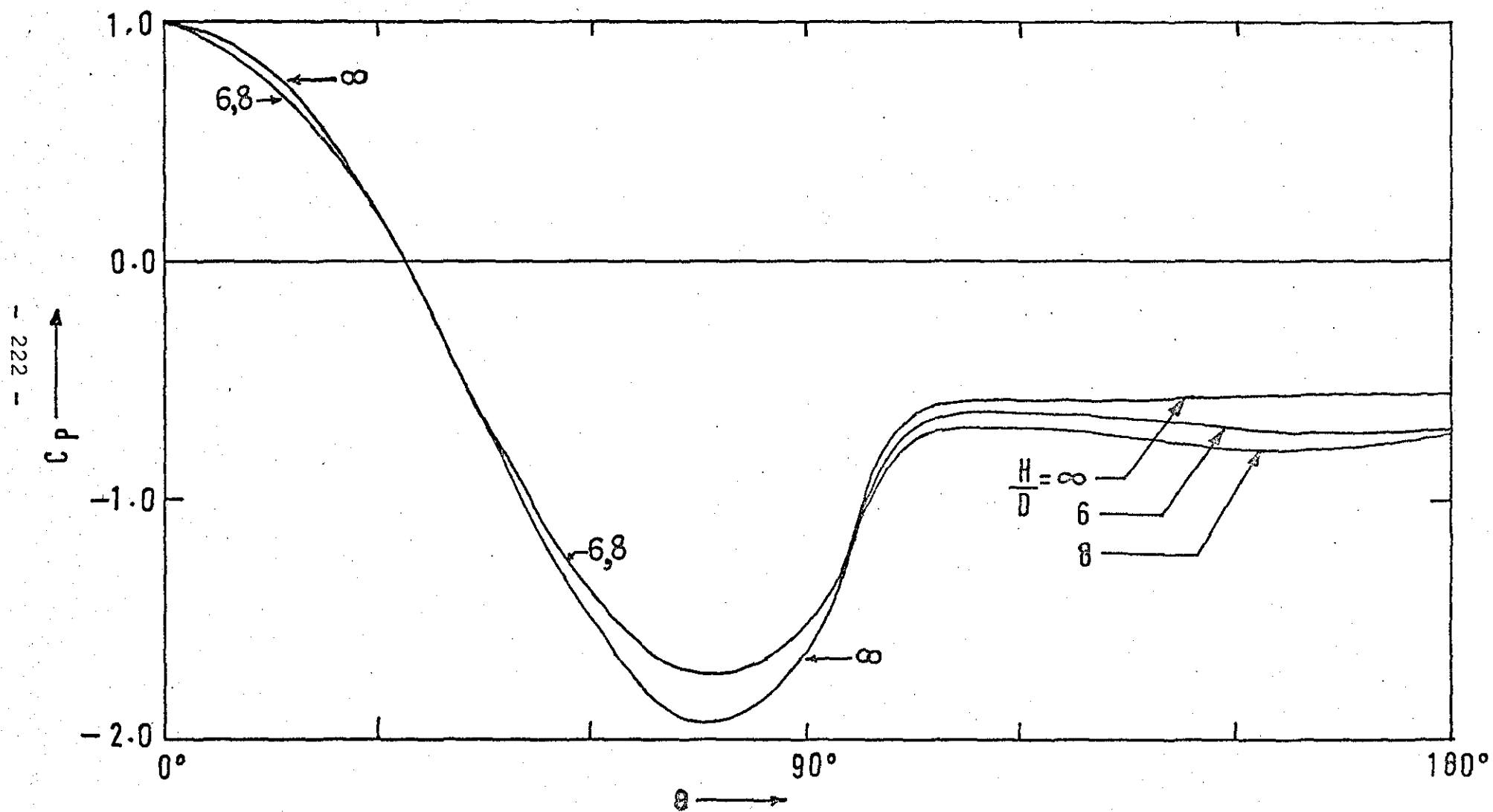
FIG. 6·1   MEAN   PRESSURE   COEFFICIENT   (Ref. 53)
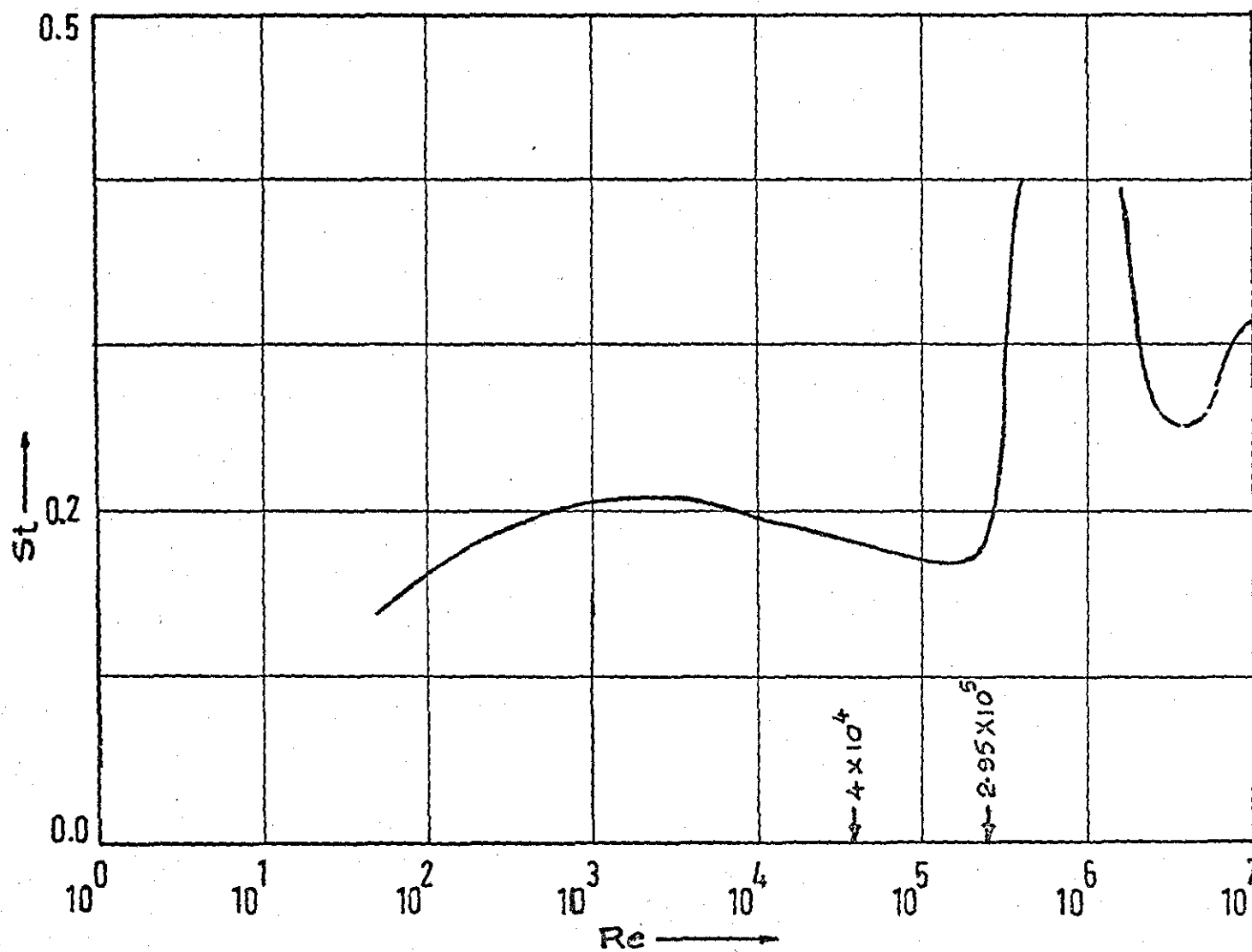
FIG. 6·2   VARIATION OF STROUHAL NUMBER WITH REYNOLDS NUMBER   (Ref. 60)
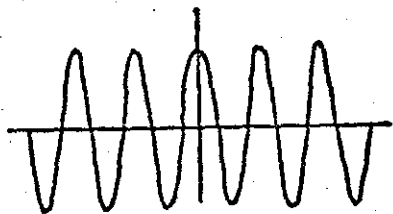
SINE WAVE
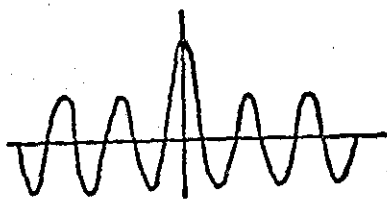
SINE WAVE + RANDOM
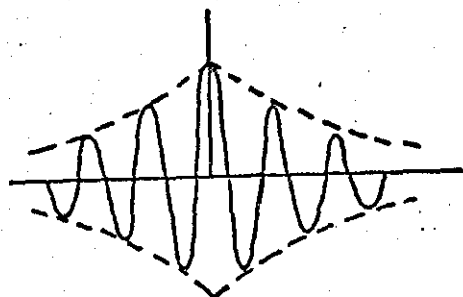
NARROW BAND RANDOM
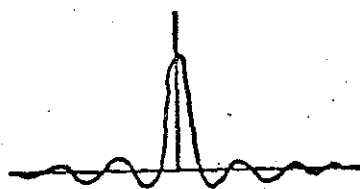
BROAD BAND RANDOM

FIGURE 6·3 TYPICAL AUTOCORRELATIONS
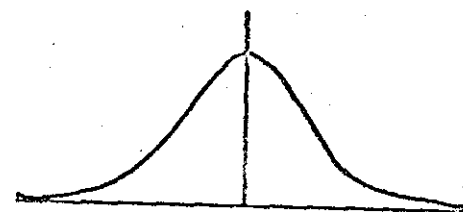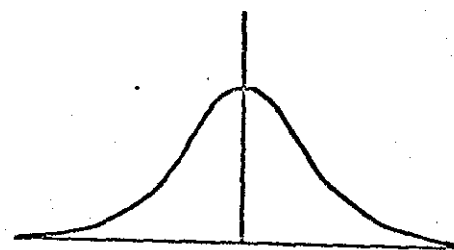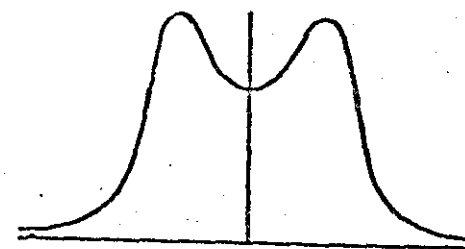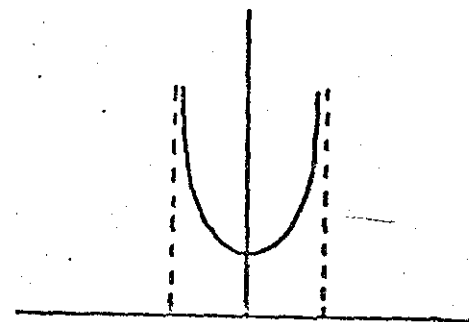
FIGURE 6·4 TYPICAL PROBABILITY DENSITIES
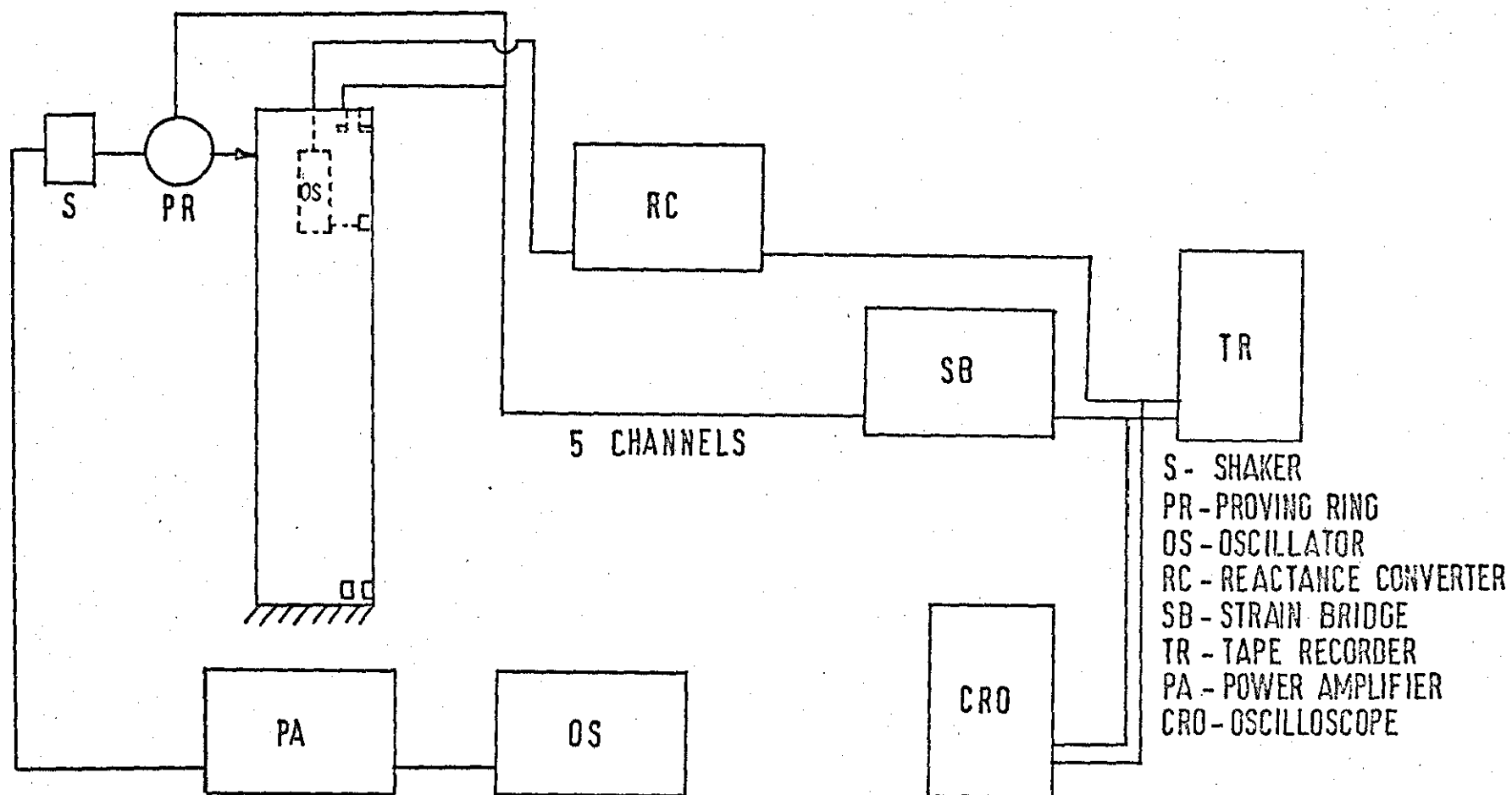
FIG. 7.1   EXPERIMENTAL SET UP FOR VIBRATIONS

S - SHAKER
PR - PROVING RING
OS - OSCILLATOR
RC - REACTANCE CONVERTER
SB - STRAIN BRIDGE
TR - TAPE RECORDER
PA - POWER AMPLIFIER
CRO - OSCILLOSCOPE

5 CHANNELS
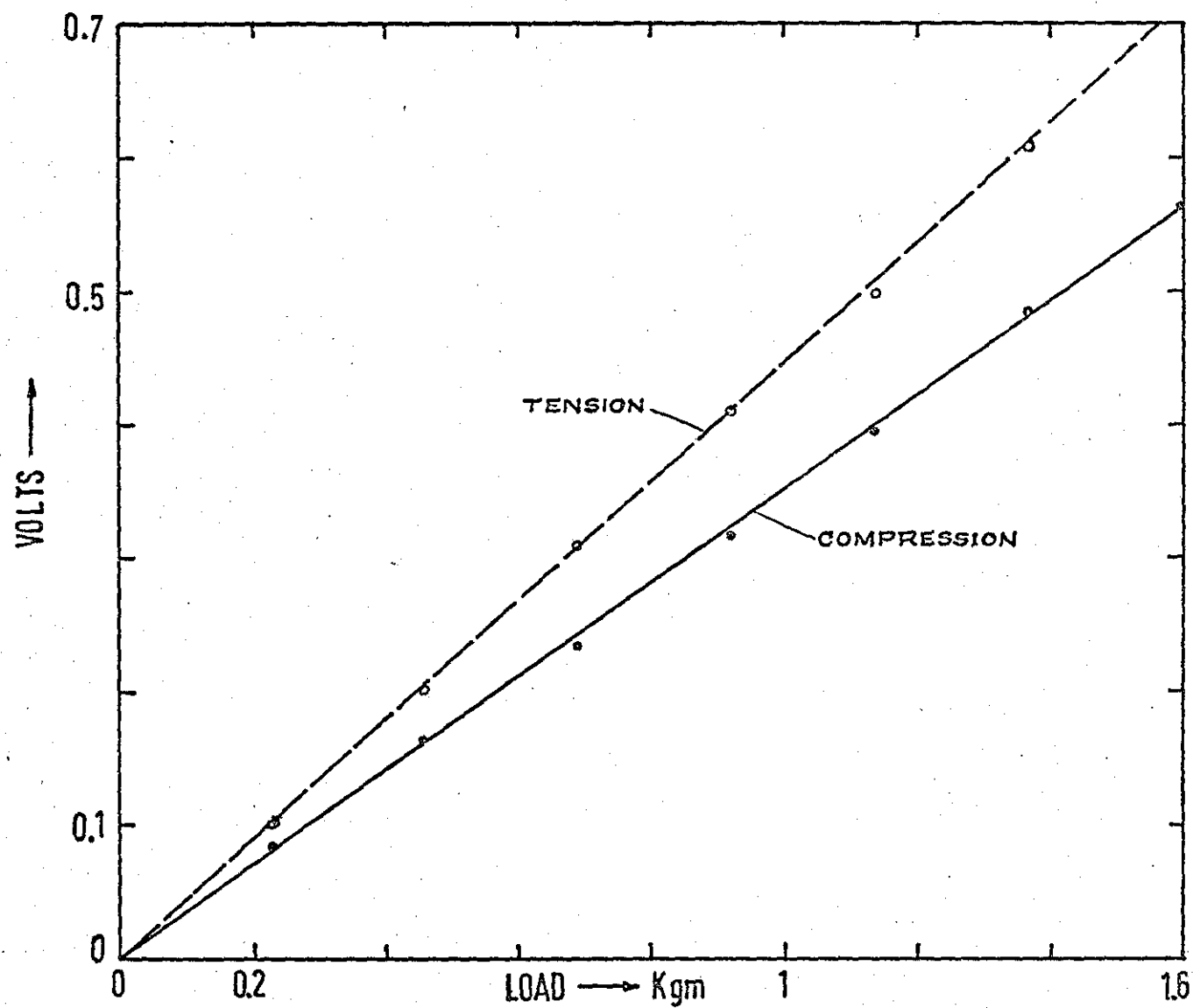
FIGURE 7·2   CALIBRATION OF PROVING RING.
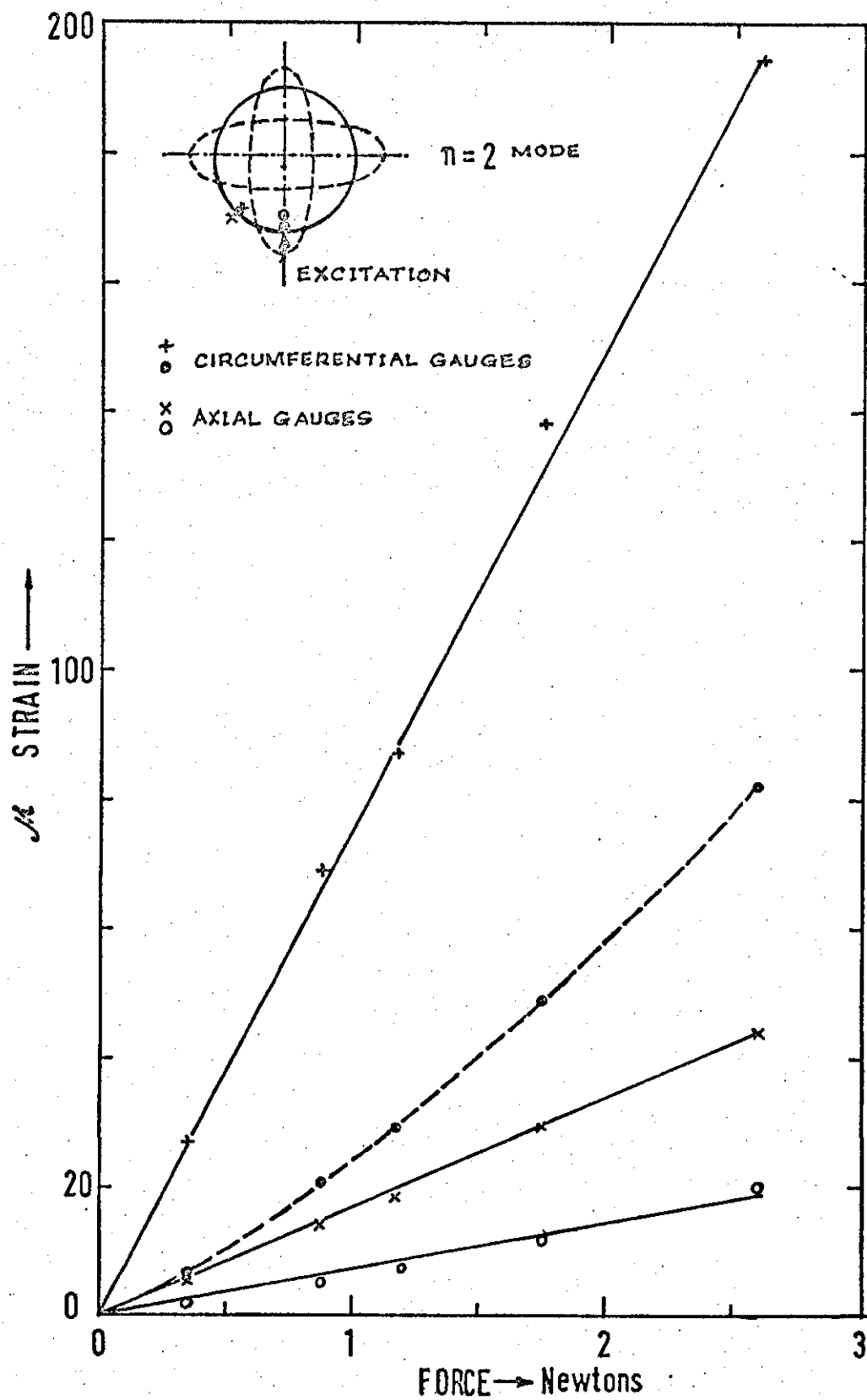
FIG.7.3   TYPICAL   FORCE – RESPONSE   PLOT   (SHELL F 5)
AT   32·5 Hz.
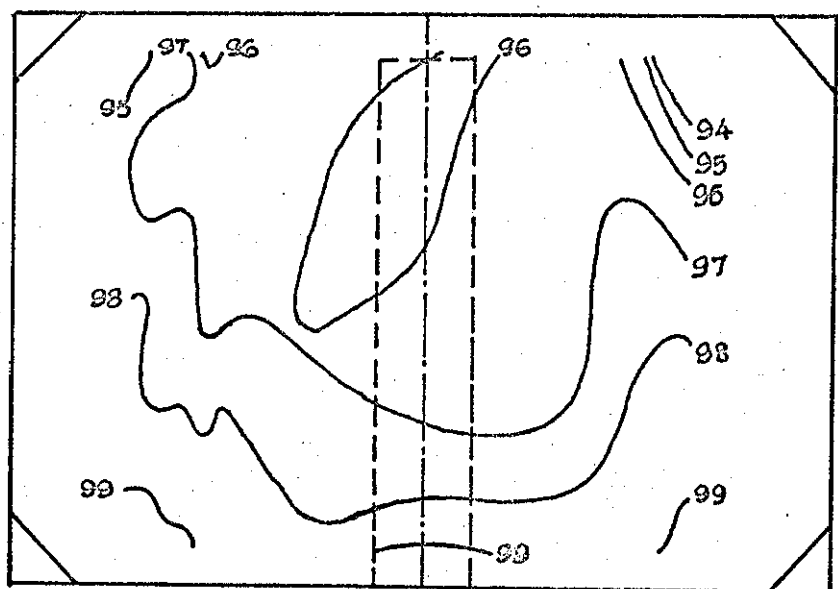
VELOCITY FT/SEC.
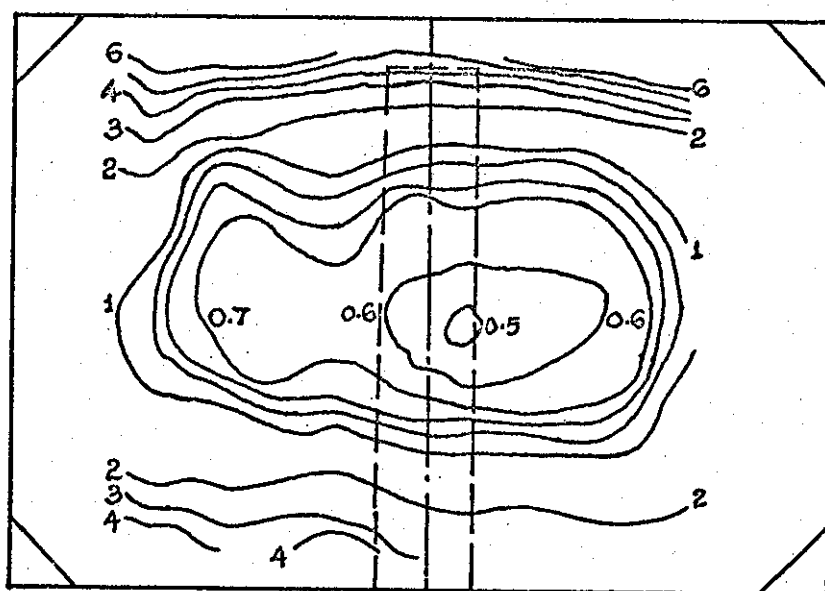
PERCENT TURBULENCE

FIG. 8·1a VELOCITY DISTRIBUTION & b. TURBULENCE
LEVELS AT APPROXIMATE MODEL LOCATION
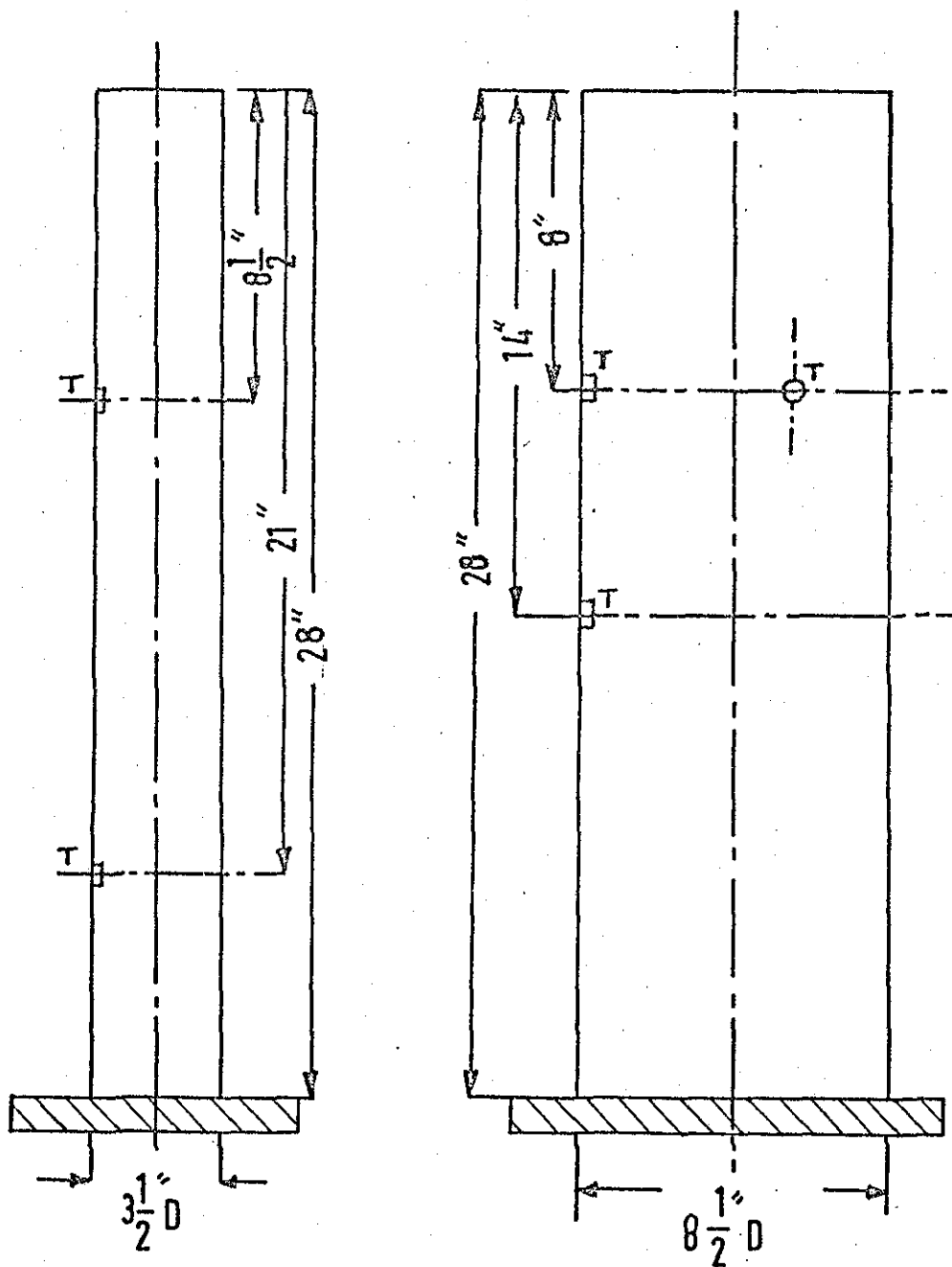
T - Location of pressure transducers

FIG. 8·2   DETAILS OF MODELS
                (LOW AR MODELS)
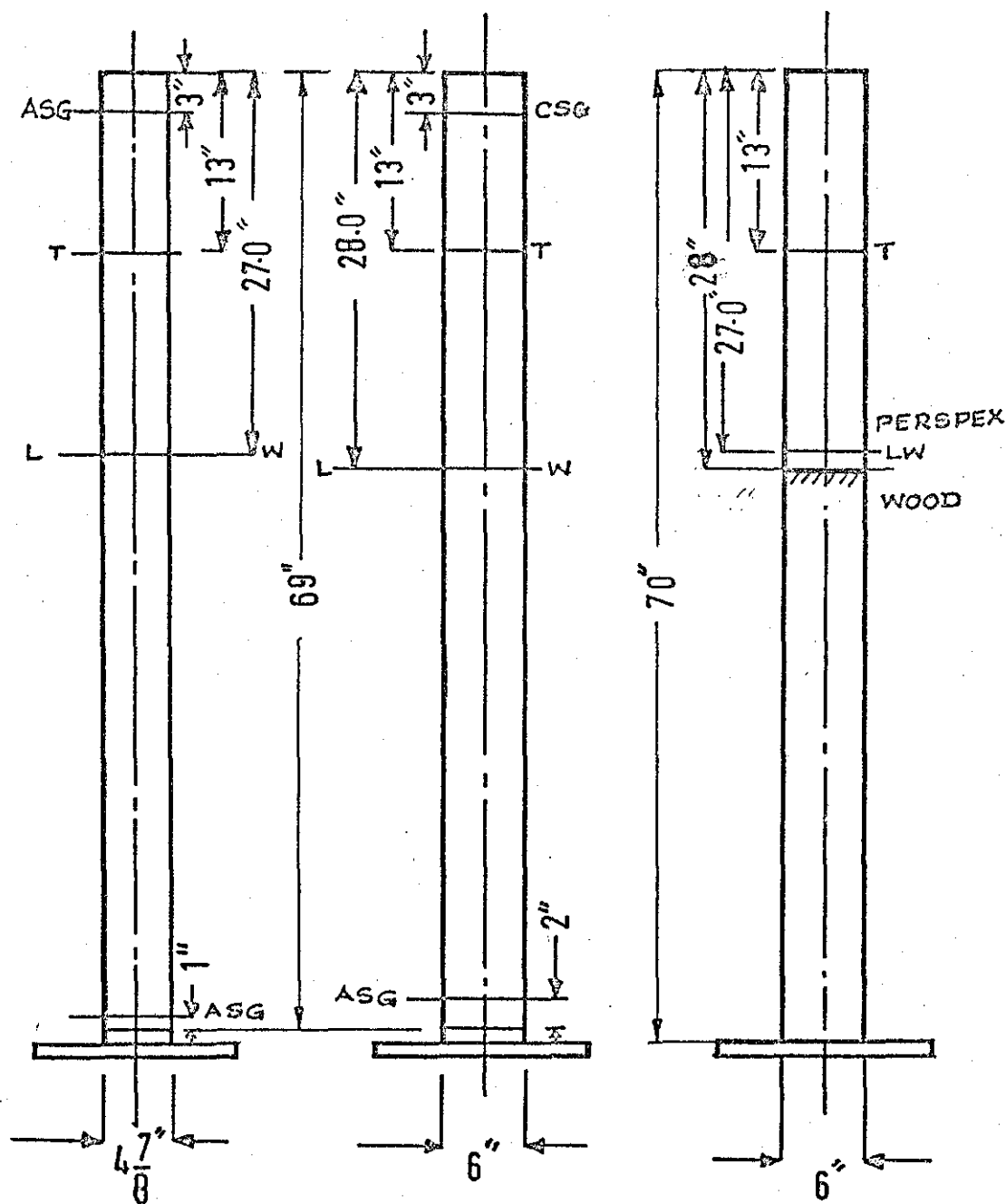
LW – Lower Wall of the Wind Tunnel
T – Pressure Transducer Location
ASG – Axial Strain Gauge Location
CSG – Circumferential Strain Gauge Location

FIG. 8·2   DETAILS   MODELS (CONT'D)   HIGH A R MODELS
a & b flexible, c rigid.

WT — WIND TUNNEL
T   — TRANSDUCER
SG — STRAIN GAUGES
RC — REACTANCE CONVERTER
DCA — DIGITAL AMMETER
CRO — OSCILLOSCOPE
TR — TAPE RECORDER
SB — STRAIN BRIDGE
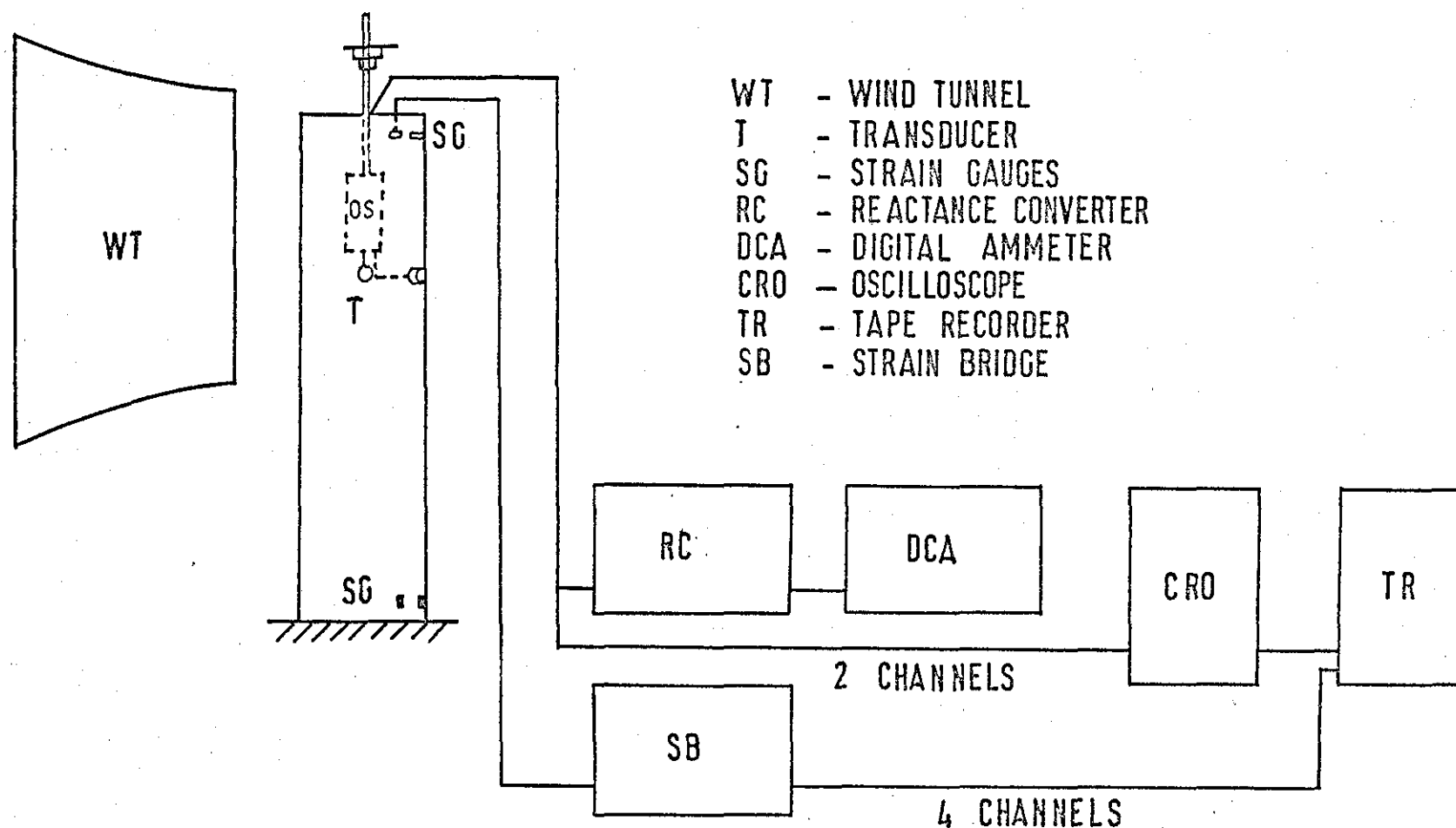
FIG. 8.3   EXPERIMENTAL SET - UP FOR WIND EXCITATION

FIG. 8.4 MICROPHONE

B- Back pressure tapping
D- Diaphragm
I - Insulator
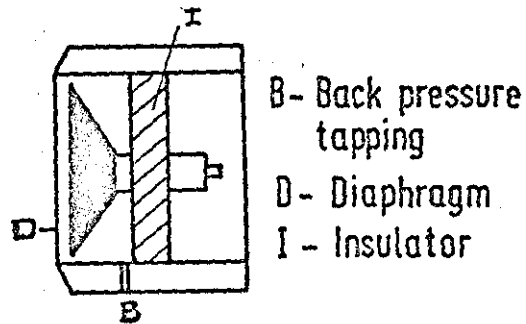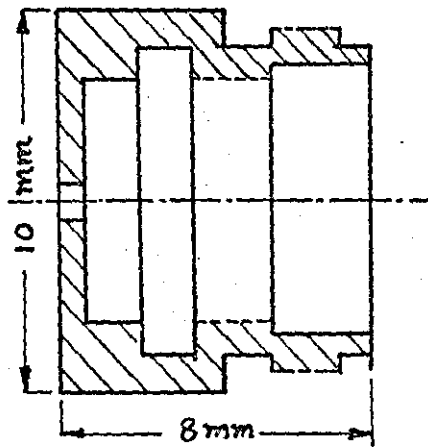
FIG.8.5 MODIFIED PROTECTIVE CAP
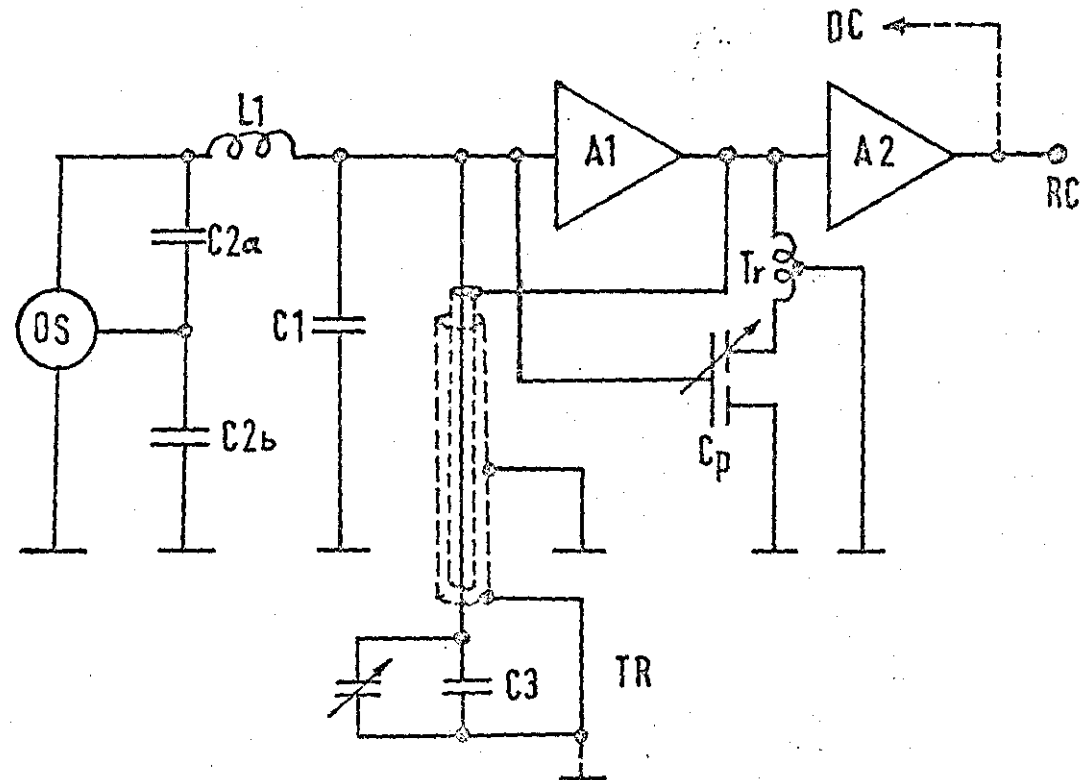
OS Clapp oscillator
TR Transducer
RC Reactance converter

FIG.8.6 OSCILLATOR CIRCUIT DIAGRAM
(Ref. DISA MANUAL)
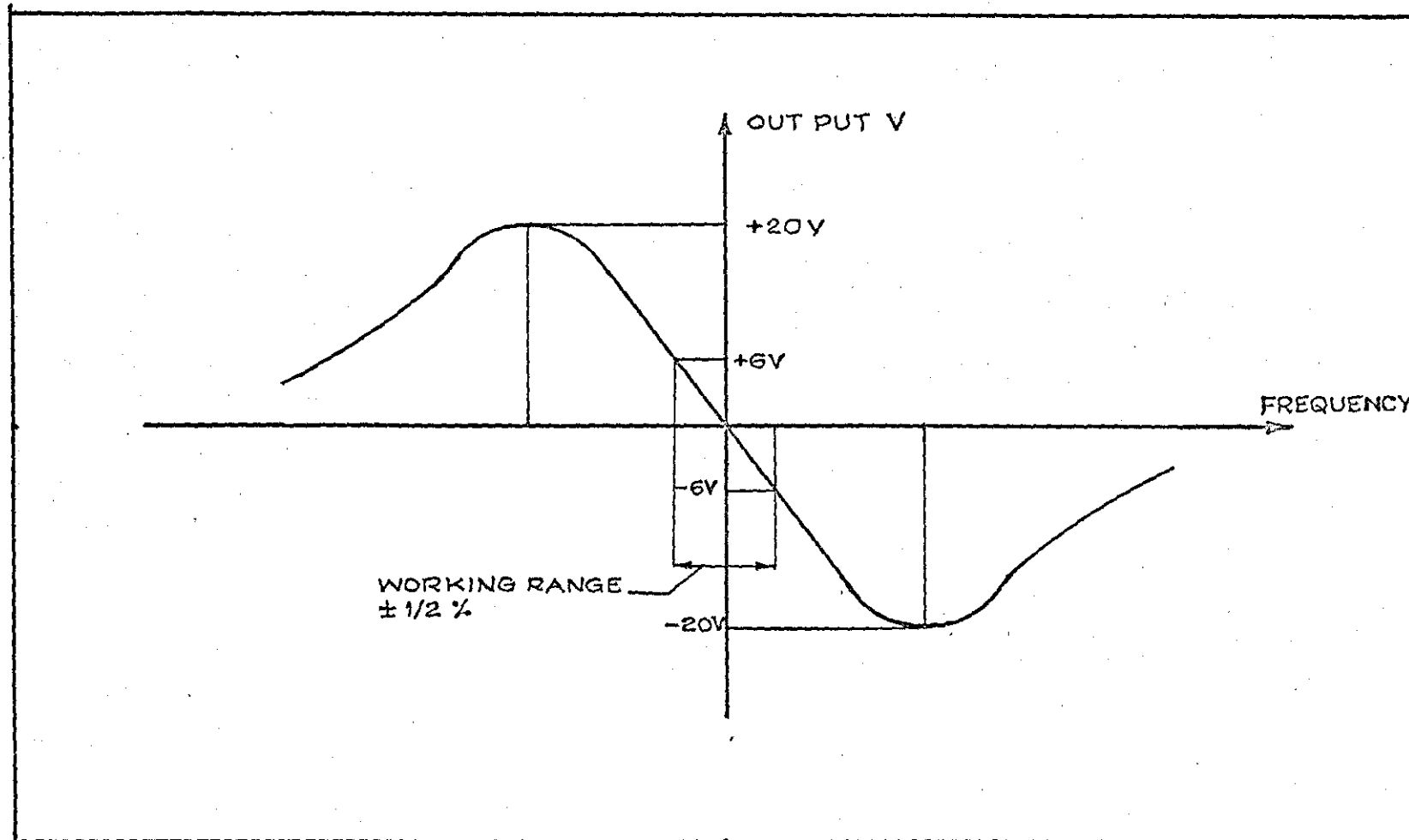
FIGURE 8·7   WORKING RANGE OF REACTANCE CONVERTER   (REF. DISA MANUAL)
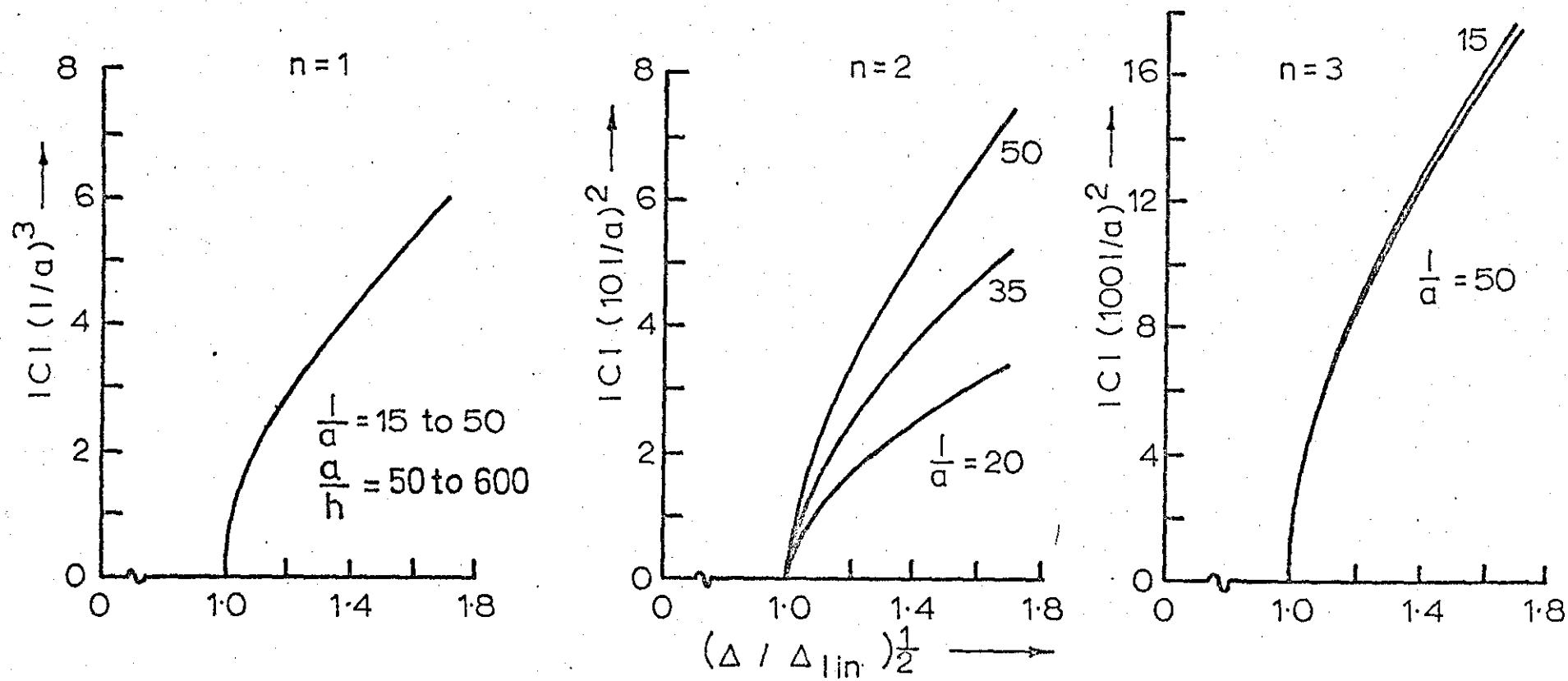
FIG.9.1   UNDAMPED   FREQUENCY - FREE   AMPLITUDE   VARIATION.   a/h = 250, m = 1.
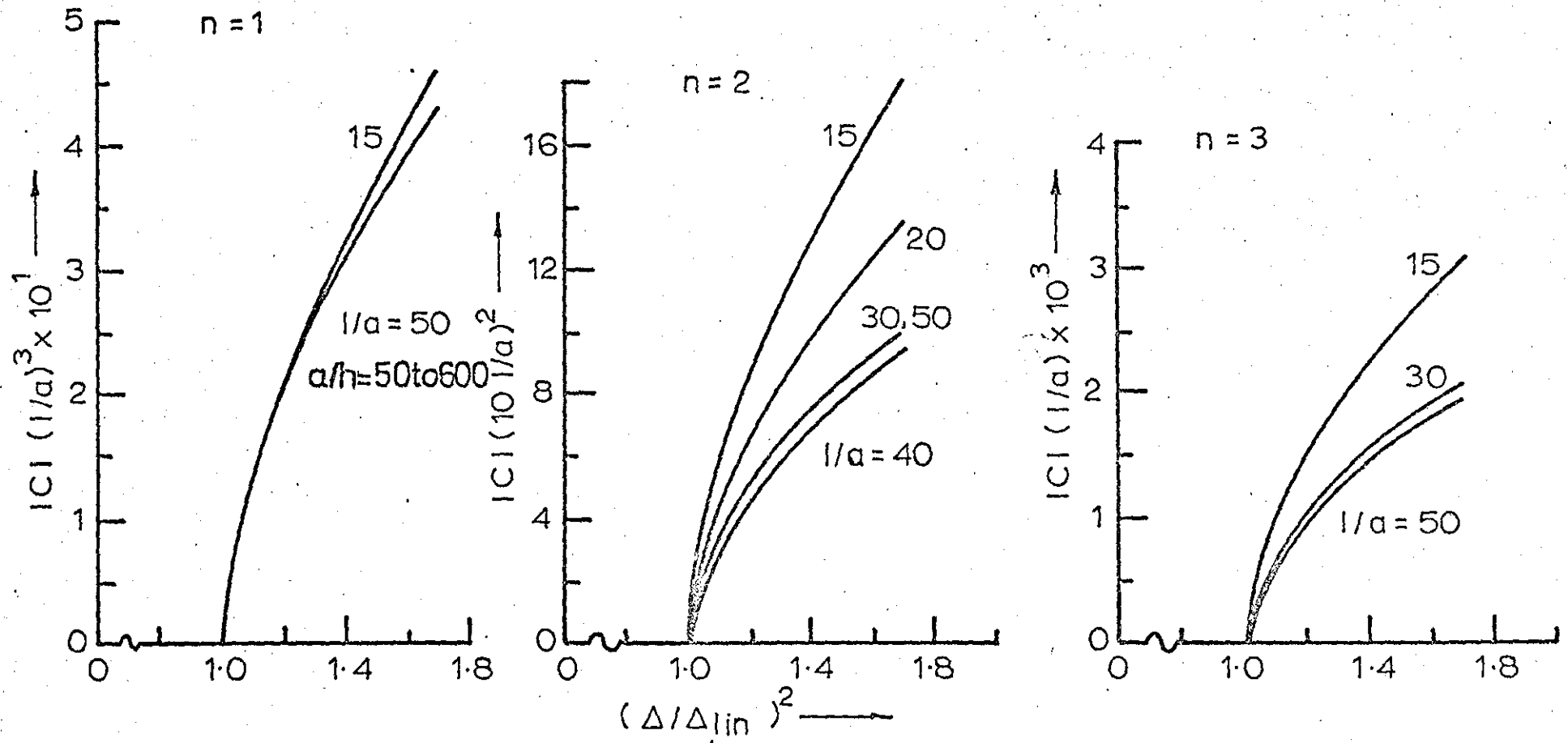
FIG.9.2. UNDAMPED FREQUENCY – FREE AMPLITUDE VARIATION. a/h = 250, m = 2.
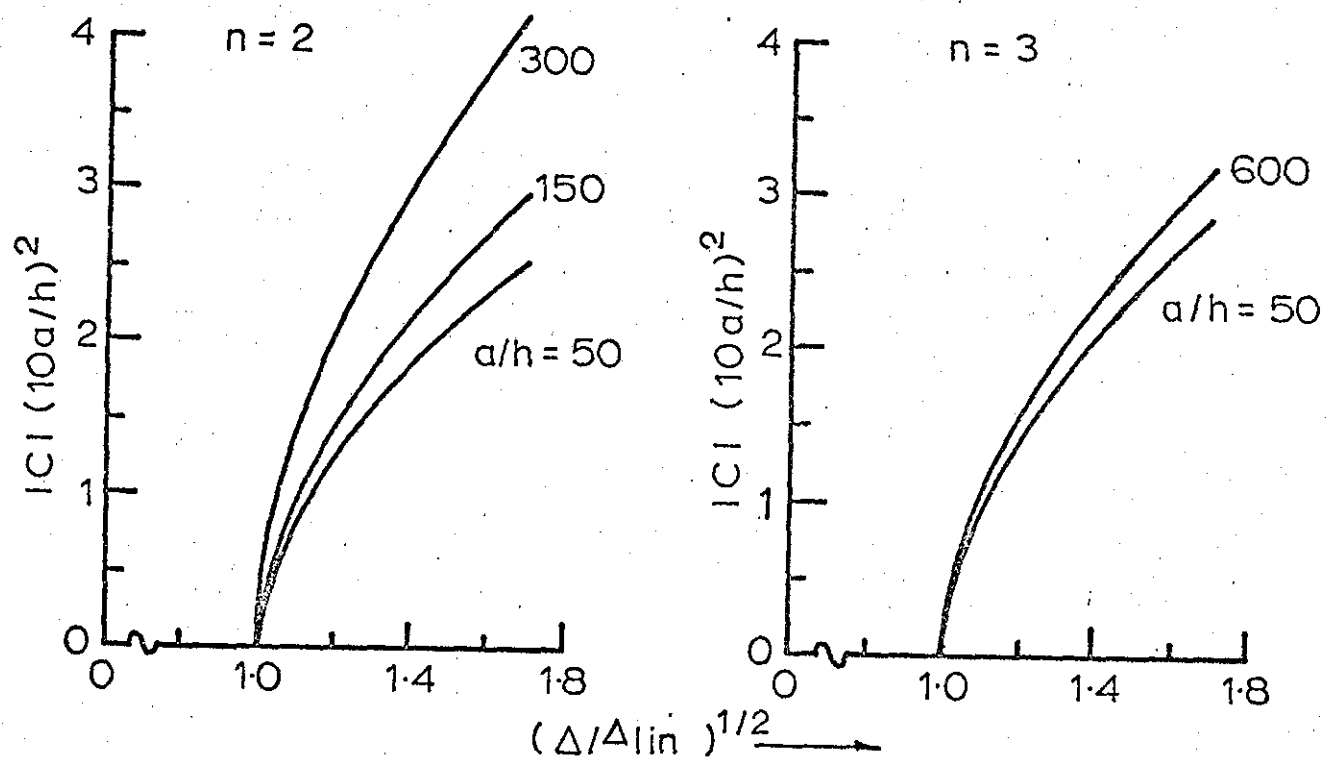
FIG.9.3   UNDAMPED   FREQUENCY – FREE   AMPLITUDE   VARIATION.

$l/a = 15$, $m = 1$
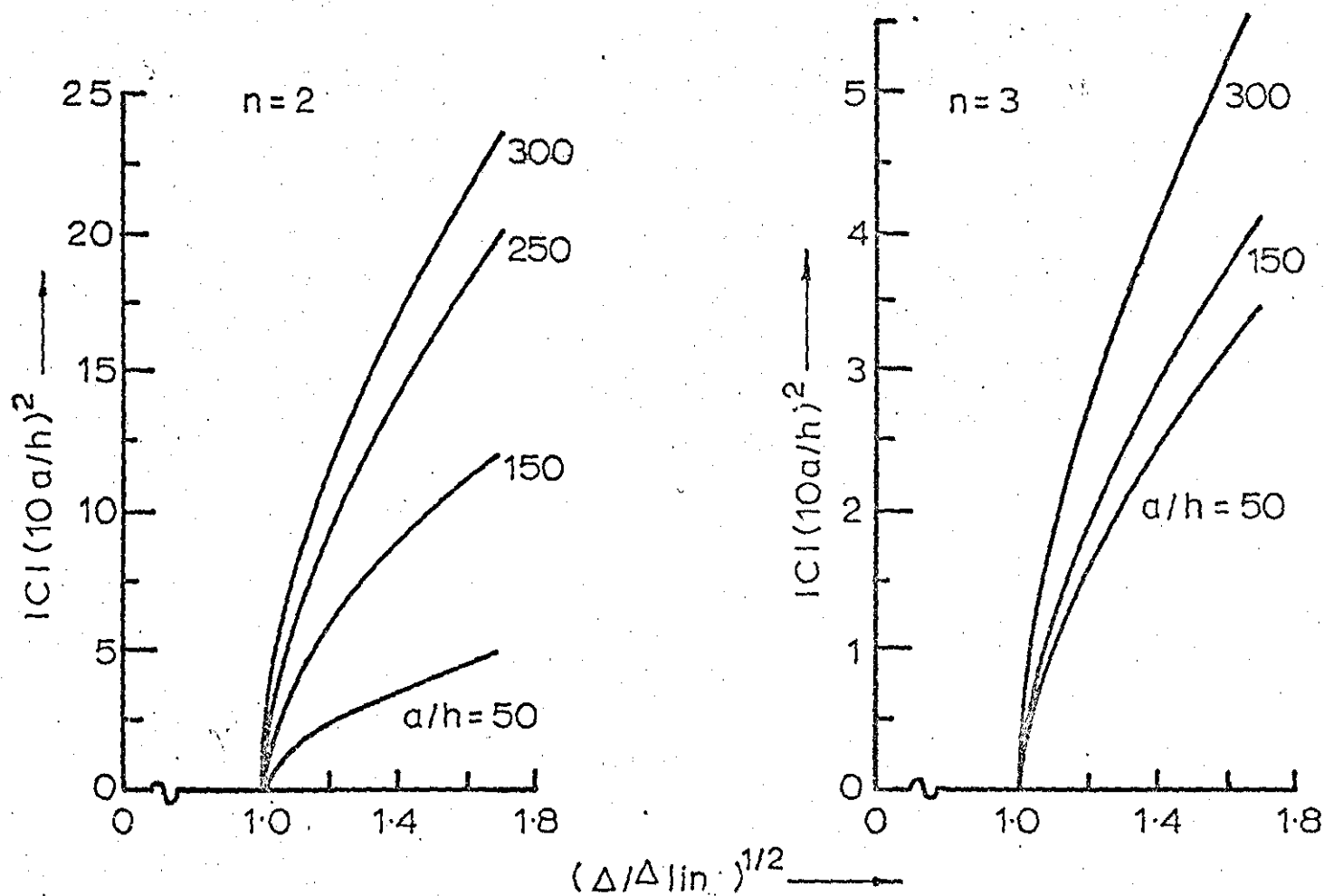
FIG.9.4 UNDAMPED FREQUENCY - FREE AMPLITUDE VARIATION.

$l/a = 15$, $m = 2$
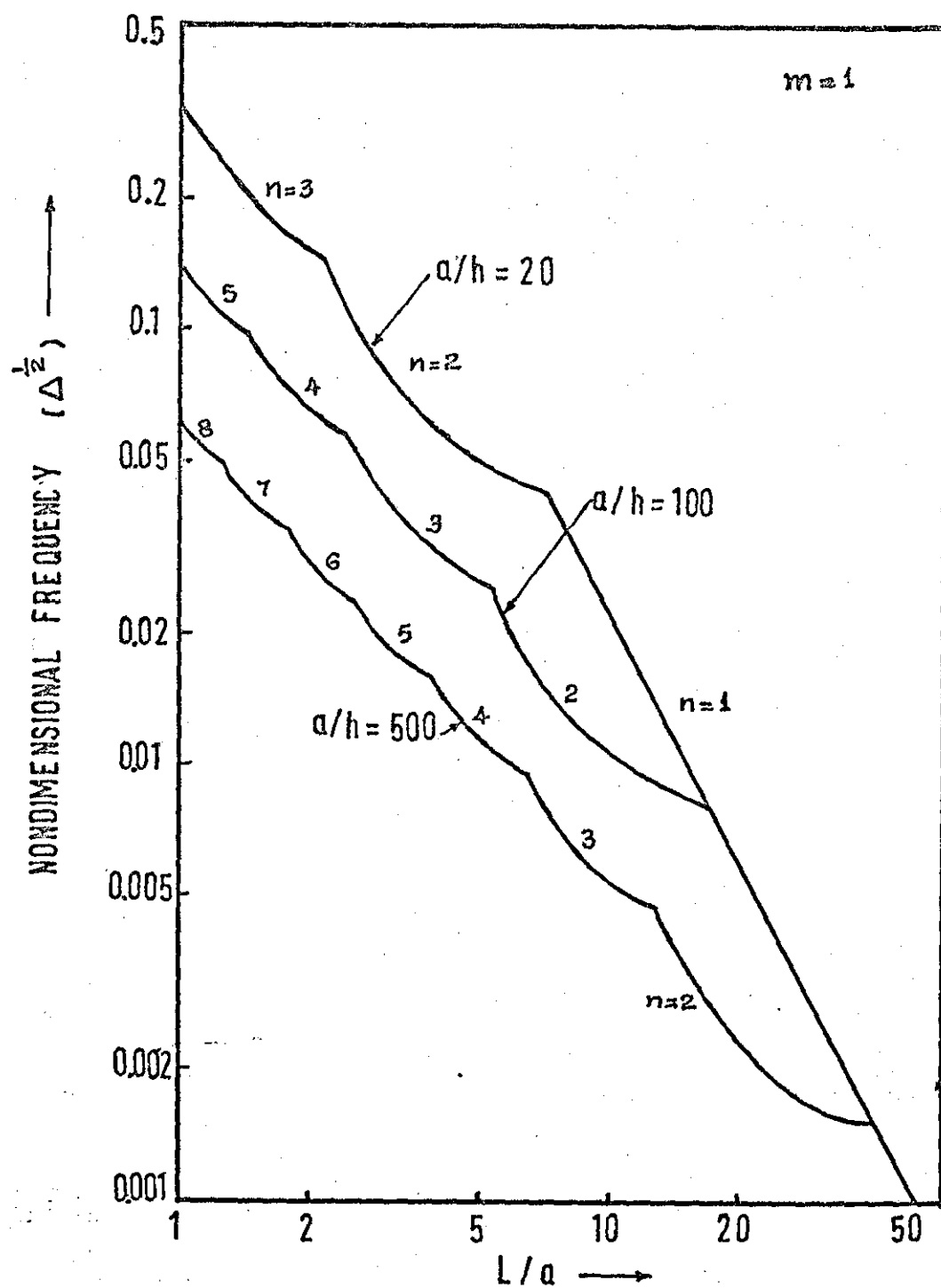
FIG.9.5   FREQUENCY ENVELOPE
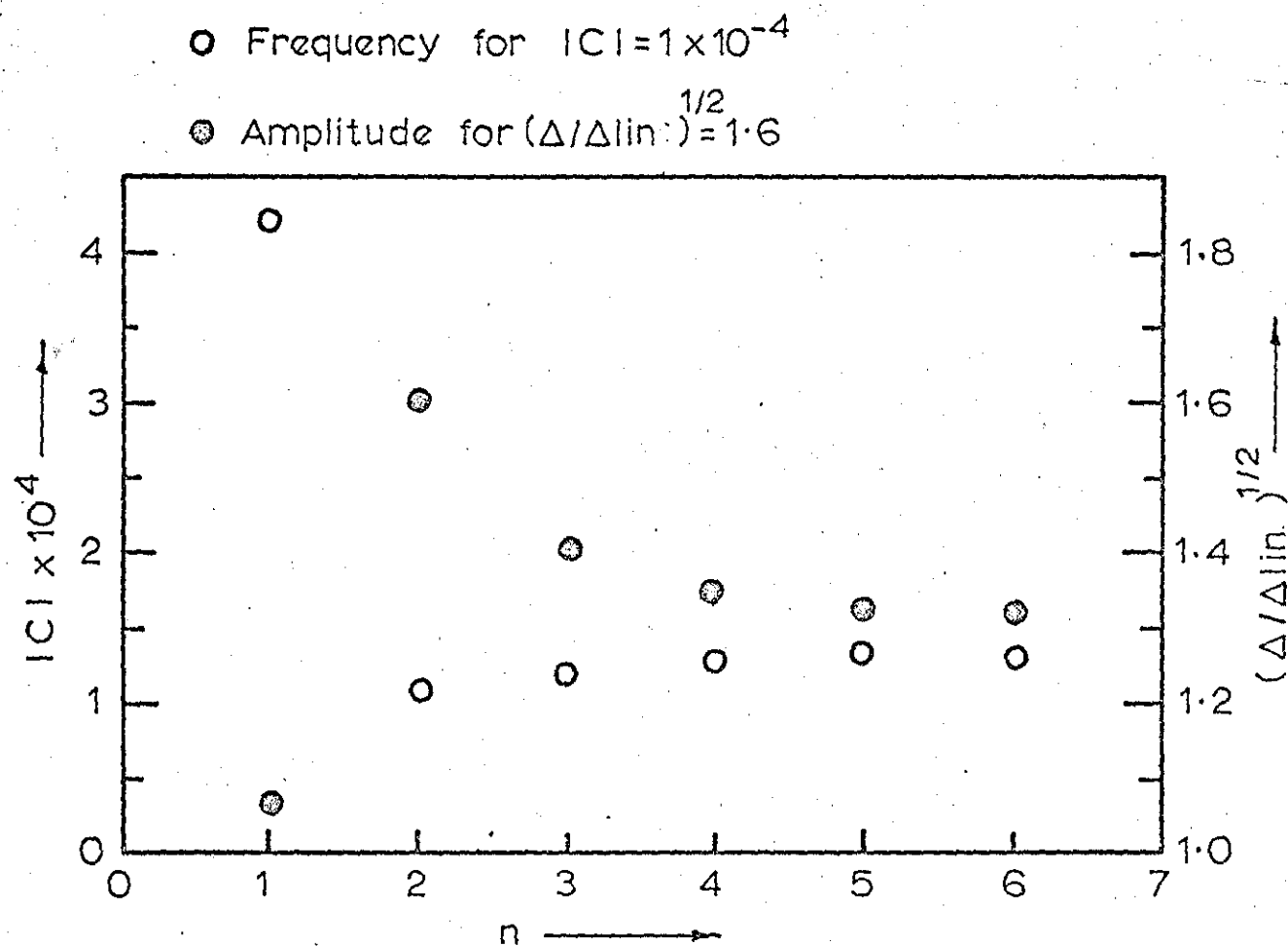
FIG.9,6. AMPLITUDE AND FREQUENCY DISTRIBUTION

l/a = 20 , a/h = 250, m=1
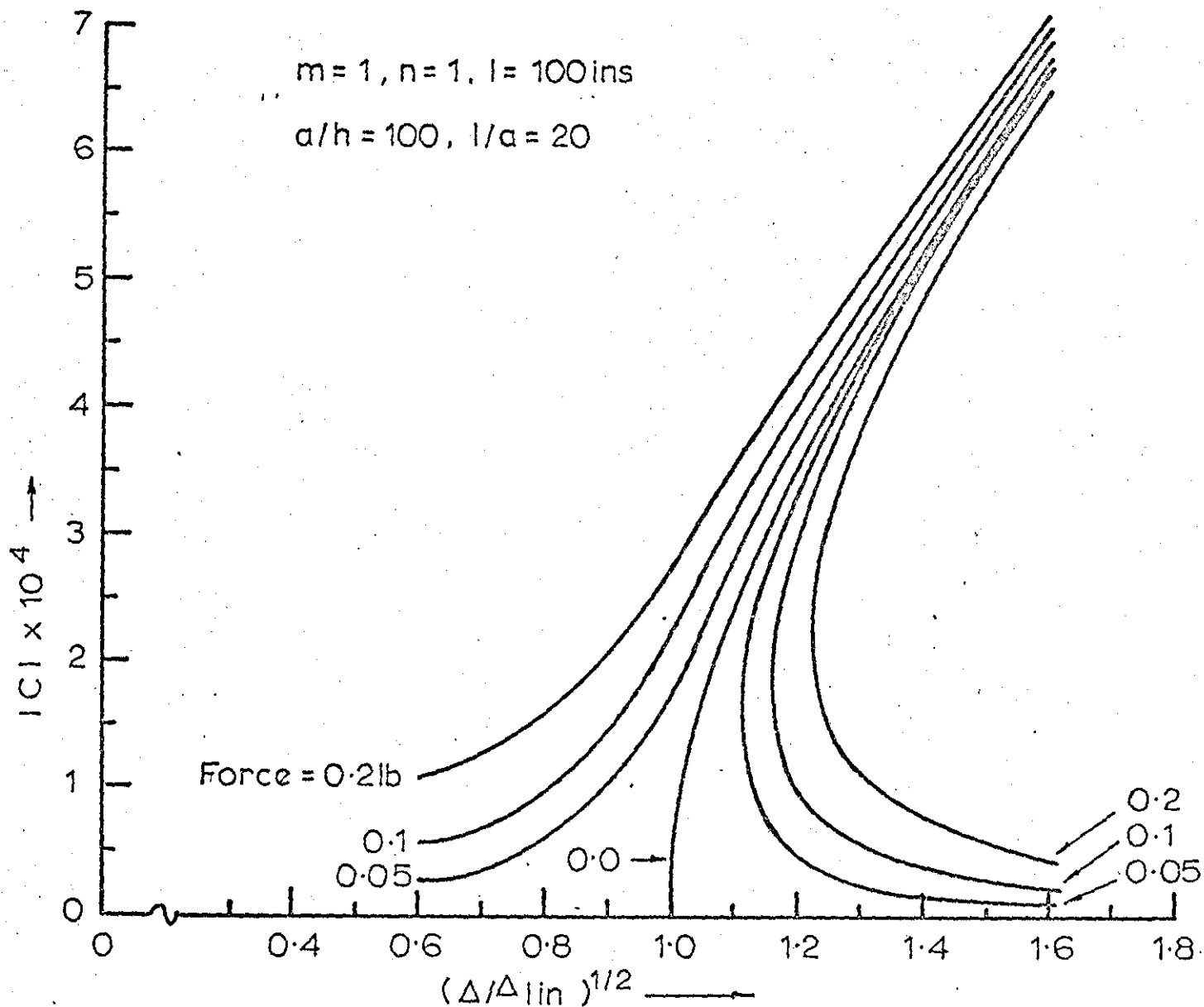
FIG.9.7 AMPLITUDE – FREQUENCY VARIATION FOR VARIOUS FORCE INPUT.
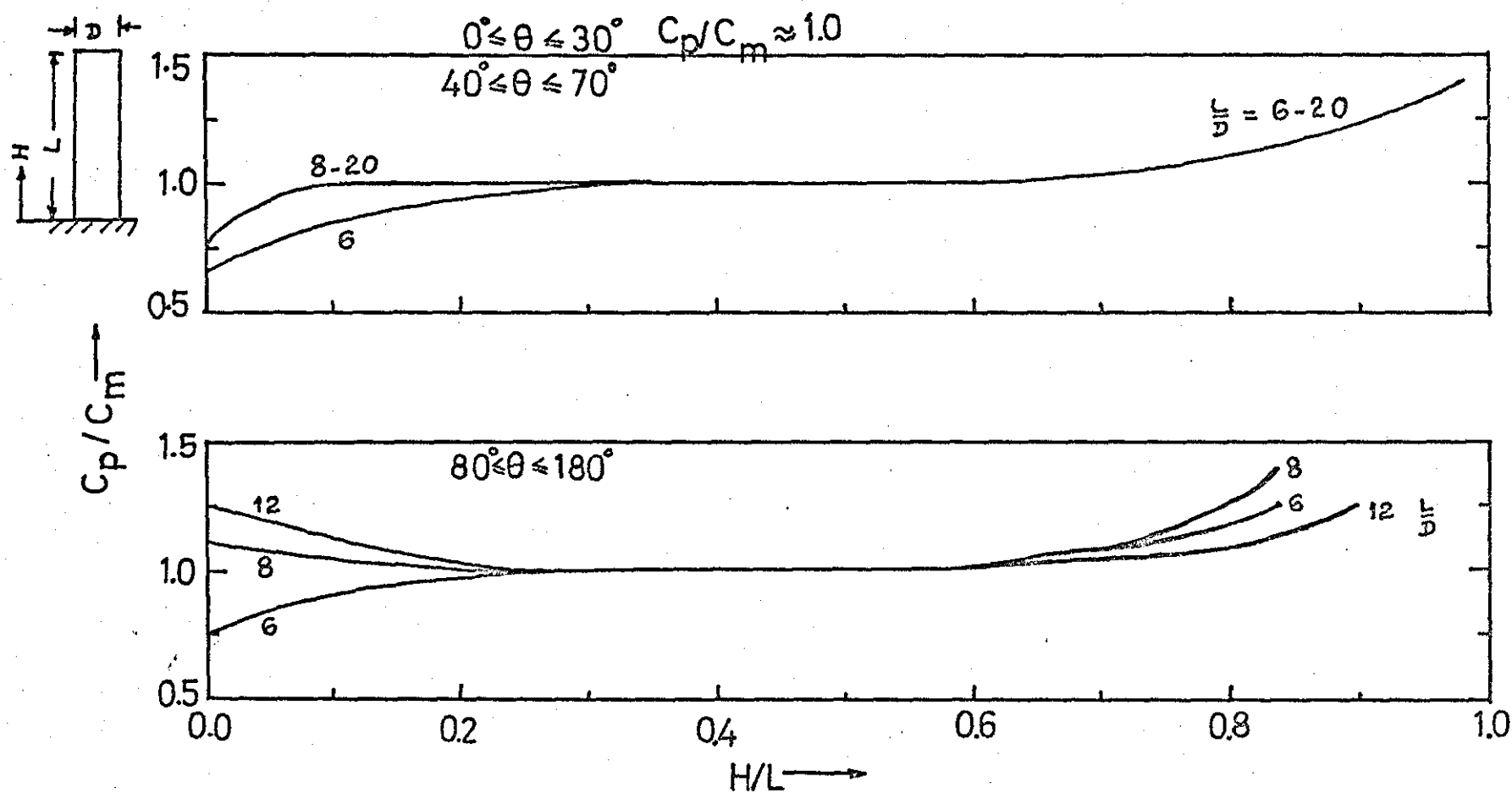
FIG 10.1   PRESSURE DISTRIBUTION AWAY FROM THE TOP (REF. 53)
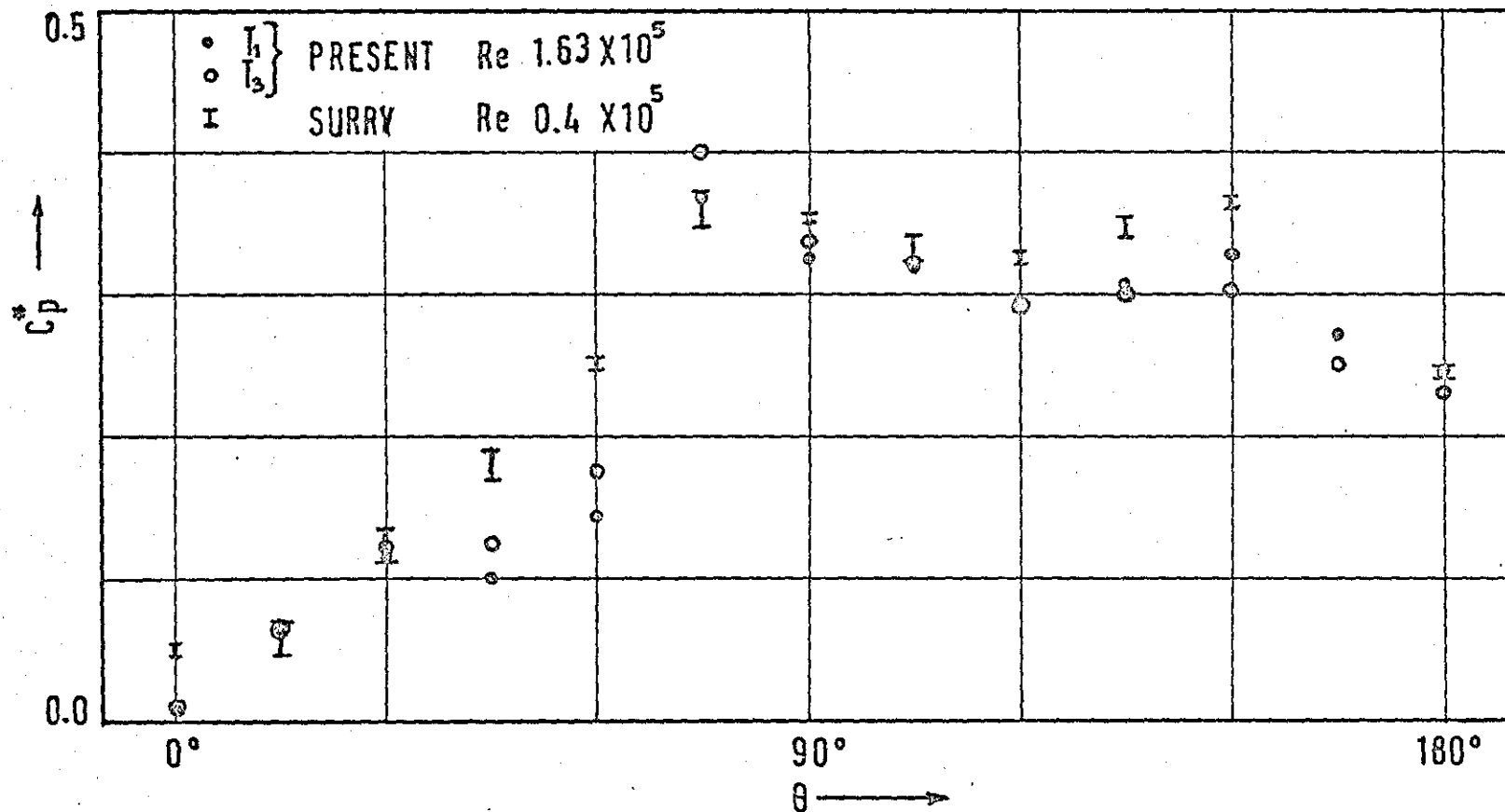
FIG. 10-2   RMS   PRESSURE   COEFFICIENT   (RUN 6, 2-D)
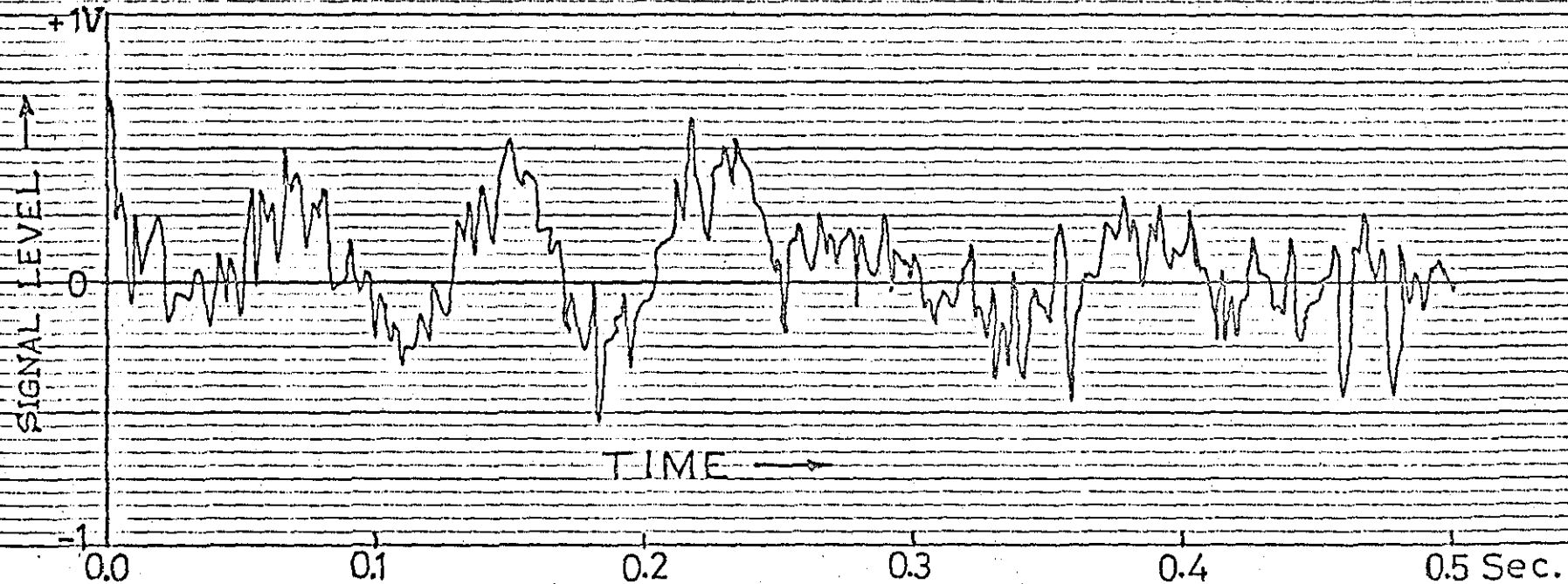
FIG 10.3   TYPICAL   PRESSURE   SIGNAL.
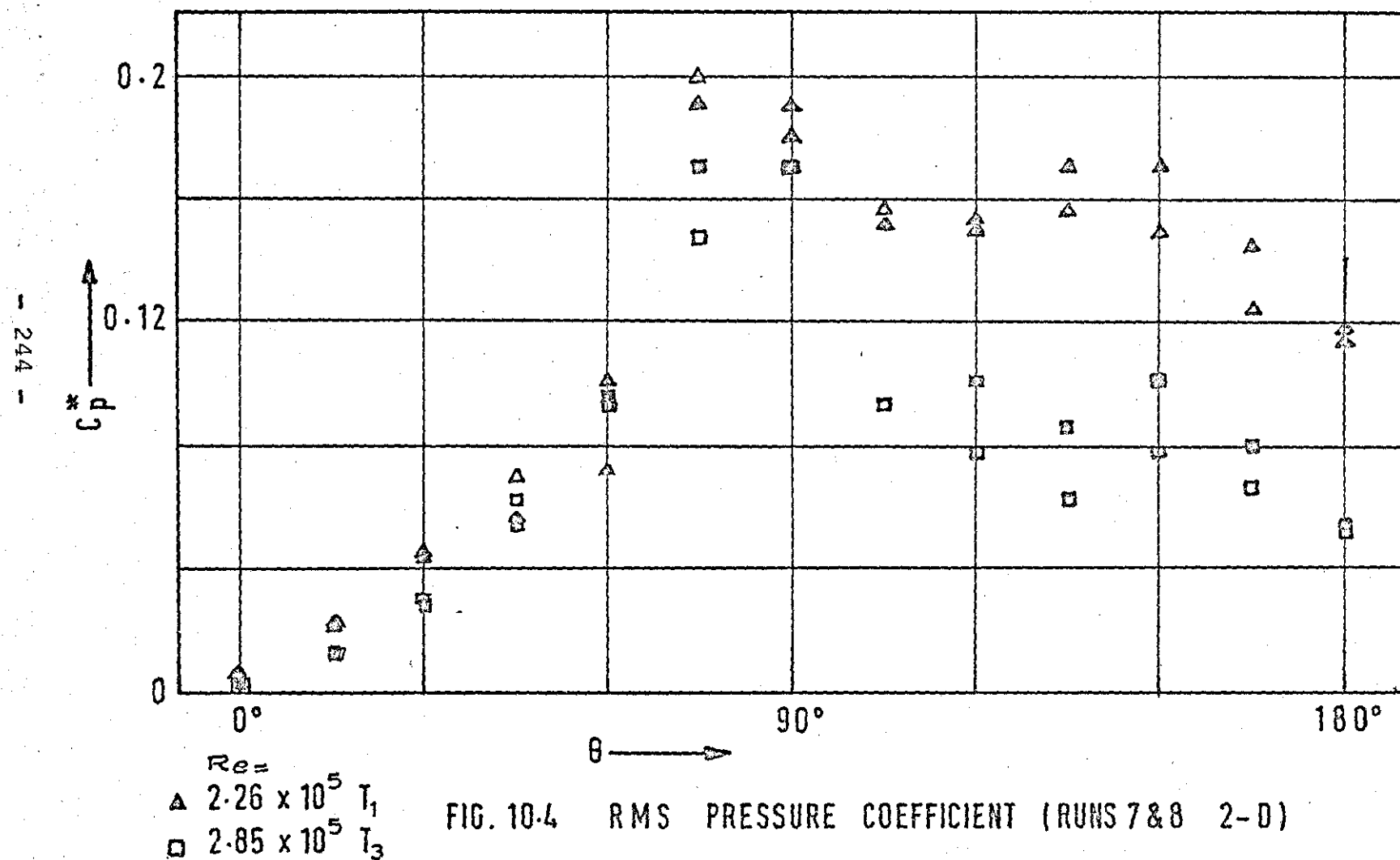
FIG. 10.4   RMS   PRESSURE   COEFFICIENT   (RUNS 7&8   2-D)

$Re=$
△ 2.26×10^5 T_1
□ 2.85×10^5 T_3

- 244 -

FIG.10·5   R M S   PRESSURE COEFFICIENT   (RUNS 1,2)
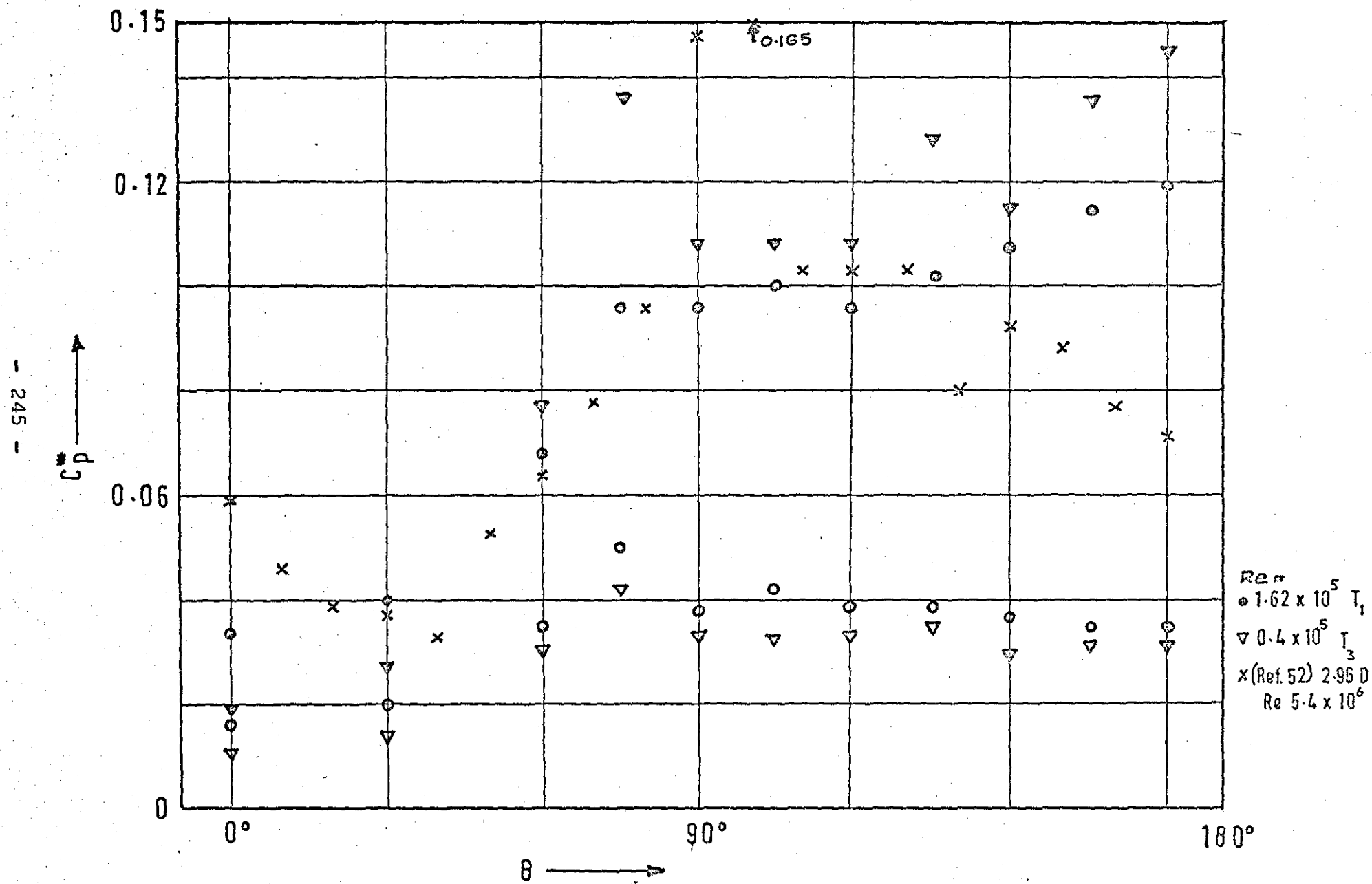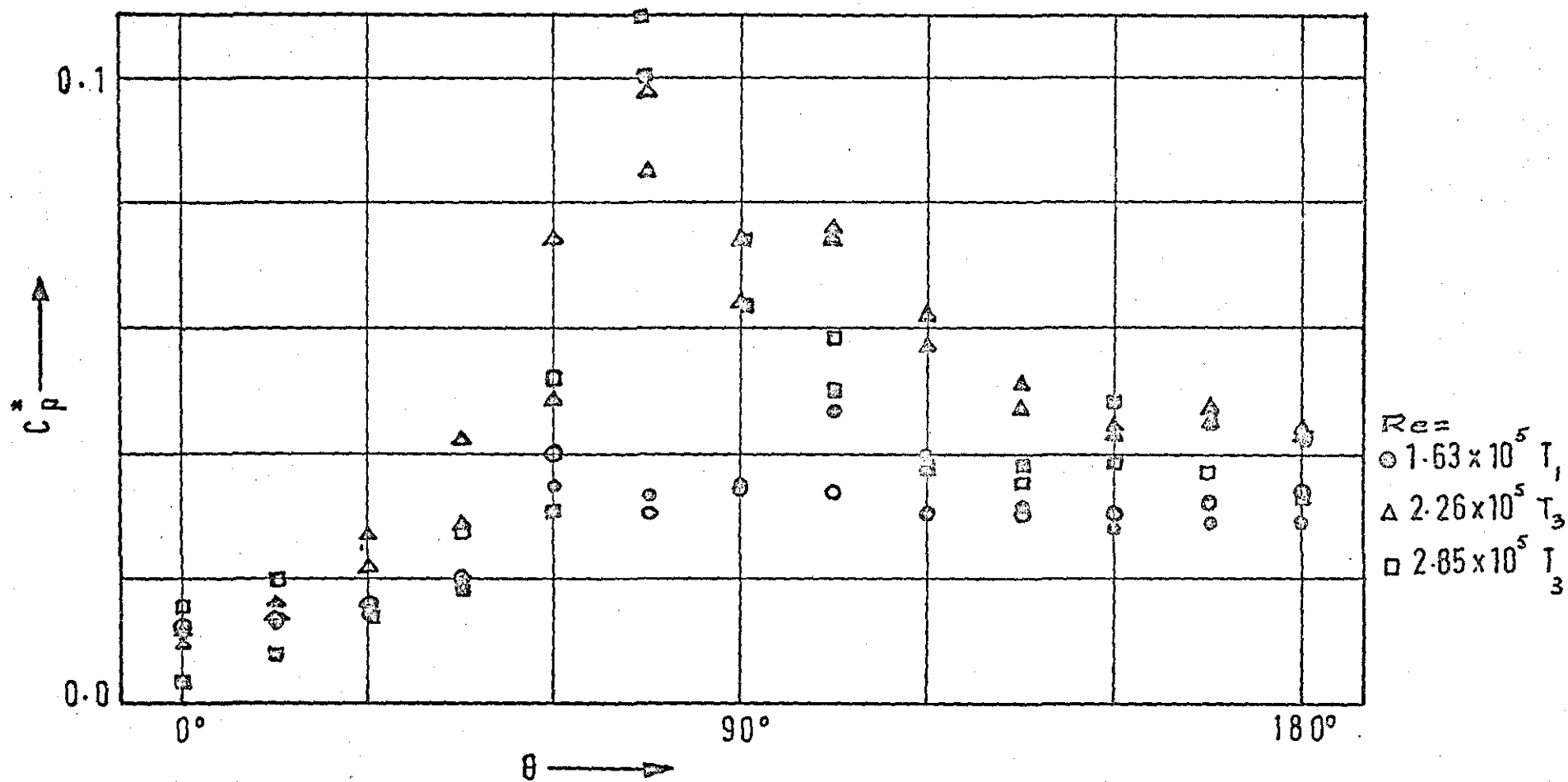
FIGURE 10·6   R.M.S. PRESSURE COEFFICIENT   (RUNS 3,4,5)
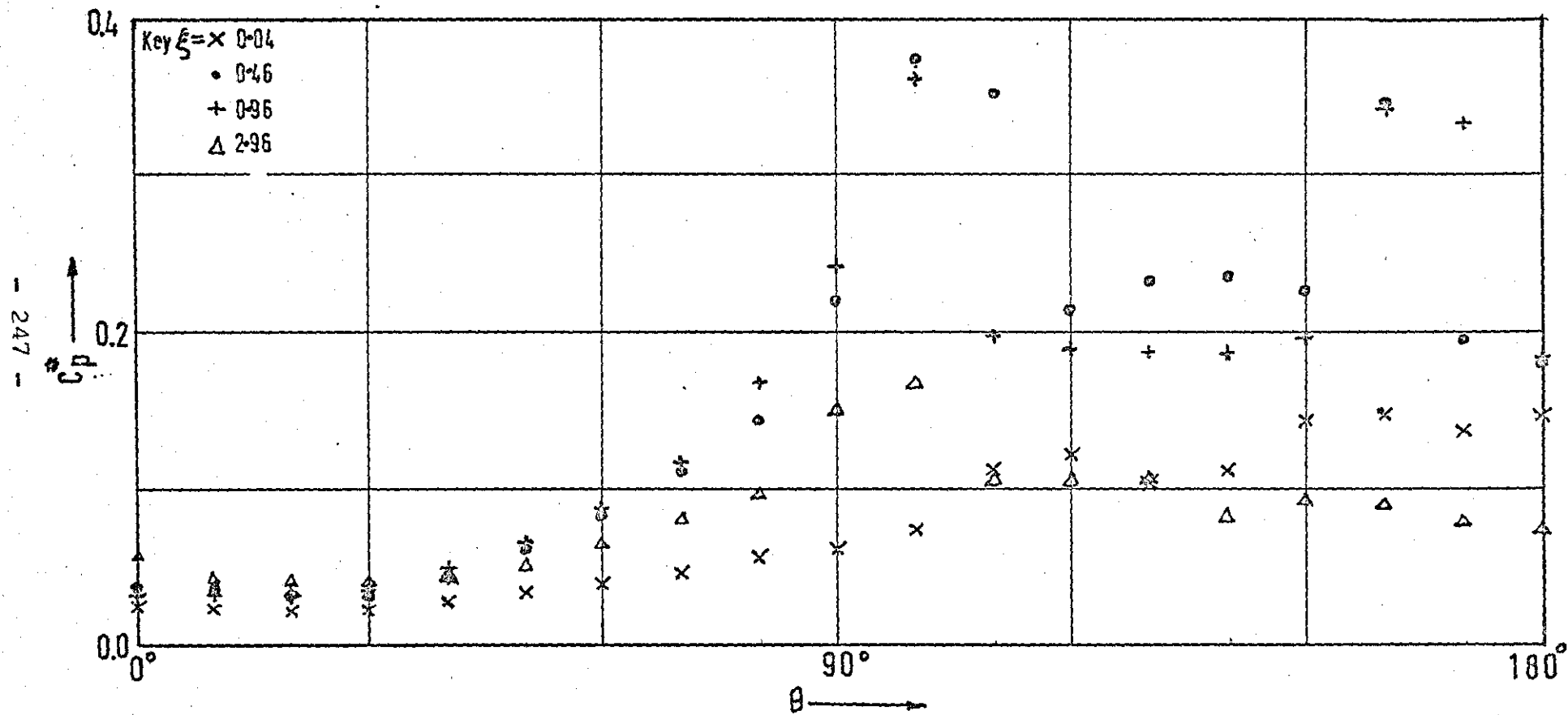
FIGURE 10.7   RMS PRESSURE COEFFICIENT (REF 52)

Re 5·4×10^6
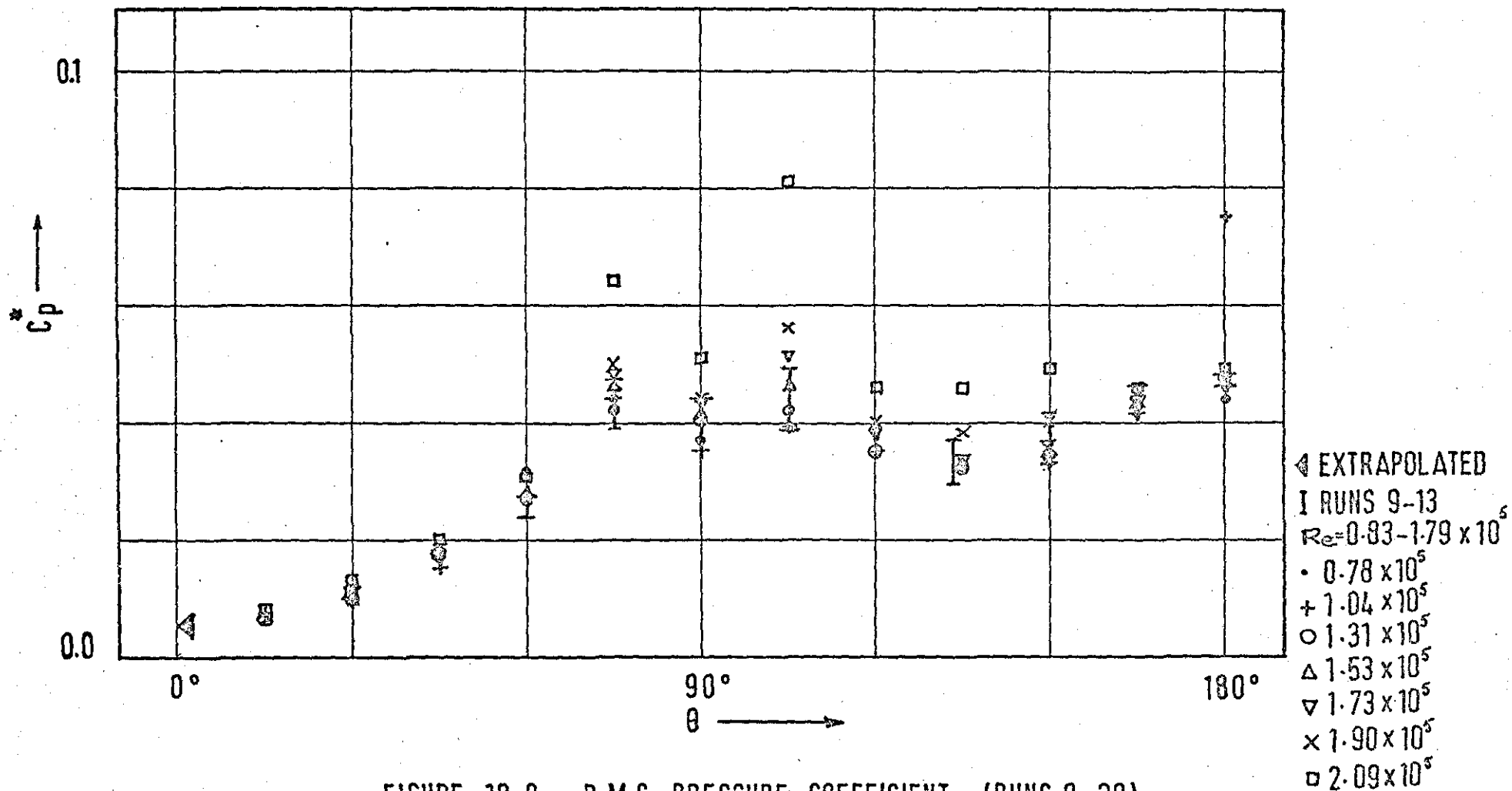
FIGURE 10·8   R.M.S. PRESSURE COEFFICIENT   (RUNS 9-20)
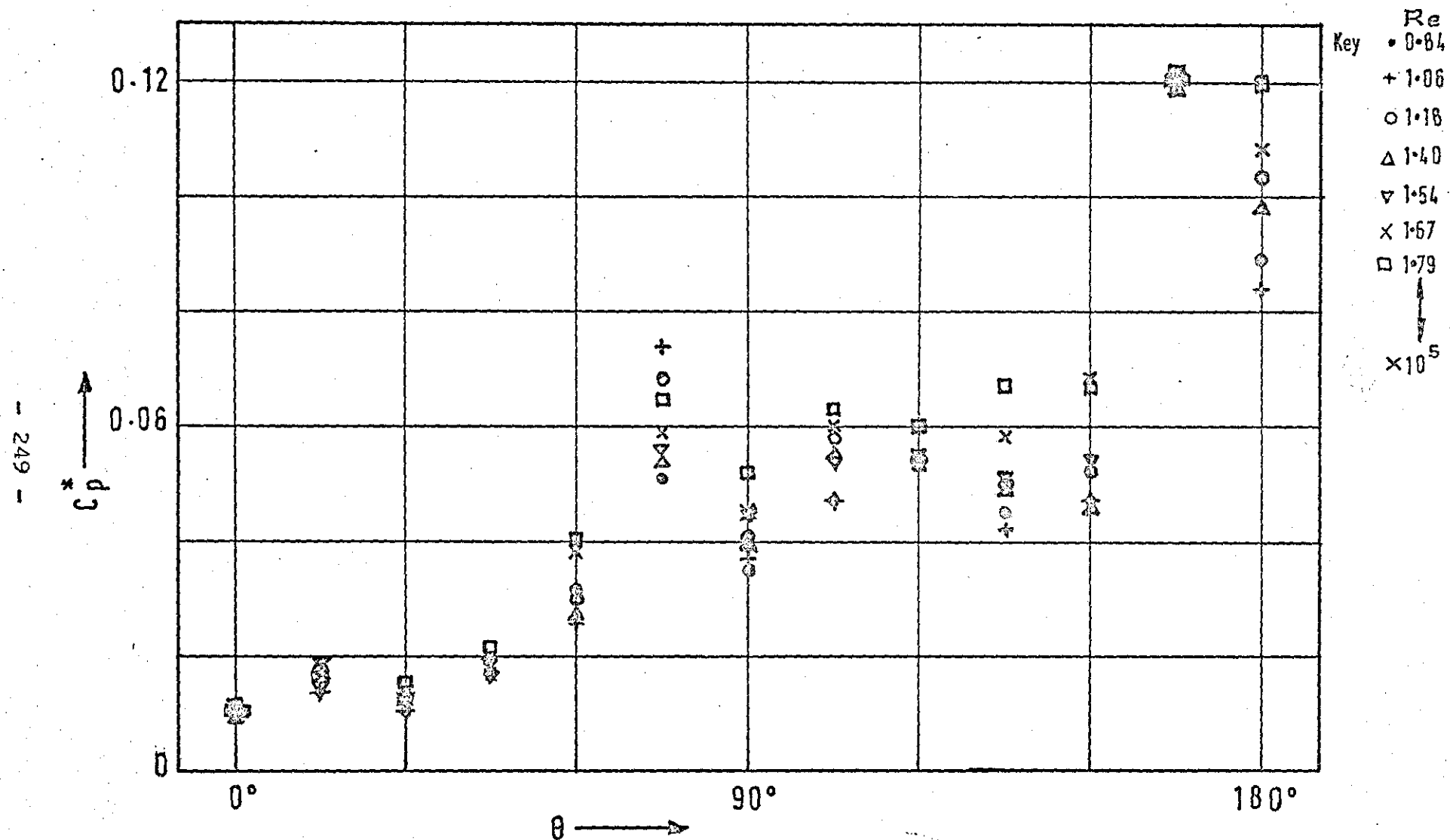
FIG 10·9   RMS PRESSURE COEFFICIENT (RUNS 21–27)
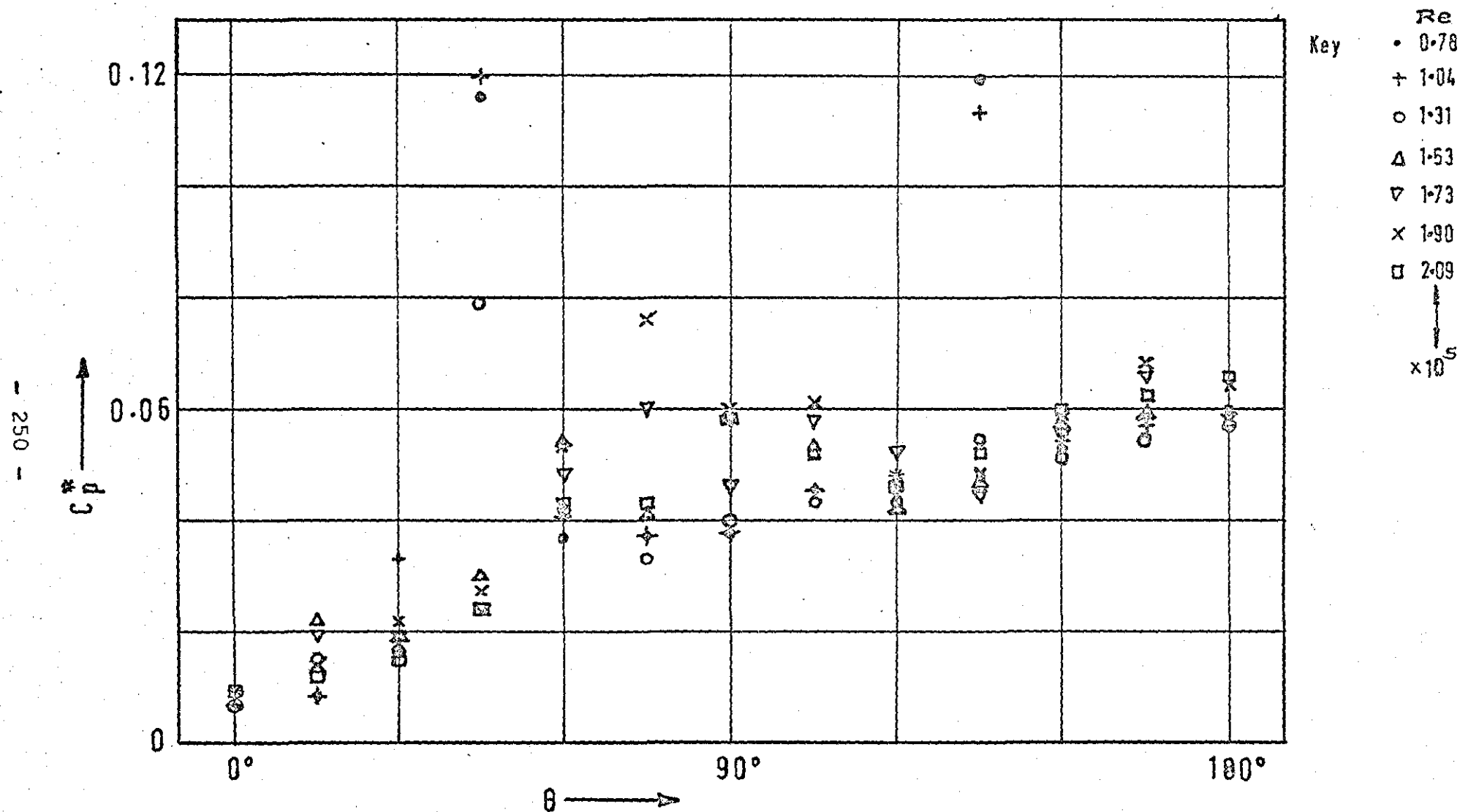
FIG 10·10 RMS PRESSURE COEFFICIENT (RUNS 28-34)
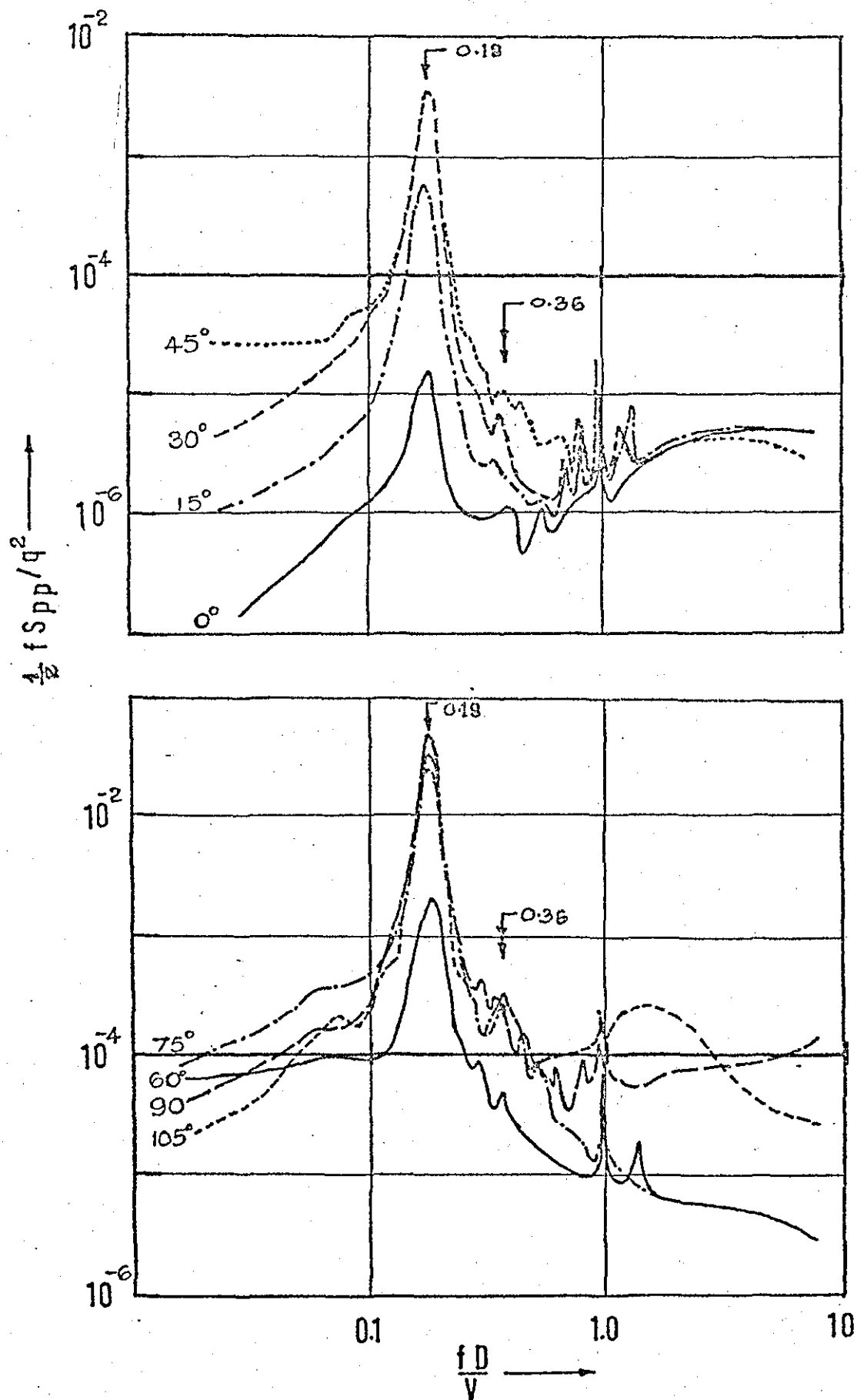
FIG. 11-1 PRESSURE POWER SPECTRA, RUN 7, T1.
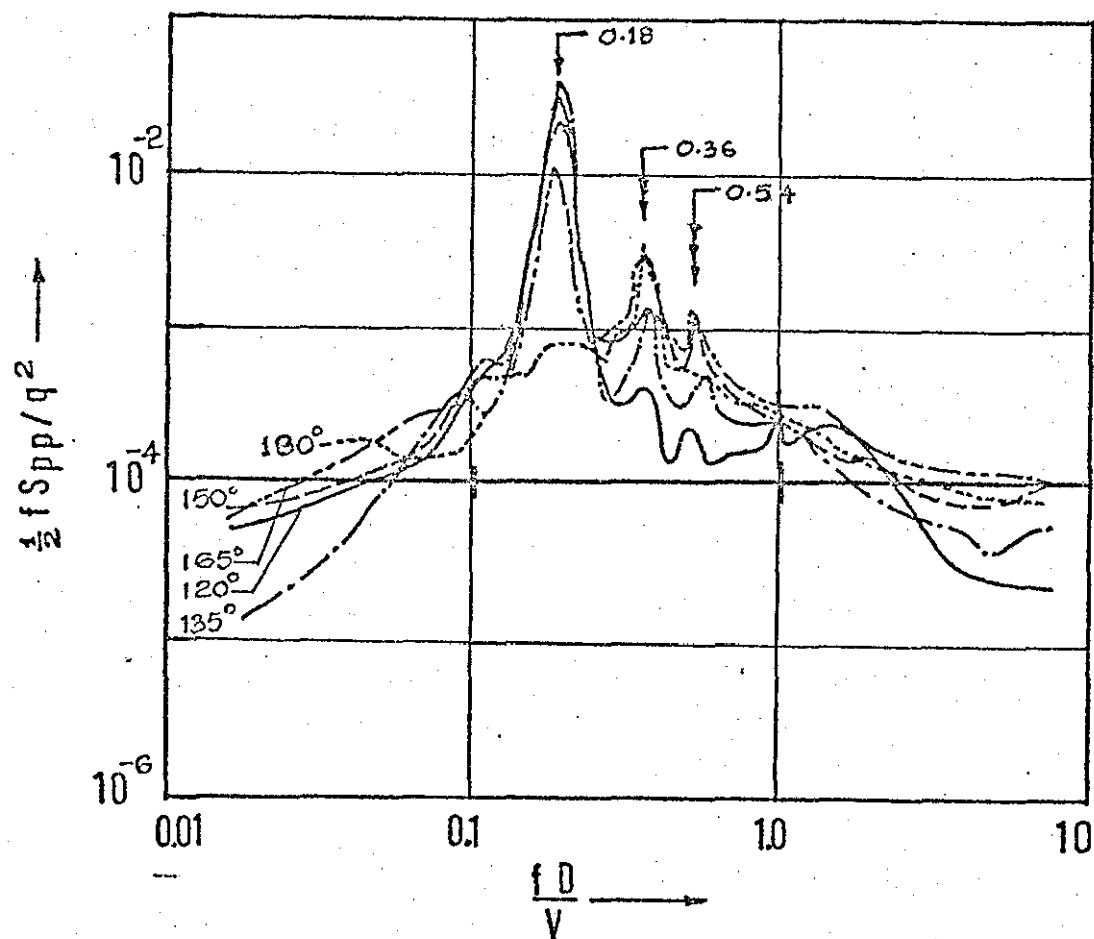
FIG. 11·1 (CONT'D) PRESSURE POWER SPECTRA, RUN 7,   T1
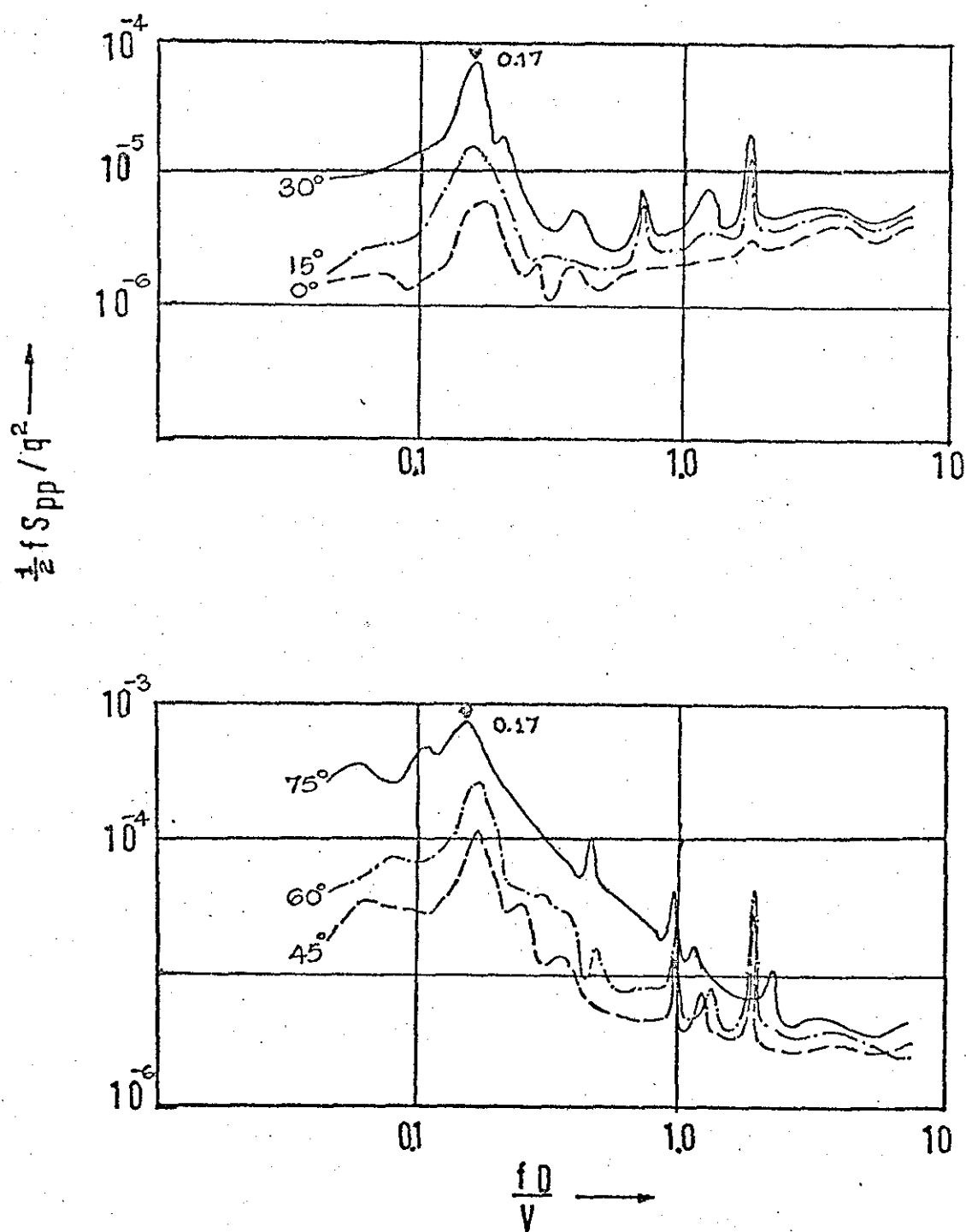
FIG. 11·2   PRESSURE POWER SPECTRA, RUN 4, T1,
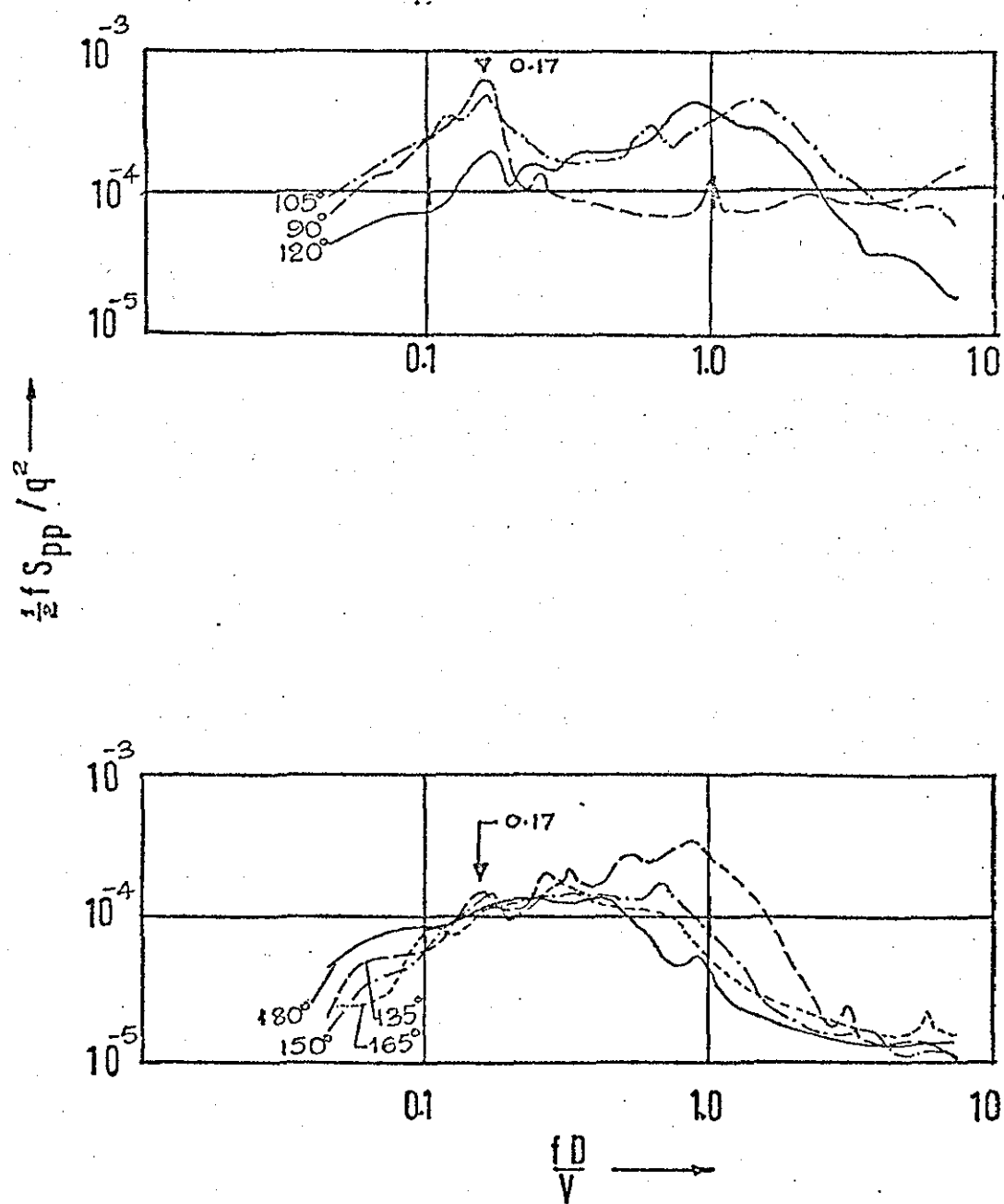
FIG. 11.2 (CONT'D)   PRESSURE POWER SPECTRA   RUN 4, T1
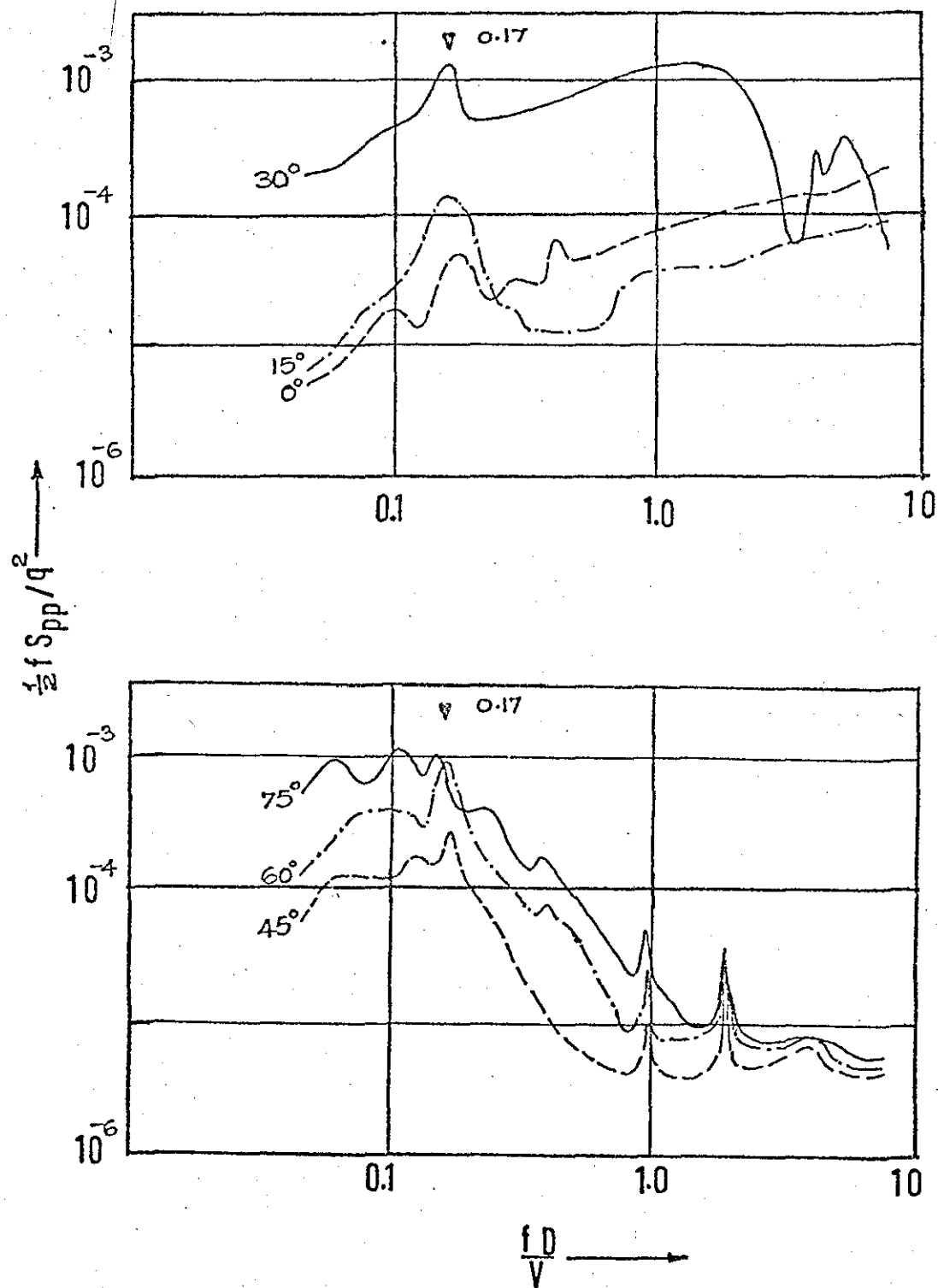
FIG 11·3   PRESSURE POWER SPECTRA
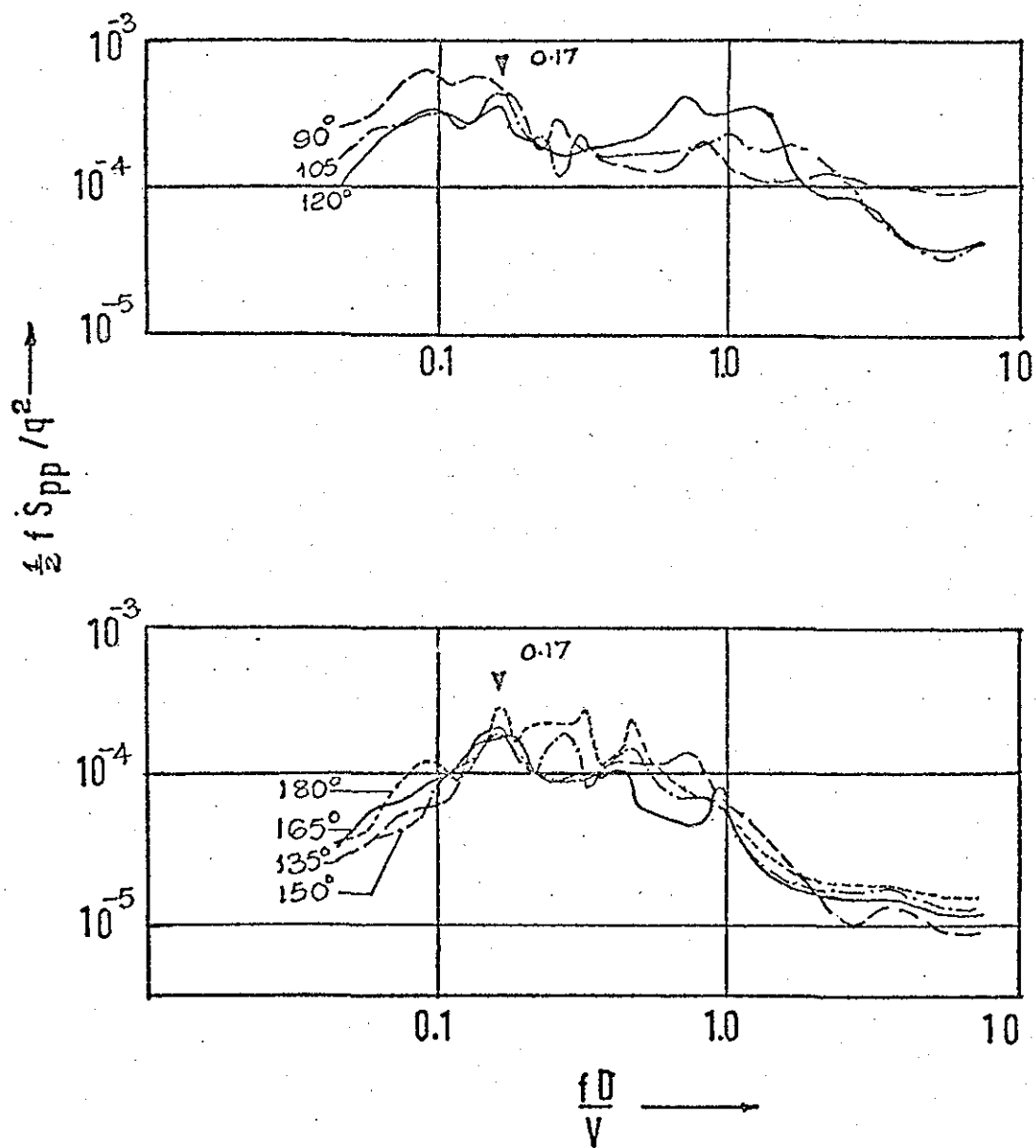
RUN 4,T3

FIG. 11·3 (CONT'D)   PRESSURE POWER SPECTRA   RUN 4, T 3.
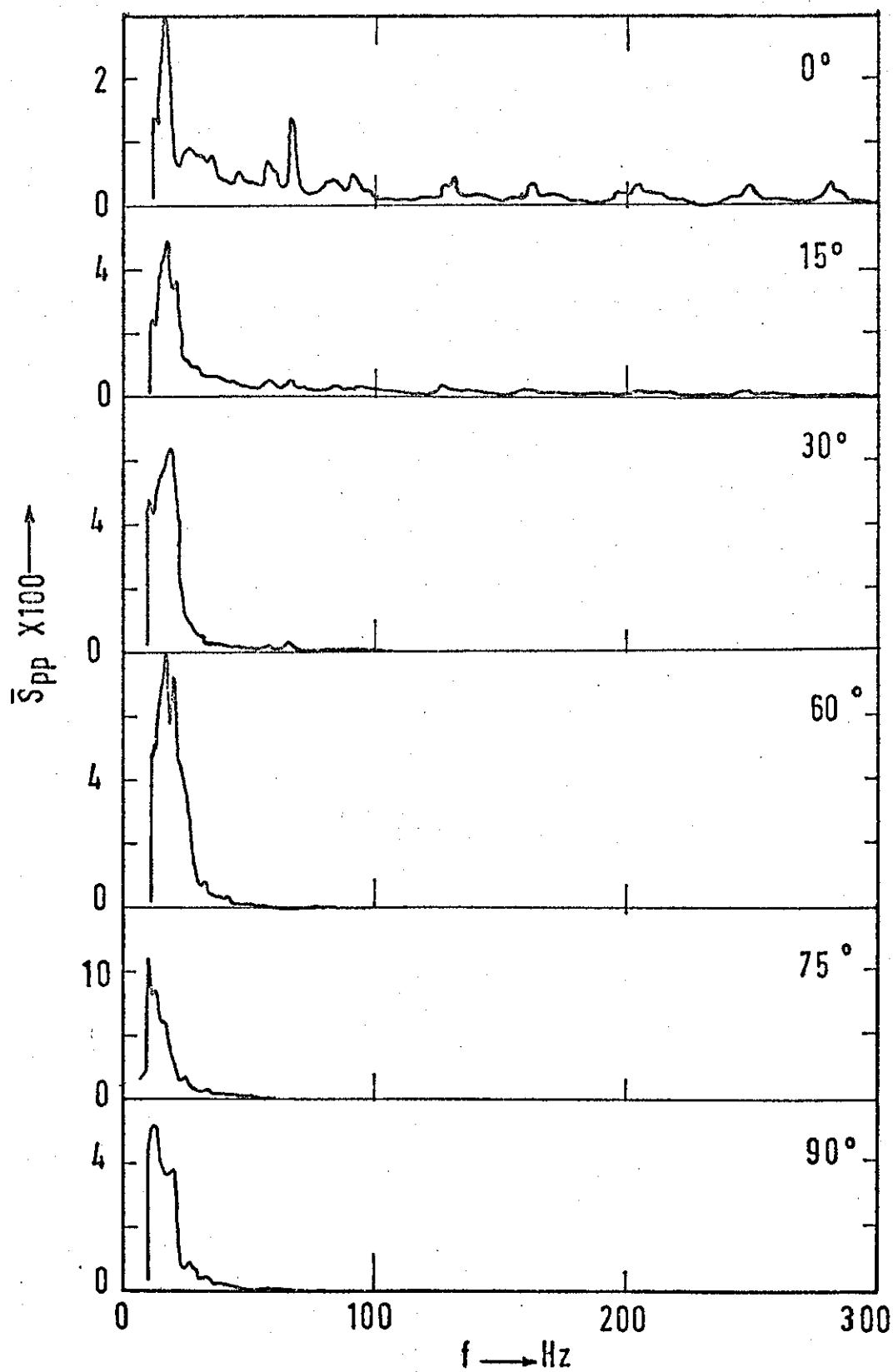
FIGURE 11.4: NORMALIZED PRESSURE POWER SPECTRA
RUN 19
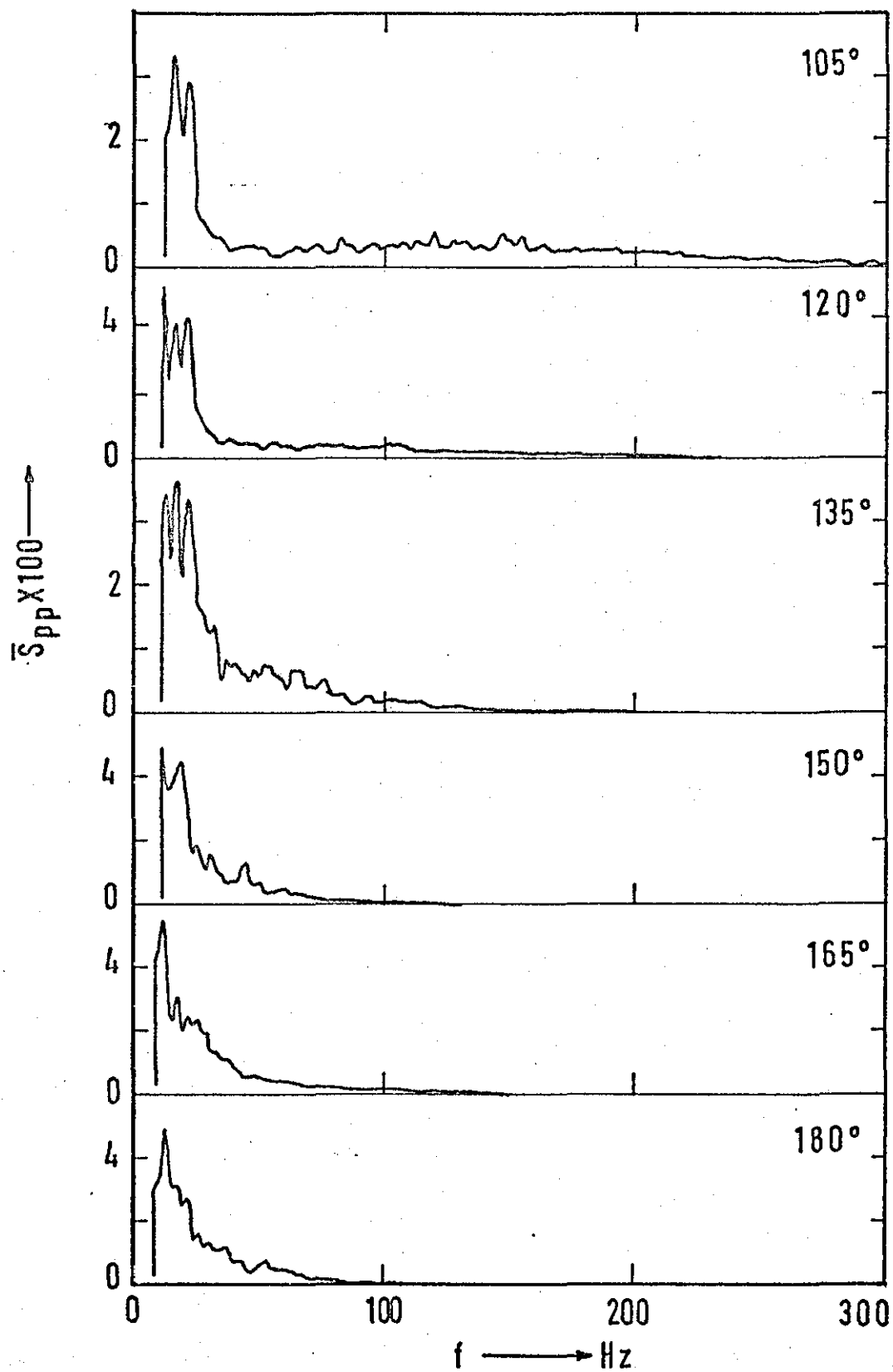
FIG. 11-4 (CONT'D) NORMALIZED PRESSURE POWER SPECTRA
RUN 19
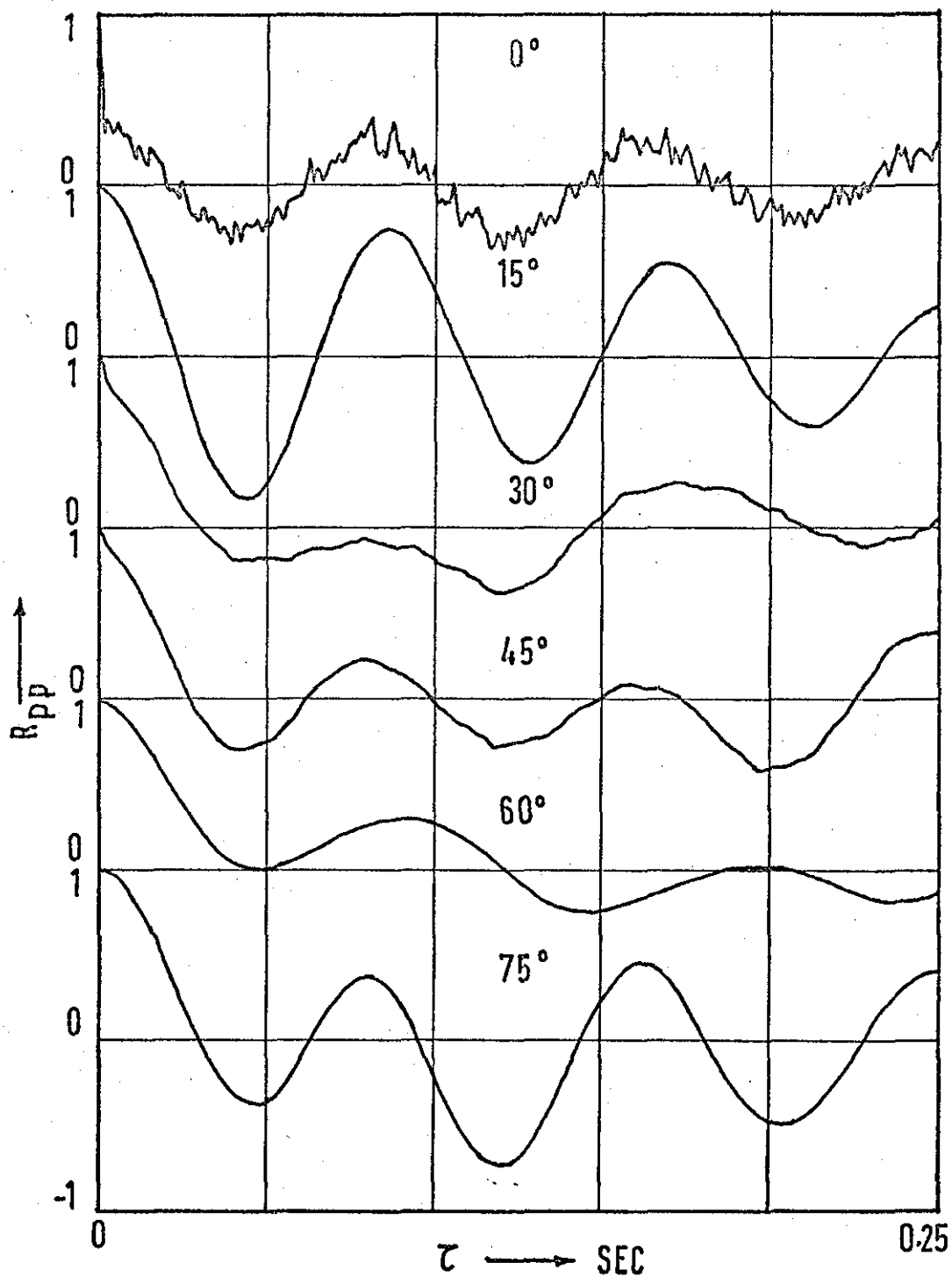
FIGURE 11·5   PRESSURE   AUTOCORRELATIONS.   RUN 7, T1, 2-D.
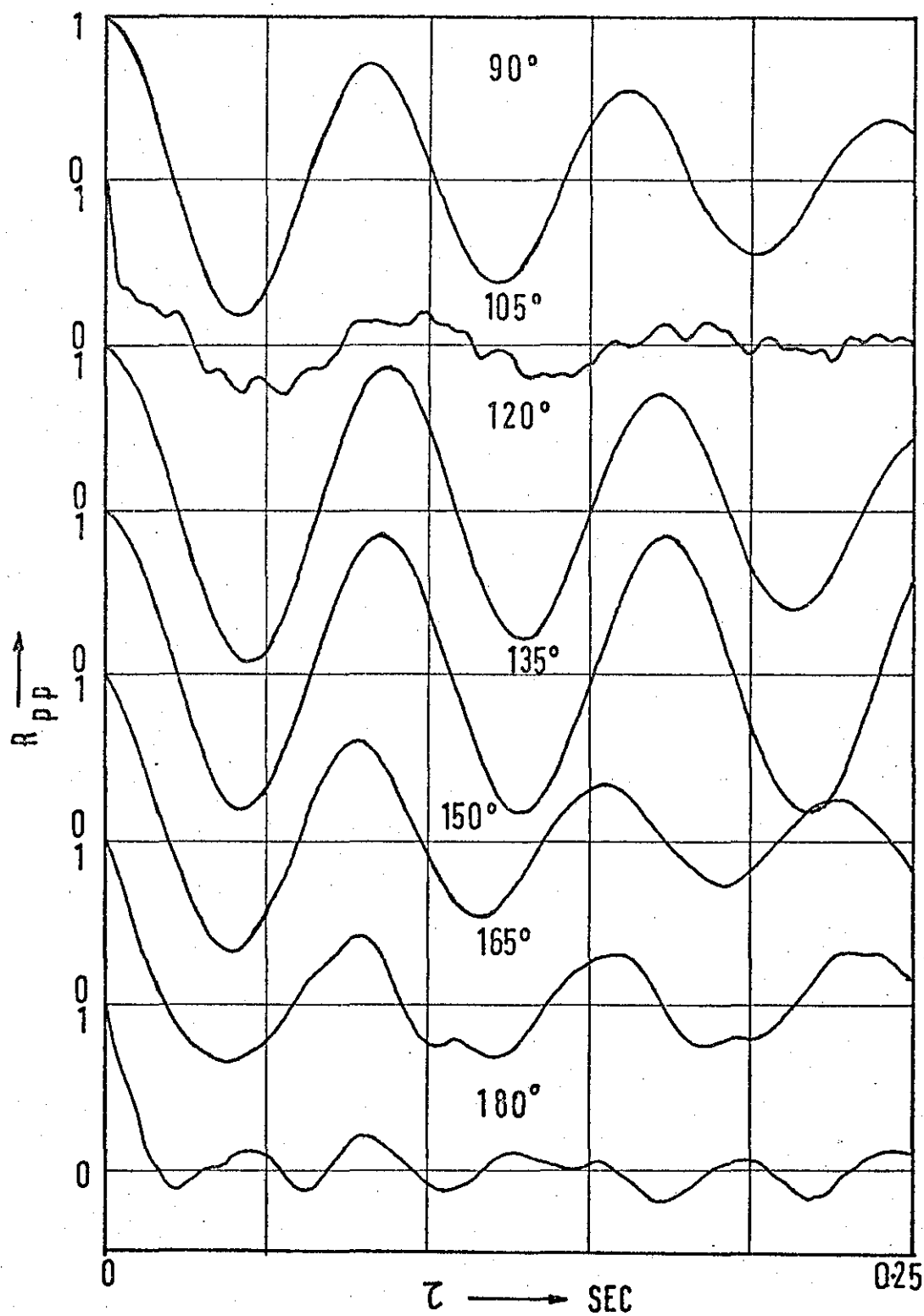
FIG. 11·5 (CONT'D)   PRESSURE AUTOCORRELATIONS   RUN 7, T₁
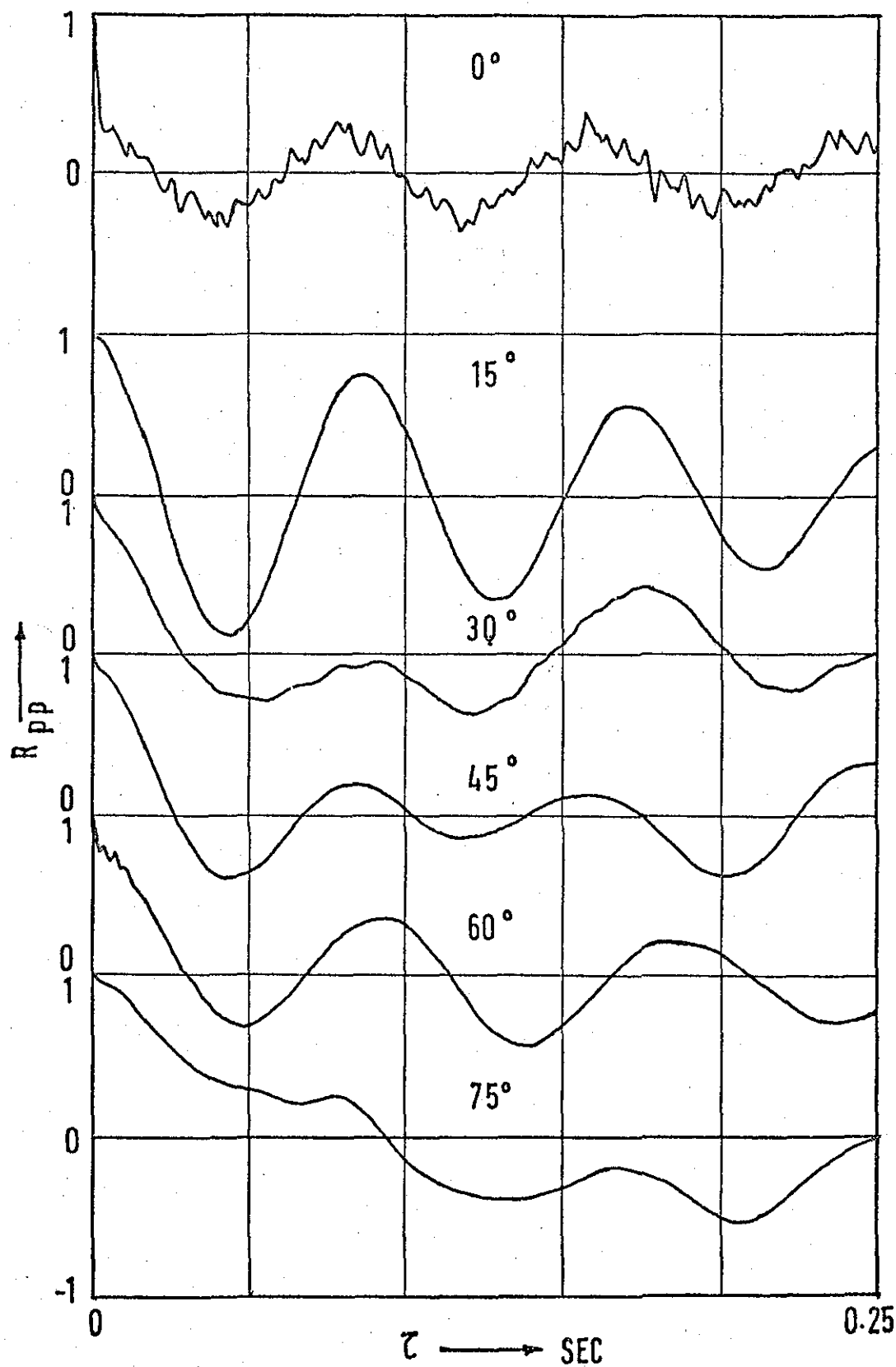
FIGURE 11·6.   PRESSURE AUTOCORRELATIONS.   RUN 7, T3, 2-D
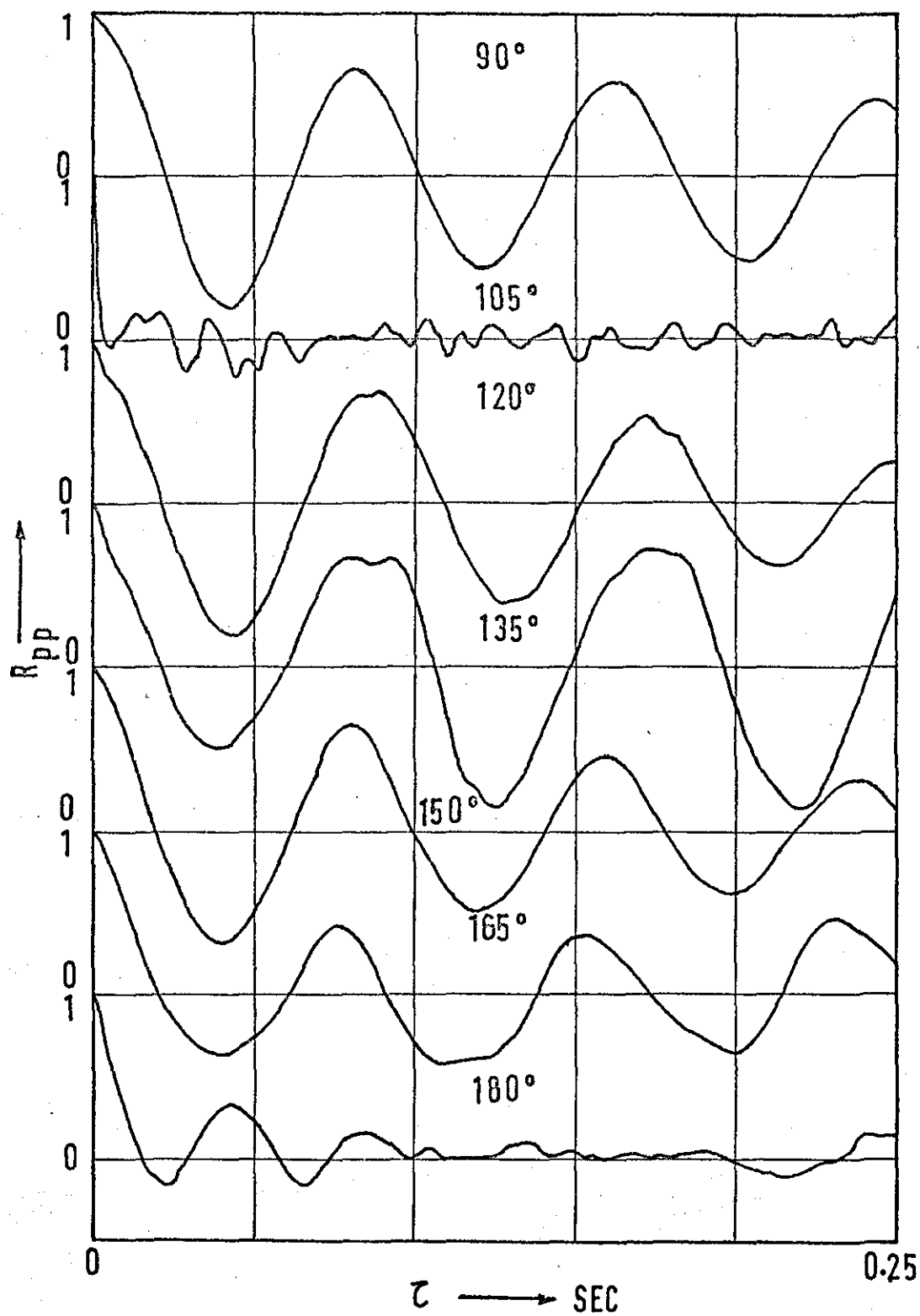
FIGURE 11·6 (CONT'D)
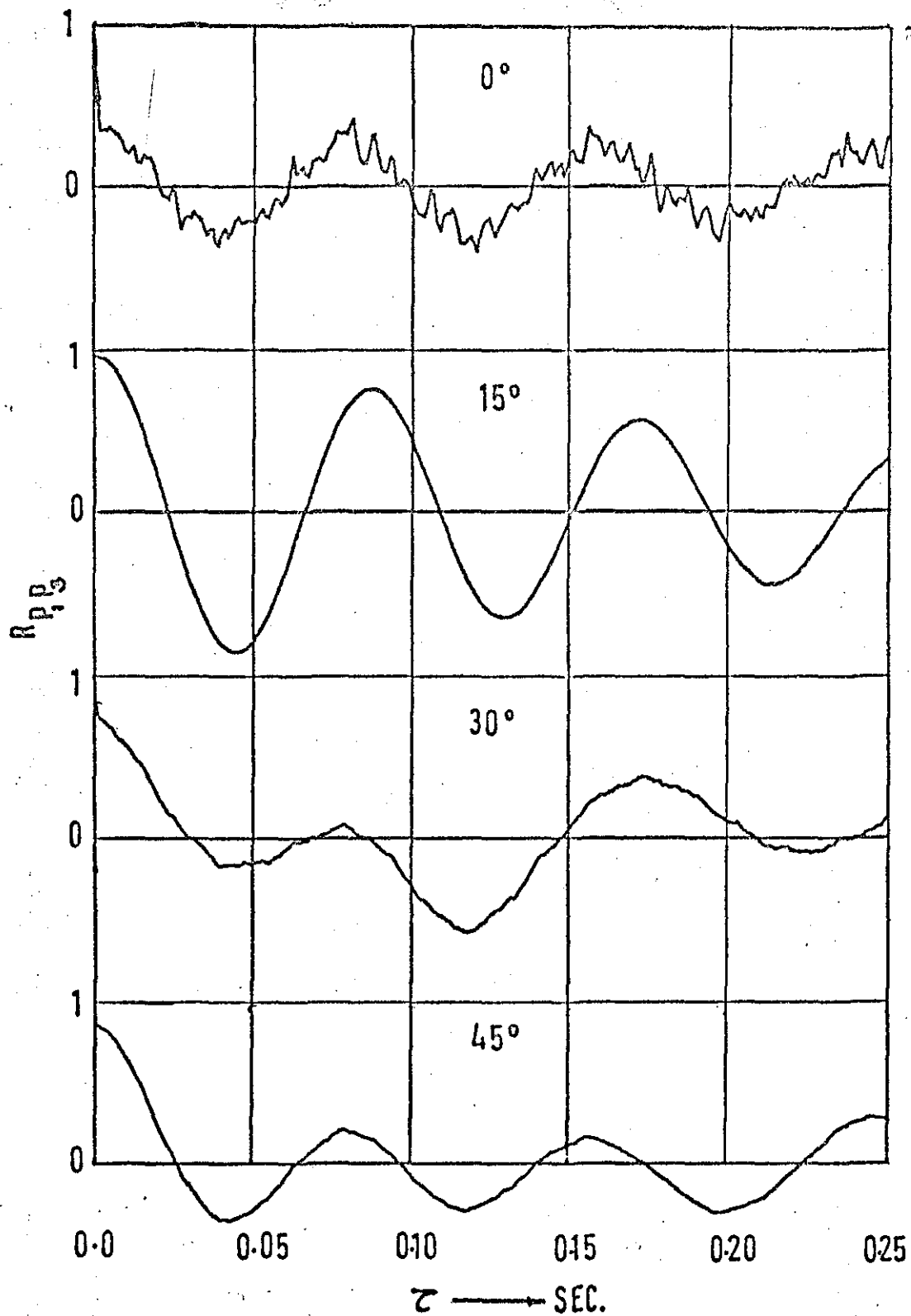
FIGURE 11·7   PRESSURE   CROSS   CORRELATIONS,   RUN 7,   2-D
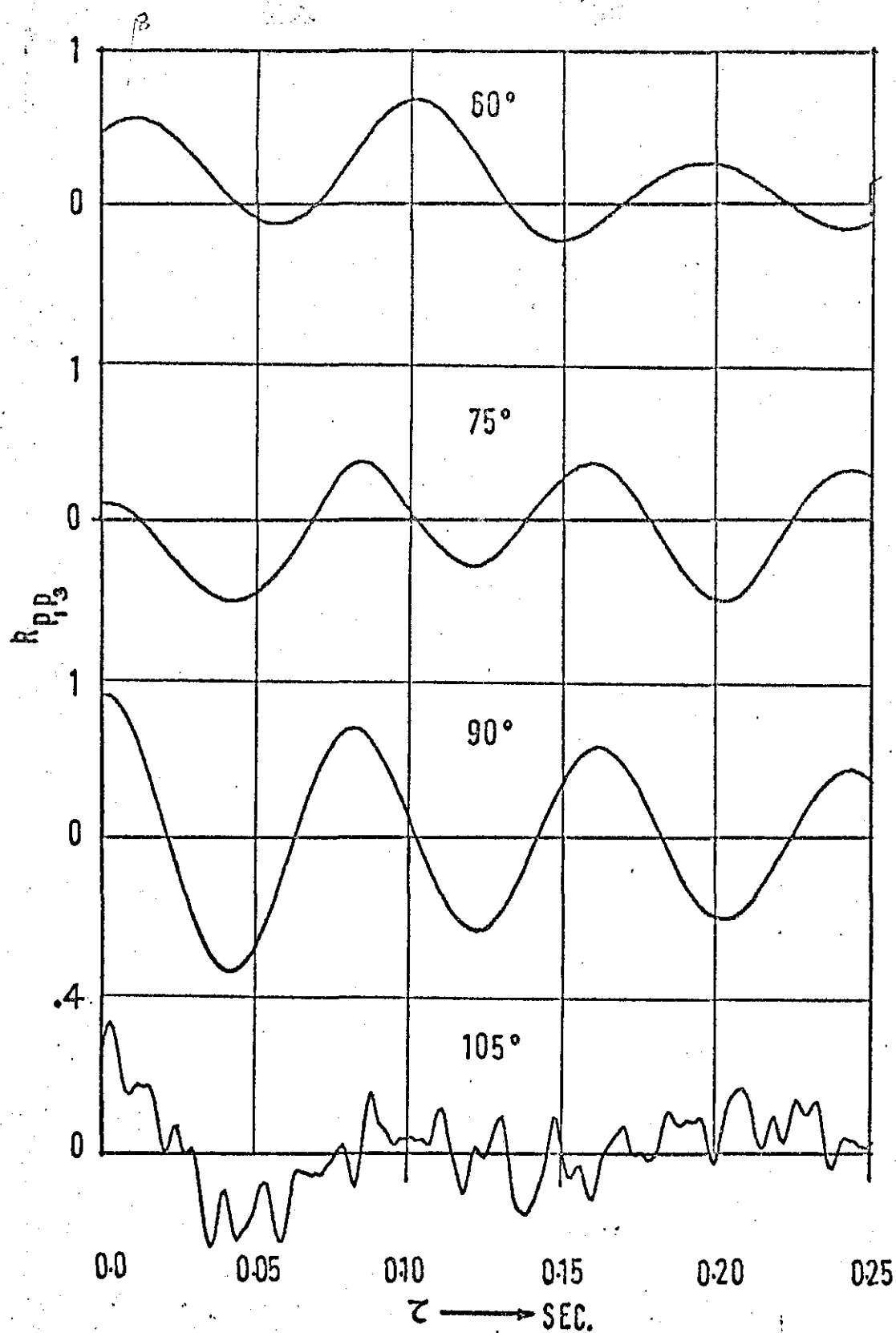
FIGURE 11·7 (CONT'D)
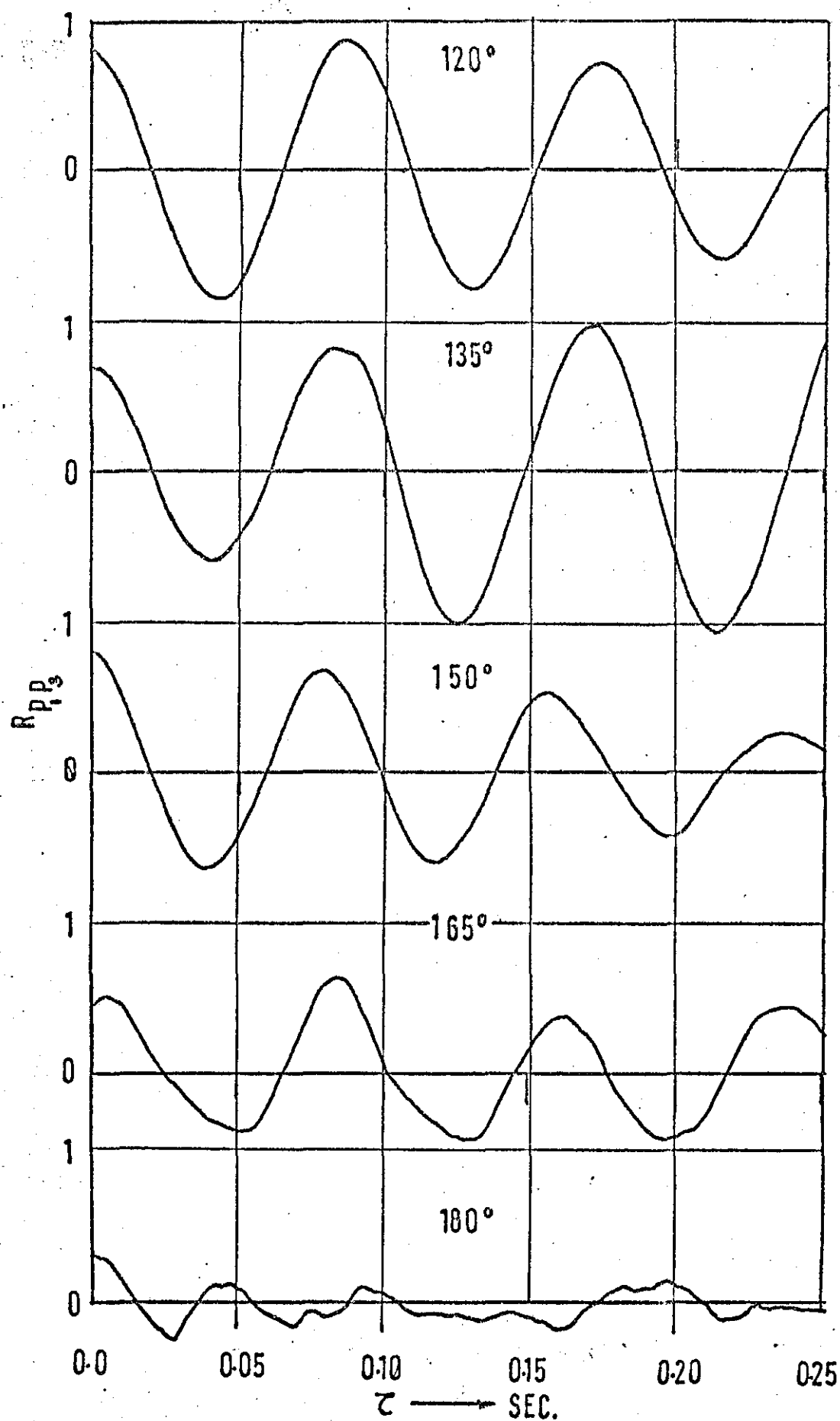
FIG. 11·7 (CONT'D)   PRESSURE CROSS CORRELATIONS, RUN 7 2-D
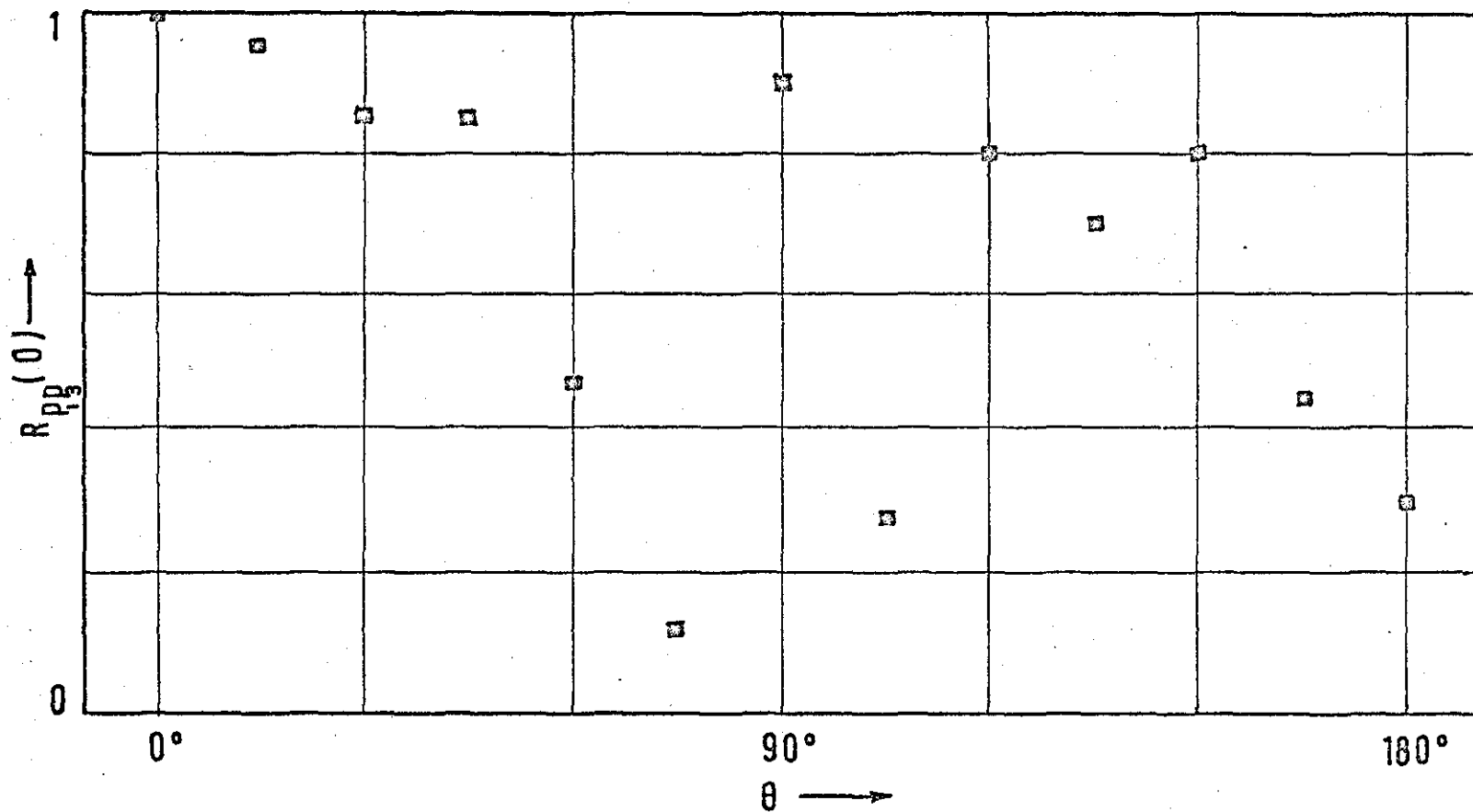
FIG. 11·8   CORRELATION   COEFFICIENT, RUN 7, 2 - D
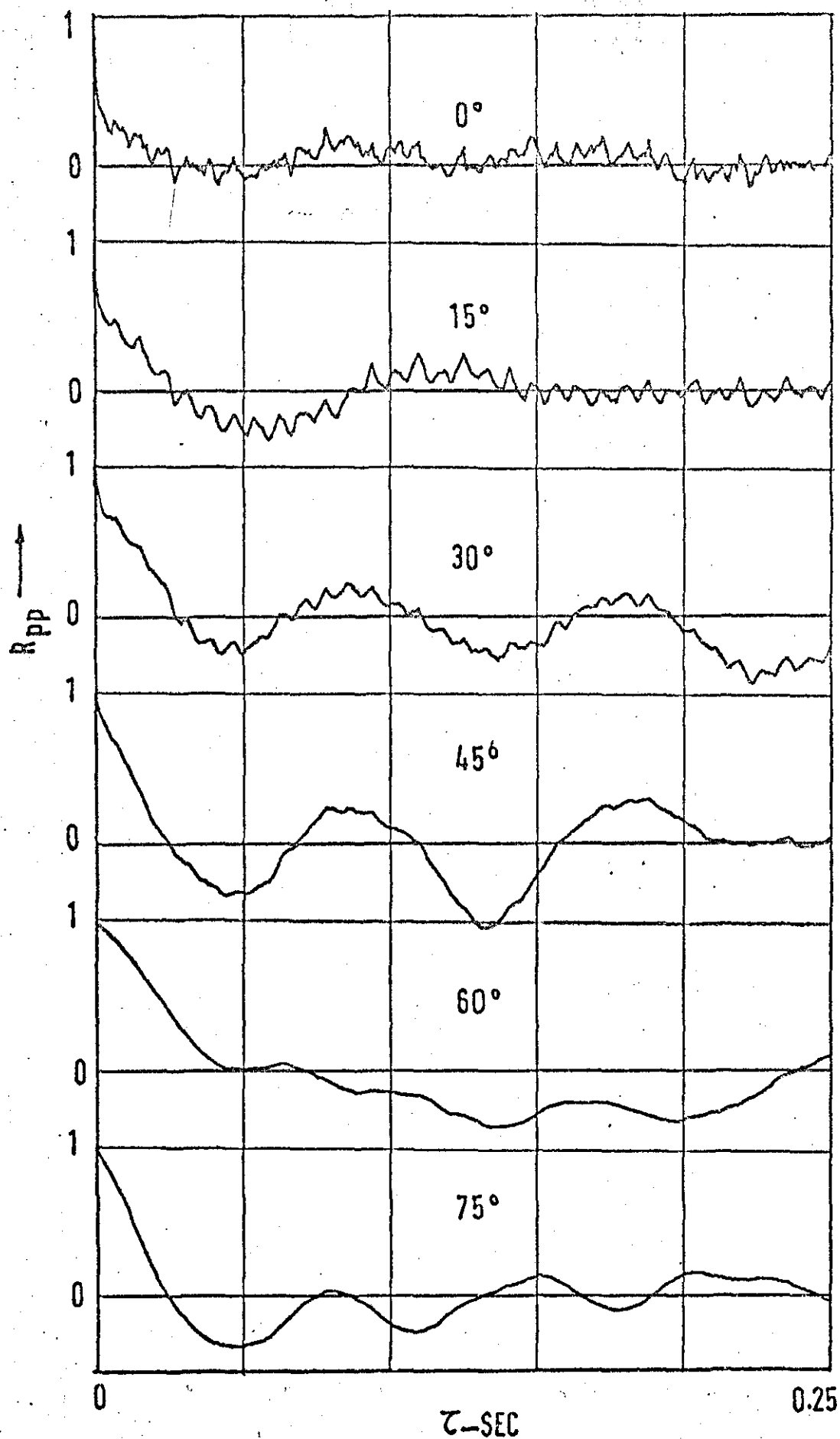
FIGURE 11·9   PRESSURE AUTOCORRELATIONS. RUN4,3-D,T1
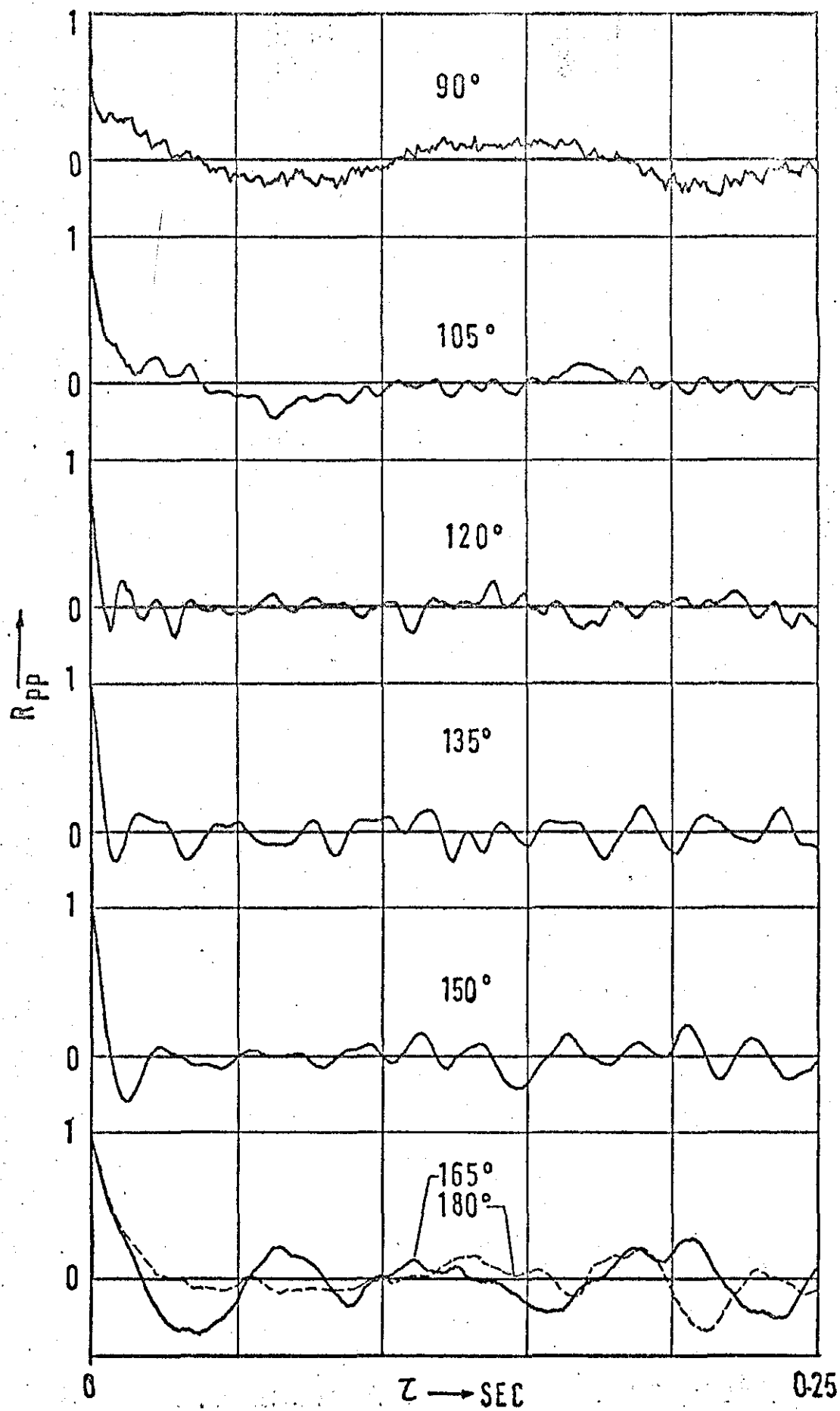
FIG. 119 (CONT'D) PRESSURE AUTO CORRELATIONS, RUN 4, T1.
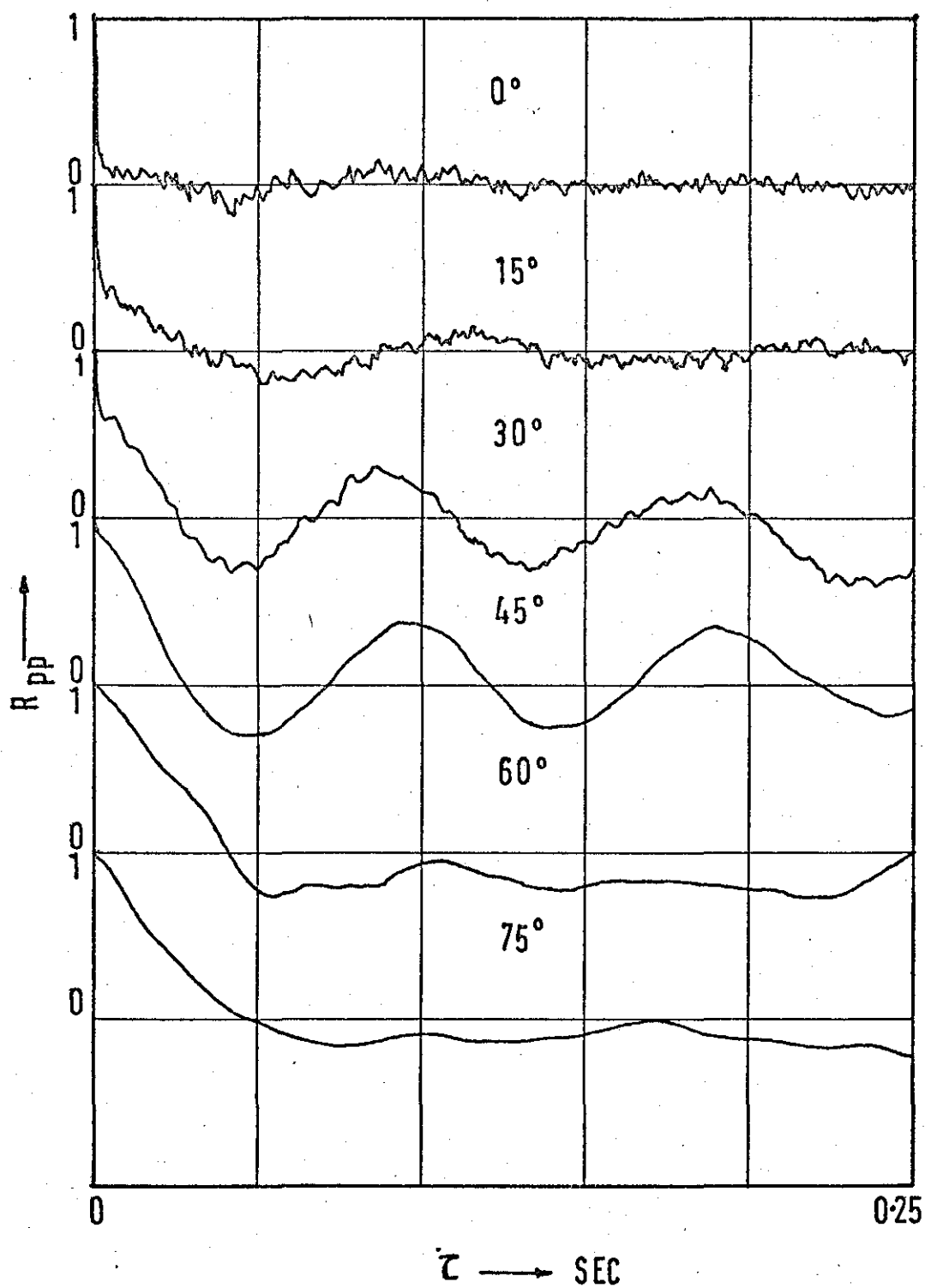
FIGURE 11-10   PRESSURE   AUTOCORRELATIONS. RUN 4, 3- D, T3
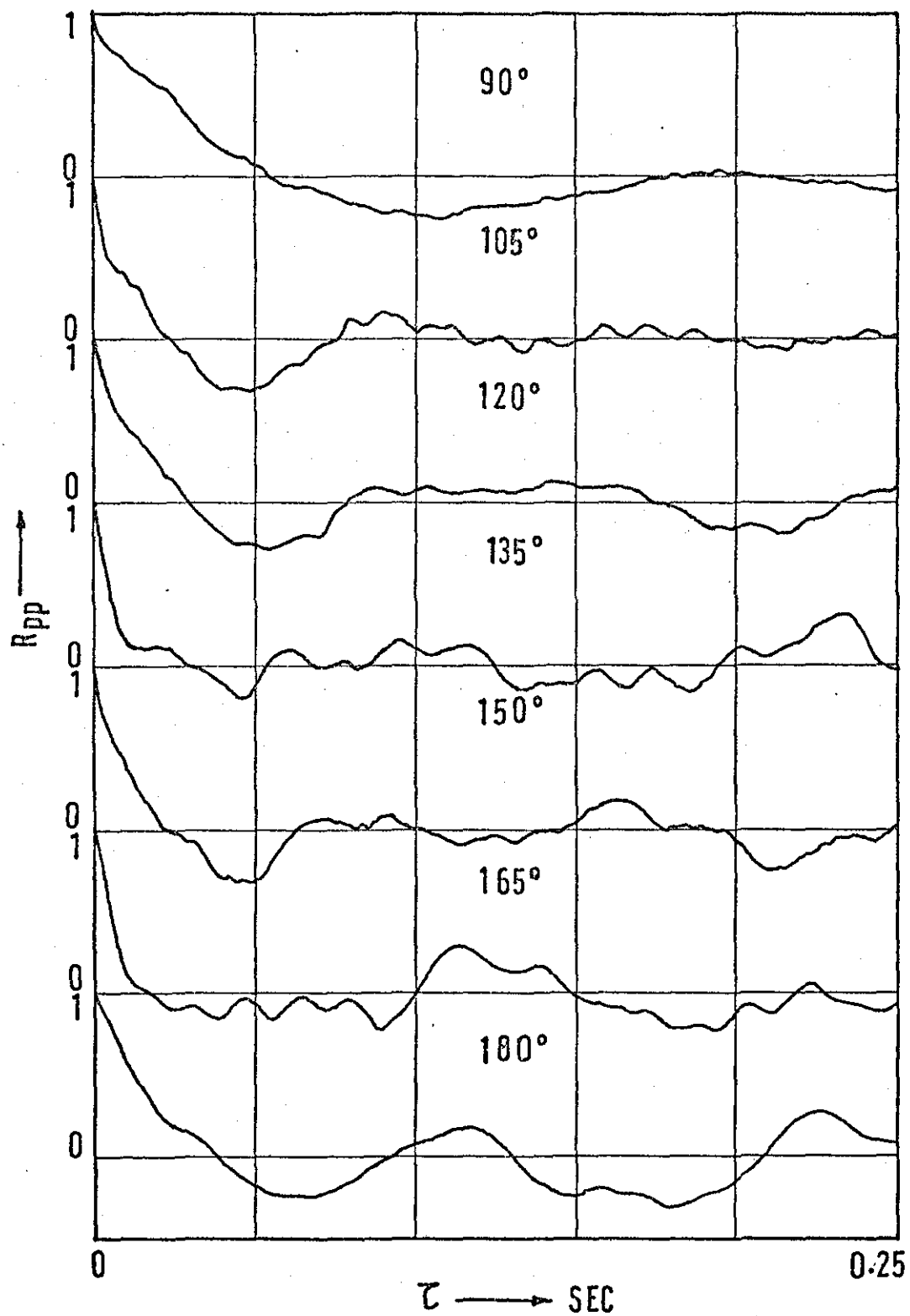
FIGURE 11·10 (CONT'D)
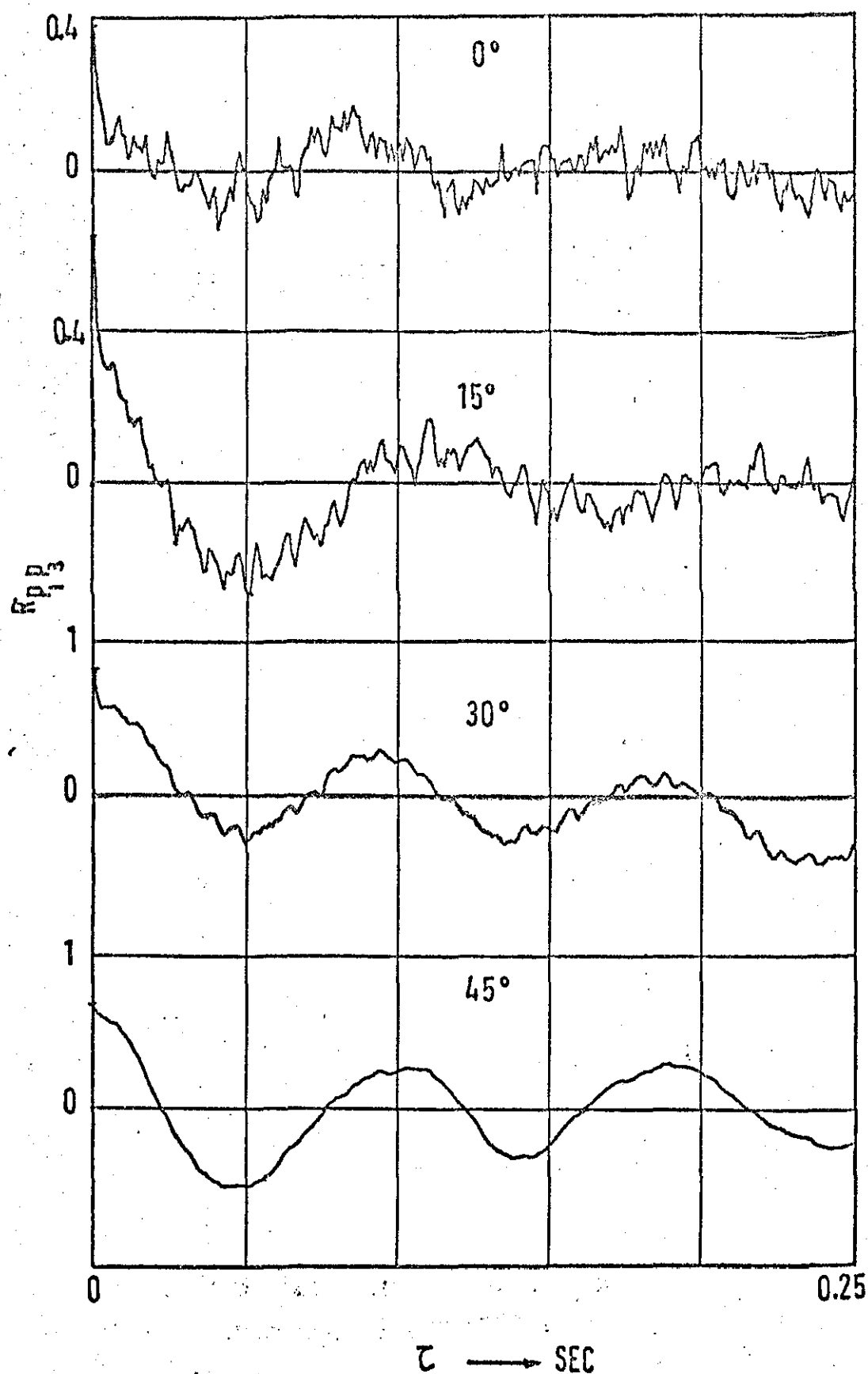
FIGURE 11·11   PRESSURE   CROSS CORRELATIONS   RUN 7, 3-D
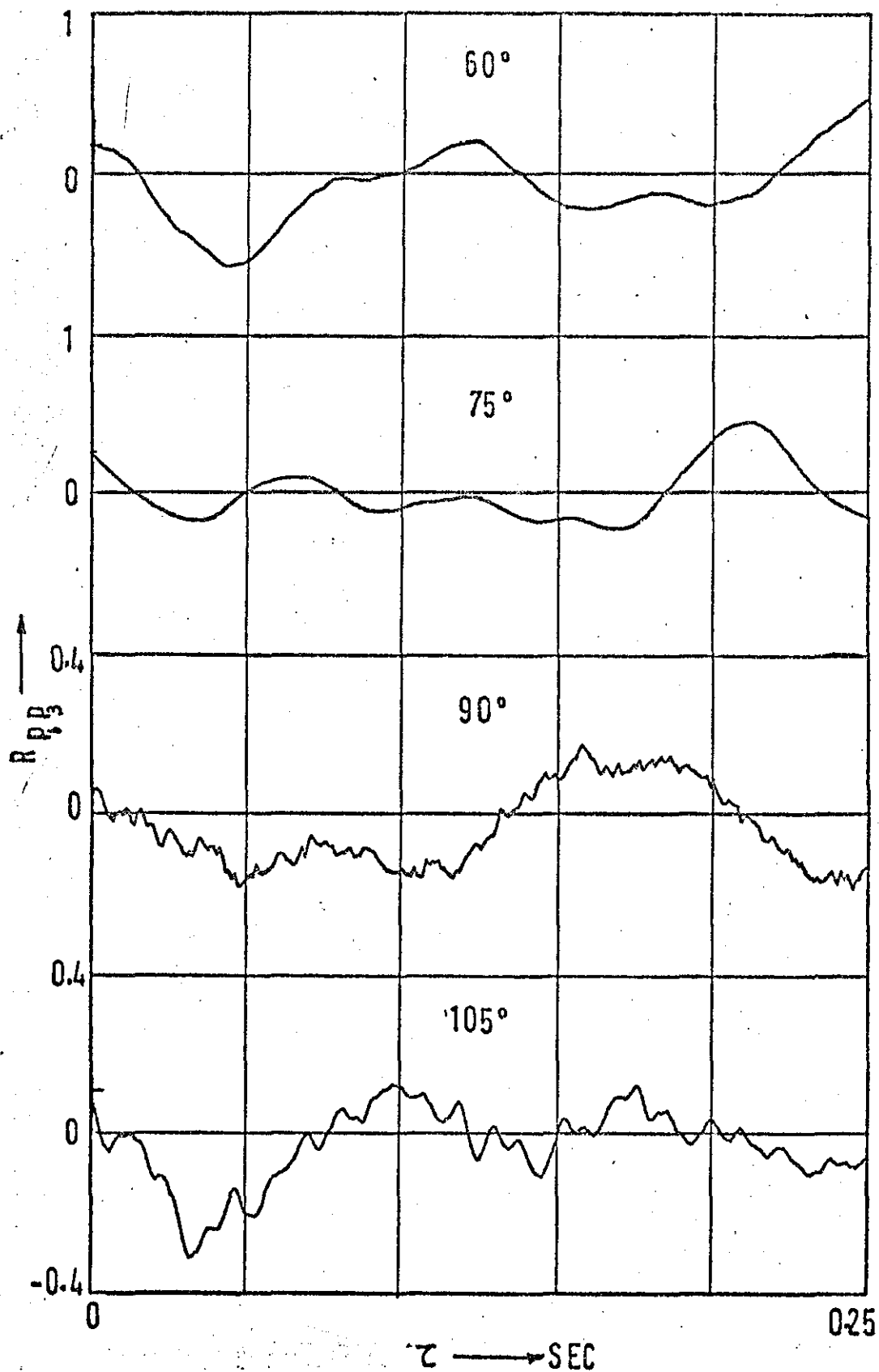
FIGURE 11·11 (CONT'D)
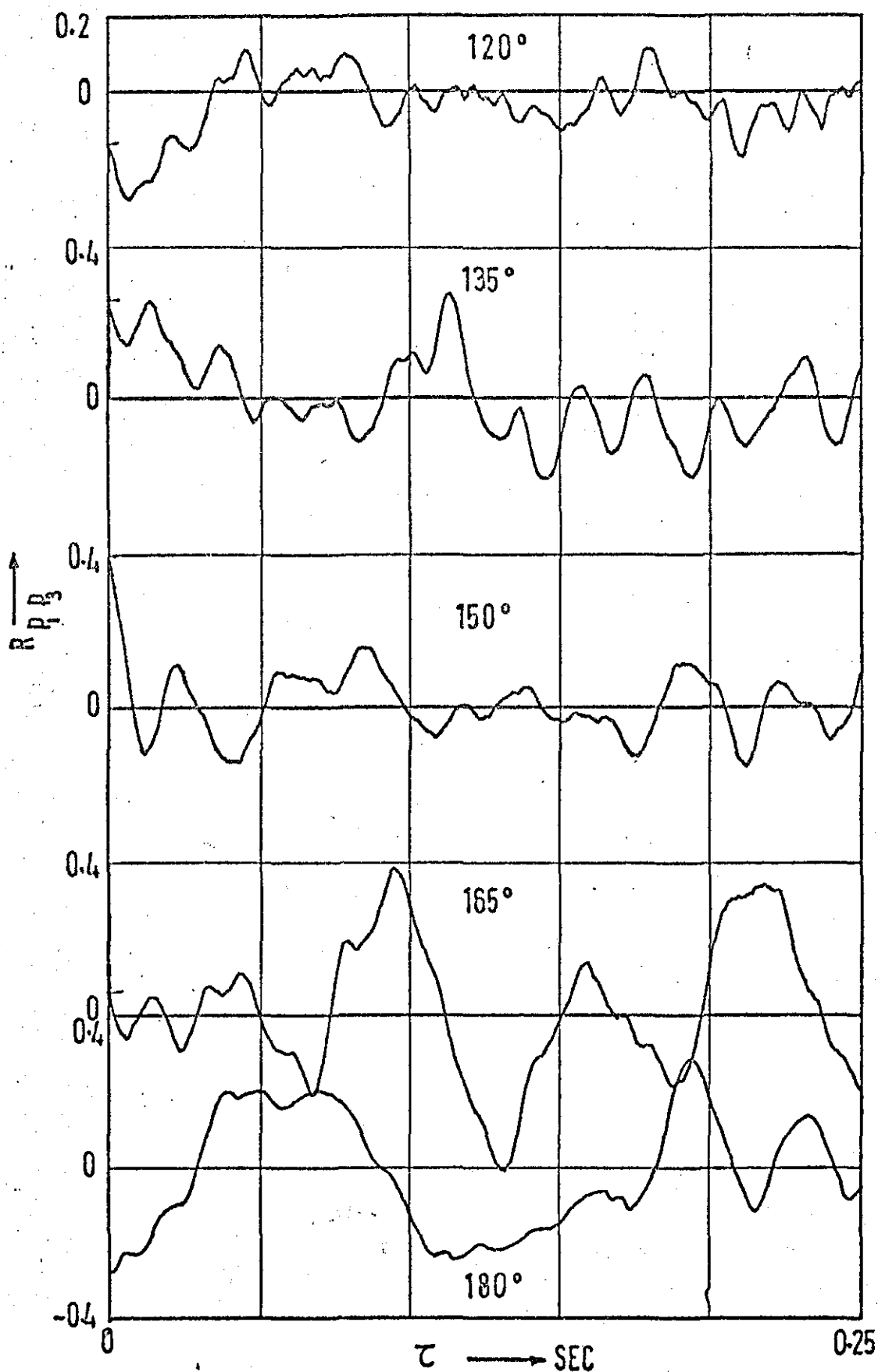
FIG. 11-11 (CONT'D) PRESSURE CROSS CORRELATIONS, RUN 4, 3-D

273+ - 274 -
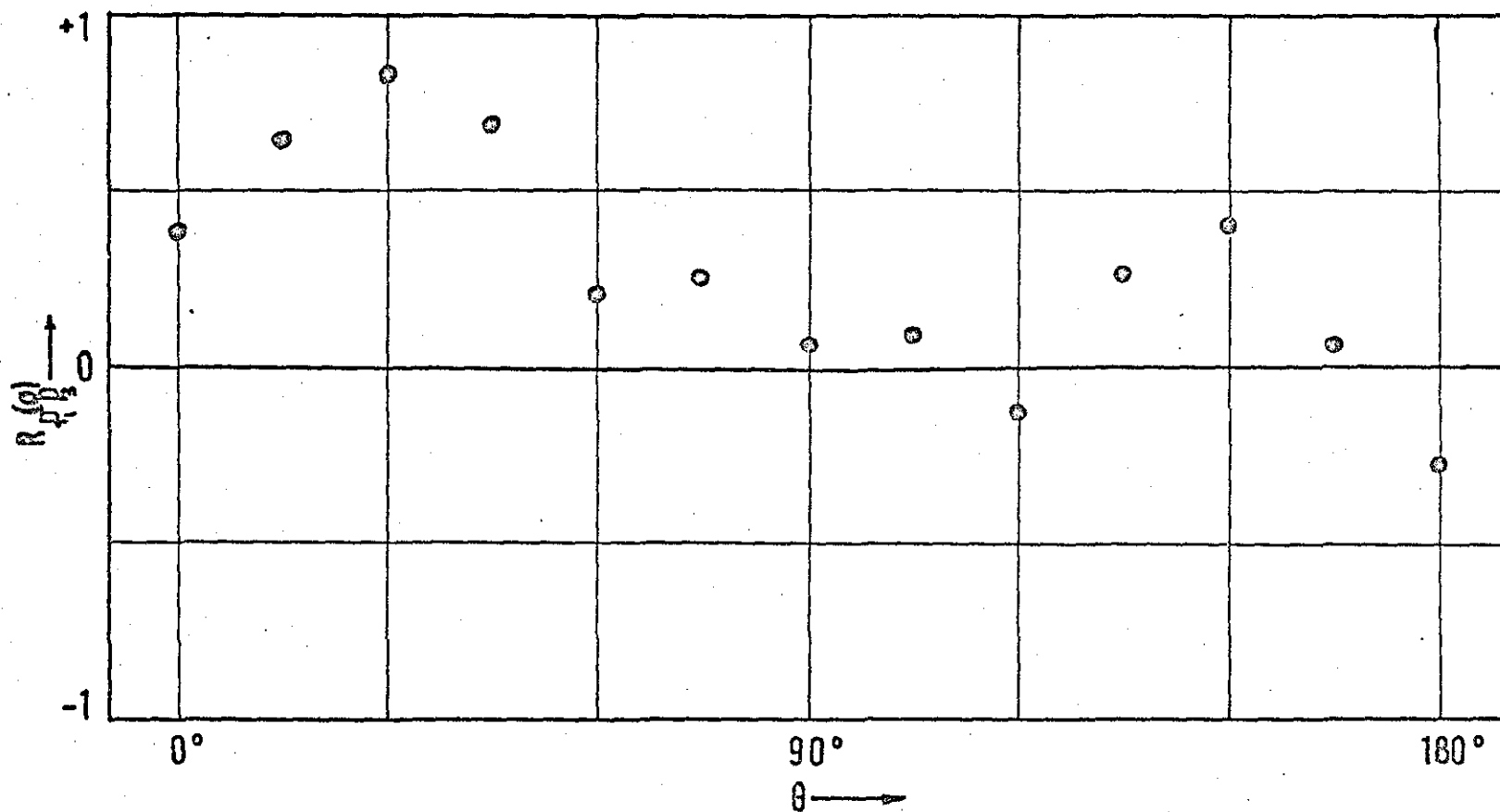
FIG. 11·12   CORRELATION   COEFFICIENT ,RUN 4, 3−D
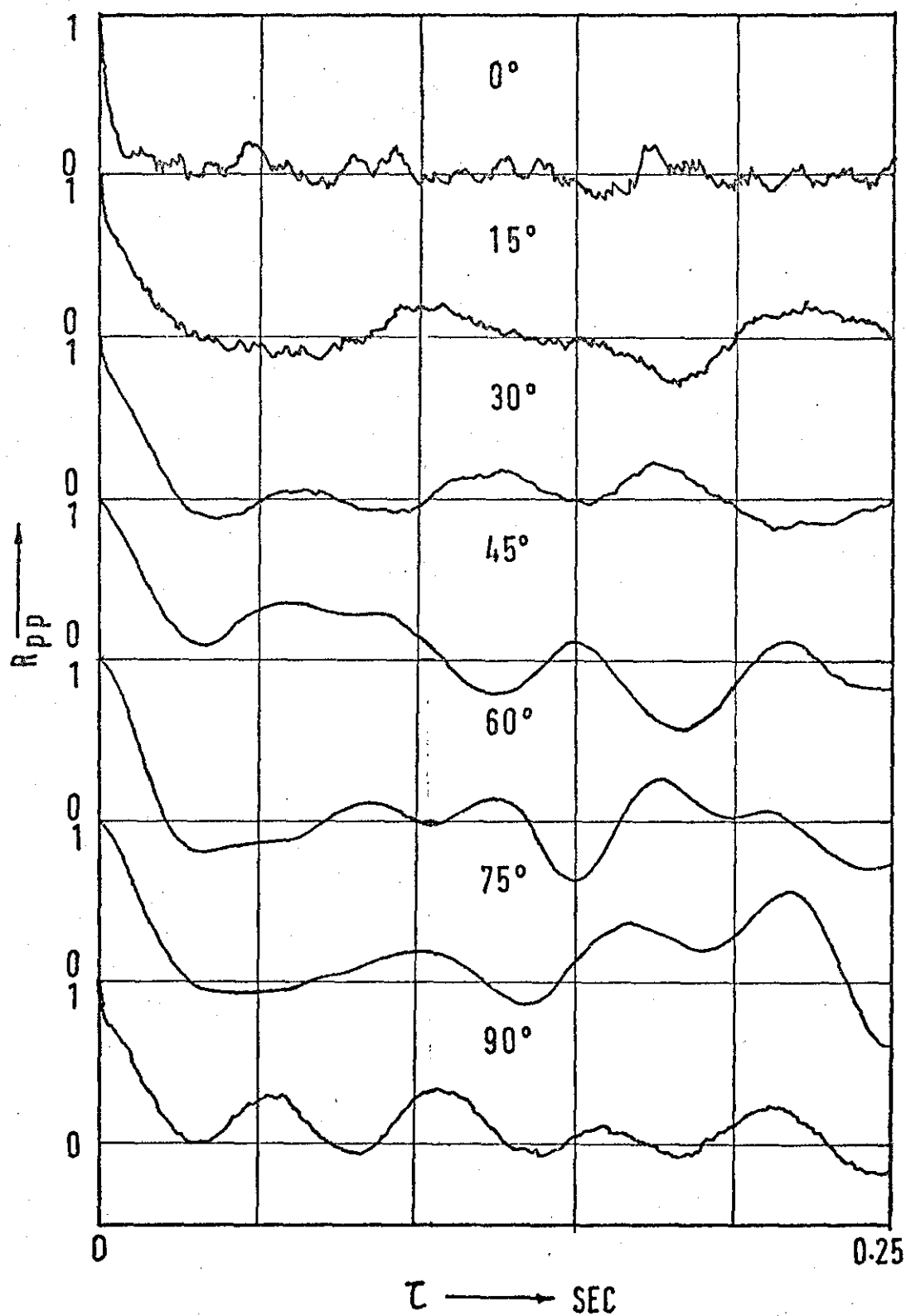
FIGURE 11·13   PRESSURE AUTOCORRELATIONS   RUN 19
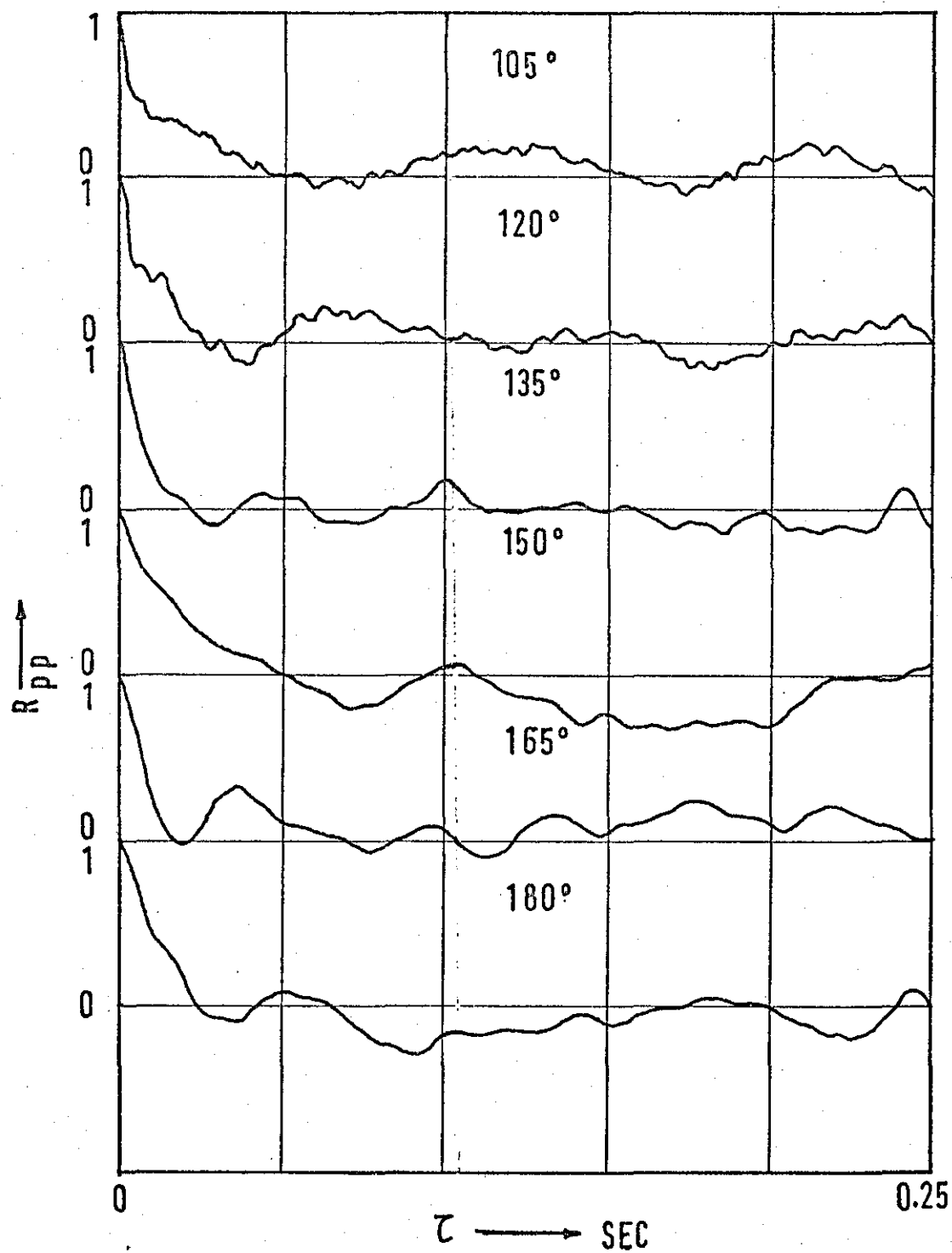
FIGURE 11-13 (CONT D)
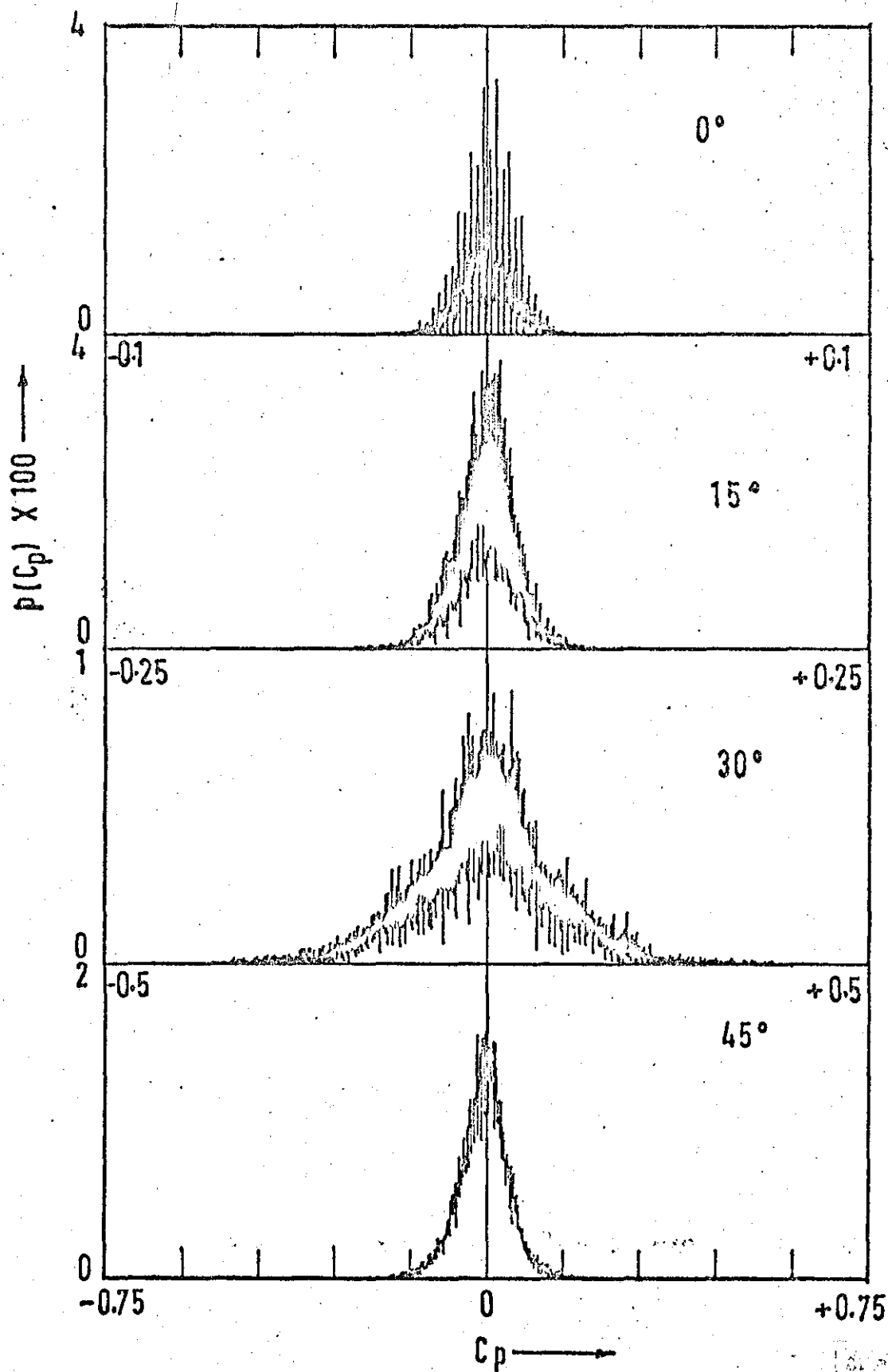
FIGURE 11·14   PROBABILITY   DENSITY   RUN 7 , T1   20480 samples
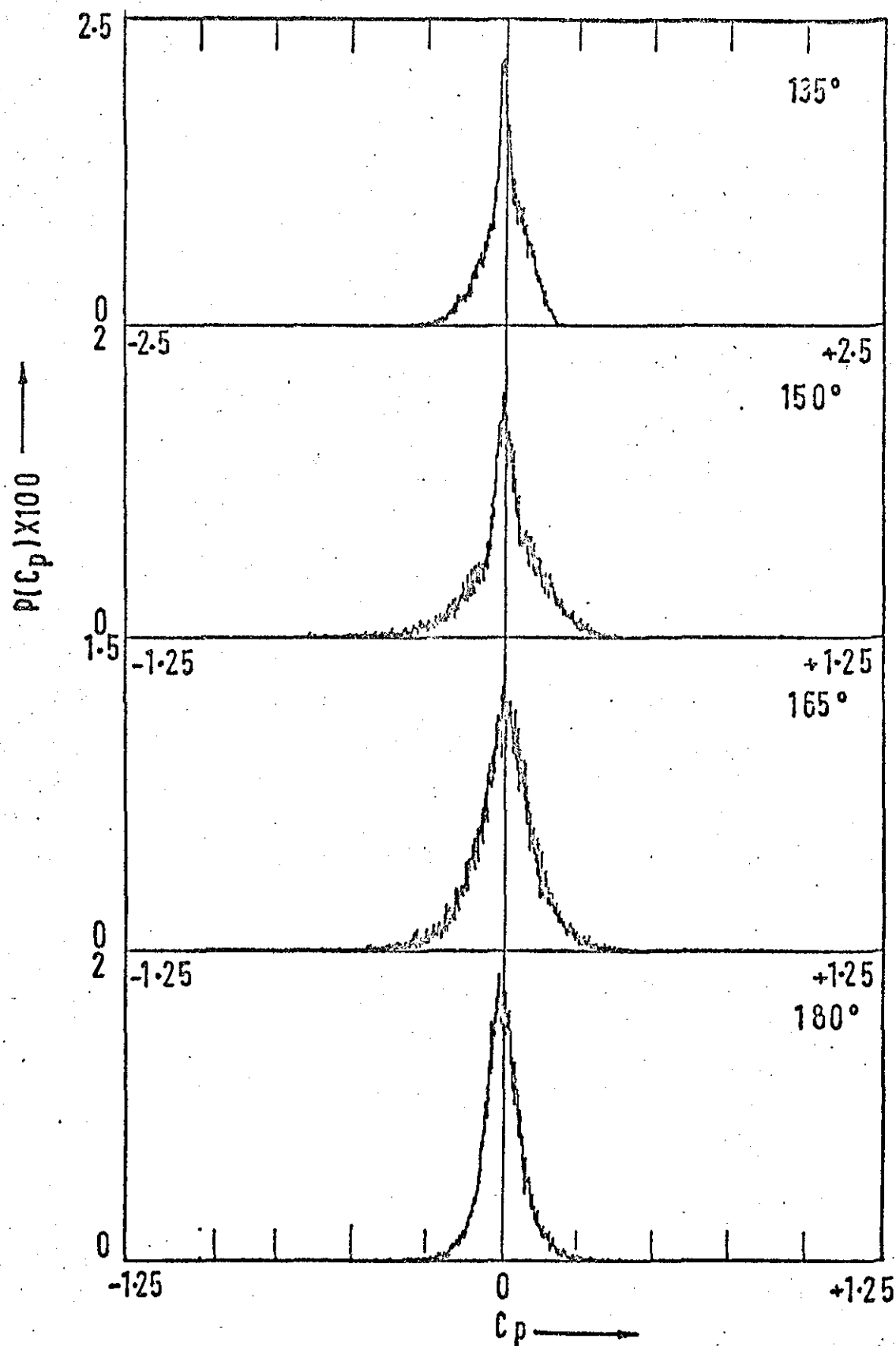
FIGURE 11-14 (CONT'D)
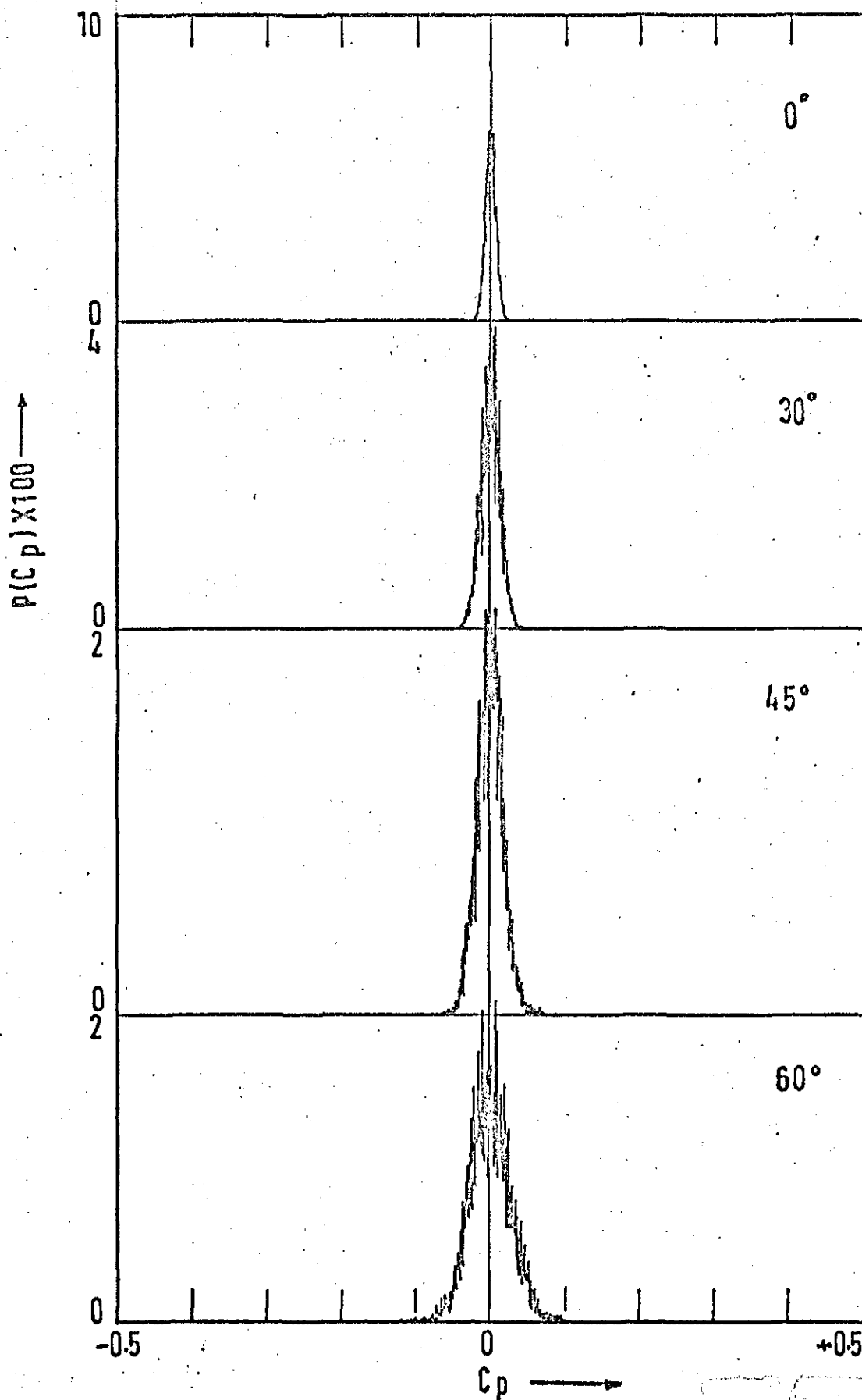
FIGURE 11·14 (CONT'D)

FIG.11·15 PROBABILITY DENSITY, RUN 4 ,T1, 2 0480 SAMPLES.
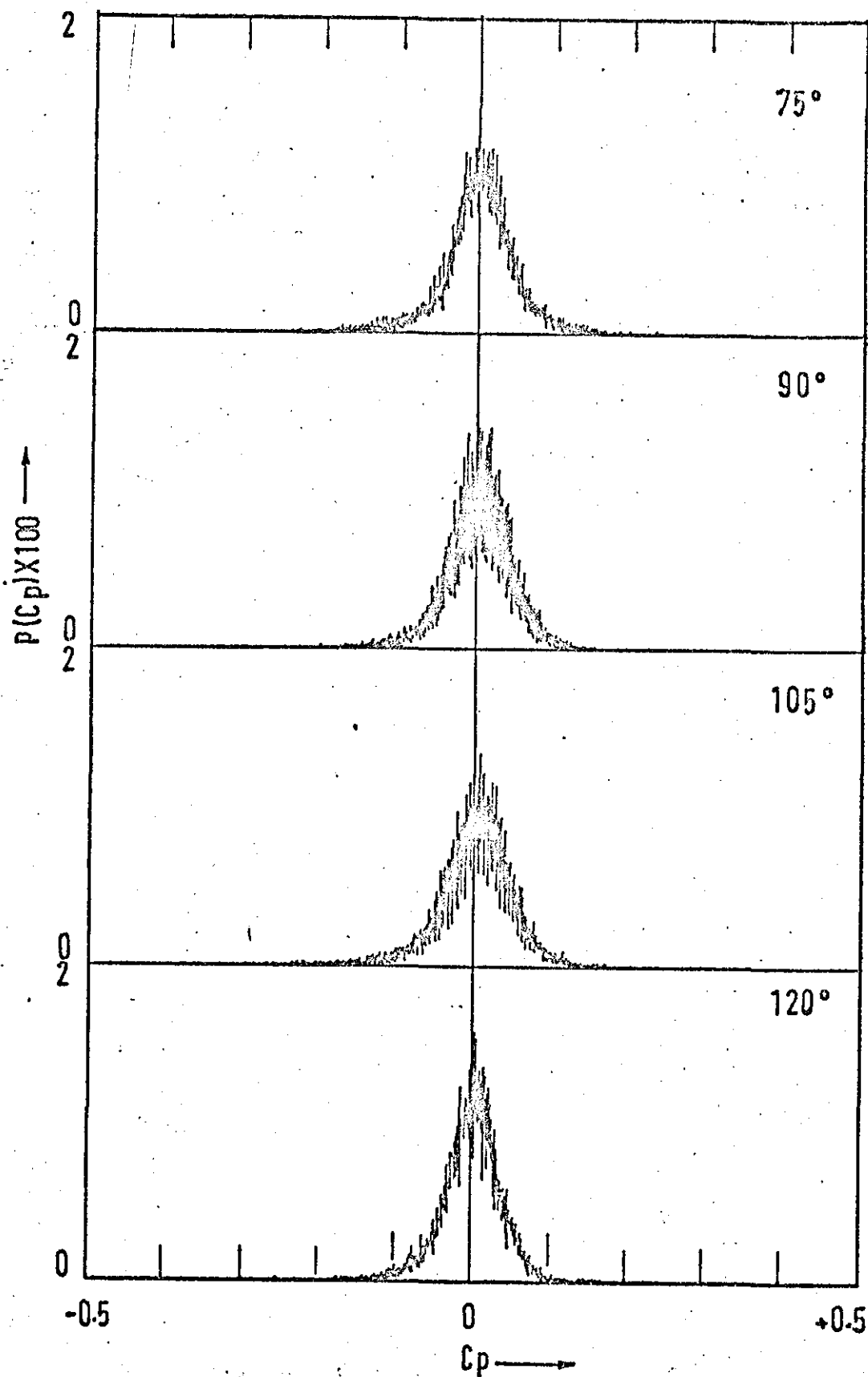
FIG. 11-15   CONT'D
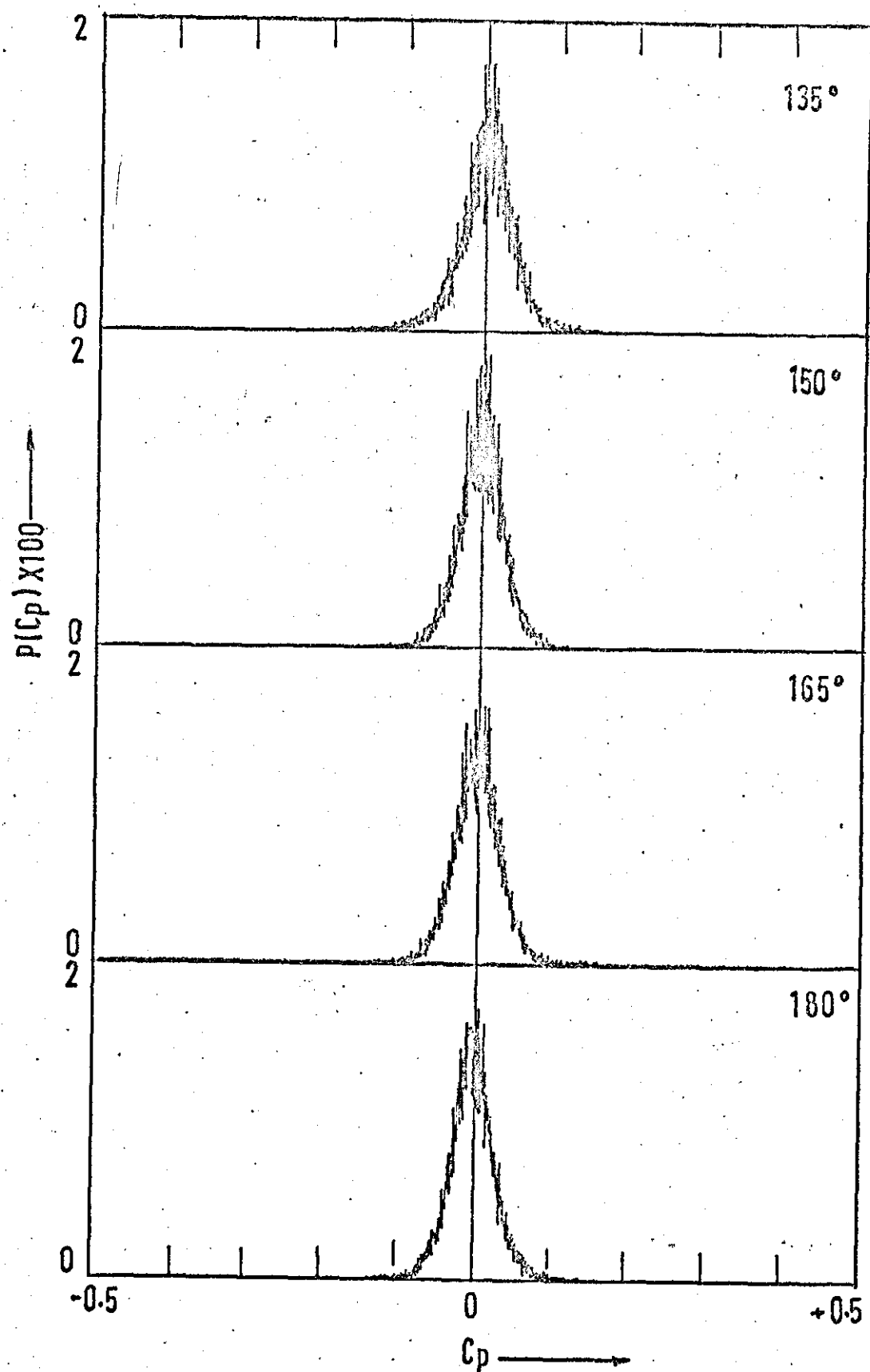
FIG. 11·15 CONT'D
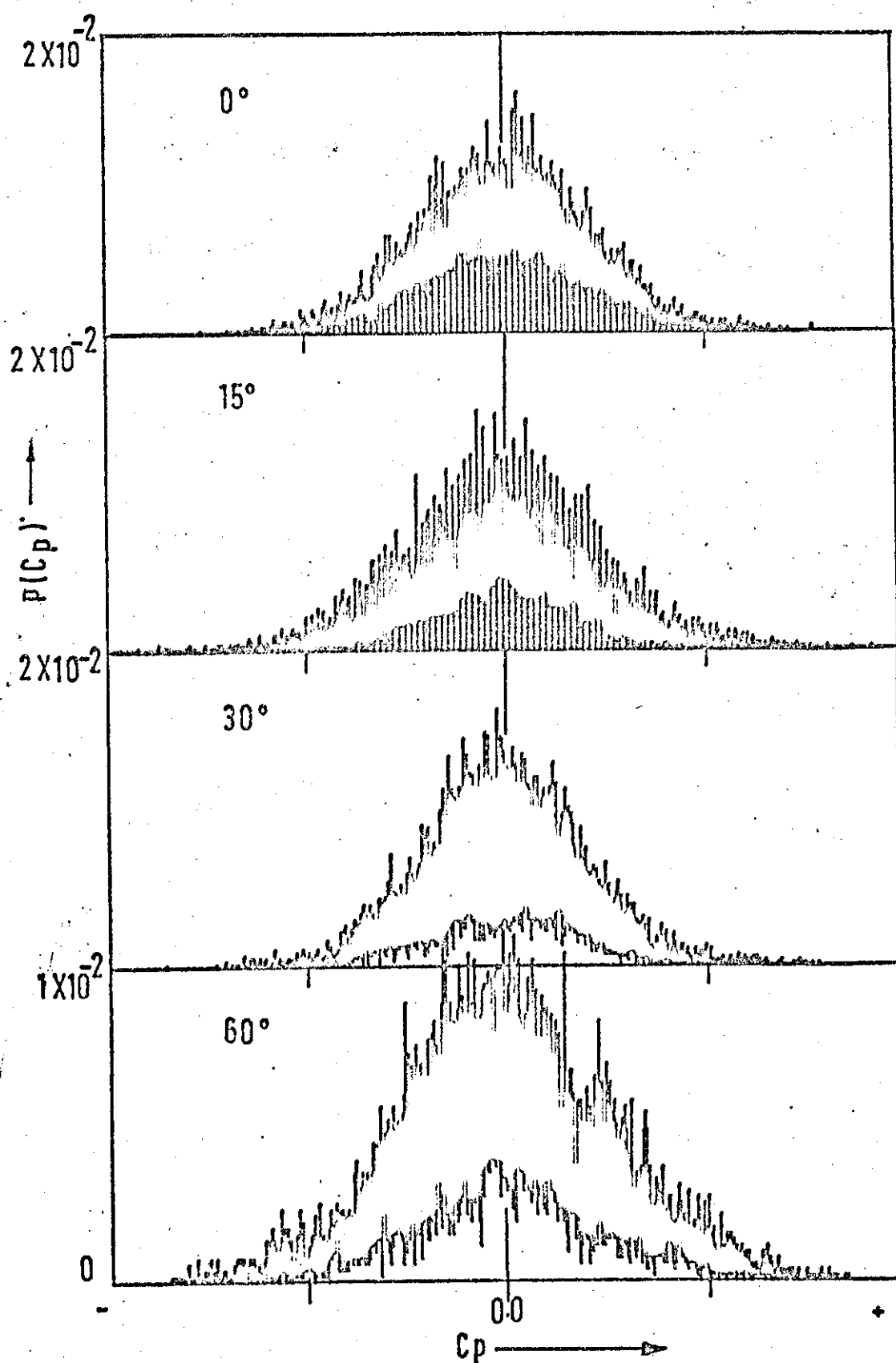
FIGURE 11-16   PROBABILITY DENSITY   RUN 19, 10240 SAMPLES
ARBITRARY C_p
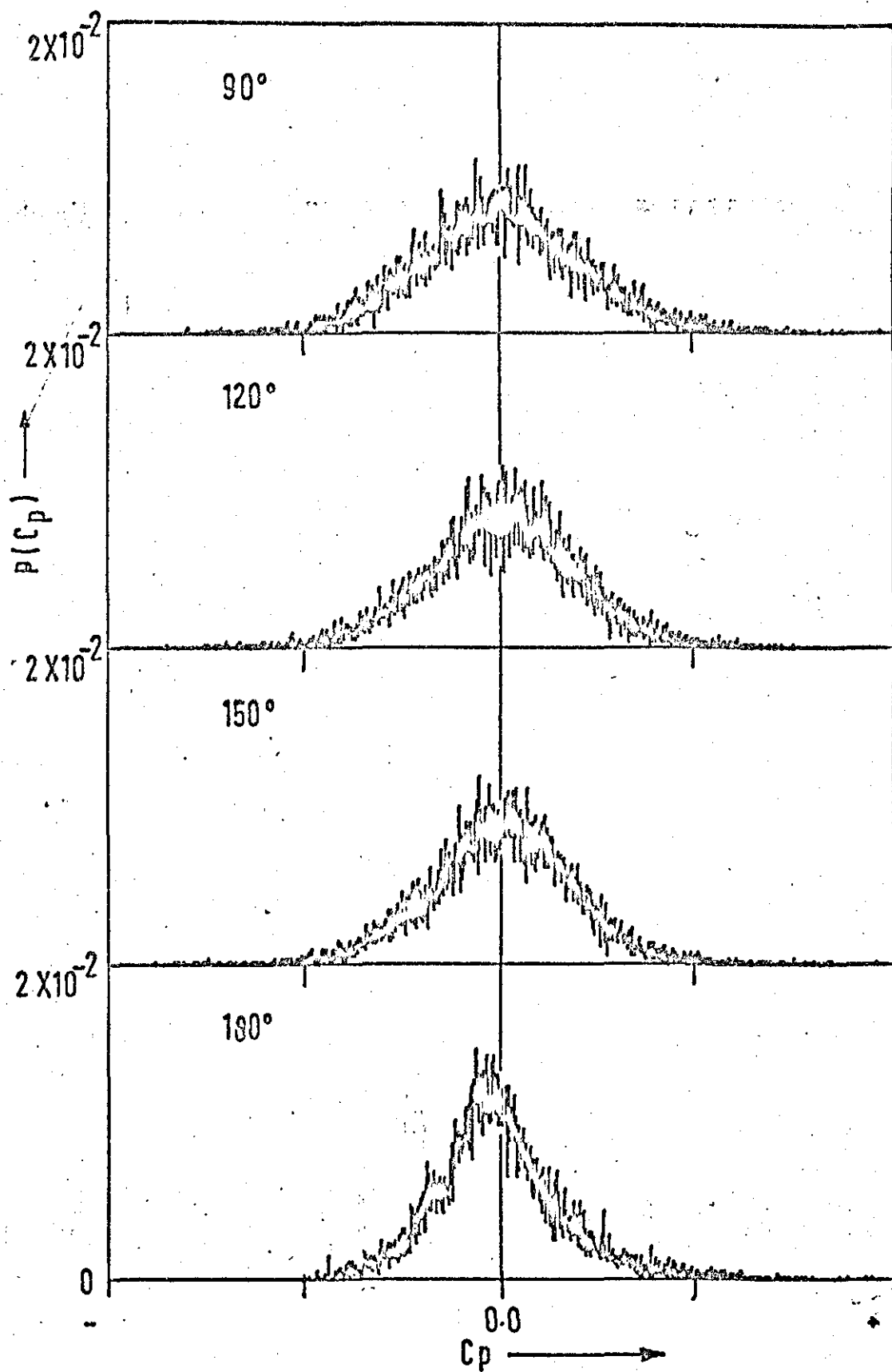
FIGURE 11·16 (CONT'D)
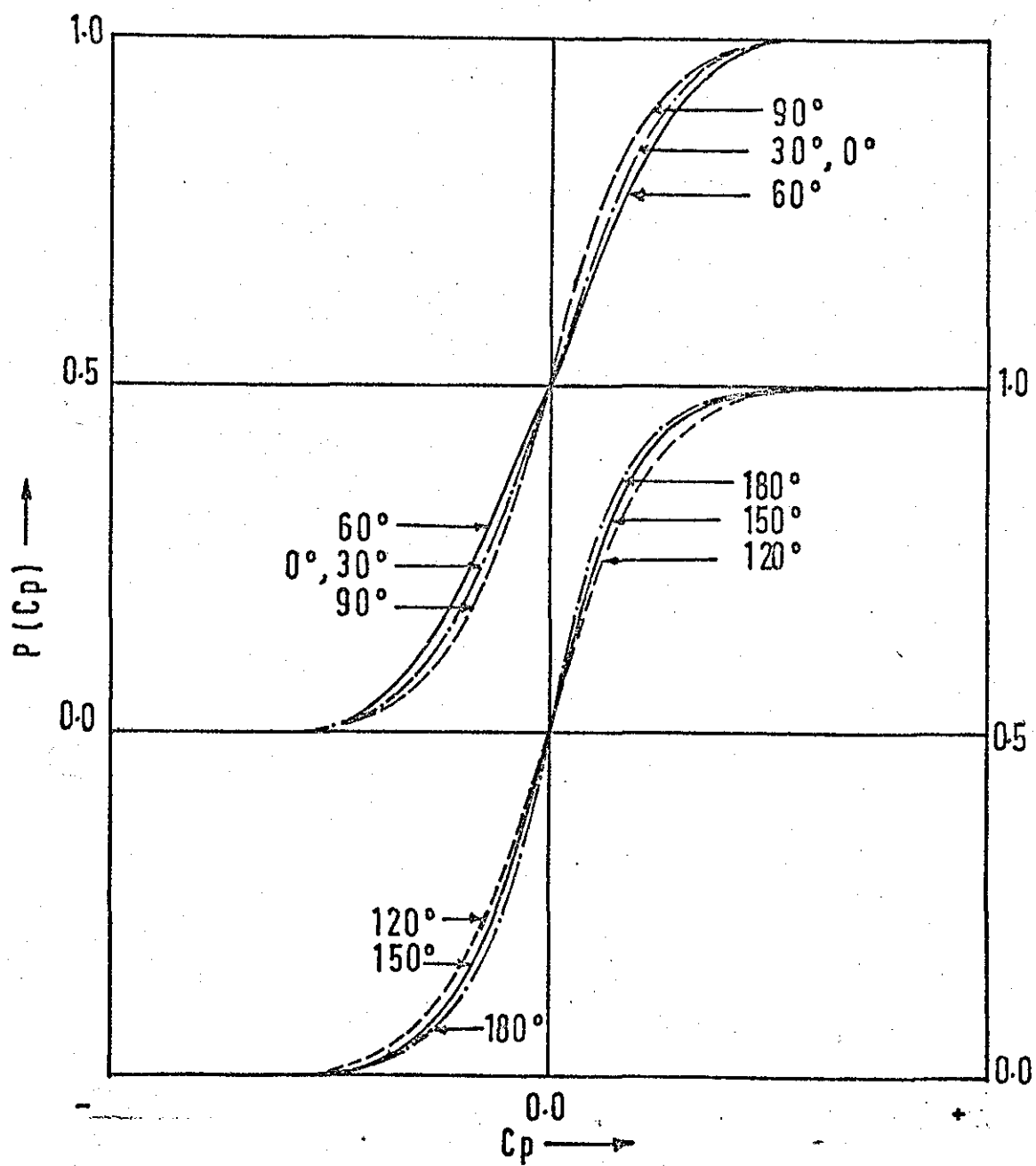
FIG. 11·17   PROBABILITY   DISTRIBUTION , RUN 19, 10240 SAMPLES
ARBITRARY C_p

FIG. 11.18. $\epsilon_{\theta\theta}$, SHELL F4 (66", 60°)

FIG.11.19. ϵ_{xx},SHELL F5 (2",0°)

The figure shows multiple spectral plots (Runs 28–34) of $\bar{S}_{ee} \times 100$ versus frequency (Hz), with the horizontal axis ranging from 0 to 200 Hz. A legend in Run 33 gives:

symbol	mode	frequency
•	1,2	27 Hz
o	1,1	46 Hz
+	2,3	86 Hz
x	2,2	93 Hz
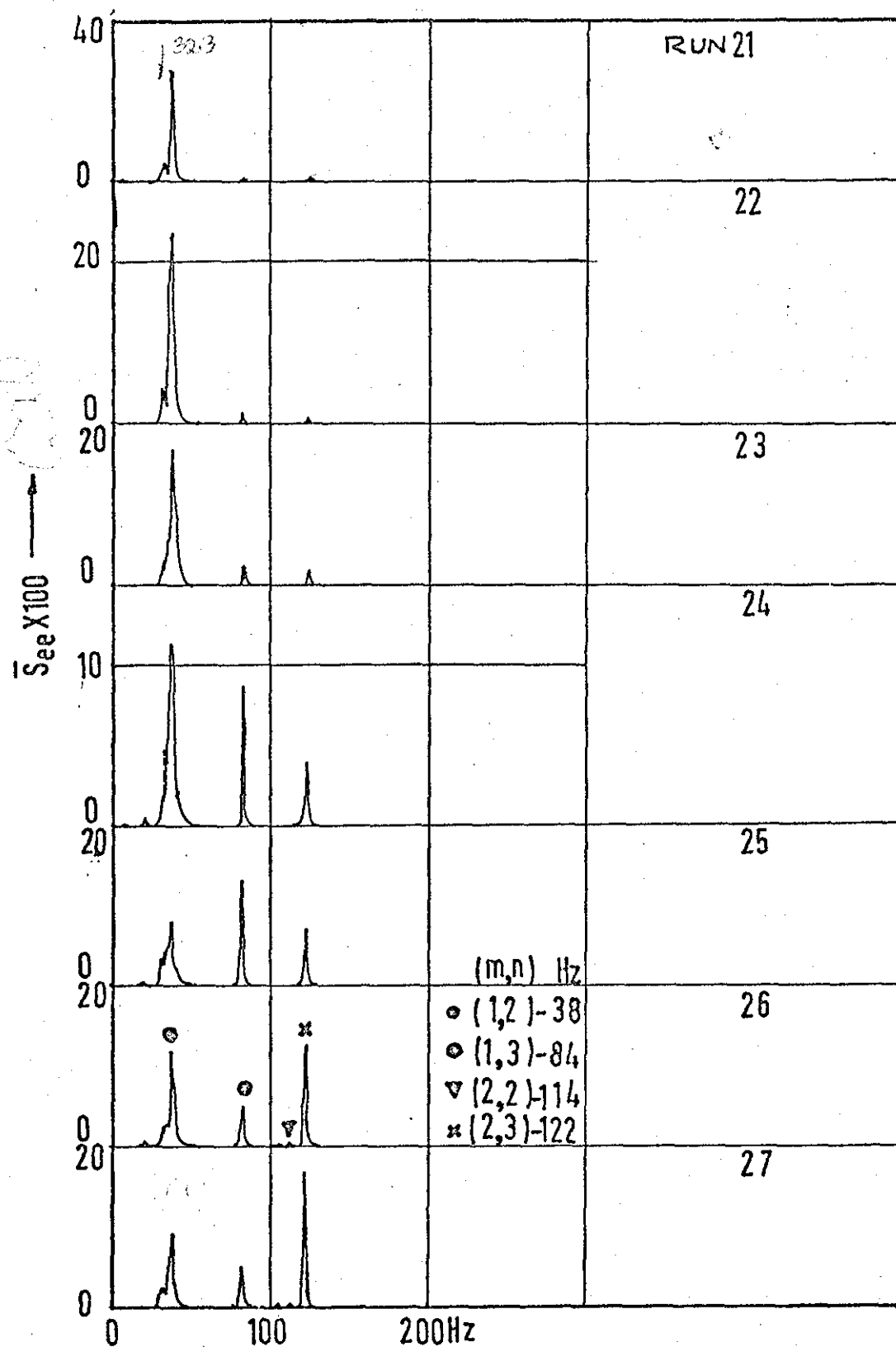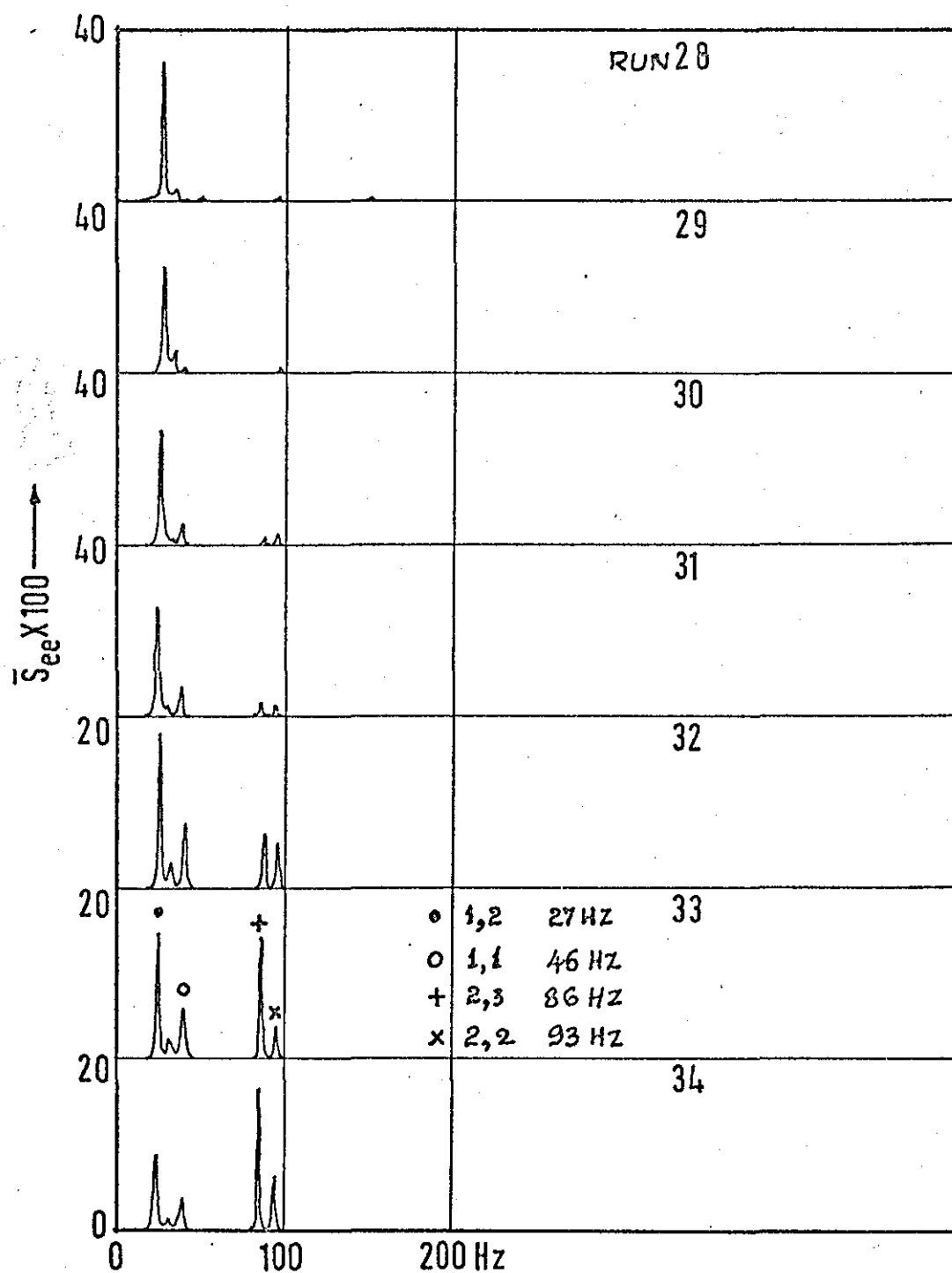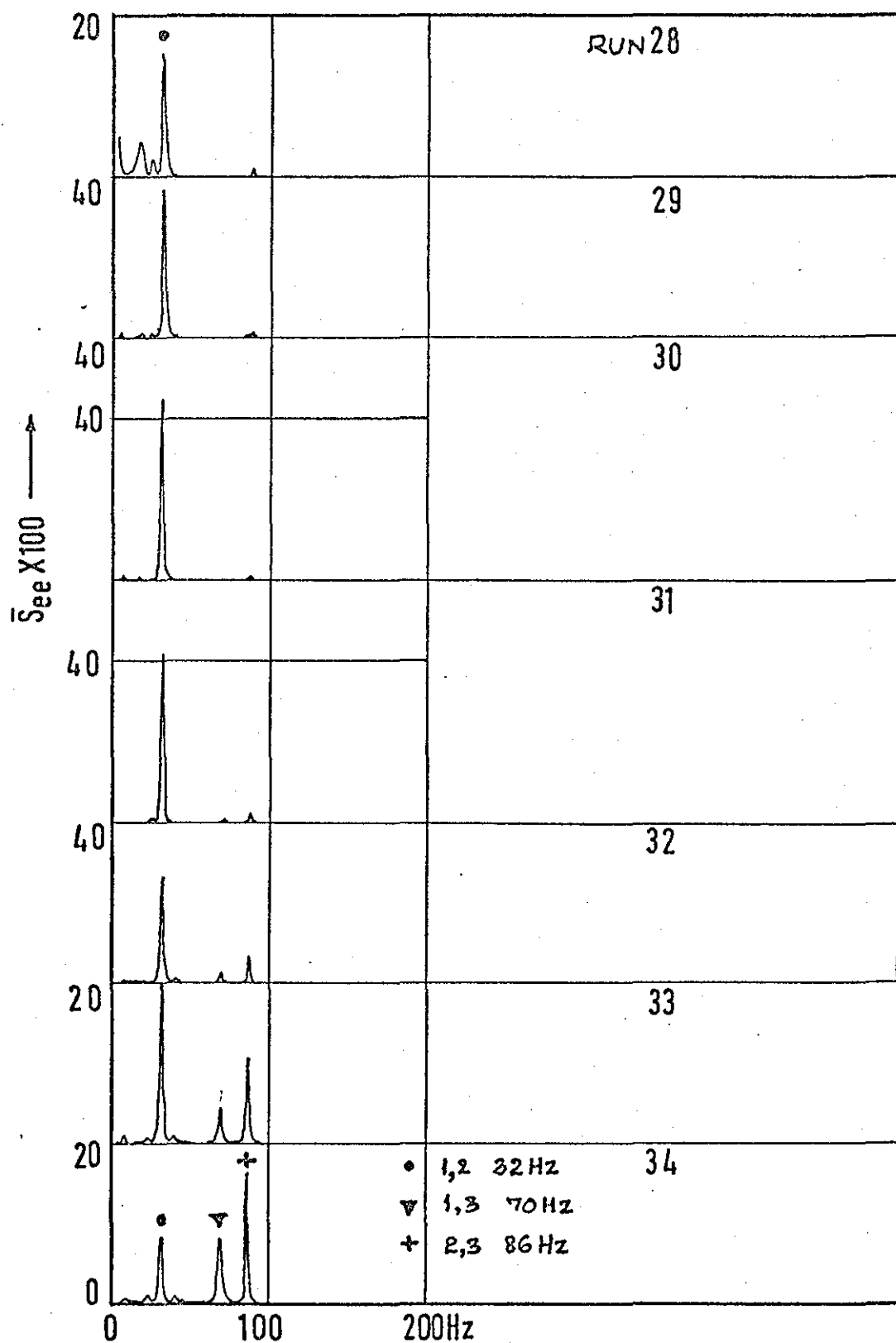
FIG. 11.20 $\epsilon_{\theta\theta}$, SHELL F5 (66", 45°)
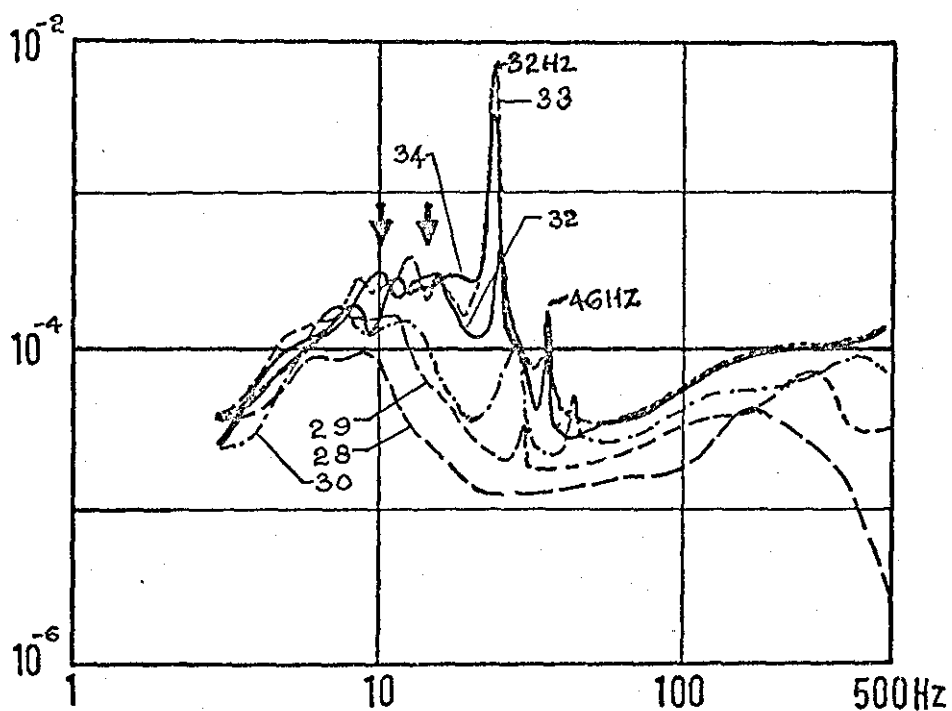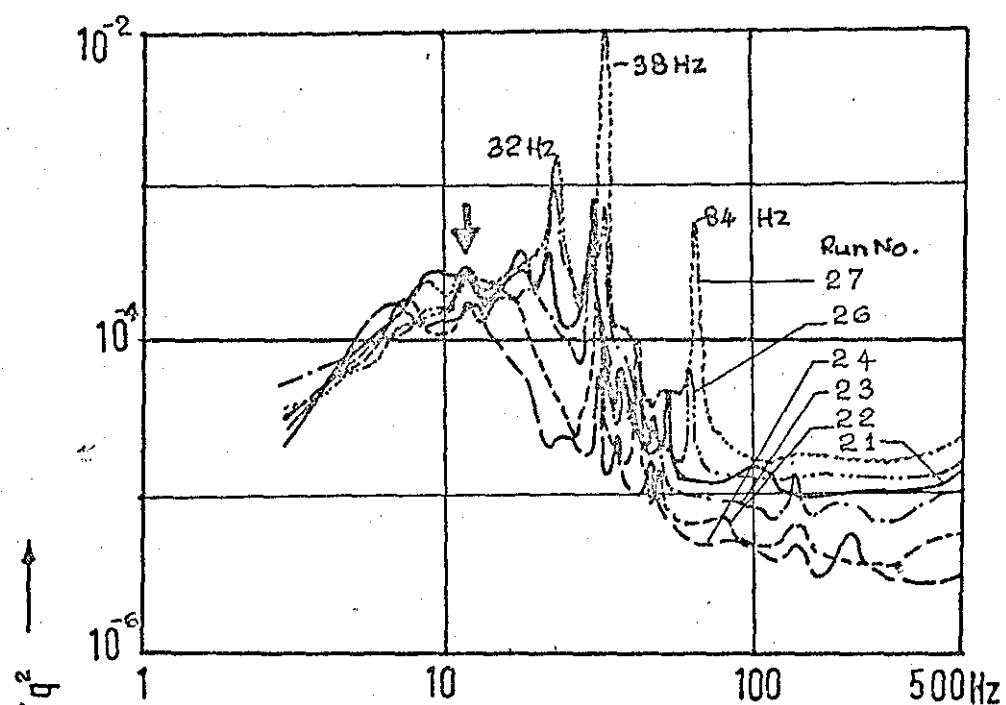
FIG.11.21 PRESSURE SPECTRA, SHELLS F4&F5 (90°)
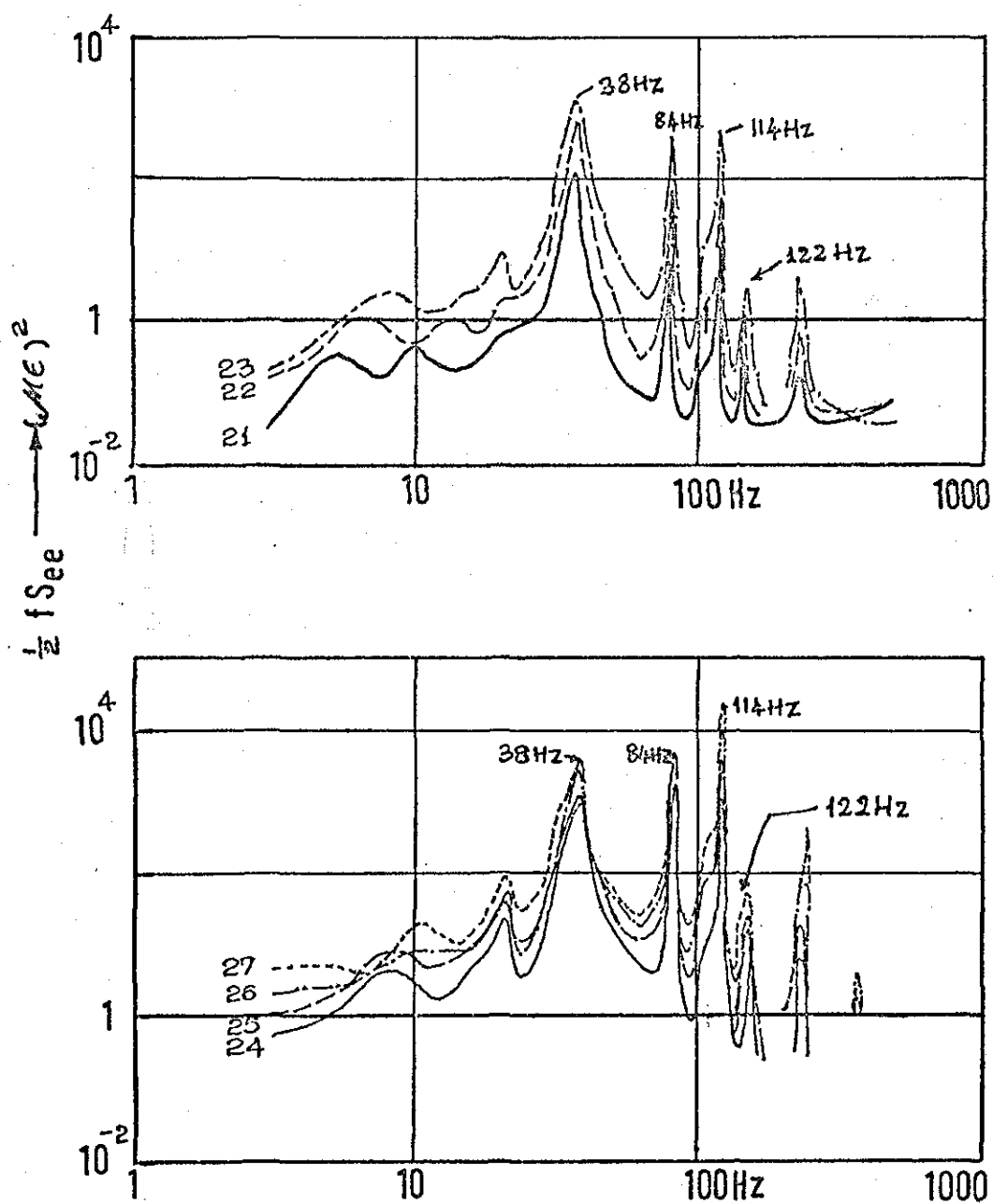
FIG. 11.22 STRAIN SPECTRA, SHELL F4(66^{n},60°),
BREATHING MODES
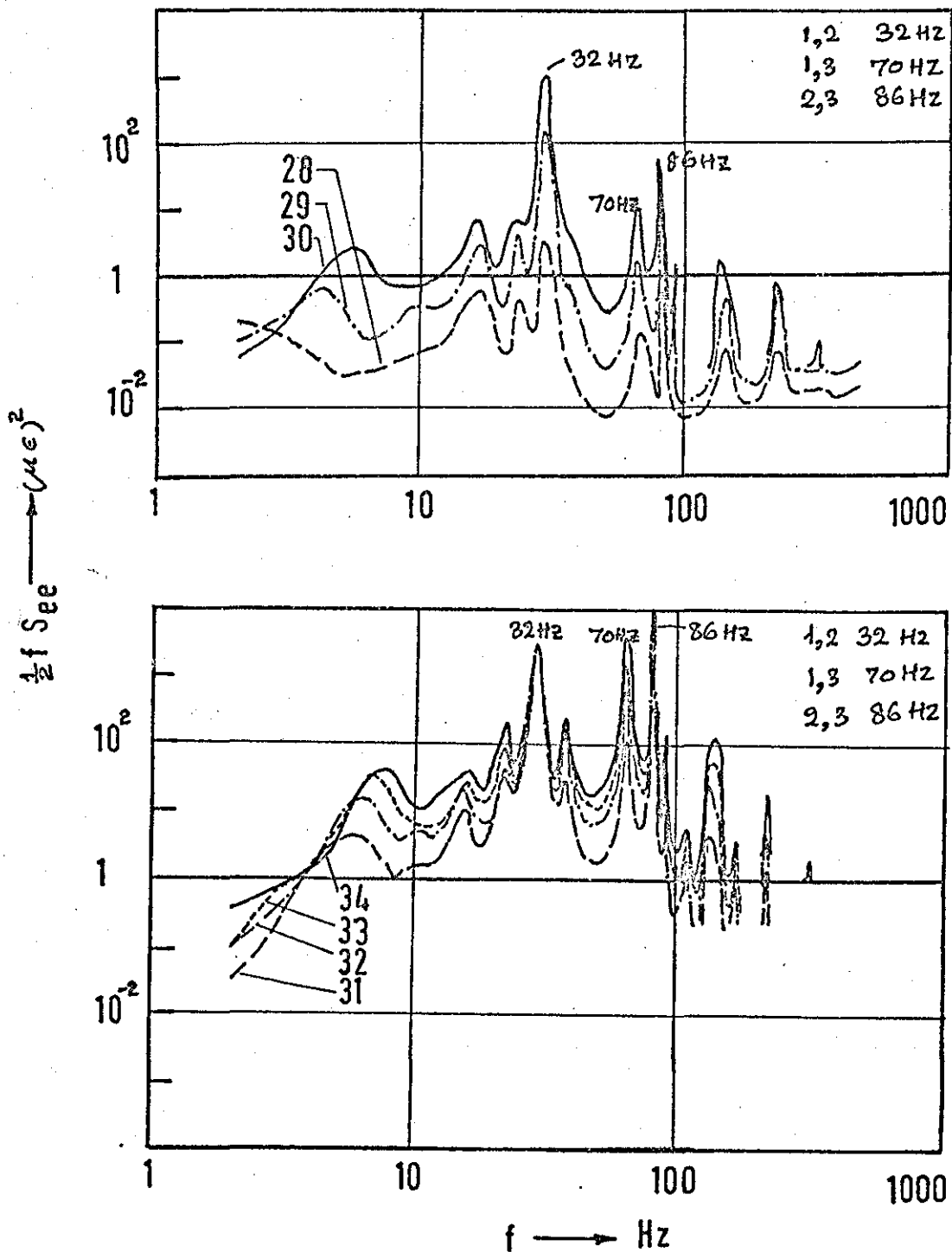
FIG. 11.23 STRAIN SPECTRA , SHELL F5(66",45°),
BREATHING MODES
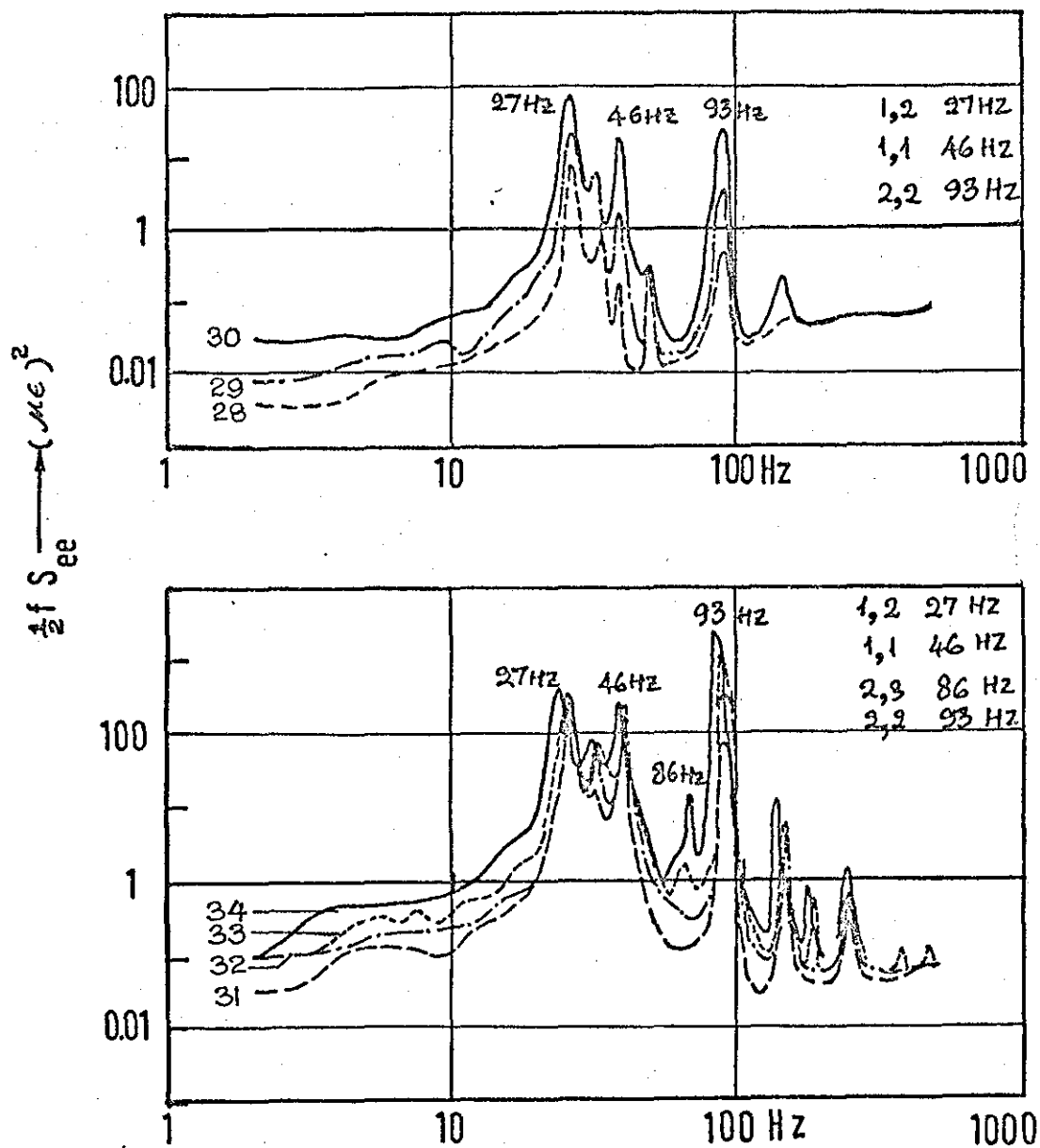
FIG. 11.24 STRAIN SPECTRA, SWAY MODES, SHELL F5 (2,0)
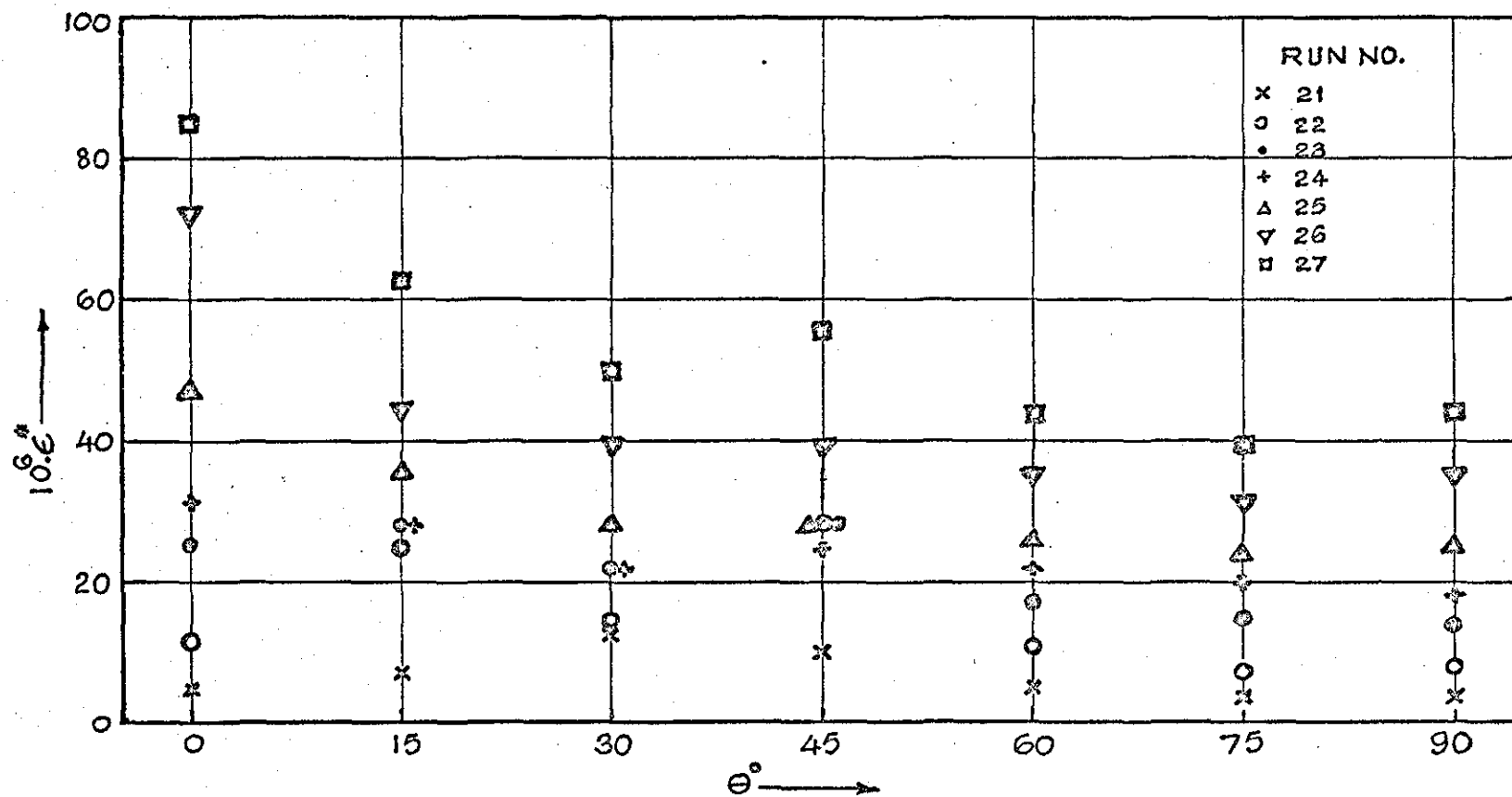
FIG.11.25   BREATHING MODES,   SHELL F4 $(66'',\overset{\circ}{\theta})$

FIG.11.26 SWAY MODES, SHELL F4(1″,θ°)
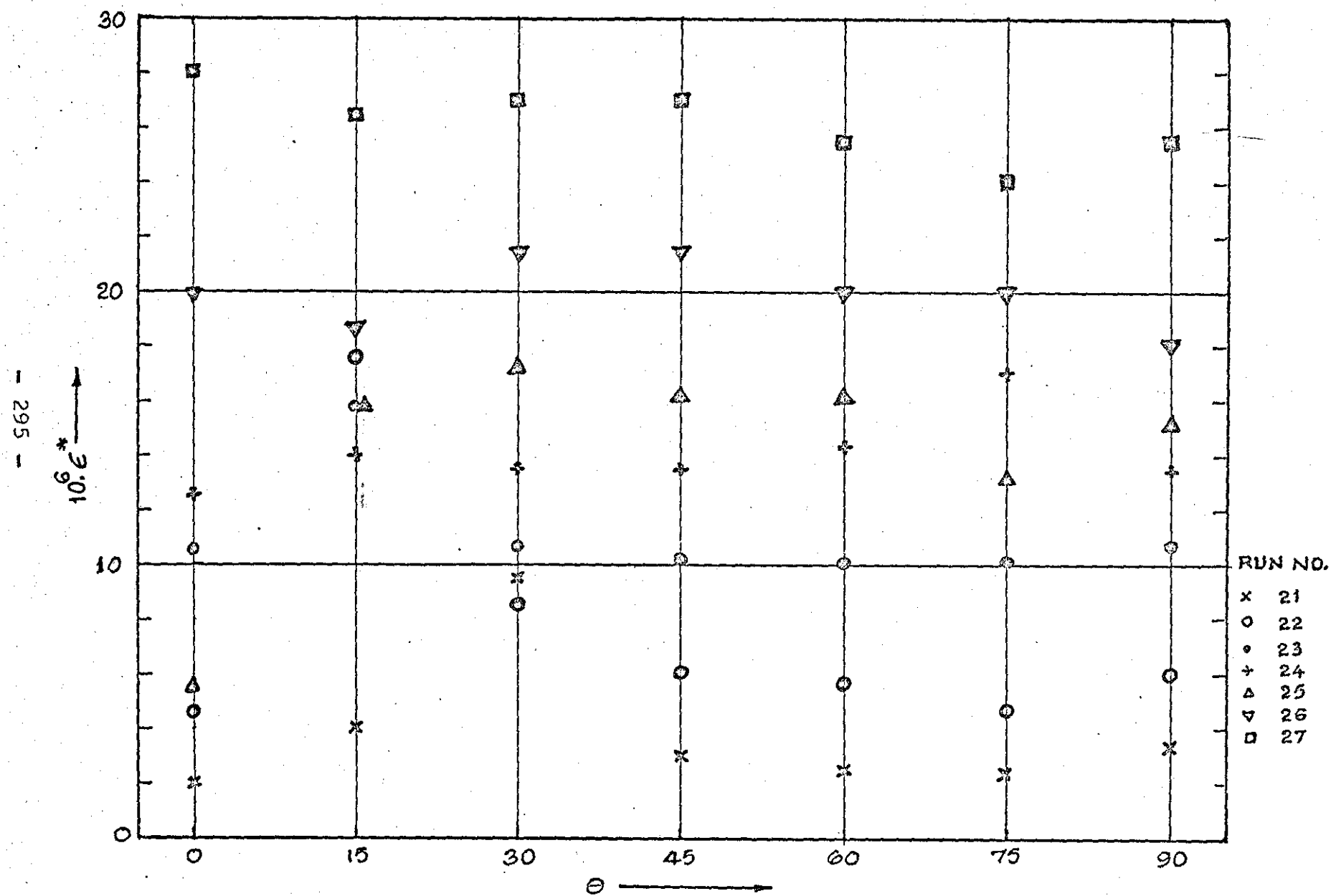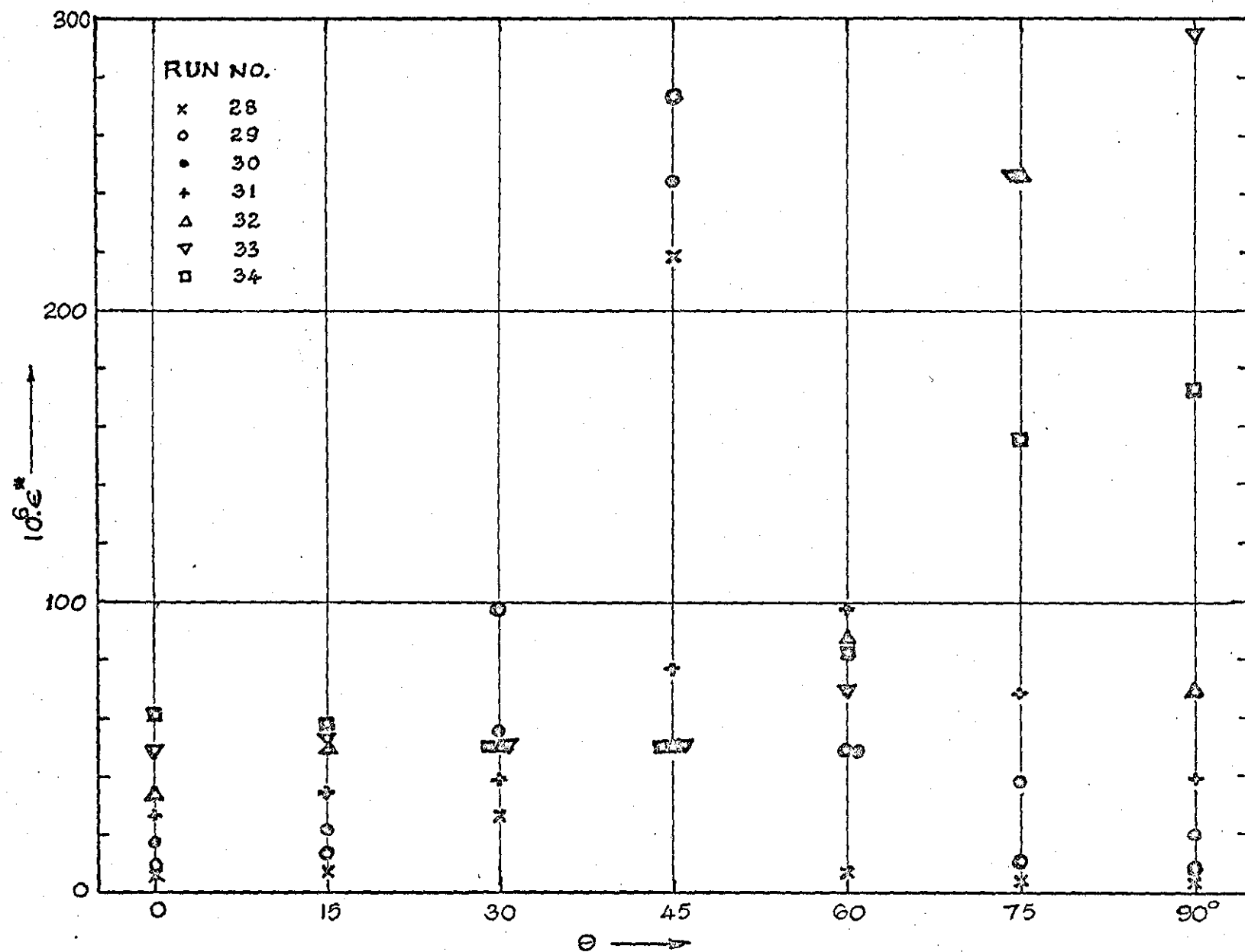
FIG. 11.27   BREATHING MODES, SHELL F5 (66", θ°)
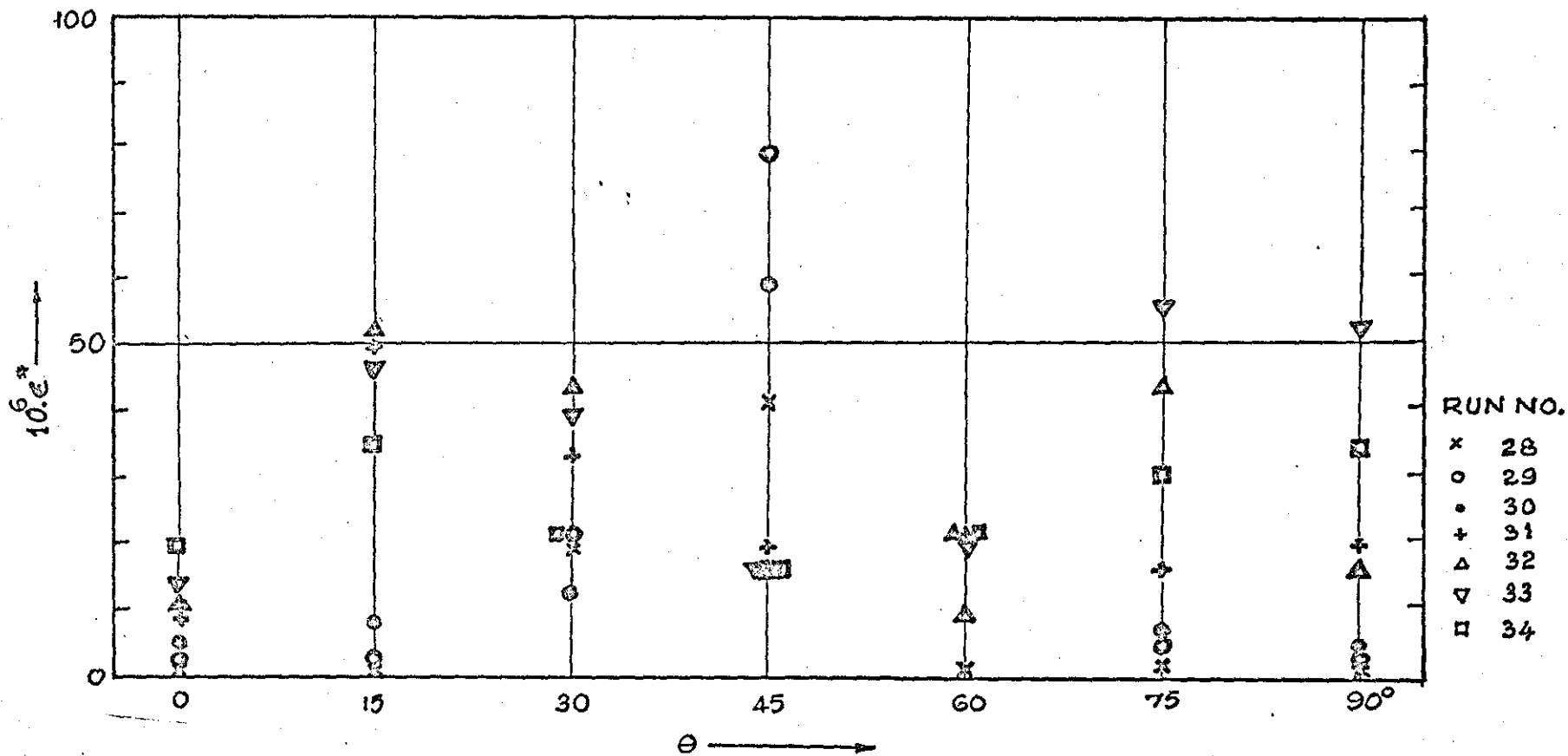
FIG.11.28   SWAY MODES, SHELL F5 (2,8)
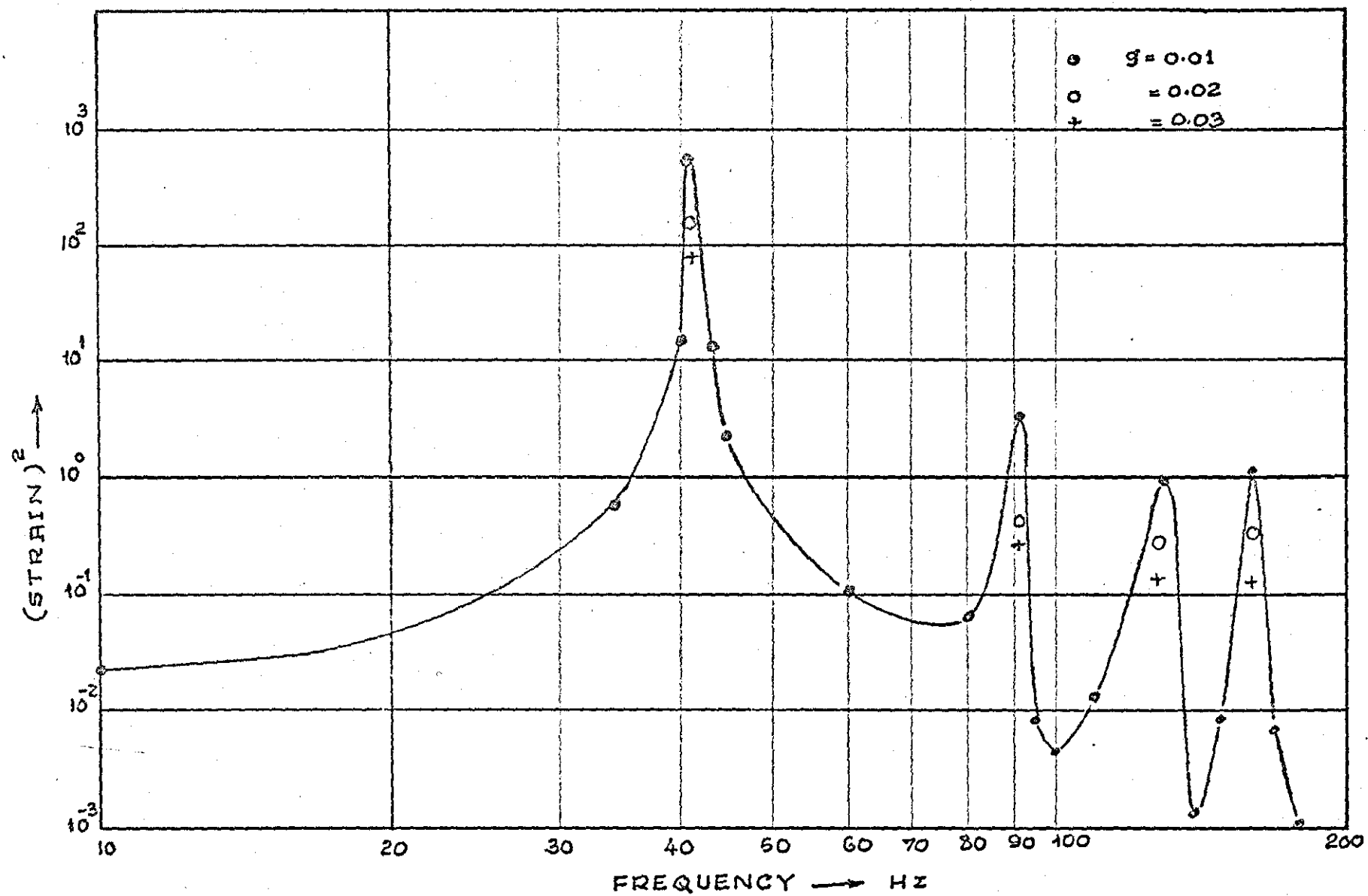
FIG. 11.29   COMPUTED STRAIN SPECTRA. SHELL F4 (66", 60°)
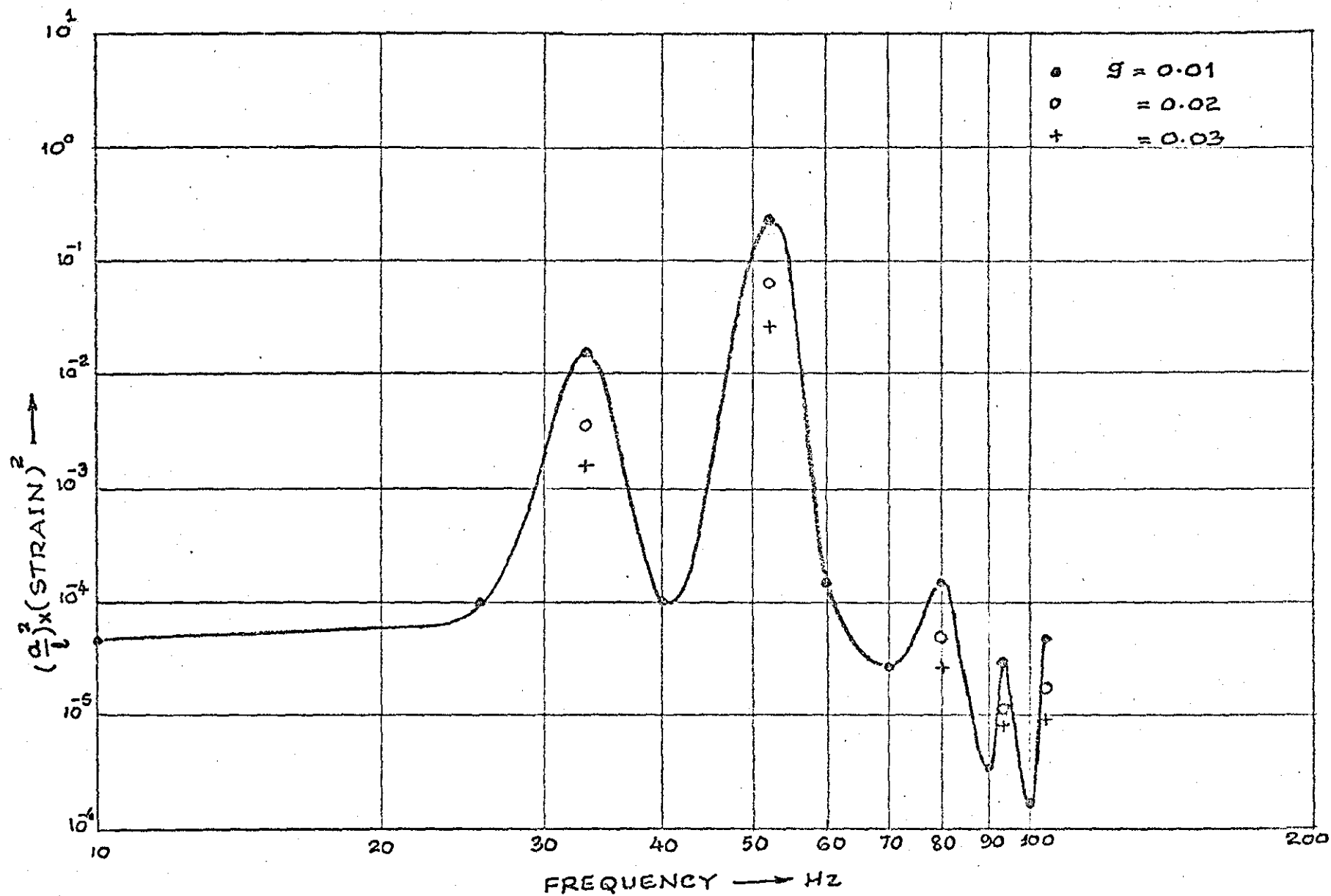
FIG. 11.30   COMPUTED STRAIN SPECTRA, SHELL F5 (2", 0°)
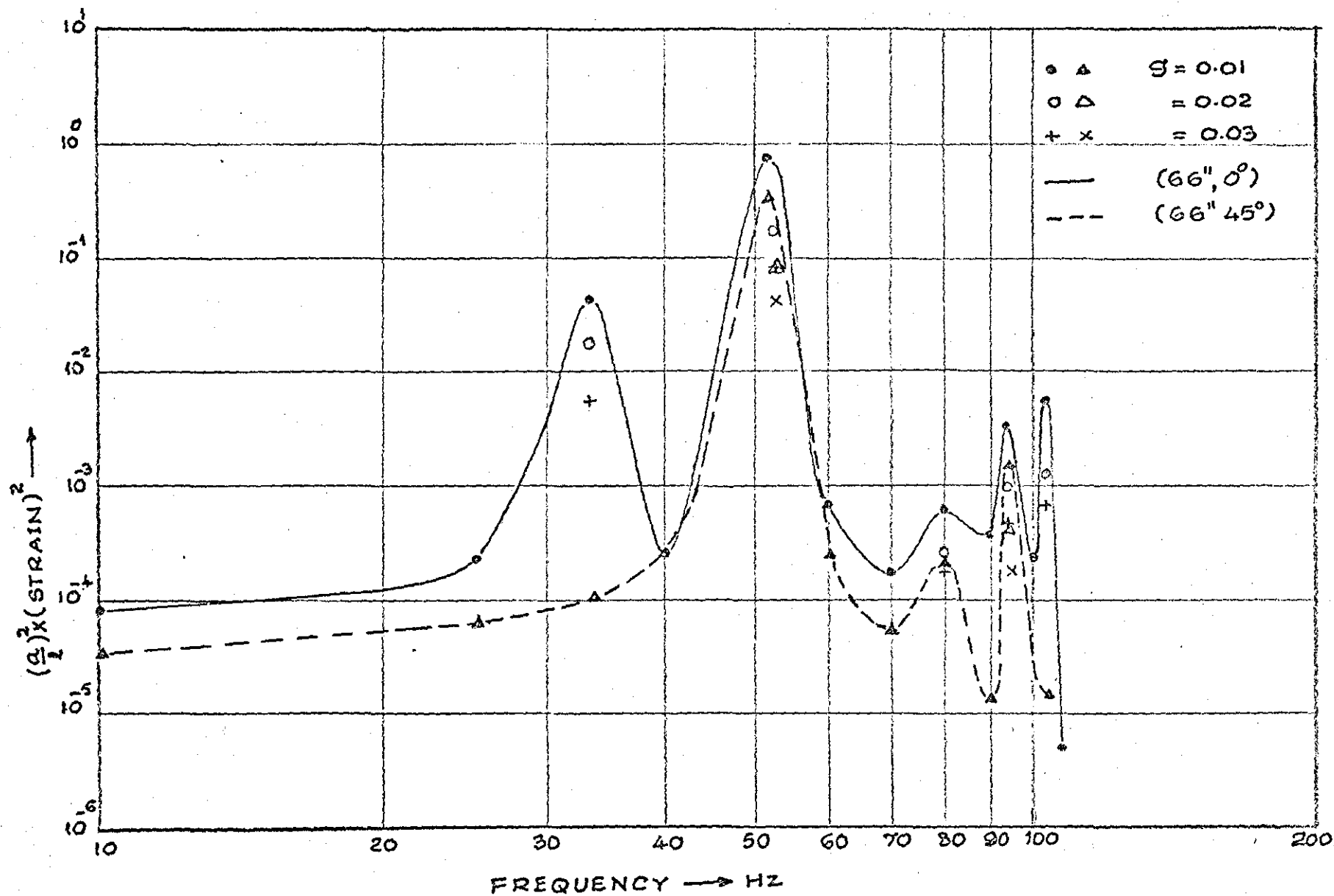
FIG 11.31   COMPUTED   STRAIN   SPECTRA,   SHELL F5
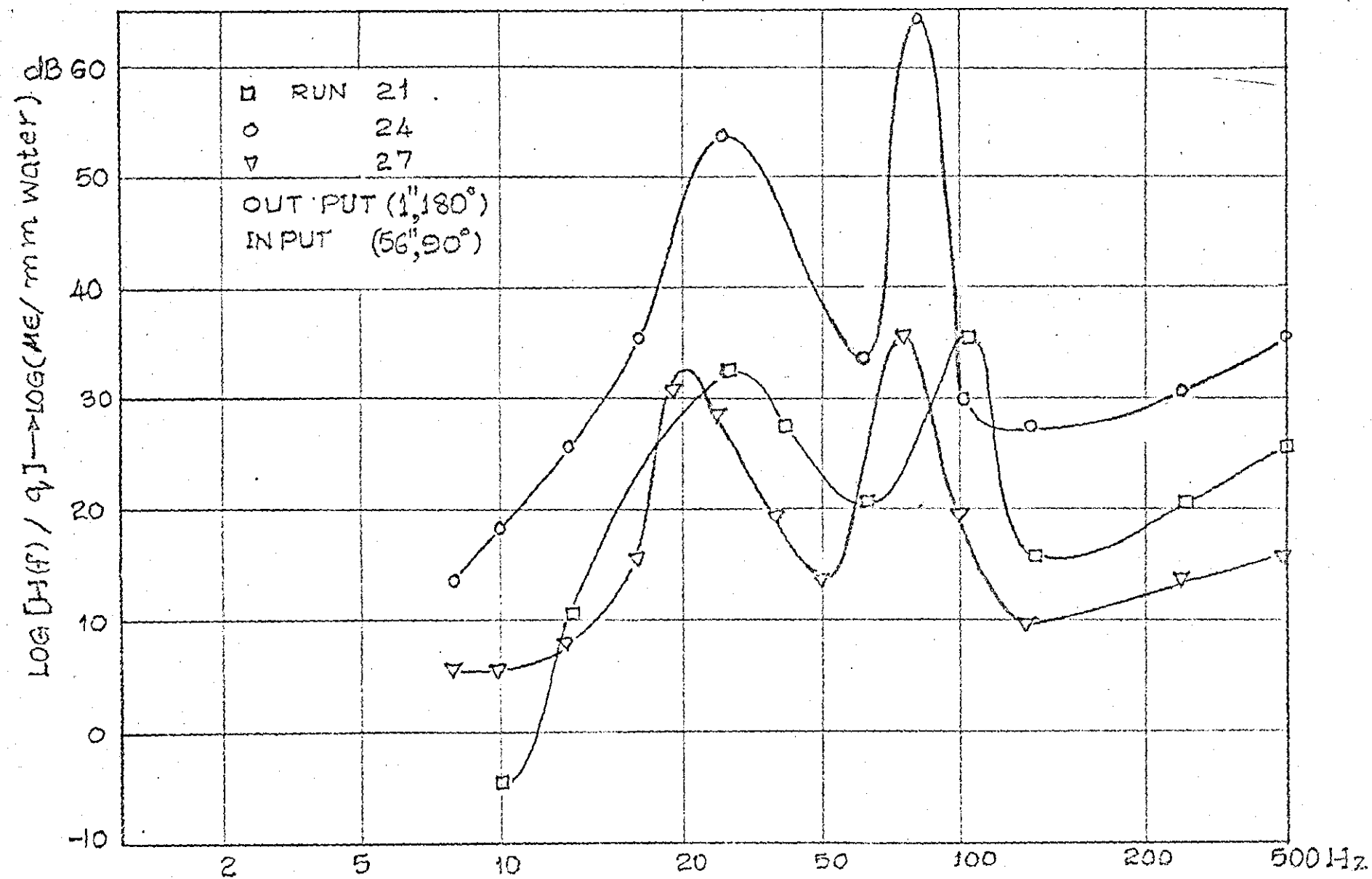
FIG. 11·32 MEASURED TRANSFER FUNCTION, SHELL F4.
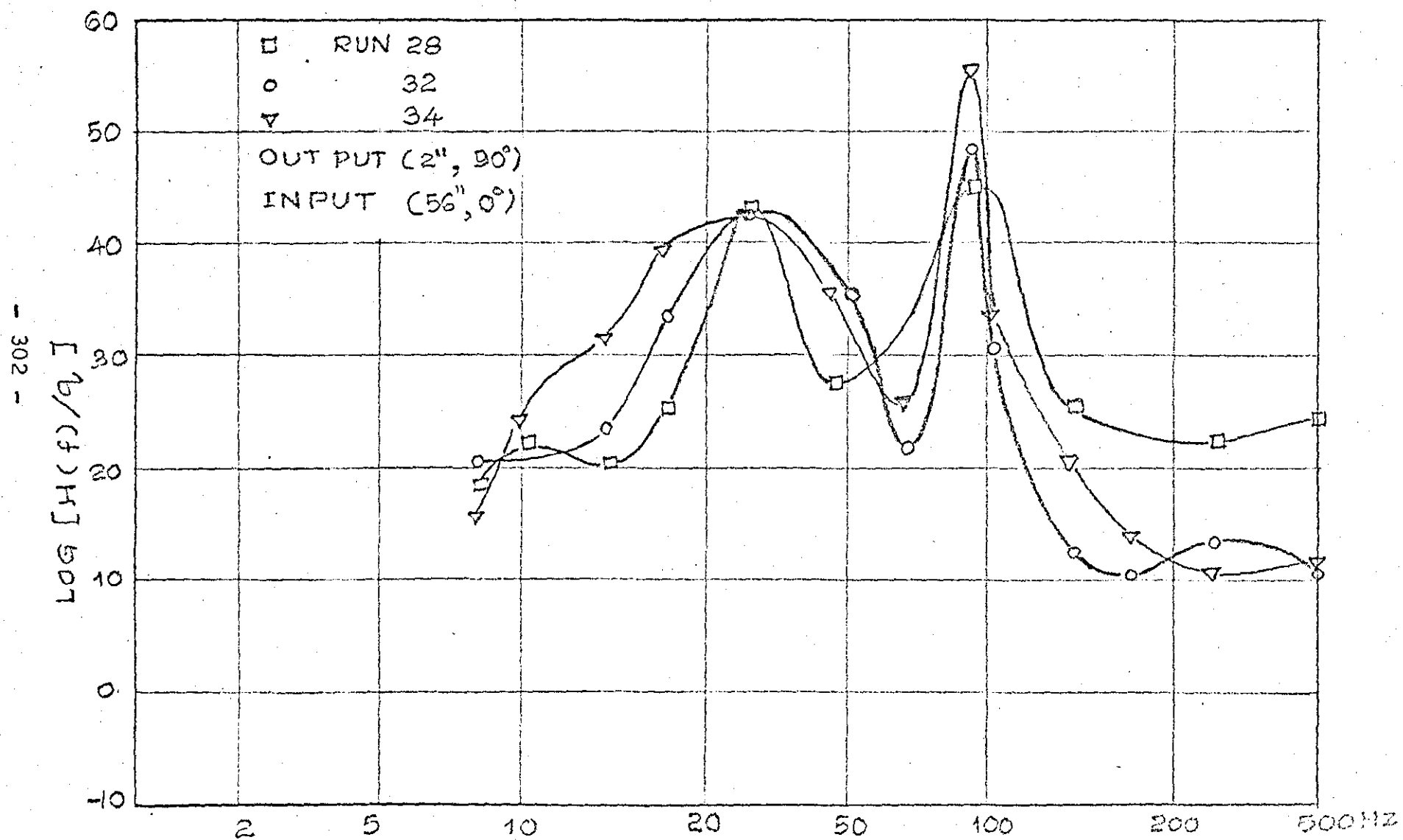
FIG. 11.33   MEASURED   TRANSFER FUNCTION, SHELL F5.
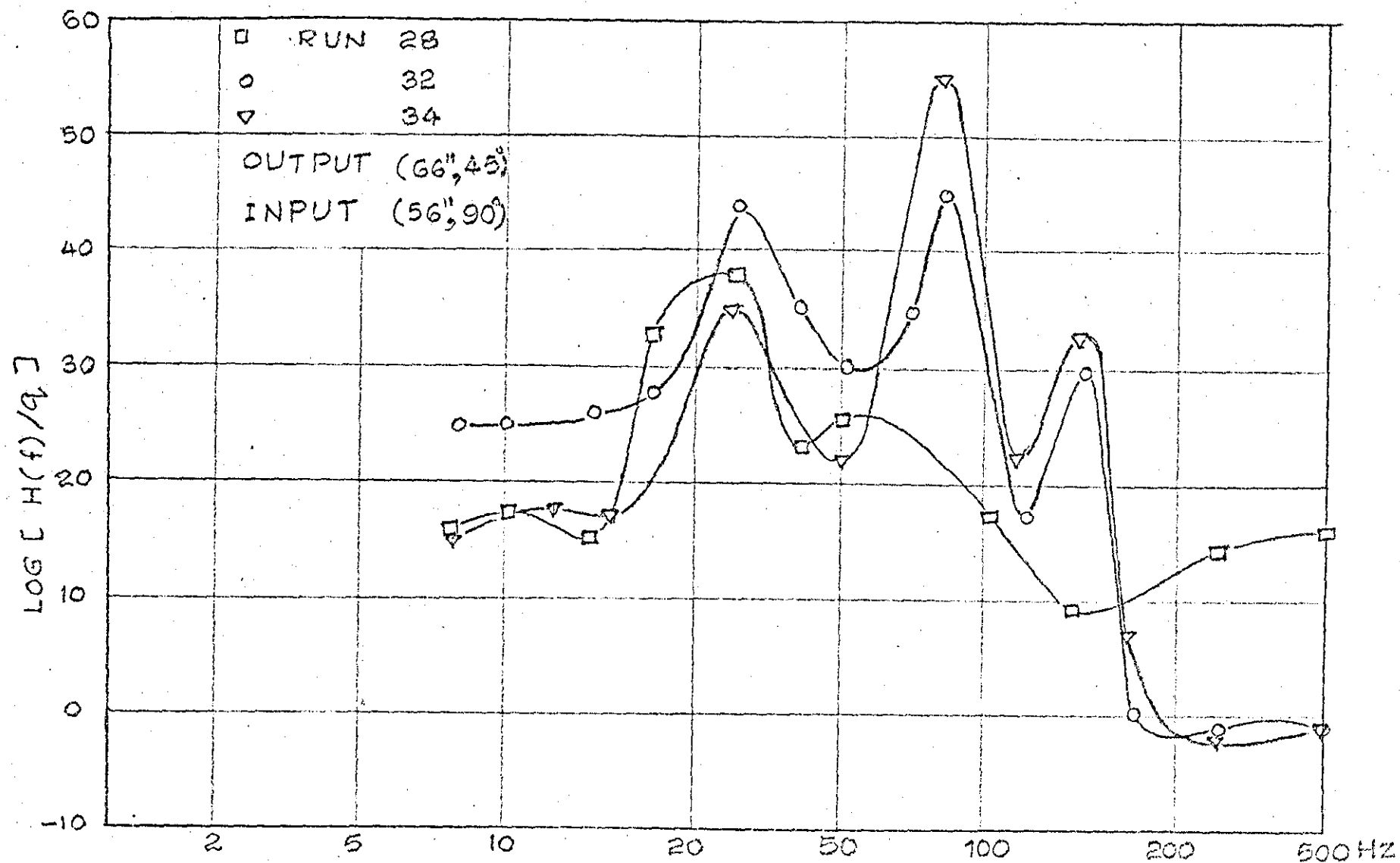
FIG. 11.34 MEASURED TRANSFER FUNCTION, SHELL F5.
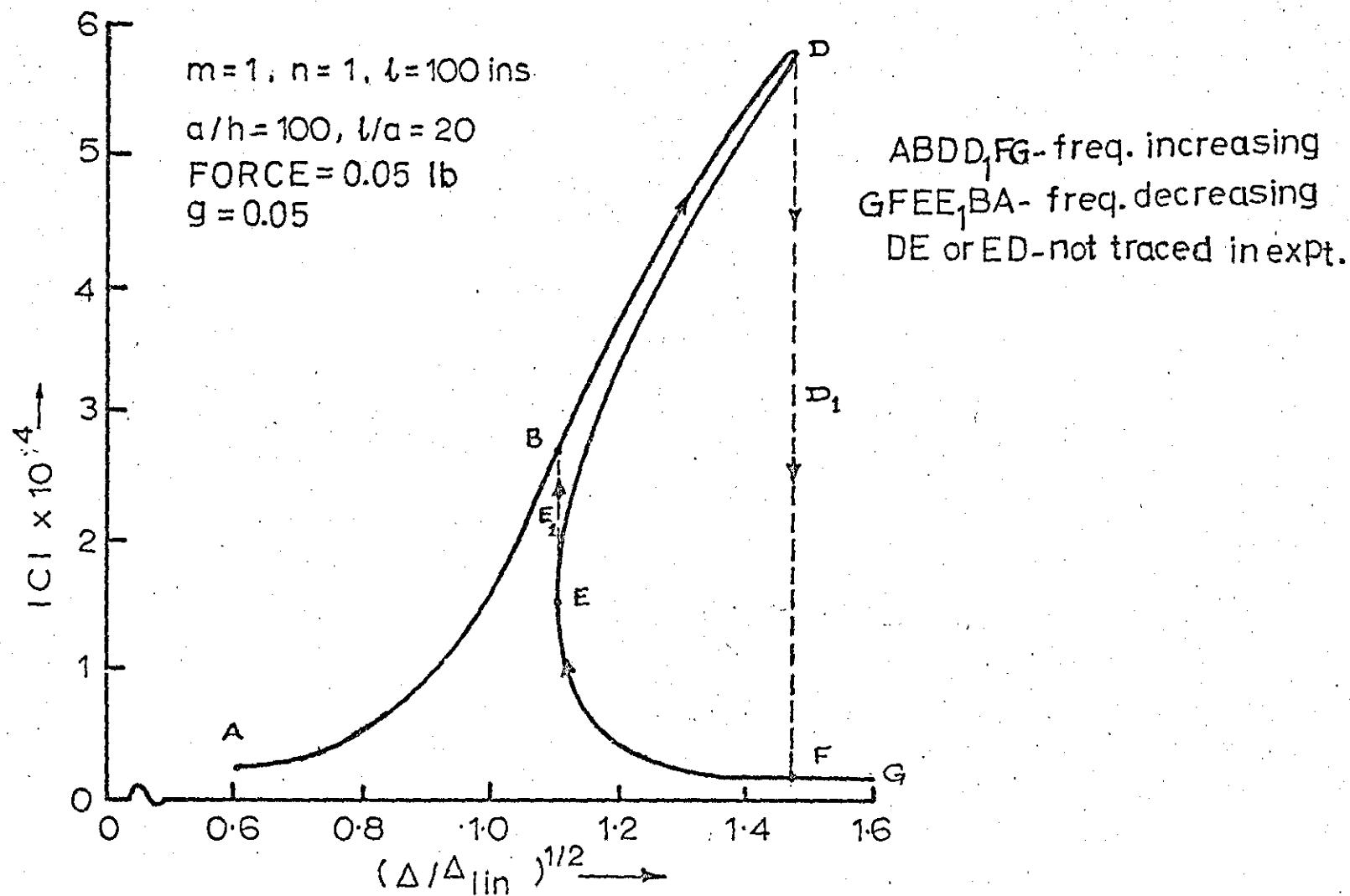
FIG.VI.1. NON-LINEAR RESPONSE WITH DAMPING.
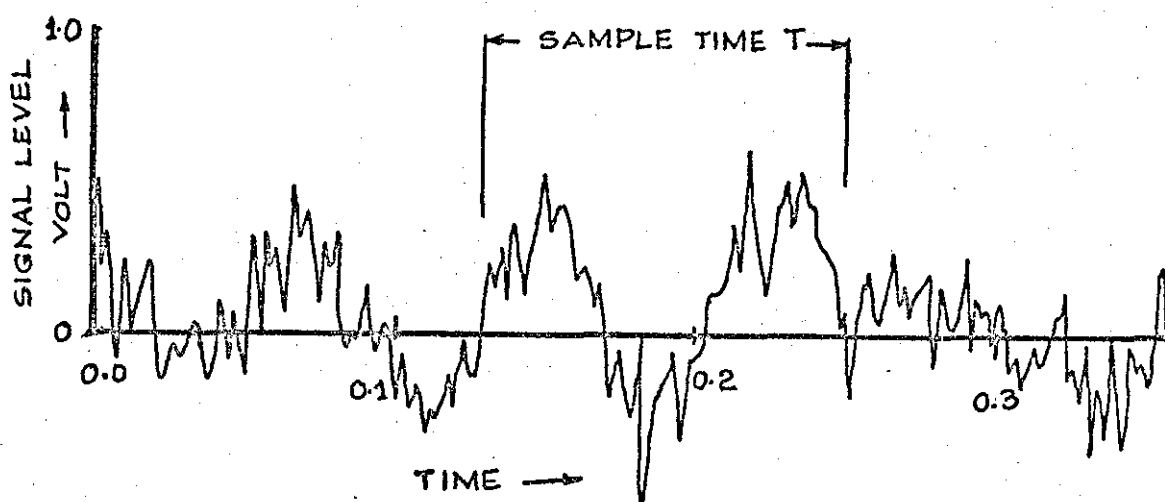
(ORIGINAL SIGNAL)
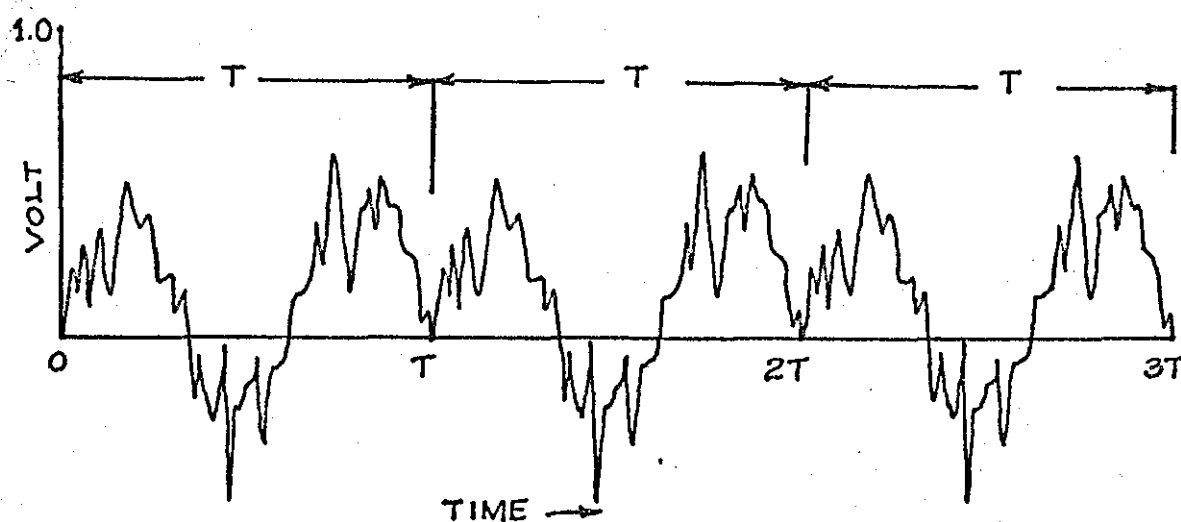
(WHAT DFT IMPLIES)

FIG. VII.1.   EFFECT OF D F T
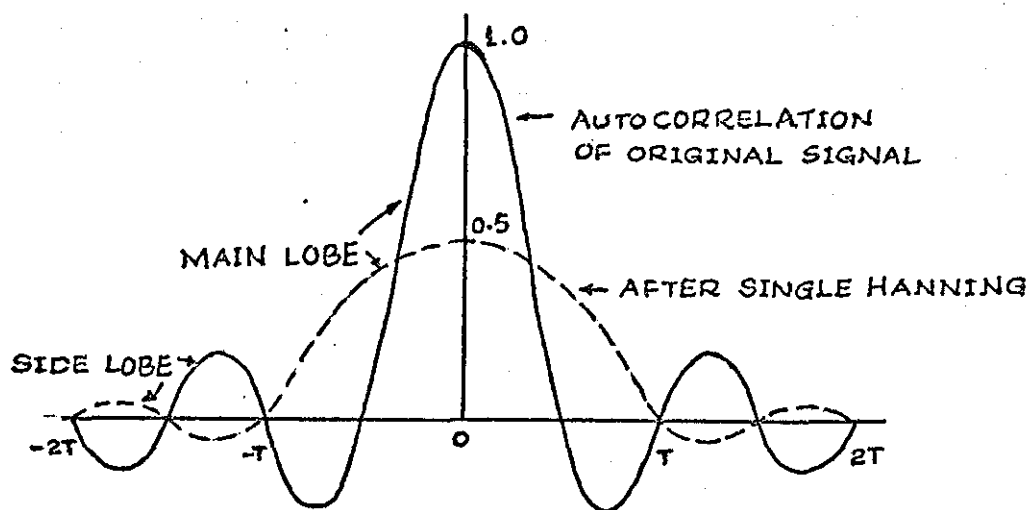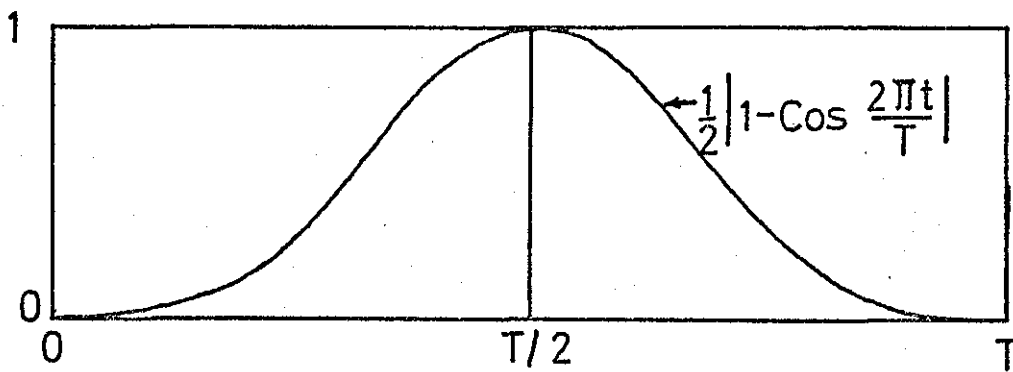
FIG.VII.2 HANNIG WINDOW & ITS EFFECT
NOTE THE REDUCTION IN AMPLITUDE
AND FREQUENCY RESOLUTION

BETZ   MANOMETER
TR   TRANSDUCER
C   CAPSULE
OS   OSCILLATOR
RC   REACTANCE CONVERTER
DCA   DIGITAL AMMETER
MM   MICRO-MANOMETER
UM   U TUBE
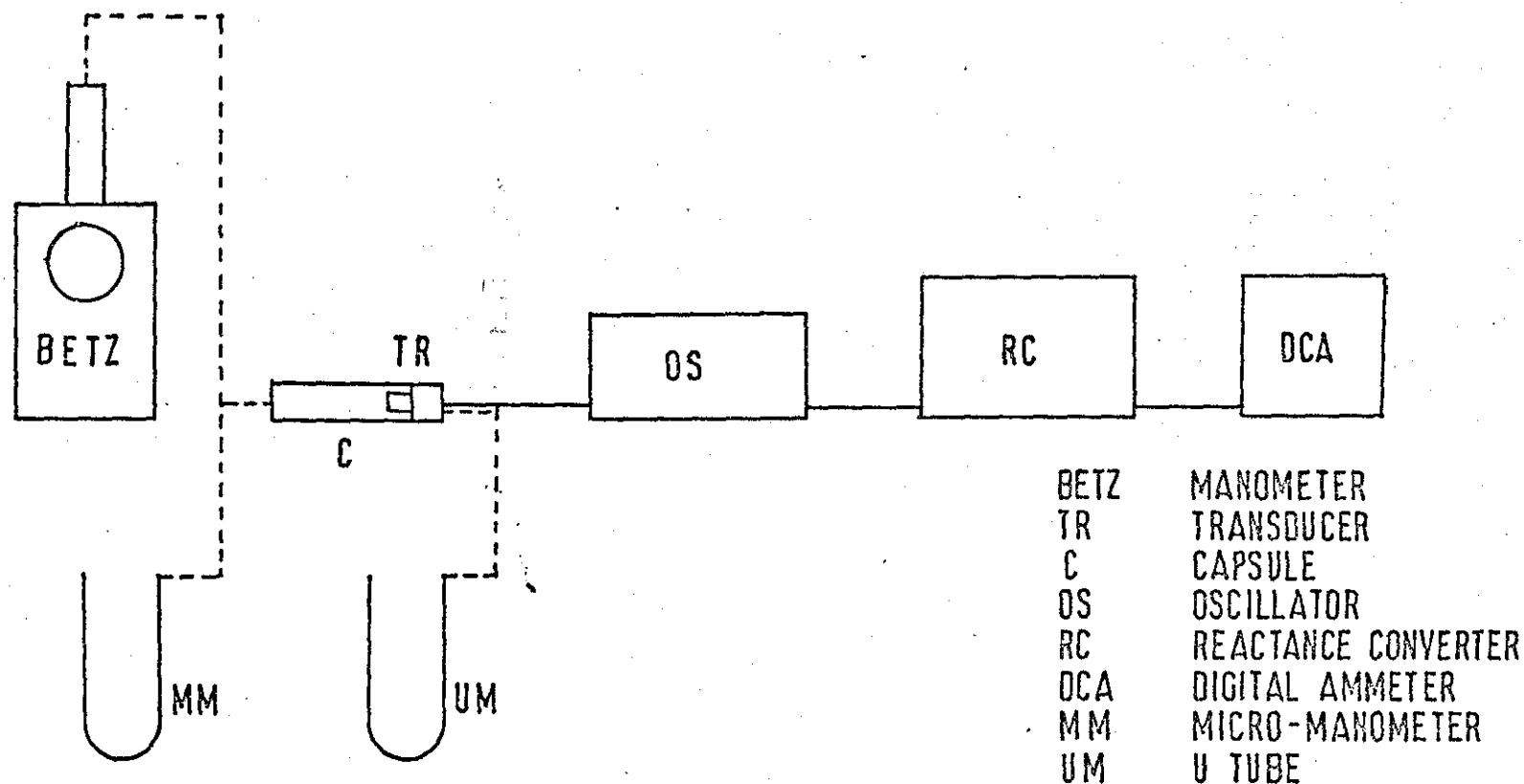
FIGURE VIII·1   SCHEMATIC DIAGRAM OF STATIC CALIBRATION SET-UP
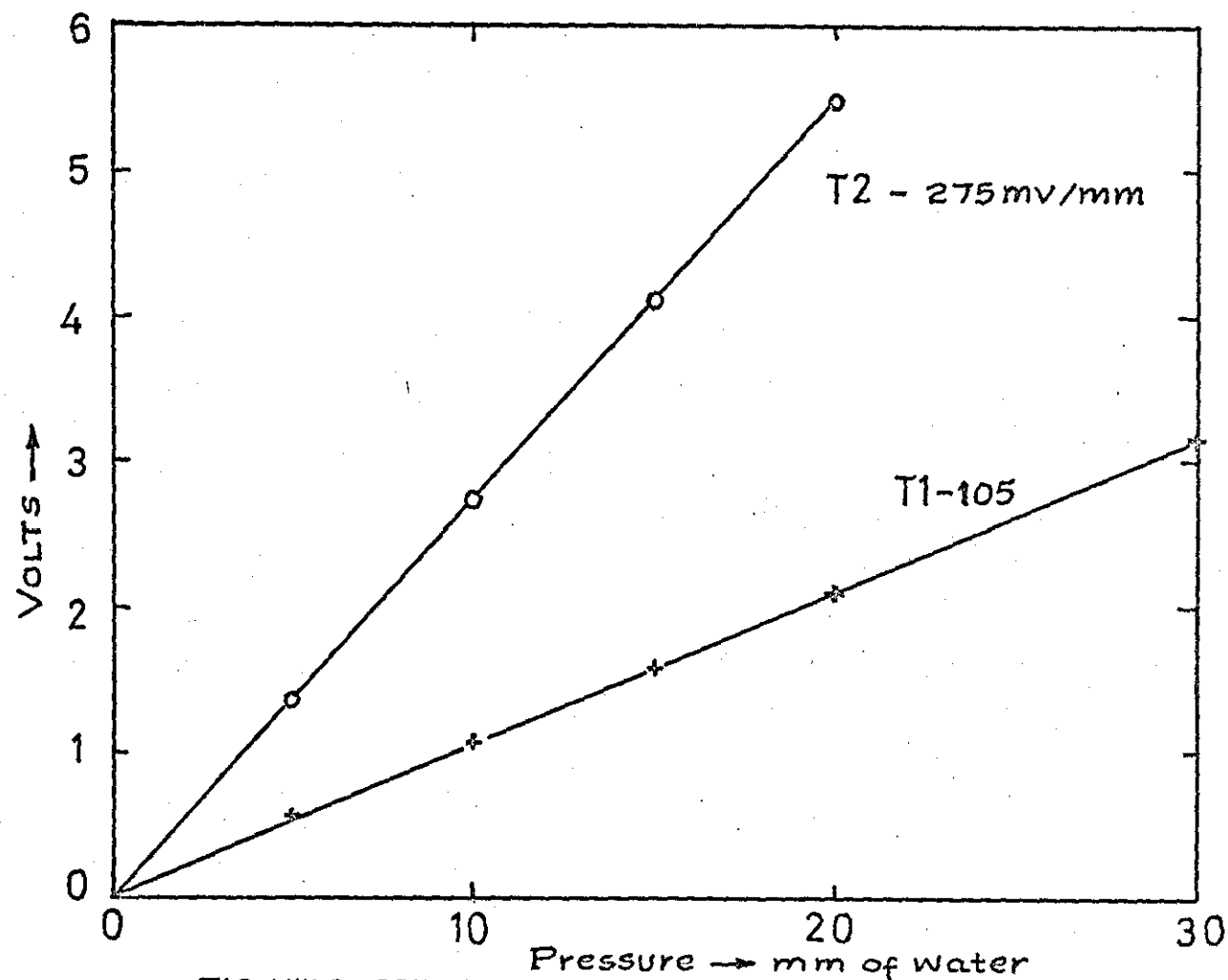
FIG VIII2 STATIC CALIBRATION CURVES FOR PR. TRANSDUCERS.

LR LEVEL RECORDER
SR SINE - RANDOM
         GENERATOR
PA POWER AMPLIFIER
MA MEASURING AMPLIFIER
RE REACTANCE CONVERTER
OS OSCILLATOR
TR TRANSDUCER
LS LOUD SPEAKER
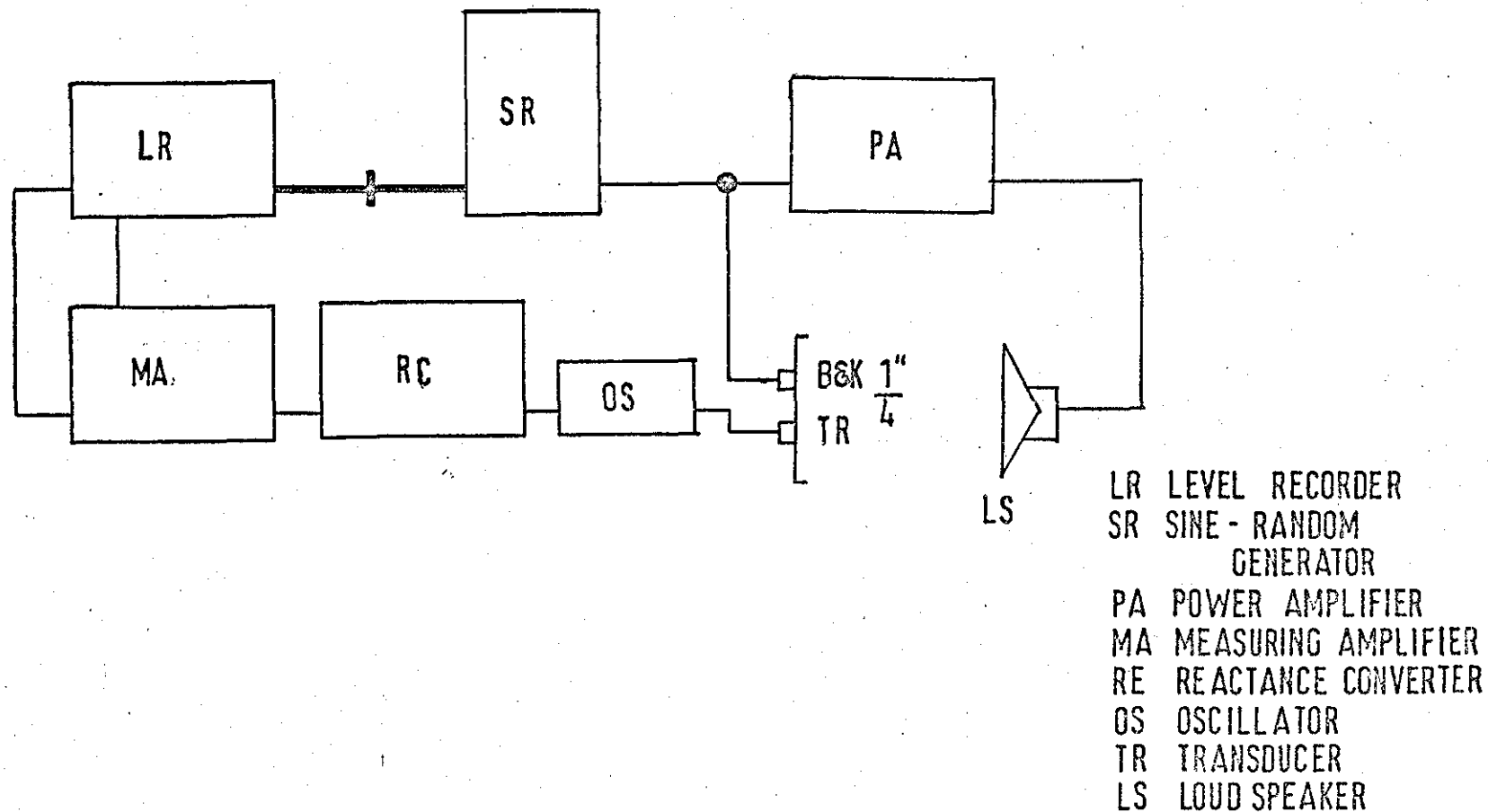
FIGURE VIII·3 SCHEMATIC DIAGRAM OF DYNAMIC CALIBRATION SET-UP
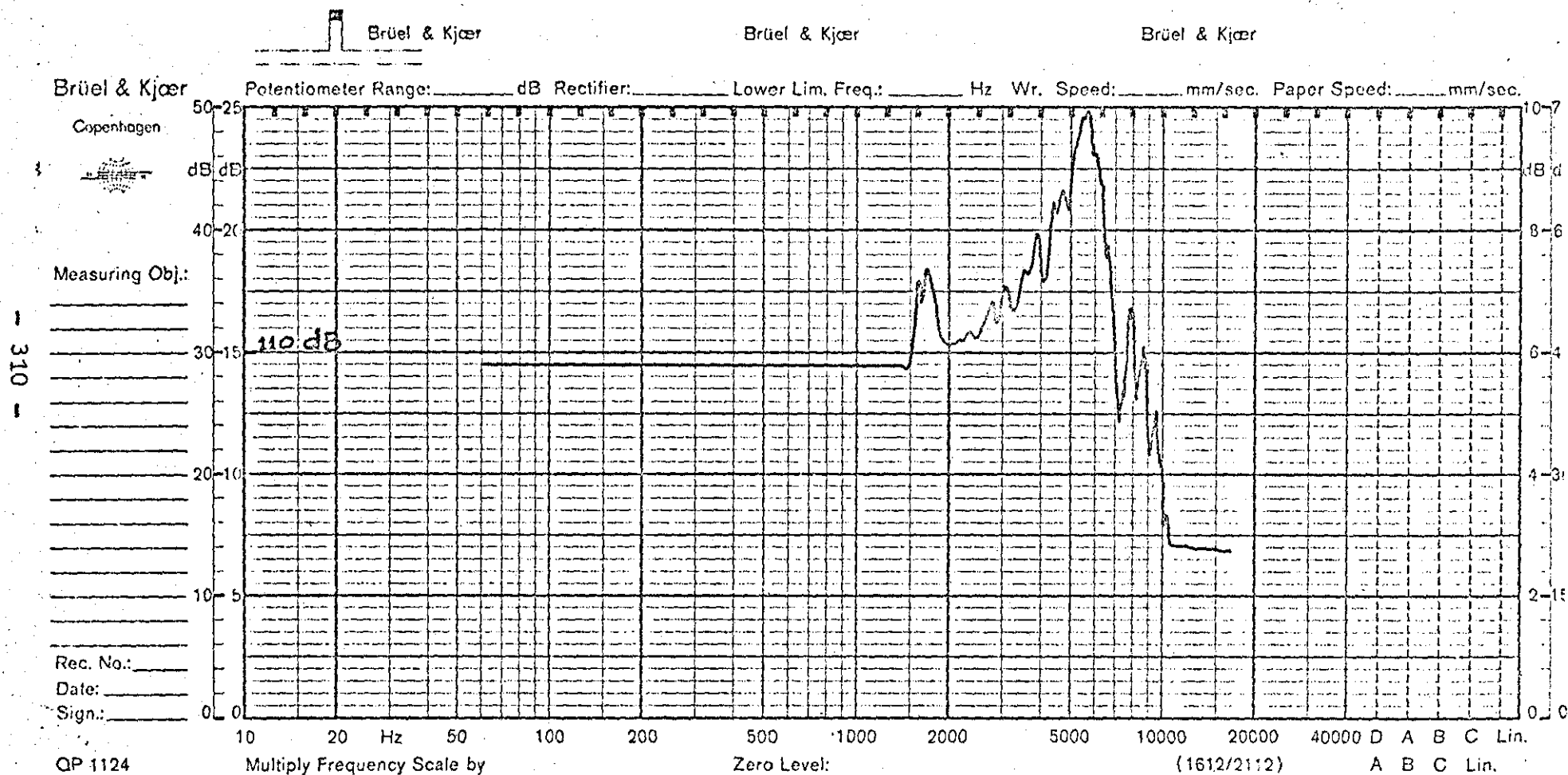
FIG.VIII.4   DYNAMIC RESPONSE CURVE FOR TRANSDUCER T1
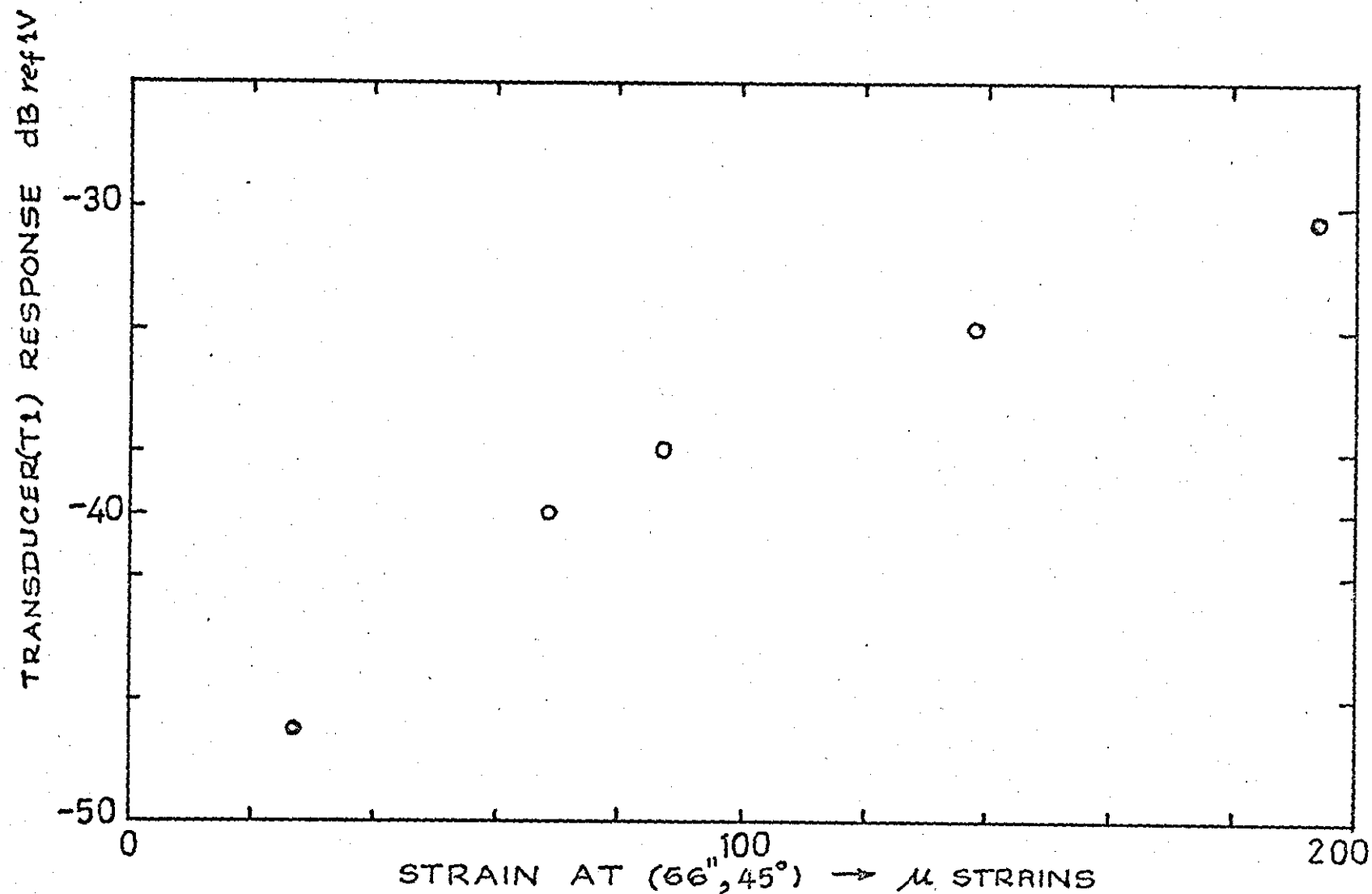
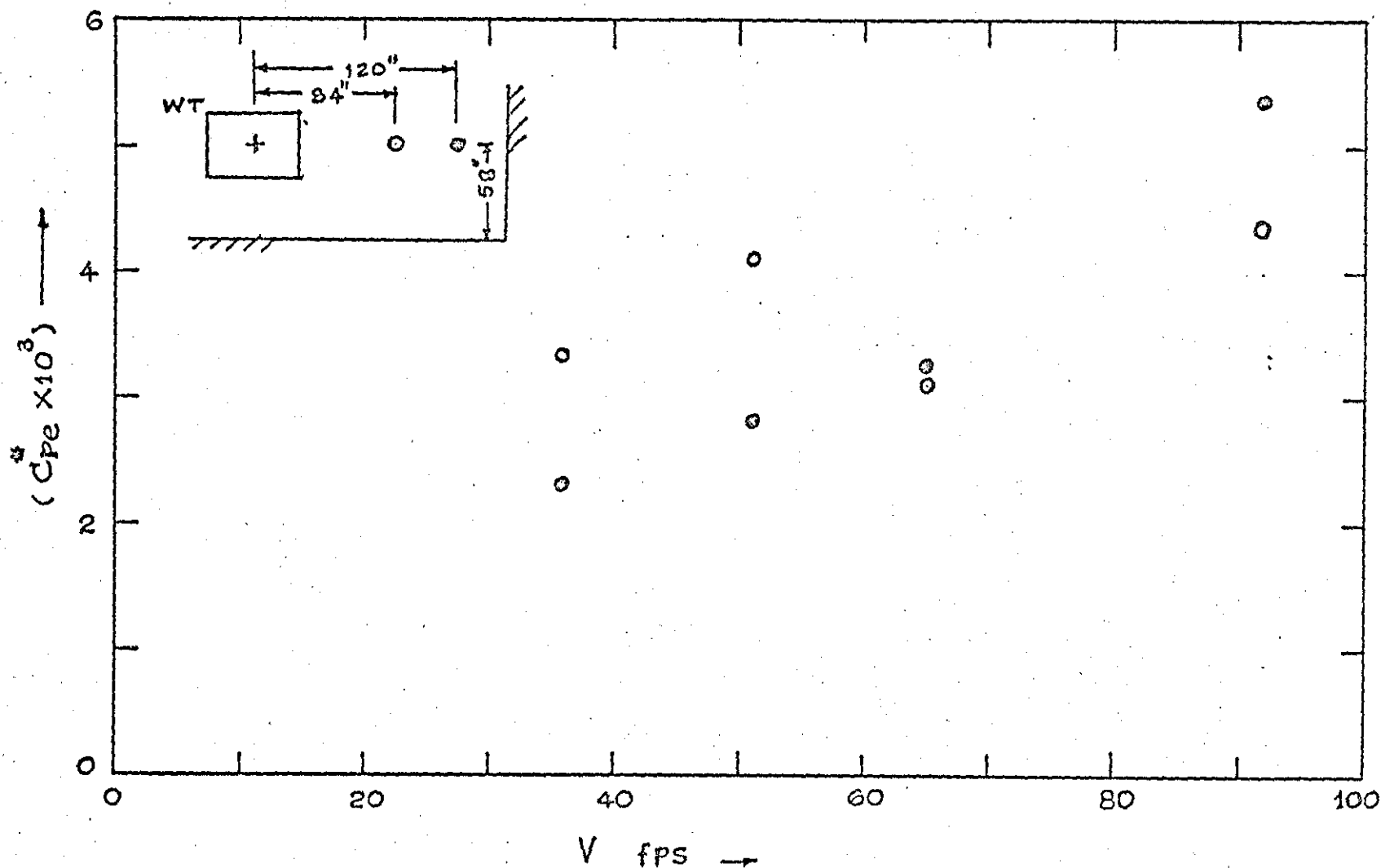FIG. VIII.5   ACCELERATION RESPONSE OF T1 AT TYPICAL STRAINS AT 32·5 Hz

FIG. 1X.1   ACOUSTIC NOISE LEVELS IN THE WIND TUNNEL LAB.

$$V_H \propto V\left(\frac{H}{10}\right)^{\propto}$$
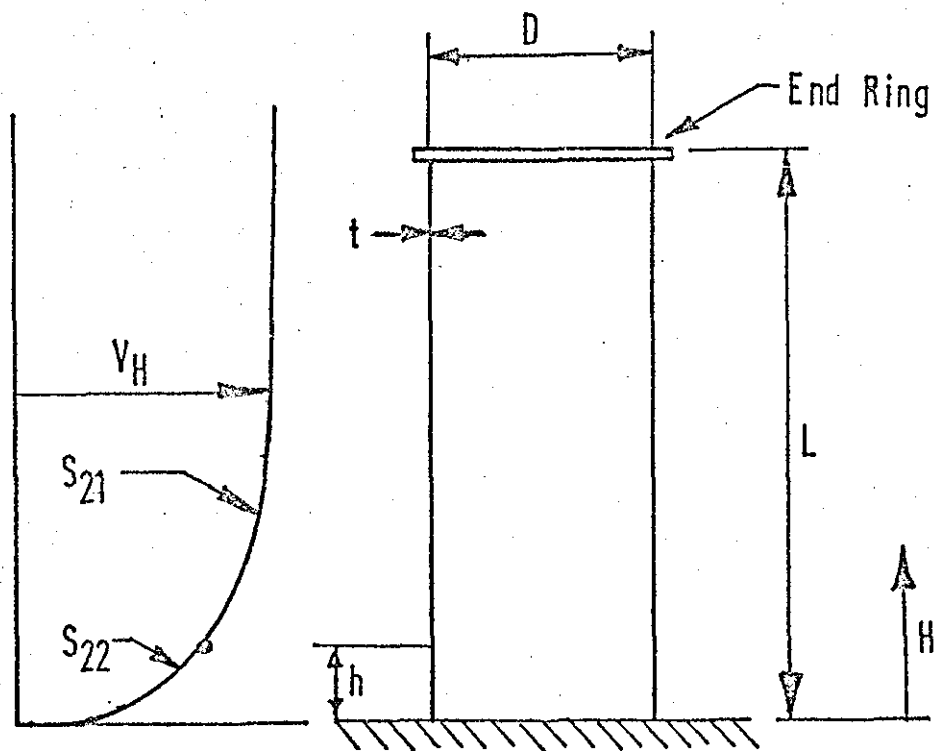
$$S_{21} = K_1 H^{\propto_1}$$

$$S_{22} = K_2 H^{\propto_2}$$

FIG XII 1 WIND VELOCITY PROFILE & SHELL GEOMETRY